Greek Society
of Experimental Mechanics of Materials

1st International Conference

Under the aegis of the European Structural Integrity Society (ESIS)

BOOK OF ABSTRACTS

Stavros K. Kourkoulis and Dimos A. Triantis
(Editors)

Athens, Greece
May 10-12, 2018

1st International Conference

BOOK OF ABSTRACTS

Greek Society of Experimental Mechanics of Materials

With the kind support of:

National Technical University of Athens

Laboratory for Testing and Materials, National Technical University of Athens

Electronic Devices and Materials Laboratory, University of West Attica

Italian Group of Fracture (IGF)

Pericles Theocaris Foundation

Vector Technologies Ltd

Telemetrics Inc.

NEOTEK

Kobatsiaris Bros SA - AMALTHEA

Daikin Klimart A.E.

Greek Society
of Experimental Mechanics of Materials

1st International Conference

Under the aegis of the European Structural Integrity Society (ESIS)

BOOK OF ABSTRACTS

Stavros K. Kourkoulis and Dimos A. Triantis
(Editors)

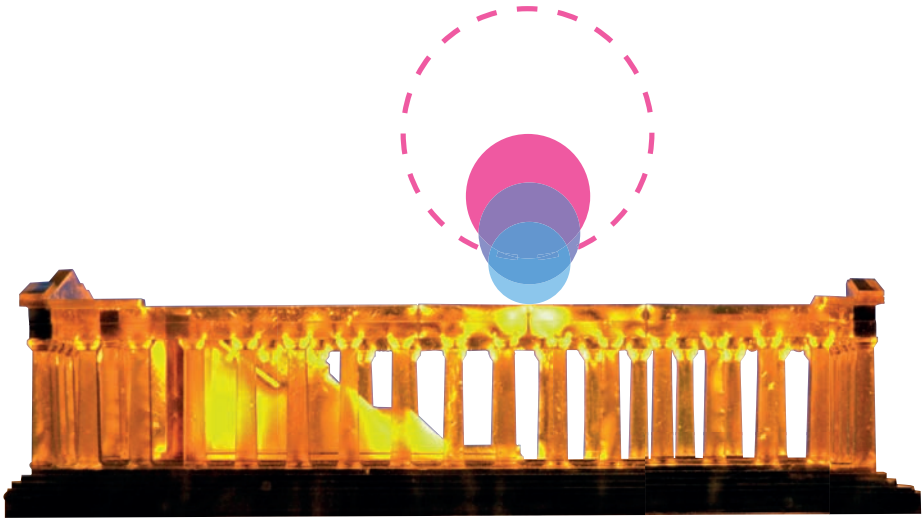

Athens, Greece
May 10-12, 2018

Greek Society of Experimental Mechanics of Materials

1st International Conference
BOOK OF ABSTRACTS

Stavros K. Kourkoulis and Dimos A. Triantis
(Editors)

Athens, Greece
May 10-12, 2018

ISSN: 2623-3541

Contents

Preface

Experimental Mechanics of Materials is currently one of the most rapidly developing areas of Mechanics, due to the extended use of novel techniques for the detection, collection and recording of experimental data, and thanks to the explosive development of computer science which enables rapid analysis and exploitation of large amounts of data. However, the effective implementation of experimental protocols is becoming increasingly difficult, rendering the cooperation of research groups of interdisciplinary background absolutely necessary.

In our country, there are quite a few research groups which are actively and successfully involved in the area of *Experimental Mechanics of Materials*. However, the interaction among them is quite limited, resulting to waste of valuable resources, in both human and financial terms. As a matter of fact, similar experimental protocols are often implemented independently in various research centers, institutes or universities. In this context, it is clear that the establishment of a closer communication and cooperation between the Greek research teams is imperative. The foundation of the *Greek Society of Experimental Mechanics of Materials* (GSEMM) is a first - even though small - step in this direction.

One of the founding objectives of the GSEMM is to strengthen the interaction between the various research teams and to disseminate the outcomes of the experimental protocols. The GSEMM is already representing Greece in the *European Structural Integrity Society* (ESIS), and has also applied for membership in the *Danubia Adria Society on Experimental Methods* (DAS) (the application will be considered at the 35th DAS Symposium, in September 2018). One of the tools available for GSEMM to achieve its objectives is the organization of workshops, seminars and conferences. As provided in the GSEMM statute, the international Conference will be regularly held every two (2) years.

This Volume contains the extended abstracts of the articles presented in the *1st International Conference of the Greek Society of Experimental Mechanics of Materials*, which will hopefully be the first of a series of conferences, contributing to the fulfilment of the set objectives. In this first Conference, conducted under the aegis of ESIS, more than 100 articles were submitted for consideration, out of which 78 were accepted by the scientific committee for presentation, on the basis of their scientific soundness and the relevance of their content with Experimental Mechanics of Materials. The articles in this volume appear according to the order of presentation in the Conference's programme.

We wish to extend our cordial thanks to the members of the International Scientific Committee of the Conference for their important contribution to the review of the submitted abstracts, and to the members of the Organizing Committee for their efforts for the smooth coordination and preparation of the Conference. Also we would like to thank the National Technical University of Athens (NTUA) for hosting the Conference, the "*Laboratory for Testing and Materials*" of NTUA, the "*Electronic Devices and Materials Laboratory*" of the University of West Attica, the "*Italian Group of Fracture*", and the "*Pericles S. Theocaris Foundation*" for offering funding to support the organization of the Conference. Furthermore, thanks are due to the companies "*Vector Technologies Ltd*", "*Telemetrics Inc*", "*NEOTEK*", "*Kobatsiaris Bros SA - Amaltheia*", and "*Daikin Klimart SA*" for their kind sponsorship.

Last, we wish to deeply thank all those who warmly embraced the initiative of the foundation of GSEMM and all those who submitted their work and presented their articles, contributing to the success of the *1st GSEMM Conference*.

Stavros K. Kourkoulis and Dimos A. Triantis

Editors

Conference Chairs

Stavros K. Kourkoulis, Professor, National Technical University of Athens

Dimos A. Triantis, Professor, University of West Attica

International Scientific Committee

The International Scientific Committee is composed of the National Representatives in the European Structural Integrity Society (ESIS) as follows:

R. Pippan, Austria

J. Pokluda, Czech Republic

S. Kourkoulis, Greece

P. Trampus, Hungary

L. Banks-Sills, Israel

F. Iacoviello, Italy

Z. Zhang, Norway

D. Kocańda, Poland

L. F. Galrão dos Reis, Portugal

P. M. Guimarães Pires Moreira, Portugal

L. Marsavina, Romania

A. Sedmak, Serbia

N. Gubeljak, Slovenia

A. Martín-Meizoso, Spain

A. J. Brunner, Switzerland

Organizing Committee

Nikolaos Alexopoulos, Assistant Professor, University of the Aegean

Cimon Anastasiadis, Professor, University of West Attica

Antonios Kyriazopoulos, Associate Professor, University of West Attica

Christos Markides, PhD, National Technical University of Athens

Dimitrios Ninos, Professor, University of West Attica

Ermioni Pasiou, PhD, National Technical University of Athens

Ilias Stavrakas, Professor, University of West Attica

Plenary Lectures

WOVEN MULTI-DIRECTIONAL COMPOSITE: MODE I FATIGUE DELAMINATION PROPAGATION

L. Banks-Sills and I. Simon
School of Mechanical Engineering, Tel Aviv University, Ramat Aviv, Israel
President of the Executive Committee of the European Structural Integrity Society

Abstract

Double cantilever beam (DCB) specimens fabricated from 15 plies of a plain woven prepreg (G0814/913) arranged in a multi-directional (MD) layup were tested by means of constant amplitude fatigue cycles under displacement control. The prepreg consists of carbon fibers in an epoxy matrix. The plies were stacked in a multi-directional arrangement in which each ply was rotated by 45^o in the ply plane with respect to each adjacent ply. Eight specimens were tested. Four different displacement cyclic ratios R_d were used, where

$$R_d = \frac{d_{min}}{d_{max}} \tag{1}$$

with d_{min} and d_{max} are the minimum and maximum displacements in a fatigue cycle. These included 0.1, 0.33, 0.5 and 0.75. It may be noted that the tests were carried out with frequencies between 4 and 6 Hz, many of them running continuously up to 3,000,000 cycles.

The delamination propagation rate da/dN was calculated from the experimental data and plotted using a modified Paris law with different functions of the mode I energy release rate $\mathcal{G}_I$. In Fig.1a, results of the delamination propagation rate da/dN are plotted vs. the range of the effective energy release rate given by

$$\Delta\hat{\mathcal{G}}_{Ieff} = \left(\sqrt{\hat{\mathcal{G}}_{Imax}} - \sqrt{\hat{\mathcal{G}}_{Imin}}\right)^2 \tag{2}$$

where $\hat{\mathcal{G}}_{Imax}$ and $\hat{\mathcal{G}}_{Imin}$ are, respectively, the maximum and minimum values of the mode I energy release rate which has been normalized with respect to the fracture toughness. It may be observed in Fig.1a that there is a good correspondence between results obtained with the same R_d-ratio.

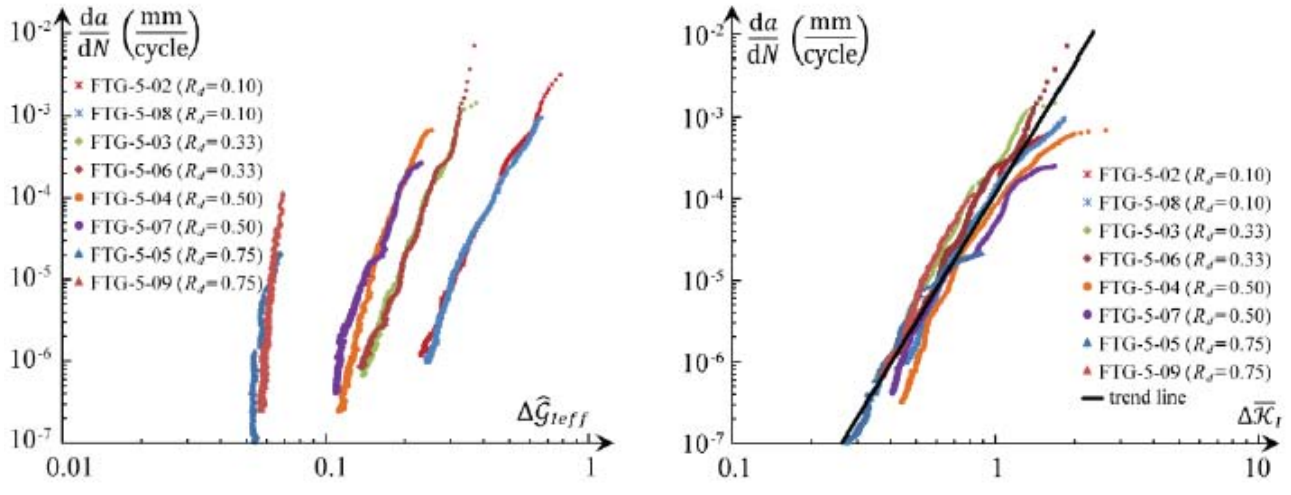

Figure 1. Delamination propagation rate as a function of (a) $\Delta\hat{\mathcal{G}}_{Ieff}$ and (b) $\Delta\bar{\mathcal{K}}_I$.

Moreover, the delamination propagation rate increases as the R_d-ratio increases for a given value of $\Delta\hat{\mathcal{G}}_{\text{Ieff}}$. Using a different parameter, it is possible to obtain a master curve for all R_d-ratios. Define

$$\Delta\bar{\mathcal{K}}_{\text{I}} = \frac{\sqrt{\hat{\mathcal{G}}_{\text{Imax}}} - \sqrt{\hat{\mathcal{G}}_{\text{Ithr}}}}{\sqrt{1-\sqrt{\hat{\mathcal{G}}_{\text{Imax}}}}} \tag{3}$$

where $\hat{\mathcal{G}}_{\text{Ithr}}$ is the normalized value of the threshold energy release rate. Using the parameter in Eq.(3), it may be observed in Fig.1b that the eight curves for different R_d-ratios unify into one master curve.

ADVANCED LABORATORY TESTING OF WEAK ROCKS TIME DEPENDENCE - MODELLING - ENGINEERING APPLICATIONS

G. Barla
Former Professor of Rock Mechanics and Numerical Modelling in Geotechnical Engineering
Politecnico di Torino, Torino, Italy
Editor of Rock Mechanics and Rock Engineering

Abstract

Time dependent behavior of weak rocks is of interest in rock mechanics and rock engineering. Typical applications are creeping slopes and landslides. This is the case of Deep Seated Gravitational Slope Deformations (DSGSDs), i.e. slow moving slopes with low rate displacement and cumulative large displacements. Another relevant example refers to tunnels in squeezing conditions, which implies large time dependent convergences during tunnel excavation and yielding in some zones around the tunnel, exceeding the limiting shear stress at which creep starts.

A very important component in investigating the time dependent behavior of rock materials is laboratory testing with advanced methods and equipment as described in the present lecture. The attention is dedicated first to an innovative servo-controlled triaxial apparatus (Fig.1a), which allows triaxial compression tests to be performed under closely controlled conditions [1]. Also described is an innovative servo controlled direct shear apparatus, which has been developed for testing rock materials under high stress, including rock joints, eventually filled [2].

Also important is the role of constitutive modelling, which is a necessary and essential tool for understanding and describing the rock time dependent behavior in view of engineering applications. With this in mind, the Stress Hardening ELastic VIscous Plastic - SHELVIP - model is presented [3]. This constitutive model couples the elastoplastic and time-dependent behavior by using a plastic yield surface and the definition of a state of overstress referred to a viscoplastic yield surface (Fig. 1b). The advantage of this model with respect to analogical or mechanical rheological models frequently used for describing the time dependent behavior is highlighted.

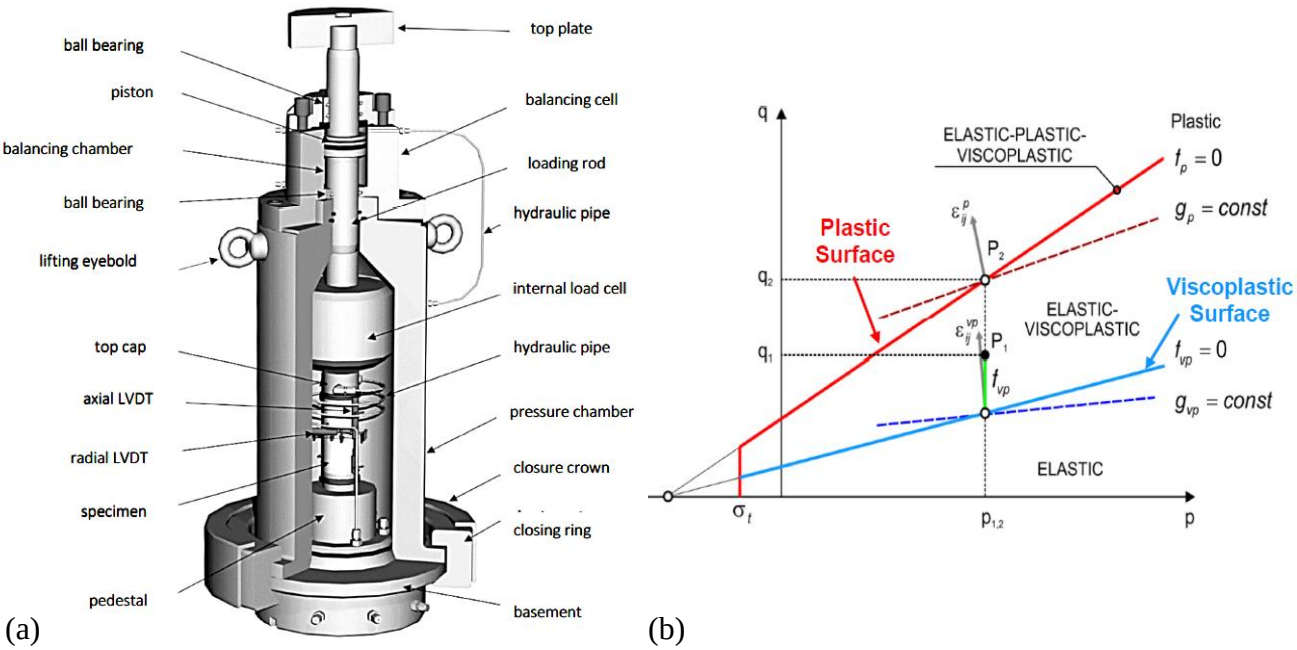

Figure 1. (a) Innovative High Pressure Triaxial Apparatus [1]. (b) SHELVIP constitutive model with q deviatoric stress and p mean stress [3].

The use of the SHELVIP model when dealing with "Complex Rock Formations" is described. This is the case of: (1) Carboniferous Formation from the new Mont Cenise Base Tunnel between Italy and France. (2) Tectonised Clay Shales in the Raticosa Tunnel, along the Bologna-Florence AV (High Speed) railway line in Italy. (3) Siltstones from the Rogun Hydroelectric Project in Tajikistan. (4) Meta-siltstones from the Kishanganga Hydroelectric Project Headrace Tunnel in Kashmir, India. Fig.2a shows a comparison between the experimental and numerical results obtained for Tectonised Clay Shales.

With the intent to highlight some rock-engineering applications, two case studies are discussed, where the design analyses performed rely significantly on the investigative tools previously described, including the SHELVIP model. The first case is the reactivation of a DSGSD during the excavation of a large size twin tunnel along the Variant of Autostrada A1, in central Italy [4]. The second case is the Mont Cenise Base Tunnel, between Saint Martin La Porte and La Praz in France. This tunnel crosses the Carboniferous Formation under a 600 m depth of cover, i.e. twice the cover along the Saint Martin La Porte access adit (Fig.2b), where very large, time dependent displacements were experienced and a dedicated support approach was adopted [5].

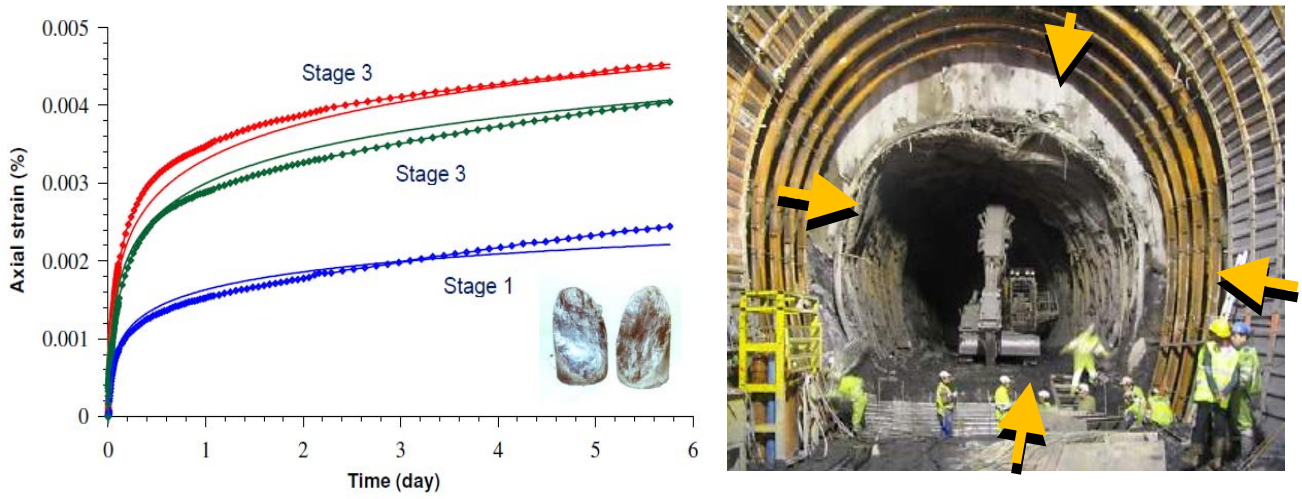

(a) (b)

Figure 2. (a) Multistage triaxial creep tests on Tectonised Clay Shales. The dotted curves show the results of testing, while the continuous lines are the results of calibration with SHELVIP. (b) "Squeezing" in the Saint Martin La Porte access adit along the Mont Cenis Base Tunnel.

References

[1] G. Barla, M. Barla and D. Debernardi (2010). New triaxial apparatus for rock, *Rock Mechanics and Rock Engineering*, **43**, 225-230.

[2] G. Barla, M. Barla and M. E. Martinotti (2010). Development of a new direct shear testing apparatus, *Rock Mechanics and Rock Engineering*, **43**, 117-122.

[3] D. Debernardi and G. Barla (2009). New viscoplastic model for design analysis of tunnels in squeezing conditions, *Rock Mechanics and Rock Engineering*, **42**, 259-288.

[4] G. Barla (2017). Numerical modelling of deep-seated landslides interacting with man-made structures, in *Proceedings of 15th International Conference of the International Association for Computer Methods and Advances in Geomechanics (15th IACMAG)*, October 19-23, Wuhan, China.

[5] G. Barla, M. Bonini and D. Debernardi (2010). Time dependent deformations in squeezing tunnels, *International Journal of Geoengineering Case Histories*, **2**, 40-65.

FATIGUE CRACK PROPAGATION IN DUCTILE CAST IRONS

F. Iacoviello and V. Di Cocco
Università di Cassino e del Lazio Meridionale, DiCeM,
via G. Di Biasio 43, 03043,
Cassino (FR), Italy
Vice-President of the Executive Committee of the European Structural Integrity Society

Abstract

Ductile Cast Irons (DCIs) are commonly considered as really interesting materials, due to their interesting combination of mechanical properties and technological peculiarities. Characterized by the high castability that is a cast irons technological peculiarity, DCIs show a very interesting combination of good mechanical properties (e.g., tensile strength and fatigue resistance). These properties are strongly influenced by the DCIs microstructure, that is defined both by the matrix (considering the morphological peculiarities like phases distribution, grains dimensions etc.) and by the graphite nodules elements, that are characterized by their shape, dimension and distribution. In addition, the presence of defects (like pores, both micro and macro) can strongly affect the DCIs mechanical behavior (e.g., considering large castings).

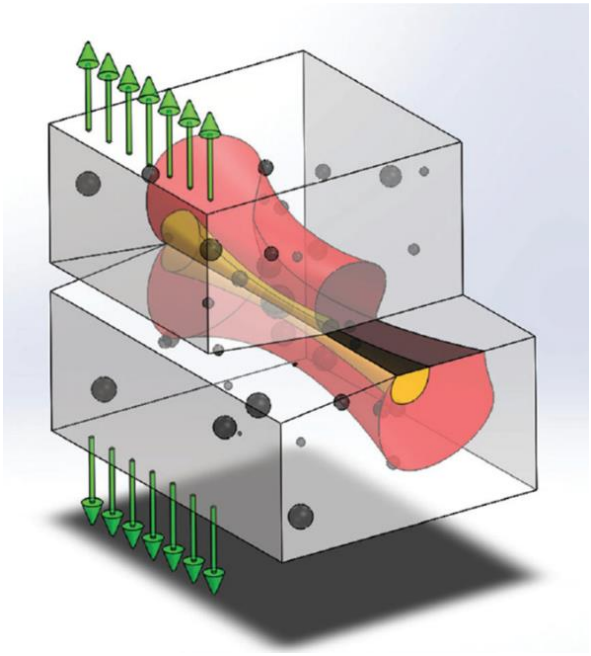

Figure 1. Ferritic DCI: reversed plastic zone (yellow), monotonic plastic zone (red), elastic zone (grey) and graphite nodules (black) ahead a fatigue crack tip.

Graphite nodules are often considered as voids embedded in a ductile matrix, but recent analysis showed that, in some matrix microstructures, matrix-graphite nodules debonding is not the most important damaging micromechanism: due to the presence of a mechanical properties gradient inside the graphite nodules, the initiation and propagation of cracks inside graphite nodules is often observed (so called “onion like mechanism”).

In this presentation the role played by the graphite elements is reviewed, starting from the simplest approach (voids embedded in a more or less ductile matrix) to more recent models that take into account the presence of mechanical gradient properties inside the graphite elements.

During the fatigue crack propagation, some different zones are obtained ahead the crack tip (reversed plastic zone, monotonic plastic zone, elastic zone) and the DCIs fatigue crack propagation depends on the interactions of these zones with the graphite nodules and the different phases of the metal matrix.

Experimental Biomechanics

ASSESSMENT OF THE RELIABILITY OF SHEAR-WAVE-BASED CALCULATIONS OF THE IN-VIVO STIFFNESS OF PLANTAR SOFT TISSUE

P. Chatzistergos, S. Behforootan, R. Naemi and N. Chockalingam
School of Life Sciences and Education, Staffordshire University, Stoke-on-Trent, United Kingdom

1. Introduction

Shear wave (SW) elastography is a non-invasive, ultrasound-based technique for the quantitative assessment of soft tissue stiffness. It involves the generation of SWs inside the imaged tissue and the measurement of their propagation speed (C_{sw}) as they expand laterally in the field of view. C_{sw} is also used to assess the tissues' shear modulus (G) and Young's modulus (E):

$$E= 3G= 3\rho C_{sw}^2 \quad (1)$$

where ρ is the tissue's density (for soft tissues ρ ≈1 kg/m^3).

SW elastography has been successfully integrated into clinical practice for the diagnosis of conditions that are strongly associated with altered tissue biomechanics such as chronic liver disease, breast cancer etc. However, its clinical use remains relatively limited mainly because of considerations about reliability and operator dependency of results.

The mechanical characteristics of the soft tissues of the sole of the foot (i.e., plantar soft tissue) are significantly affected by conditions such as diabetes, highlighting the need for reliable, clinically relevant methods to assess their biomechanics. In this context, this study combines in-vivo mechanical testing with Finite Element (FE) modelling to assess, for the first time, the reliability of SW-based calculations of Young's modulus of the plantar soft tissue.

2. Methods

A bespoke ultrasound indentation device was used to test the heel-pads of five healthy volunteers under quasi-static loading. During testing, the participants' feet were fixed on the loading frame and the plantar soft tissue of the heel was compressed through a linear-array ultrasound probe (SL 15-4 Linear transducer, SuperSonic Imagine Ltd) (Fig.1). The applied force was recorded using a load cell while C_{sw} and conventional B-mode ultrasound images were recorded by the ultrasound unit. After the end of the tests, B-mode ultrasound images were used to measure the initial thickness of the heel pad, and its bulk deformation to calculate the force/deformation graph of the indentation test. SW images for zero compression were used to assess the tissue's C_{sw} and Young's modulus (E_{sw}).

A previously validated technique for the inverse engineering of subject specific material coefficients of the heel-pad was used [1]. According to this technique, subject-specific FE models of the indentation test were designed based on the recorded ultrasound images. The heel bone was assumed to be completely rigid while the mechanical behavior of the heel pad was simulated using the Ogden hyperelastic (1st order) material model:

$$W = \frac{\mu}{\alpha}\left(\bar{\lambda}_1^{\alpha} + \bar{\lambda}_2^{\alpha} + \bar{\lambda}_3^{\alpha} - 3\right) + \frac{1}{d}(J-1)^2 \quad (2)$$

where $\bar{\lambda}_p^{\alpha}\,(p=1,2,3)$ is the deviatoric principal stretches, J is the determinant of elastic deformation gradient and μ, α and d are material coefficients. Assuming that the heel pad is nearly incompressible the values of the material coefficients were inverse engineered to minimize the difference between the numerical and the experimental force/deformation curves of the indentation tests. The subject specific coefficients were then used to calculate the tissue's stress/strain graph and its initial slope (E_{FE}). Pearson's correlation analysis was performed to assess the assosiation between SW- and FE-based calculations of Young's modulus.

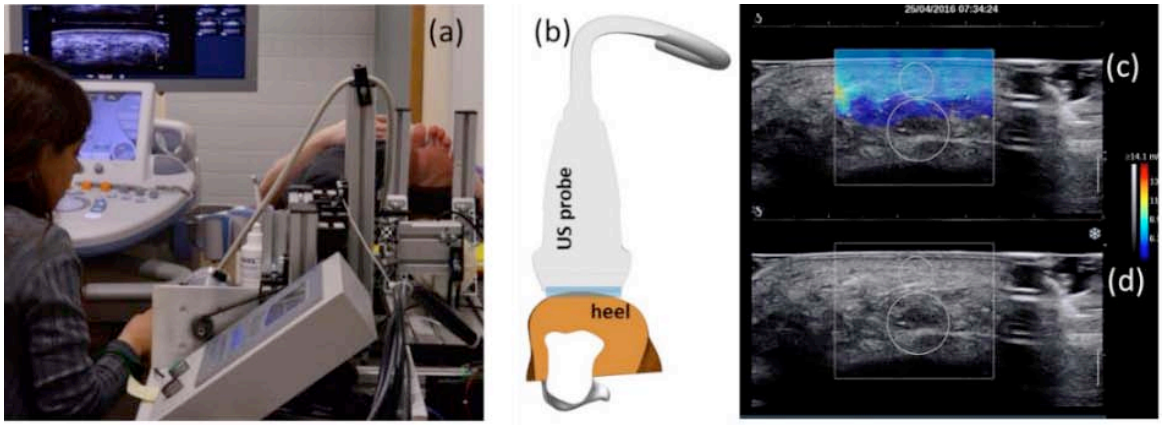

Figure 1. (a) The in-vivo testing set-up and (b) the relative position of heel and ultrasound probe. (c) Typical output images of SW elastography and (d) conventional B-mode ultrasound imaging.

3. Results

The average(±stdev) of C_{sw} was equal to 7.4(±1.5) m/sec. Average(±stdev) values for the SW-based and FE-based Young's modulus was E_{sw}=167(±64) kPa and E_{FE}=520(±330) kPa, respectively (average difference of 62%(±15%)). Pearson's correlation revealed a strong positive correlation between C_{sw} and E_{FE} (r=0.848, n=5, p=0.035).

4. Discussion and conclusions

The calculation of soft tissue stiffness from C_{sw} (Eq.1) is based on the assumption that SWs propagate in an incompressible, homogeneous, isotropic and linearly elastic material [2, 3]. Even though no tissue in the human body fully meets these conditions, SW elastography has been proven to provide satisfactory reliable estimations of stiffness for relatively large uniform tissues such as the liver [4].

In the case of the plantar soft tissue, the results of this study revealed a significant and consistent underestimation of the tissue's initial in-vivo stiffness. At the same time, SW speed was found to be strongly correlated to in-vivo stiffness. According to the manufacturers guidelines C_{sw} and E_{sw} were measured for zero compression. Because of this, the E_{SW} measured here can only be considered as an estimation of the initial slope of the tissue's stress/strain graph.

These findings indicate that the direct assessment of plantar soft tissue's Young's modulus based on C_{sw} is unreliable and should be avoided. However, this does not reduce the value and clinical relevance of C_{sw} which could be a very useful measurement in comparative studies.

Acknowledgment

Technical support from SuperSonic Imagine Ltd. is acknowledged.

References

[1] S. Behforootan, P. E. Chatzistergos, N. Chockalingam and R. Naemi (2017). A clinically applicable non-invasive method to quantitatively assess the visco-hyperelastic properties of human heel pad, implications for assessing the risk of mechanical trauma, *J Mech Behav Biomed Mater*, **68**, 287-295.

[2] J. Bercoff, M. Tanter and M. Fink (2004). Supersonic shear imaging: A new technique for soft tissue elasticity mapping, *IEEE Trans Ultrason Ferroelectr Freq Control*, **51**, 396-409.

[3] E. Widman, E. Maksuti, D. Larsson, M. W. Urban, A. Bjällmark and M. Larsson (2015). Shear wave elastography plaque characterization with mechanical testing validation: A phantom study, *Phys Med Biol*, **60**, 3151-3174.

[4] S. Bota, H. Herkner, I. Sporea, P. Salzl, R. Sirli and A. Neghina (2013). Meta-analysis: ARFI elastography versus transient elastography for the evaluation of liver fibrosis, *Liver Int*, **33**, 1138-1147.

AN INDENTATION METHODOLOGY FOR MEASURING THE ELASTIC PROPERTIES OF BIOLOGICAL PATCHES USED IN HUMAN CAROTID ENDARTERECTOMY

I. D. Gavardinas[1] and A. E. Giannakopoulos[2]
[1] Department of Civil Engineering, University of Thessaly, Volos, Greece
[2] Mechanics Division, National Technical University of Athens, Athens, Greece

1. Introduction

Carotid artery atherosclerosis and stenosis is an important public health issue. Atherosclerosis is one of the most common cardiovascular diseases. It is described as artery "thickening", leading even to occlusion, thus causing a cessation of blood flow. This process takes place over a long period, e.g., 50 to 60 years. The succeeding decrease of the artery lumen is also known as stenosis. Atherosclerosis is a gradual calcification phenomenon, during which a stiff, bone-like deposit is accumulated, termed as the atheromatous or atherosclerotic plaque.

One of the techniques mostly preferred for the treatment of atherosclerosis is carotid endarterectomy (CEA). It entails a longitudinal arteriotomy, which extends beyond the plaque, both proximally and distally, in order to remove the plaque. It is typically followed by the use of a patch angioplasty closure technique. A patch is sutured around the incision and mounted on the healthy artery wall so as to ensure continuity and normal operation of the artery. A schematic of CEA is illustrated in Fig.1. There are several types of patches used in CEA, synthetic (Dacron, PTFE) or biological (bovine pericardium) ones.

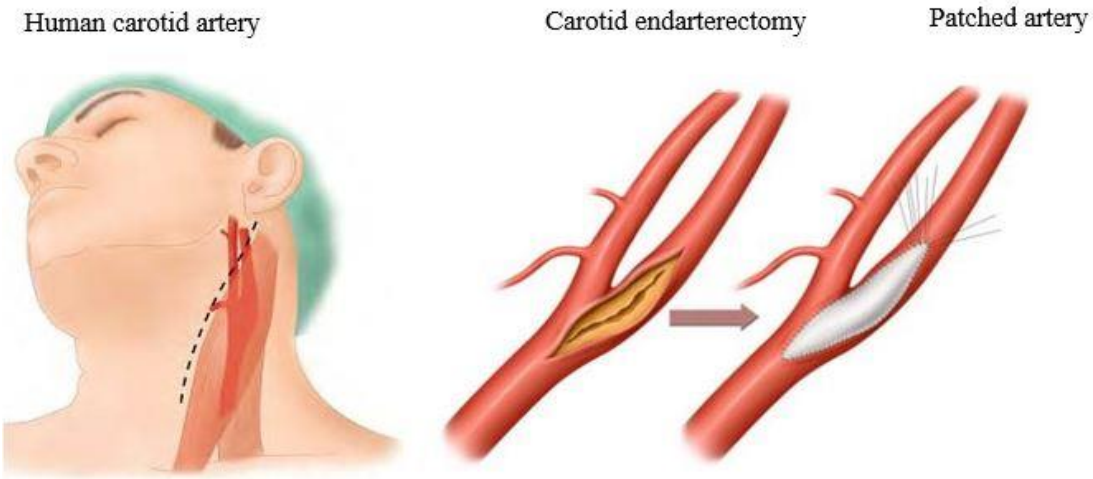

Figure 1. Human carotid endarterectomy.

In this work, an indentation methodology for measuring the elastic properties of biological patches is proposed. The methodology is a simple, non-destructive one and could be further exploited for the mechanical characterization of other biomaterials.

2. Materials and methods

In this study, commercial bovine pericardium patches, exhibiting a hyperelastic response are studied [1]. The methodology commences with an indentation experiment. The work by Briscoe et al. [2], who solved the linear elasticity contact problem (no friction considered), is taken into account. In this manner, an indentation procedure is constructed, in order to obtain the Young's modulus, E, of the material under consideration and relevant metrics (hardness, indentation depths etc.). Use is made

of the results from ref.[3], where it was proven that indentation of hyperelastic materials is described by linear incompressible elasticity.

The indentation depth h relates to the contact radius a, according to:

$$\frac{h}{a}=\frac{1}{\tan\theta}\left[\frac{\pi}{2}-\arcsin\left(\frac{b}{a}\right)\right]-\cos\theta\left[\left(\left(\frac{a}{b}\right)^2-1\right)^{1/2}-\frac{a}{b}\right] \tag{1}$$

and the vertical load P relates to the elastic modulus of the material as:

$$\frac{P(1-\nu^2)}{2E_o b^2}=\frac{1}{2}\left(\frac{a}{b}\right)^2\frac{h}{a}-\left(\left(\frac{a}{b}\right)^2-1\right)^{1/2}\left(\frac{(a/b)^2+2}{6}\cos\theta-\frac{1}{2\tan\theta}\right)+\frac{1}{6}\left(\frac{a}{b}\right)^3\cos\theta \tag{2}$$

An M-type Shore durometer according to ASTM D2240-05 standard was used. The hardness number H_M relates explicitly to the applied force P and the indentation depth h:

$$P=0.324+0.0044\,H_M\ \ N \tag{3}$$

$$\frac{h}{b}=12.941\left(1-\frac{H_M}{100}\right), \tag{4}$$

where b is a geometric feature of the indentor (dimension of length). Having measured the material hardness, the aforementioned equations are combined to calculate E and a.

3. Results

The hardness H_M and the Young's modulus E for two commercial bovine patches were acquired. For the first patch it was obtained H_M=62.90, E= 4.701 MPa, while for the second one H_M=69.40, E= 6.356 MPa. This non-sophisticated technique may be easily implemented to mechanically characterize several other biomaterials.

Acknowledgements

This work was supported by the "Excellency II" ("ARISTEIA II") Action of the "Operational Programme for Education and Lifelong Learning", project "Fatigue of Materials used in Vascular Surgery-FaMaVaSu", conducted by the Greek General Secretariat for Research and Technology (GSRT).

References

[1] M. S. Sacks (2000). Biaxial mechanical evaluation of planar biological materials, *J. Elast.*, **61**, 199-246.
[2] B. J. Briscoe, K. S. Sebastian and M. J. Adams (1994). The effect of indenter geometry on the elastic response to indentation, *J. Phys. D: Appl. Phys.*, **27**, 1156-1162.
[3] T. Zisis, V. I. Zafiropoulou and A. E. Giannakopoulos (2015). Evaluation of material properties of incompressible hyperelastic materials based on instrumented indentation of an equal-biaxial prestretched substrate, *Int. J. Solids Struct.*, **64-65**, 132-144.

STRESS - STRAIN RELATIONS DURING AXIAL LOADING OF HYPERTENSIVE RATS' AORTAS AND THE THERAPEUTIC ROLE OF CHIOS MASTIC GUM

E. D. Pasiou[1], A. I. Tzani[2], I. P. Doulamis[2], P. S. Konstantopoulos[2] and D. N. Perrea[2]
[1] Laboratory for Testing and Materials, National Technical University of Athens, Greece
[2] Laboratory for Experimental Surgery and Surgical Research "N.S. Christeas", Medical School, National and Kapodistrian University of Athens, Athens, Greece

1. Introduction

Among the most common causes related to morbidity and mortality worldwide is hypertension, which is associated with "target organ damage" (e.g., left ventricular hypertrophy, kidney failure etc.) [1]. Drugs are the most usual treatment worldwide but their side effects cannot be ignored [2]. In this direction, certain dietary patters are recommended by the American Heart Association (AHA) and the American College of Cardiology (ACC) as an alternative approach to reduce hypertension [3]. Chios mastic gum (CMG) is here considered as a possible strong anti-hypertensive agent since it possesses considerable anti-oxidant and anti-inflammatory properties [4]. CMG is the resinous sap produced from the "Pistacia Lentiscus var. Chia" trees which are exclusively cultivated at the south part of Chios Island in Greece [5] and its effect on the biomechanical properties of the aorta is studied here.

2. Animals

16-week-old male Wistar rats, weighing 300-350 g, were obtained from the Animal Division of the "Experimental Center of Demokritos" (Athens, Greece) and they were housed in the Laboratory for Experimental Surgery and Surgical Research "N.S. Christeas", Athens Medical School, in a controlled environment, in cages under European standards. The "*Guide for the Care and Use of Laboratory Animals*" and the EU legislation (Directive 2010/63/EU) were followed.

Xylazine (10 mg/kg) and ketamine (70 mg/kg) were injected into the rats for their anesthetization and a stenosis was induced on the left renal artery using a 0.2 mm silver clip. For comparison reasons, the same surgical procedure was followed on sham-operated rats without placement of the renal artery clip. The rats with systolic blood pressure >160 mm Hg were considered hypertensive. After 8 weeks, the rats were separated into three groups: 1) SHAM (6 rats): sham-operated rats, 2) 2K1C (9 rats): operated rats with stenosis, 3) 2K1C+CMG (10 rats): operated rats with stenosis who received daily 40 mg/kg body weight Chios Mastic Gum powder dissolved in their drinking water for 2 weeks. The CMG administration started 8 weeks after surgery and it was maintained for 2 additional weeks.

3. Experimental protocol

After euthanasia, the outer (D) and the lumen inner (d) of each aorta were measured and its cross-sectional area (CSA) was determined simulating the aorta as a circular ring, i.e., $CSA=\pi(D^2-d^2)/4$.

The biomechanical protocol was realized at the Laboratory for Testing and Materials, National Technical University of Athens, in an electromechanical loading frame (10 kN MTS INSIGHT™) especially designed for biomechanical tests (Fig.1a). In order to obtain accurate measurements of the applied load, an external certified load cell (DBCR-100N-002-000) of 100 N capacity and sensitivity equal to 0.02 N was used. The overall elongation of the central section of the specimens was measured with a video extensometer (RTSS Videoextensometer, Limess Messtechnik & Software Gmbh) the distance resolution of which is equal to 0.5 μm at 100 mm Field of View. This contactless method requires only two markers which are painted on the specimen at a distance L_o from each other before the experiment and it does not affect the tissue at all. The videoextensometer measures the distance between the two markers during the whole loading procedure (embedded gray-scale photo in Fig.1b), providing the elongation of the specimen (ΔL). The axial strain is obtained by simply dividing ΔL over L_o.

All experiments were carried out under quasi-static loading, i.e., under constant displacement rate equal to 1 mm/min. The maximum load, the maximum stress (max load over the CSA) and the modulus of elasticity (the slope of the stress-strain curve) of each tissue were determined after the tests.

4. Results and conclusions

The main advantage of the present protocol is that it permitted reliable determination of reduced quantities, i.e. stresses and strains, rather than forces and elongations. Most aortas fractured relatively far from the loading grips as it can be seen in the embedded coloured photo of Fig.1b. The ones fractured in the immediate vicinity of the grips were excluded from the analysis. Based on the raw data obtained, no differences were observed concerning the fracture load of all specimens (~2.7 kN). As a next step, the data of the cross-sectional area of each aorta were taken into account and the axial stress developed in the tissues was calculated. Taking also advantage of the data of the video-extensometer, the axial stress-axial strain curves were derived (Fig.1b). The results could be characterized more than just encouraging. The maximum stress developed in the hypertensive aortas (2K1C) is almost 40% lower than the maximum stress of the SHAM ones (~8.85 MPa) but when rats consumed CMG the maximum stress attained by the aorta approaches the SHAM ones. Similar results were obtained concerning the modulus of elasticity of the aorta which is slightly increased in hypertensive rats while its value is reduced in case of 2K1C+CMG. Another interesting point is that 2K1C aortas are much more brittle that the SHAM ones, a property which is significantly improved when CMG is consumed by the rats. In brief, CMG seems to greatly nullify the negative effects of hypertension on the overall biomechanical response of aortas, as it is clearly seen in Fig.1b.

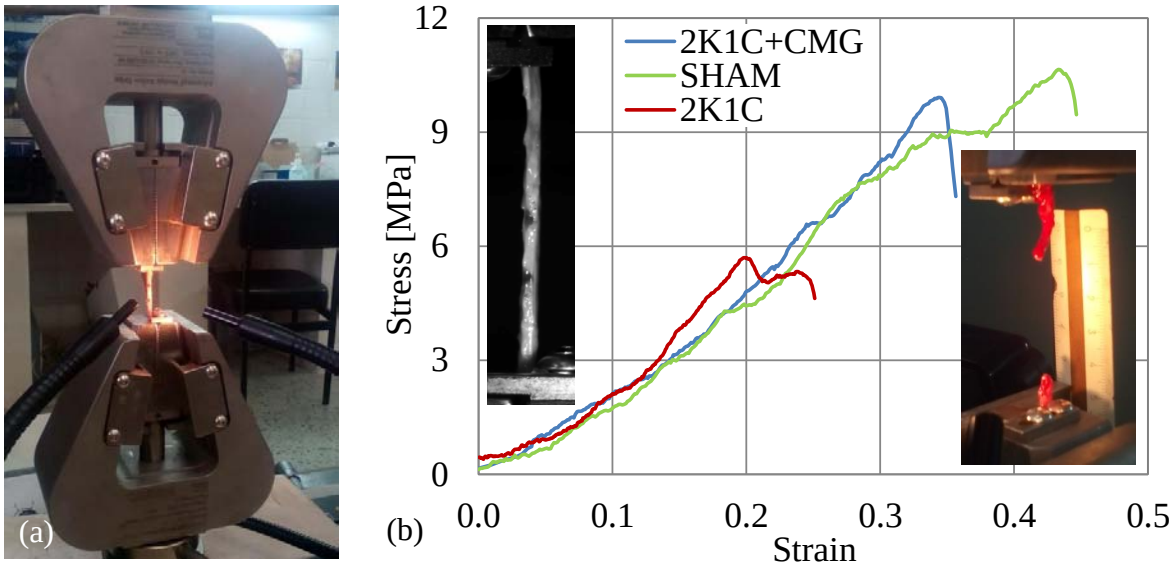

Figure 1. (a) A typical aorta during loading. (b) Typical stress-strain graphs.

References

[1] G. Pickering (1972). Hypertension. Definitions, natural histories and consequences, *Am. J. Med.*, **52(5)**, 570-583.

[2] Y. G. Tedla and L. E. Bautista (2016). Drug side effect symptoms and adherence to antihypertensive medication, *Am J Hypertens.*, **29(6)**, 772-779.

[3] R. H. Eckel et al. (2014). 2013 AHA/ACC guideline on lifestyle management to reduce cardiovascular risk: A report of the American College of Cardiology/American Heart Association Task Force on Practice Guidelines, *J Am Coll Cardiol.*, **63**, 2960-2984.

[4] M. Mahmoudi, M. A. Ebrahimzadeh, S. F. Nabavi, S. Hafezi, S. M. Nabavi and S. Eslami (2010). Anti-inflammatory and antioxidant activities of gum mastic, *Eur Rev Med Pharmacol Sci.*, **14(9)**, 765-769.

[5] K. S. Dimas, P. Pantazis and R. Ramanujam (2012). Review: Chios mastic gum: a plant-produced resin exhibiting numerous diverse pharmaceutical and biomedical properties, *In Vivo*, **26(5)**, 777-785.

EXPERIMENTAL STUDY OF THE MECHANICAL RESPONSE OF HUMAN URETER

D. C. Petsepe[1], D. P. Sokolis[2] and S. A. Papadodima[3]
[1] Department of Mechanics, National Technical University of Athens,
[2] Laboratory of Biomechanics, Center of Clinical, Experimental Surgery, and Translational Research,Biomedical Research Foundation of the Academy of Athens,
[3] Department of Forensic Medicine and Toxicology, Medical School, University of Athens.

1. Introduction

The ureters are paired tubular structures that propel urine produced by the kidneys to the urinary bladder. Their conduit function is clearly mechanical, and there is clinical motivation to study their biomechanical properties since they may be subject to iatrogenic or other types of mechanical trauma. The ureter has been largely overlooked heretofore in the study of the biomechanics of soft biological tissues, although there has been significant motivation to use its biomechanical properties as inputs to mathematical models of ureteral function. The present study aims to determine the biomechanical properties of human ureter in relation to age and gender and it is divided into two main sections.

2. Methodology

In the first section histological analysis was used for quantification of collagen contents and thickness/area of the ureteral layers, with concomitant geometrical analysis of zero-stress and no-load states, and inflation /extension testing to biomechanically characterize with the Fung-type model the ureters from twelve (12) cadavers. Both ureters were harvested within 24 h of death from the subjects whose bodies had been preserved at 4 °C before autopsy at the Department of Forensic Medicine and Toxicology, Athens University Medical School. The inflation/extension measurements and geometrical characteristics of zero-stress/no-load states (Fig.1a) were used to calculate biomechanical parameters, assuming that ureters are nonlinear, pseudo-elastic, anisotropic, incompressible, and homogeneous tubes subjected to finite deformation, whose radially cut-open state is stress-free. The internal diameter d_i during inflation/extension was calculated from:

$$d_i = \sqrt{d_e^2 - \frac{4A_0}{\pi\lambda_Z}} \tag{1}$$

The circumferential and axial stretch ratios λ_θ, λ_z were calculated relative to the zero-stress state as:

$$\lambda_\theta = \frac{s}{S},\ \lambda_Z = \frac{\ell}{L} \tag{2}$$

where S was the zero-stress state circumference of the ureter and s that at the no-load or loaded states, and L and ℓ were the ex situ and in situ lengths. The circumferential residual strains E_θ were determined at the internal and external wall boundaries using the Green strain definition:

$$E_\theta = \frac{1}{2}\left(\lambda_\theta^2 - 1\right) \tag{3}$$

Mean strain E_θ was calculated via mid-wall circumference a zero-stress and loaded states, given by $S=(S_e+S_i)/2$ and $s=(s_e+s_i)/2$. Mean values of normal stress components (2nd Piola–Kirchhoff definition) in the circumferential and axial directions S_θ and S_z were determined as follows:

$$S_\theta = \frac{Pd_i}{\lambda_\theta^2(d_e - d_i)} \quad S_z = \frac{4F + P\pi d^2}{2\pi\lambda_z^2(d_e^2 - d_i^2)} \tag{4}$$

where P was the intraluminal pressure and F the axial force (Fig.1a).

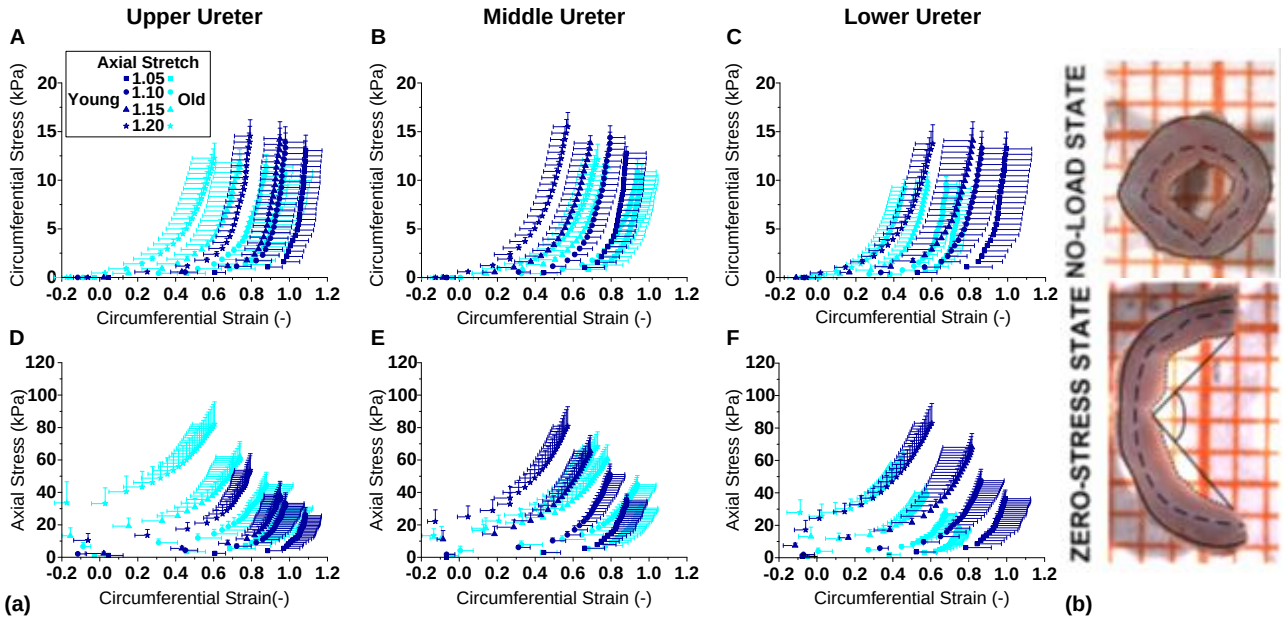

Figure 1. (a) Circumferential (A–C) and axial Cauchy stress (D–F) against circumferential strain data at four axial stretch ratios for the upper, middle, and lower ureter of young (dark blue fill) and old subjects (light blue fill). (b) Open and close sector of human ureter. Determination of the no-load and zero-stress states.

In the second part of the study definite zero-stress/no-load geometrical characterization at fifteen regions along the ureter of 21 human cadavers are reported, estimating the opening angle, residual strains and dimensional parameters (Fig.1b) [1, 2].

3. Results and discussion

Tissue properties do not differ ($p>0.05$) between the left and right ureter. Regional heterogeneity is established that was profoundly age-related but seldom gender-related. In younger subjects, the axial stress-circumferential strain curves for upper ureter are shifted to smaller stresses, and the model parameter a_2 representing axial stiffness is smallest ($p<0.05$). The upper ureter undergoes axial stiffening with advanced age.

Aging increases ($p<0.05$) the collagen content of upper ureter to favor a near-uniform regional distribution. Wall thickness increases with age, it is not constant throughout its length (it increases towards from the upper to the middle and then decreases to the lower part), unlike the opening angle and residual strains. The curvature of ureter in the no-load state increases steadily and significantly along the first half of ureter and decreases in the second half. Finally, gender affects little ($p> 0.05$) the opening angle and morphometry of the no-load and zero-stress states.

The presented data will provide insight into the biomechanical response of ureter under zero and physiologic stress conditions and the relationship between ureteral remodeling and aging. Importantly, they may also be used to inform finite element models and computational studies simulating the ureter.

References

[1] D. P. Sokolis, D. C. Petsepe, S. A. Papadodima and S. K. Kourkoulis (2017). Age- and region-related changes in the biomechanical properties and composition of the human ureter, *J. Biomechanics*, **51**, 57-64.

[2] D. C. Petsepe, S. K. Kourkoulis, S. A. Papadodima and D. P. Sokolis (2018, to appear). Regional and age-dependent residual strains, curvature and dimensions of the human ureter, *Proc. of the Institution of Mechanical Engineers Part H - Journal of Engineering in Medicine*, doi: 10.1177/0954411917750192.

BIOMECHANICAL STUDY OF UTEROSACRAL LIGAMENT AND THE POTENTIAL ROLE OF PLATELET RICH PLASMA FOR THE MANAGEMENT OF PROLAPSE

Ch. Spiliopoulou[1], E.L. Chrysanthopoulou[2,3], V. Pergialiotis[2], D. N. Perrea[2], S. K. Doumouchtsis[2,4,5] and S. K. Kourkoulis[1]

[1] National Technical Univ.of Athens, Dept of Mechanics, Laboratory of Testing and Materials
[2] Lab of Exp. Surgery and Surgical Research N.S. Christeas, Nat. & Kapodistrian Univ. of Athens
[3] Dept of Obstetrics and Gynaecology, Queen's Hospital, Rom Valley Way, Romford, Essex, UK
[4] Dept of Obstetrics and Gynaecology, Epsom and St Helier University Hospitals NHS Trust, UK
[5] St George's University of London, London, UK

1. Introduction

The uterosacral ligament (USL) is crucial for pelvic organ support. It was previously considered that it consists of only connective tissue, however recent studies indicate that it contains, also, smooth muscle cells [1]. In case the stiffness of USL is reduced, it cannot properly undertake its role and Pelvic Organ Prolapse (POP) appears. Patients with POP have an intrinsic deficit of a gene, responsible for the development of the USL [2]. The USL of women with POP is characterized by increased amounts of collagen III and matrix metalloproteinase 2 (MMP-2) [3]. Given that collagen III is essential in tissue elasticity and extensibility, it is assumed that it is responsible for the tissue laxity.

2. Prolapse and the potential role of platelet rich plasma for its management

It is estimated that about 30% of women over the age of fifty years suffer from uterine prolapse [4]. The dysfunction of ligaments supporting the uterus is multifactorial. Current evidence suggests that the duration of labour, the neonatal birth weight and parity are independent factors that increase the risk of uterine prolapse [5]. The transition to menopause is, also, associated with urogenital atrophy, which results in ligament atrophy, relaxation of the pelvic floor and uterine prolapse, while it appears that the incidence of prolapse increases with age. Laparoscopic and vaginal procedures involving USL suspension have been developed however, but complications have been reported [6].

Recently, an alternative approach for managing of prolapse is proposed, based on the implementtation of an injectable agent, which could enforce the ligaments. This principle with autologous substances could limit the side effects of synthetic materials. Fibrin adhesives and PRP have been used in various fields in the past 30 years, but they have not been used for treatment of urogynaecological problems. Research projects investigating the regenerative abilities of plasma offer options of using an autologous substance with adhesive, healing, and haemostatic properties at low cost [7]. In this context, injecting an autologous adhesive factor to the ligaments might have promising results in the treatment of POP, by enforcing the ligaments and restoring normal anatomy, with minimal, complications. Platelet rich plasma (PRP) is extremely rich in growth factors and cytokines, which regulate tissue reconstruction. Although it has been previously used in orthopaedics, it has never been used in urogynaecology.

Figure 1. The experimental set up and detailed view of a gripped specimen.

3. The experimental protocol

An experimental protocol is here described (Fig.1), aiming to assess the potentiality of PRP for the treatment of POP. A total of 17 rats were sacrificed, classified in three distinct groups: 7 of them were nulliparous, 3 multiparous and 7 multiparous with PRP (plasma rich platelets) injection. All rats weighed between 220 g and 245 g. PRP

was prepared based on a standardized protocol and was injected in USLs, after surgical exposure of them. These rats were ready for study 6 weeks after injection. The same technique was used for all rats which were anaesthetized and midline incision was performed. Uterus and ovaries were exposed and the pelvis with rectum and genital tract were separated from the body.

Direct tension tests were performed using an electromechanical loading frame (MTS Insight), equipped with a properly calibrated load-cell of capacity equal to 100 N. The sacrum-uterus complex was placed horizontally. The force was exerted to the ligaments using a hook, placed between the body of the uterus and the rectum and attached to the upper clamp. Another clamp fixed to the base of the frame was used to immobilize the sacrum (Fig.1). The tests were implemented quasi-statically, under displacement-control mode, at a rate of 0.4 mm/min. The displacement was imposed monotonously until fracture of one of the USLs.

4. Results and conclusions

Load and displacement were recorded as functions of time. Typical force-elongation (F-δL) curves are plotted (Fig.2). The failure load and the stiffness (slope of the linear portion of the F-δL plot) of the ligament were determined together with the energy absorbed (area beneath the F-δL plot) during loading. Although the project is still in progress, some quite encouraging conclusions are drawn. The failure load and the stiffness of the USLs of rats treated with PRP appear increased compared to those of untreated multiparous rats, approaching the respective values of nulliparous rats.

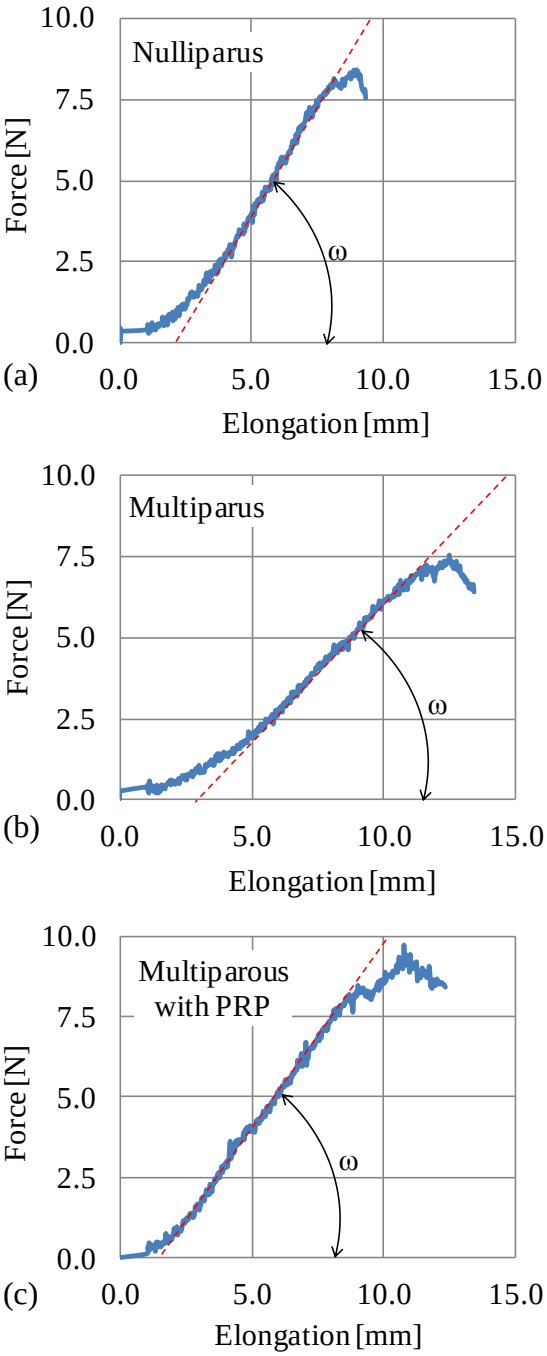

Figure 2. Force vs. elongation for characteristsic specimens: (a) Nulliparous; (b) Multipaqrous and (c) Multiparous with PRP rats.

References

[1] R. Ramanah et al. (2009). Anatomical and histological study of the uterosacral ligament: practical surgical consequences, *J Gynecol Obstet Biol Reprod*, **38**, 304-311.
[2] K. Connell et al. (2008). HOXA11 is critical for development and maintenance of uterosacral ligaments and deficient in pelvic prolapse, *J Clin Invest*, **118**, 1050-5.
[3] B. Gabriel et al. (2006). Increased expression of matrix metalloproteinase 2 in uterosacral ligaments is associated with pelvic organ prolapsed, *Int Urogynecol J Pelvic Floor Dysfunct*, **17(5)**, 478-482.
[4] E. C. Samuelsson et al. (1999). Signs of genital prolapse in a Swedish population of women 20 to 59 years of age and possible related factors, *Am J Obstet Gynecol*, **180(2 Pt 1)**, 299-305.
[5] N. Joseph et al. (2016). Clinical profile of uterine prolapse cases in South India, *J Obstet Gynaecol India*, **66(Suppl 1)**, 428-434.
[6] L. Turner et al. (2016). Comparison of complications and prolapsed recurrence between laparoscopic and vaginal uterosacral ligament suspension for treatment of vaginal prolapse, *Int Urogynecol J*, **27**, 797-803.
[7] E. Kon et al. (2011). Platelet-rich plasma (PRP) to treat sports injuries: evidence to support its use, *Knee Surg Sports Traumatol Arthrosc*, **19(4)**, 516-527.

SHOULDER JOINT SHAPE IS RESCUED AS DEVELOPMENT PROGRESSES WHEN LIMB MUSCULATURE IS ABSENT IN THE MURINE EMBRYO

V. Sotiriou and N. C. Nowlan
Imperial College London, London, United Kingdom

1. Introduction

Osteoarthritis is a condition affecting 15% of the world's population [1] having a lot of implications notwithstanding altering the mechanical properties of the cartilage in the joints [2]. Congenital conditions involving the developing joints such as developmental dysplasia of the hip (DDH) and arthrogryposis can lead to osteoarthritis early in life which in turn requires invasive methods such as hip replacement to re-establish patients' health. Reduced or abnormal fetal movements can affect joint development, leading to conditions such as developmental dysplasia of the hip and arthrogryposis [3]. It has been shown in the mouse that joints are differentially affected by the lack of musculature [4, 5], but the effects of absent muscle across prenatal development have not been characterised. In this study, image registration is used to investigate shape differences between the articular surfaces of normal and muscleless-limb murine embryonic shoulder joints across two developmental stages (Theiler Stage (TS) 24 and 27, roughly corresponding to embryonic days 15.5 and 18.5 respectively).

2. Methods

Five control and five muscleless-limb Splotch-delayed (which lack skeletal muscle) embryos for each stage were dissected, their limbs stained for bone and cartilage, and imaged with optical projection tomography. Scapular and humeral rudiments were segmented in Mimics and 3D shapes created. Rigid image registration was used to consistently align the segmented rudiments and an average shape of control and muscleless-limb rudiments was created for each stage. Shape changes between controls and mutants were visualised using 3D representations and 2D outlines in relevant planes, and quantified using nine consistently performed measurements. T-tests were performed to identify significant differences between control and muscleless-limb rudiments at each stage.

3. Results

At developmental stage TS24, the muscleless-limb glenoid cavity did not have as circular a profile as the control (Fig.1A, ii) and the humeral head was flattened (Fig.1A, iii, arrow). The height and width of the TS24 muscleless-limb glenoid cavity were significantly larger and the length of the long axis of the muscleless-limb humeral head was significantly smaller (Fig.1B) when compared to the controls. However, at TS27, the glenoid cavity and humeral head shapes resembled those of the controls (Fig.1C). This was corroborated by the measurements performed, since none were significantly different between control and muscleless-limb embryos (Fig.1D).

4. Discussion

These results demonstrate for the first time that joint shape can recover from the absence of skeletal muscle and spontaneous fetal movements. This has relevance for understanding the influence of timing of fetal movements for developmental joint disorders. This could help one identify the onset of conditions such as DDH leading to its early diagnosis and treatment from a very young age; a development that could diminish the risk of developing osteoarthritis in a very young age and assure that the joints retain their biomechanical function without any major intervention. Ongoing work is investigating if other major joints respond equally to extended paralysis over development**.**

Acknowledgements

This research was funded by the ERC under the EU 7th Framework Programme (Grant: 336306).

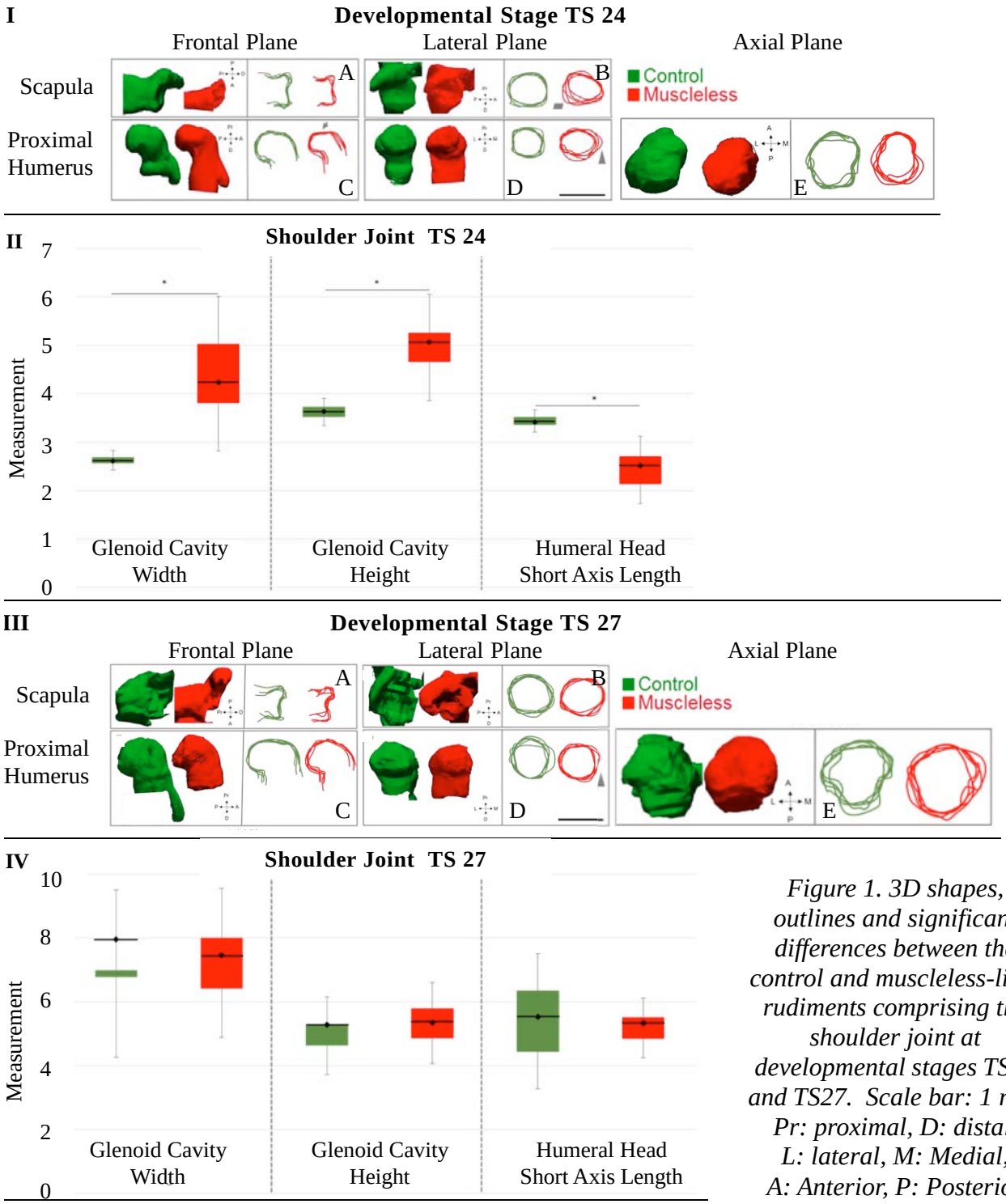

Figure 1. 3D shapes, outlines and significant differences between the control and muscleless-limb rudiments comprising the shoulder joint at developmental stages TS24 and TS27. Scale bar: 1 mm. Pr: proximal, D: distal, L: lateral, M: Medial, A: Anterior, P: Posterior

References

[1] V. L. Johnson and D. J. Hunter (2014). The epidemiology of osteoarthritis, *Best Practice & Research Clinical Rheumatology*, **28(1)**, 5-15.
[2] E. Obeid, M. Adams and J. Newman (1994). Mechanical properties of articular cartilage in knees with unicompartmental osteoarthritis, *Bone & Joint Journal*, **76(2)**, 315-319.
[3] N. C. Nowlan (2015). Biomechanics of foetal movement, European Cells & Materials, **29**, 1-21.
[4] N. C. Nowlan et al. (2010). Developing bones are differentially affected by compromised skeletal muscle formation, *Bone*, **46(5)**, 1275-1285.
[5] J. Kahn et al. (2009). Muscle contraction is necessary to maintain joint progenitor cell fate, *Developmental Cell*, **16(5)**, 734-743.

Sensing Techniques 1

ADVANCED IMAGE METHODS FOR STRUCTURAL INTEGRITY ASSESSMENT

P. José Sousa, B. V. Farahani, F. Barros, P. J. Tavares and P. M. G. P. Moreira
INEGI - Institute of Science and Innovation in Mechanical and Industrial Engineering, Porto, Portugal

1. Introduction

Recent trends in structural integrity monitoring resource increasingly to high-resolution imaging methods and image-based sensing. This topic is driven by a clear increase in resolution and accuracy requirements that can only be approached by these advanced, non-contact, full field methods. Among the imaging methodologies of choice, there is a clear gap in resolution between interferometric and non-interferometric techniques, although consistent advances in image processing algorithms keep narrowing that difference. On the other hand, interferometric methods have been kept, for the most part, within the realm of academia research, and only seldom do they leave laboratory facilities into the field, where real world conditions are subject to a vast amount of different kinds of complex inconveniences, such as a plethora of noise sources, operational changes of all sorts, temperature drifts and so many other impediments. Here again, recent progress in some of these methods, coupled with fresh ingenious proposals, have resulted in increased robustness, to a point where some field applications have been targeted with success, and progress in this regard continues to advance this very day. In the following, both interferometric and non- interferometric image methods will be discussed, with a particular focus on real-world applications, whether on laboratorial grounds or on the field.

2. Interferometric methods

2.1 Electronic Speckle Pattern Interferometry (ESPI)

There are two main setup types for ESPI, with sensibility to out-of-plane or in-plane displacements respectively. In both of them, the laser goes through a beam splitter in order to generate two separate beams. In the case of out-of-plane ESPI, one of these, the object beam, is used to illuminate the target object. Some of the reflected illumination goes through a lens to a beam splitter, where it will interfere with the reference beam and continue to the camera. In the other case, both beams are used to illuminate the object from two different places. This will lead to their interference that is captured by a camera. It is common for commercial systems to integrate multiple ESPI arrangements and to be able to toggle quickly between them.

2.2 Speckle Pattern Shearing Interferometry (Shearography)

Shearography aims at causing interference between the object wavefront and a shifted copy of itself. It should be also noted that in Shearography, unlike ESPI, a reference beam is not used. Various ways to create the shearing effect have been proposed [1], the most common strategies include common path Michelson, birefringent and beam splitter type shearing interferometer [2]. However, the base principle remains the same among all of these. The target object is illuminated with a constant wavelength laser and reflects light into a beam splitter, which redirect light along one of two paths: towards mirrors M1 or M2. The latter is tilted, which means that when the light returns to the beam splitter, it is slightly laterally shifted in respect to the light that comes from M1. This will cause interference between the light from these two sources. The amount of shear is dependent on the tilt angle.

3. Non-interferometric methods

3.1 Digital Image Correlation (DIC)

Currently, DIC is a well-established method in experimental procedures to evaluate the mechanical behaviour of the material, particularly the fracture properties, fatigue and failure modes in a variety

of structural components. As an illustration, the stress intensity factor (SIF) can be evaluated by DIC analysis due to its simplicity [3]. In addition, DIC was applied on a hybrid experimental/numerical methodology which a numerical SIF calculation hinges upon a stress field obtained from DIC [4]. Compared to interferometric methods used for similar purposes, DIC offers the advantage of allowing for a less complex experimental setup and less thoroughly controlled experimental conditions. All that is needed for a simple 2D DIC test is a digital camera, a light source and a speckle pattern on the desired surface that can be achieved, for instance, by spray-painting. It is also versatile in the sense that it can be used in combination with a variety of digital image acquisition tools, such as microscopes. The main disadvantage is the lower accuracy of strain measurements when compared to interferometry-based techniques; it is therefore not recommended for small deformations [5].

3.2 Thermoelastic Stress Analysis (TSA)

TSA is an optical technique to evaluate the stress distribution in engineering fields, based on thermal variations. Thermoelastic data can be effectively used to evaluate principal stresses and principal strains on specimen's surfaces and crack growth rates. As previous works demonstrated [6], the TSA method can be employed to determine the SIF under mode I fatigue loading. For instance, Rocca et al. [7] employed the TSA method to analyse non-linear thermoelastic effects on Iron and Nickel, and found that the stress might influence the specific heat and thermal expansion coefficient. Later on, Dillon [8] generalized the non-linear thermoelasticity equations within the deviatory components of strain, where the non-linearity of stress-strain was considered instead of the geometric non-linearity.

References

[1] M. Grediac and F. Hild (2012). *Full-field measurements and identification in solid mechanics*. London: Wiley- ISTE.
[2] ASTM International (2007). *ASTM E2581-07, Standard Practice for shearography of polymer matrix composites, sandwich core materials and filament-wound pressure vessels in aerospace applications*, West Conshohocken, PA.
[3] R. Cintrón and V. Saouma (2008). S*train Measurements with the Digital Image Correlation System Vic-2D*, Boulder.
[4] P. J. Tavares, T. Ramos, D. Braga, M. A. P. Vaz and P. M. G. P. Moreira (2015). SIF determination with digital image correlation, *International Journal of Structural Integrity*, **6(6)**, 668-676.
[5] B. Pan, K. Qian, H. Xie and A. Asundi (2009). Two-dimensional digital image correlation for in-plane displacement and strain measurement: a review, *Measurement Science and Technology*, **20(6)**, 62001.
[6] B. V. Farahani, P. J. Tavares and P. M. G. P. Moreira (2016). SIF determination with thermoelastic stress analysis., *Procedia Structural Integrity*, **2**, 21482155.
[7] R. Rocca and M. B. Bever (1950). The Thermoelastic effect in iron and nickel as a function of temperature, *Trans. AIME*, **158**, 327333.
[8] O. W. Dillon (1962). A nonlinear thermoelasticity theory, *Journal of the Mechanics and Physics of Solids*, **10(2)**, 123-131.

INVESTIGATING THE MECHANICAL PROPERTIES OF ADDITIVELY MANUFACTURED STRUCTURES USING FBG SENSORS

D. Karalekas and S. N. Economidou
Laboratory of Advanced Manufacturing Technologies and Testing,
University of Piraeus, Piraeus, Greece

1. Introduction

Fused Deposition Modeling (FDM) is a currently advancing technique among the various that comprise the family of Additive Manufacturing technologies (AM). With numerous applications in many fields, FDM is constantly drawing attention owing to being reliable, versatile and cost-effective. In accordance with all 3D printing methods, FDM machines employ a virtual Computer Aided Design (CAD) model to produce a physical object through the consecutive deposition of material layers. The working principle of FDM is based on the melt extrusion process: the thermoplastic filament is heated above its T_g to a semi-molten state and cools rapidly after its deposition [1]. Throughout this reoccurring procedure, the temperature variations trigger the development of thermal stresses and strains, the build-up of which within the structure is associated with serious quality issues such as delamination, buckling and cracking. Moreover, the anisotropy that FDM structures present is related to the morphology of the internal architecture, which in a way resembles the structure of a laminate composite material [2, 3]. As a result, the investigation of material properties within the structure is crucial to the successful manufacturing of polymeric AM parts subjected to heat and external loading. In this study, the employed FBG sensor was integrated within the tested specimens in contrast to other studies where the sensor was glued onto the external surface of the test coupon.

2. Materials, methods and results

For the fabrication of all the specimens, a MakerBot Replicator 2X was employed and the material used was ABS-P400. Each specimen had a single-mode optical fiber longitudinally embedded within its midplane, during the building process. The fibers of 0.125 mm in diameter had a measuring grating length of 3 mm and their reference Bragg wavelength was 1550 nm. For the preparation of the test coupons and their tensile testing the ASTM D638 [4] was selected. According to the chosen standard, dog bone-shaped specimens (Type IV) were built using the building parameters selected for the previous cases. The raster orientations featured were 0^o, 30^o, 45^o, 60^o and 90^o, in order to investigate the dependence of the tensile properties on the raster orientation. After fabrication, the specimens were subjected to tensile loading using an INSTRON testing machine, with a displacement rate of 5 mm/min. An extensometer was attached on one of the specimen's flat surfaces for the monitoring of the tensile strains, while the FBG wavelength recordings where simultaneously taken for the same time steps.

Some characteristic stress-strain curves for the 0^o and 90^o raster orientations are shown in Figs.1 and 2, respectively.

3. Conclusions

The experimental results demonstrate the ability of an embedded FBG sensor to monitor the tensile test in the early stages of the applied tensile loading. The strains calculated using the optical fiber readings were in very good agreement with the corresponding ones recorded by the extensometer, until the external loading reaches a critical value in which fiber-material debonding occurs. However, prior to debonding an accurate measurement of the Young's modulus is feasible.

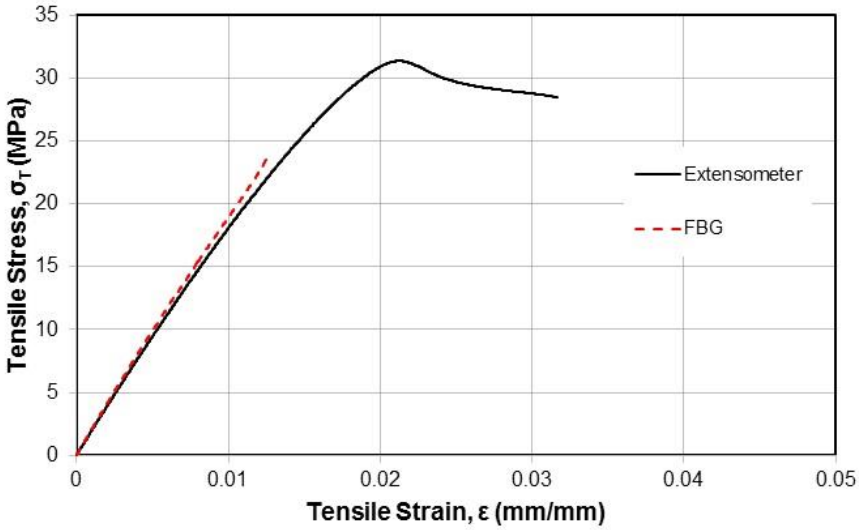

Figure 1. Comparison of stress-strain curves as obtained by an extensometer and embedded FBG sensor for 0-deg raster orientation.

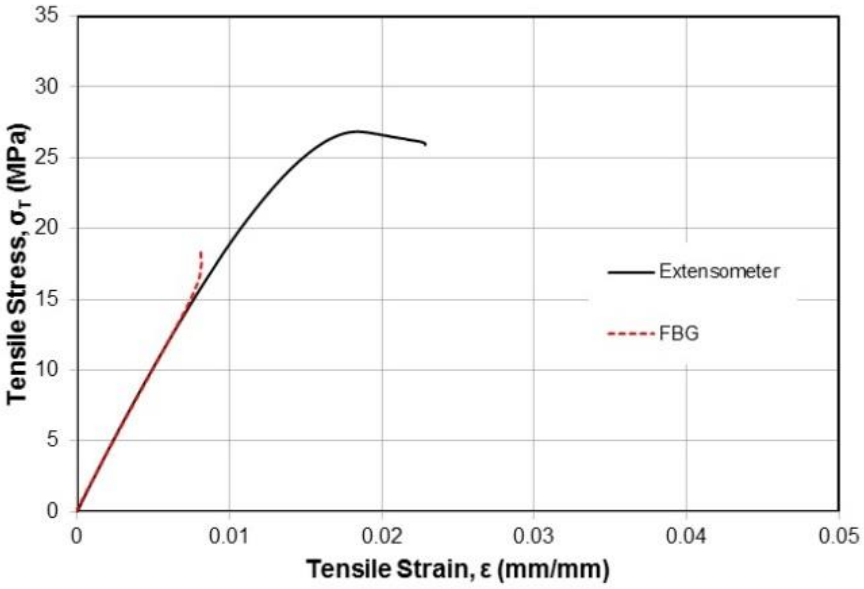

Figure 2. Comparison of stress-strain curves as obtained by an extensometer and embedded FBG sensor for 90-deg raster orientation.

Acknowledgment

This work has been partly supported by the University of Piraeus Research Center.

References

[1] S. N. Economidou and D. Karalekas (2016). Optical sensor-based measurements of thermal expansion coefficient in additive manufacturing, *Polym. Test.*, **51**, 117-121.
[2] S. H. Ahn, M. Montero, D. Odell, S. Roundy and P.K. Wright (2002). Anisotropic material properties of fused deposition modelling ABS, *Rapid Prototyp. J.*, **8(4)**, 248-257.
[3] A. Bellini and S. Güçeri (2003). Mechanical characterization of parts fabricated using fused deposition modeling, *Rapid Prototyp. J.*, **9(4)**, 252-264.
[4] ASTM (1997). *D638-03 Standard Test Method for Tensile Properties of Plastics*, American Society for Testing and Materials, Conshohocken, PA, USA.

STRAIN MONITORING SYSTEM FOR STEEL AND CONCRETE STRUCTURES

E. Cheilakou[1], N. Tsopelas[1], A. Anastasopoulos[1], D. Kourousis[1], D. Rychkov[2], R. Gerhard[2], B. Frankenstein[3], A. Amditis[4], Y. Damigos[4] and C. Bouklas[4]

[1] MISTRAS GROUP HELLAS A.B.E.E., Metamorphosi, Athens, Greece

[2] Applied Condensed-Matter Physics Group (ACMP), Institute of Physics and Astronomy, Faculty of Science, University of Potsdam (UP), Postdam, Germany

[3] Teletronic Rossendorf GmbH (TTronic), Radeberg, Germany

[4] Institute of Communications and Computer Systems (ICCS), Zografou, Athens, Greece

1. Introduction

The present work is part of a collaborative H2020 European funded research project called SENSKIN that aims to improve Structural Health Monitoring (SHM) for transport infrastructure through the development of an innovative monitoring and management system for bridges. The integrated SENSKIN solution comprises of a novel skin-like sensor capable of measuring strains in a surface area, a reliable communication system ensuring robust delivery of the sensor data and a Decision Support System (DSS) for proactive condition-based structural intervention. The system aims to enhance the performance of transportation infrastructures by improving safety, service continuity in case of disruptive events, capacity, resiliency to changes in traffic demand and climate, cost-effectiveness, sustainability and reliability. The SENSKIN technology will be implemented in the case of steel and concrete bridges, which will serve as reference structures to field-evaluate and validate its performance on actual bridge environment against a conventional health monitoring solution developed by Mistras Group Hellas [1].

2. The objective of the present protocol

The main objective of the present work is to implement the autonomous, fully functional strain monitoring system based on commercially available and off-the-shelf components, which will be used for the direct comparison between the performance of the innovative SENSKIN sensors and the conventional strain sensors commonly used for structural monitoring of bridges [2]. For this purpose, the mini Structural Monitoring System (mini SMS) of Physical Acoustics Corporation, a comprehensive data acquisition unit, designed specifically for long term unattended operation in outdoor environments, was selected.

The mini SMS is armed with many features, including data collection, alarming, historical trending and data storage, and accepts all sensors and signal sources using voltage or 4-20 mA current loops from strain gauges, temperature sensors, vibration, displacement, inclinometers and various other transducers, offering solution for a wide range of applications of SHM of structures. For the completion of the conventional system, foil strain gauges were selected, driven by special conditioners manufactured by Mistras Group able to operate on a 4-20 mA current loop.

3. Results and conclusions

A presentation and comprehensive description of the above-mentioned conventional strain monitoring system will be provided in this paper. Experimental tests, carried out aiming to investigate the influence of various factors such as strain gauge length, type of bridge configuration and bonding process on the long-term stability (zero drifting) of strain measurements at ambient temperature, will be presented. Furthermore, loading tests were performed for the validation of the performance and response of the system in monitoring the strains developed in steel beam elements subject to loading regimes.

Representative results obtained from the experimental testing of the integrated system have, also, been included in this paper.

Finally, the serious benefits of potential combination of strain-based installations with Acoustic Emission SHM systems (already widely in use in bridges worldwide) is discussed, since it will additionally offer real-time detection and location of micro-cracking and monitoring of possible damage propagation in critical points of the structure.

Acknowledgements

Acknowledgements are attributed to the SENSKIN project "SENsing SKIN' for Monitoring-Based Maintenance of the Transport Infrastructure", which is collaboration between the following organisations: ICCS, UP, EOAE, RISA, TECNIC, ERRA, MGH, USTUTT, TRL Ltd, DNDI, FEHRL, TTronic. The project is coordinated and managed by ICCS. Project duration: June 2015 - March 2019. The project has received funding from the EU Horizon 2020 Research and Innovation programme, topic: MG-8.1a-2014 (MOBILITY for GROWTH 2014-2015) - Smarter design, construction and maintenance, under Grant Agreement 635844.

References

[1] J. R. Watson, P. T. Cole and A. A. Annastasopoulos (2004). Condition assessment of concrete hinge joint bridges, in *Proceedings of the 3rd International Conference on Emerging Technologies in NDT*, 26-28 May 2003, Thessaloniki, Greece, D. Hemelrijck, A. Anastasopoulos, N.E. Melanitis (eds.), A. A. Balkema, Netherlands 2004, ISBN 90 5809 645 9 (Volume) - 90 5809 645 7(CD), 281-285.

[2] T. Tamutus, R. Gostautas and J. Watson (2015). Does structural health monitoring provide safety and maintenance or confusing data?, *Materials Evaluation*, **73(3)**, 354-359.

THE INFLUENCE OF ECCENTRICITY ON THE DISPLACEMENT FIELD IN A CIRCULAR RING

M. G. Tsousi, E. D. Pasiou and Ch. F. Markides
Laboratory for Testing and Materials, Department of Mechanics,
School of Applied Mathematical and Physical Sciences,
National Technical University of Athens, 157 73, Athens, Greece

1. Introduction

The ring test was proposed [1] as a potential substitute of the Brazilian-disc test, in an attempt to cure drawbacks of the latter related to stress concentrations, along the disc-jaw interface, deteriorating the validity of the results obtained. Taking into account the fact that at the points of expected failure the stress field in the ring consists exclusively of a single tensile component, it is reasonable to check whether this particular advantage is affected by parasitic factors, like slight eccentricity of the hole with respect to the center of the disc. This study is part of a wider project, aiming to the analytical, experimental and numerical determination of the stress field in a disc with an eccentrically drilled hole. The first stage of this project is achieved in terms of analytical treatment using Muskhelishvili's complex potentials [2], while the experimental approach (described here) is carried out using the 3D Digital Image Correlation technique (3D-DIC), which determines the full-field displacement fields developed. Emphasis is given to the experimental quantification of the effect of eccentricity on the displacement field, based on the data provided by the 3D-DIC system along strategic loci.

2. Experimental protocol

The specimens were made of poly-methyl-methacrylate-A (commercially known as PMMA or plexiglass). The mechanical properties and constants of the specific material batch were determined by means of standardized uniaxial tests. The values finally adopted were E=3 GPa for the elastic modulus and ν=0.38 for Poisson's ratio. For the implementation of the main experimental protocol the device suggested by the International Society for Rock Mechanics (ISRM) for the standardized realization of the Brazilian-disc test was used [3], properly mounted to a 10 kN electromechanical MTS-Insight frame, as shown in Fig.1a. The overall experimental set-up can be seen in Fig. 1b. The specimens were circular discs with a hole, either centrally or eccentrically drilled. Their radius was equal to R_o=50 mm and their thickness was equal to t=10 mm. The radius of the hole was constant and equal to R_{in}=25mm. The specimens were classified into two categories, either based on the angle between the line of centers and the loading axis ($\theta=0^o$ (y-axis), $\theta=90^o$ (x-axis) and $\theta=45^o$), or according to the distance, δ, between the centers of the disc and the hole ($\delta=R_o/8$, $R_o/4$ and $R_o/2$).

One of the lateral surfaces of the specimens was painted white and an arbitrary black speckle pattern was sprayed on it, according to the requirements of the DIC technique. The specimens were then placed between the jaws of the ISRM apparatus and were photographed before loading (the specific status is considered as the "undeformed" one, ignoring the own weight of the upper jaw).

The experiments were carried out under quasi-static conditions and displacement control mode at a rate of 0.3 mm/min. During loading, successive photos of the specimens were taken at predefined time steps (one photo every four seconds). The raw data were then appropriately elaborated and the distribution of the three dimensional displacement field all over the loaded specimen was obtained.

3. Results and discussion

Two cases are considered for the orientation of the line of centers, i.e., along and normal to the loading line. For the first case, the Cartesian components of the displacements of the characteristic point A along the x-axis (u) and normally to it (v) are shown in Fig.2a. For small eccentricities the

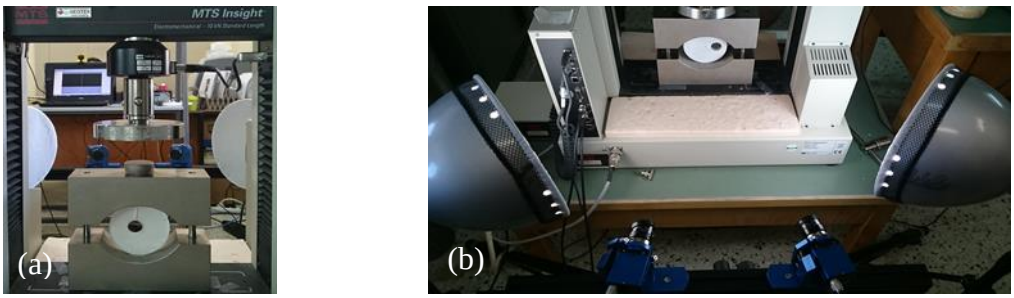

Figure 1. (a) The ISRM device for the standardized implementation of the Brazilian-disc test. (b) The experimental set-up.

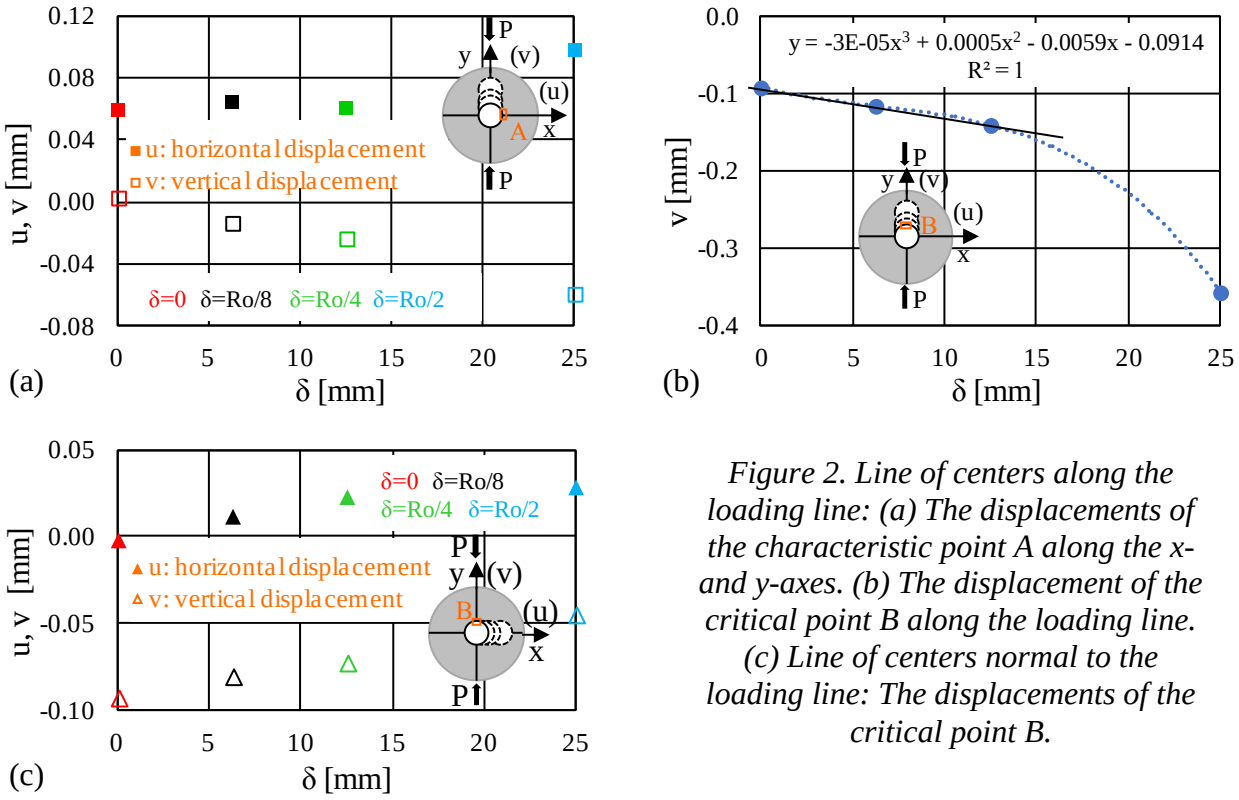

Figure 2. Line of centers along the loading line: (a) The displacements of the characteristic point A along the x- and y-axes. (b) The displacement of the critical point B along the loading line. (c) Line of centers normal to the loading line: The displacements of the critical point B.

the magnitude of the u-component of the displacement field is almost constant, while that of the v-component increases monotonously. Regarding the displacement field of the critical point B (i.e., the point at which fracture is expected), it is observed that the v-component strongly depends on the eccentricity (see Fig.2b). This dependence is almost linear for small eccentricities while for larger ones it is excellently approximated by the non-linear function described in Fig.2b. For the second case, the displacement components again for the critical point B are plotted in Fig.2c. The absolute value of the v-component decreases constantly and the opposite is true for the u-component. Moreover, for large eccentricities the u-displacement becomes comparable to the v-ones.

References

[1] E. Ripperger and N. Davis (1947). Critical stresses in a circular ring (paper no 2308), *Trans. Am. Soc. Civ. Eng.*, **112**, 619-627.

[2] N. I. Muskhelishvili (1963). *Some Basic Problems of the Mathematical Theory of Elasticity*. Groningen, Noordhoff.

[3] ISRM (1978). Suggested methods for determining tensile strength of rock materials, *Int. J. Rock Mech. Min. Sci.*, **15(3)**, 99-103.

EXPERIMENTAL AND NUMERICAL ANALYSIS OF THE MECHANICAL BEHAVIOR OF A GFRP COMPOSITE WITH EMBEDDED PVA-CNT FIBER

S. Prasing[1], P. Papanikos[2], P. Poulin[3] and N. D. Alexopoulos[1]
[1] University of the Aegean, Dept. of Financial Engineering, Chios, Greece
[2] University of the Aegean, Dept. of Product and Systems Design Engineering, Ermoupolis, Greece
[3] Université de Bordeaux, Centre de Recherche Paul Pascal - CNRS, Pessac, France

1. Introduction

Composite materials are widely used in aerospace applications, as they possess superior mechanical and physical properties in comparison to most structural metallic materials. Nevertheless, a significant drawback is that their complex internal structure gives rise to complex failure modes [1]. Hence, it is exceptionally difficult to accurately evaluate their structural health. To this end, it is of imperative importance to develop non-intrusive, embedded sensors that can correctly measure, in real time, the strain field as well as damage propagation within the material. However, most existing state-of-the-art sensors present certain disadvantages, such as increased cost, difficulty in integration, unreliable data due to noise as well as local degradation of the mechanical properties of the composite material [2, 3].

A non-intrusive method that can be used for monitoring purposes of carbon-reinforced composites is the exploitation of the electrical resistance change (ERC) of the reinforcing fibers under varying strain fields, and therefore the carbon reinforcement itself can be used as an embedded sensor of the composite [4]. Nevertheless, this method cannot be exploited for other non-conductive reinforcing fibers, e.g. glass fibers. For that reason, another strategy for such materials was to make the matrix of the composite material electrically conductive in order to apply the ERC methodology on measuring the matrix properties. This can be achieved by dispersing an electrically conductive strengthening phase, e.g. Carbon Nanotubes (CNTs) [5], or by enhancing the electrical properties of glass fibers by growing or attaching CNTs on the fiber [6]. However, these methods present several limitations, such as the agglomeration of individual CNTs in a polymer matrix [7] and the reduction in the mechanical properties of the fibers when CNTs are grown on them with most of the conventional techniques [8].

2. Materials and methods

To overcome the above mentioned limitations, the ERC concept can be exploited by embedding a non-structural fiber on the composite that can be exploited only for sensing purposes, e.g. a polyvinyl alcohol-carbon nanotubes (PVA-CNT) fiber [9]. This embedded fiber can provide information about the structural health of the composite by utilizing the ERC method when changes in strain/damage are induced to the structure.

The working principle of the sensor fiber is that the CNTs form an electrically conductive network within the PVA matrix of the fiber, which is altered as the fiber deforms and it can be measured and correlated to strain and/or damage [9]. In addition, it was found that pre-stretching of the PVA-CNT fibers before being embedded into the composite, enables for higher screening of the ERC values and therefore enables for better monitoring of the composite material [10]. However, a factor responsible for possibly incorrect measurements from the fiber, are the high shear stresses that occur and ultimately result in the debonding of the fiber from the matrix. In the present work, a numerical analysis of the PVA-CNT fiber embedded in a GFRP for sensing purposes was conducted to investigate the load transfer mechanisms between the composite fiber and the polymer matrix.

A 3-dimensional finite element model was developed to investigate the effect of uniform axial fiber strain on the measured ERC from experimental data. Only a part of the experimental specimen was modelled to save computational power. The PVA-CNT fiber, the composite material and their interface were modelled as three separate bodies. The model was subjected to quasi-static tensile loading and a progressive damage accumulation scheme was utilized to evaluate the strain evolution.

Parameters affecting the bonding between the embedded fiber and the composite's matrix such as the interfacial shear strength, interfacial thickness, stiffness of the interface and the pre-stretch ratio of the sensor (fiber), were also investigated. A comparison was made with relative experimental data, where different composite fiber pre-stretch ratios were embedded in the specimens. In the experimental tests, the PVA-CNT fiber was embedded in a symmetric unidirectional GFRP composite, which consisted of 10 plies of the woven fabric S2-6781, with an Araldite LY564/Aradur 2954 epoxy resin and hardener.

3. Results and discussion

Correlation between strain and ERC for the GFRP specimen with an embedded PVA-CNT fiber (without pre-stretching) is shown in Fig.1. It is evident that, by increasing the tensile force, ERC and strain values increase with R^2=0.9169 and R^2=0.9937, respectively. Hence, it is validated that the PVA-CNT fiber can be used to detect strain changes in the composite.

The numerical analysis showed that the interfacial shear strength had the greatest effect on the bonding strength between the fiber and the matrix. Higher shear strength values delayed the debonding initiation significantly that occurred at higher mechanical loads.

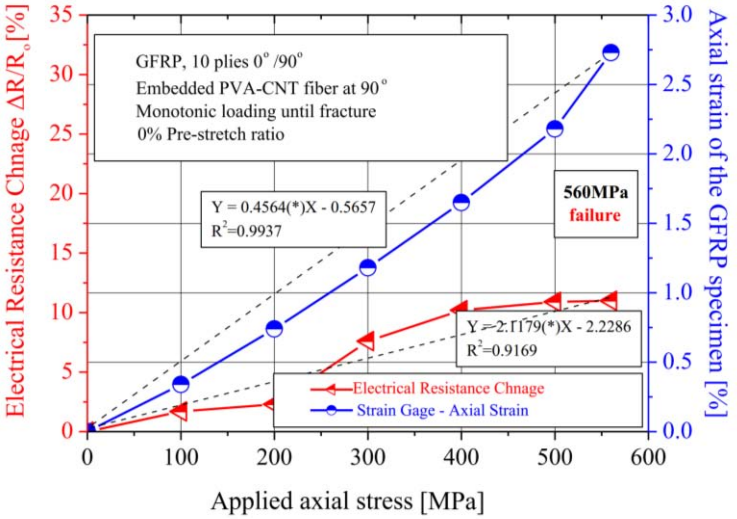

Figure 1. Correlation between axial strain and ERC values of a GFRP specimen with embedded PVA-CNT fiber under monotonic quasi-static loading until fracture.

Additionally, any changes in the interfacial thickness do not seem to affect the fiber stress transfer or at the fiber/matrix debonding load. However, small interfacial thickness values seem to increase marginally the shear stress at the interface, with a greater variance for higher interfacial shear stress.

References

[1] T. Jollivet, C. Peyrac and F. Lefebvre (2013). Damage of composite materials, *Procedia Eng.*, **66**, 746-758.
[2] A. Papantoniou, G. Rigas and N. D. Alexopoulos (2011). Assessment of the strain monitoring reliability of Fiber Bragg Grating sensor (FBGs) in advanced composite structures, *Compos. Struct.*, **93**, 2163-2172.
[3] H. P. Konka, M. A. Wahab and K. Lian (2012). The effects of embedded piezoelectric fiber composite sensors on the structural integrity of glass-fiber epoxy composite laminate, *Smart Mat. Struct.*, **21**, 015016.
[4] K. Schulte and Ch. Baron (1989). Load and failure analyses of cfrp laminates by means of electrical resistivity measurements, *Comp. Sci. Technol.*, **36**, 349-356.
[5] G. J. Gallo and E. T. Thostenson (2016). Spatial damage detection in electrically anisotropic fiber-reinforced composites using carbon nanotube networks, *Comp. Struct.*, **41**, 14-23.
[6] D. He et al. (2017). Design of electrically conductive structural composites by modulating aligned cvd-grown carbon nanotube length on glass fibers, *ACS Appl. Mater. Interfaces*, **9**, 2948-2958.
[7] J. Zhang, Q. Wang, L. Wang and A. Wang (2007). Manipulated dispersion of carbon nanotubes with derivatives of chitosan, *Carbon*, **45**, 1917-1920.
[8] W. B. Down and R. T. K. Baker (1995). Modification of the surface properties of carbon fibers via the catalytic growth of carbon nanofibers, *J. Mater. Res.*, **10**, 625-633.
[9] N. D. Alexopoulos, C. Bartholome, P. Poulin and Z. Marioli-Riga (2010). Structural health monitoring of glass fiber reinforced composites using embedded carbon nanotube (CNT) fibers, *Compos. Sci. Technol.*, **70**, 260-271.
[10] N. D. Alexopoulos, C. Jaillet, C. Zakri, P. Poulin and S. K. Kourkoulis (2013). Improved strain sensing performance of glass fiber polymer composites with embedded pre-stretched polyvinyl alcohol-carbon nanotube fibers, *Carbon*, **59**, 65-75.

EXPERIMENTAL INVESTIGATION OF SPUR GEAR STRENGTH USING PHOTOELASTICITY

K. G. Raptis and A. Savaidis
Department of Mechanical Engineering Educators,
School of Pedagogical and Technological Education, Athens, Greece

1. Introduction

The significance of toothed gears for power and motion transmission is proved by the fact that they are the machine elements mostly used in a large range of engineering applications. Their mechanical behavior is critical for the performance of the assembly in terms of reliability and fatigue endurance. A key factor of their behavior is the design of the gear tooth towards optimized stress distribution. The proposed work focuses on the experimental investigation of the stress field around a gear tooth subjected to a point load.

2. Gear subjected to point load

In the case of a spur gear subjected to a point load maximum bending stress occurs when the load is applied on a special spot, which is called Highest Point of Single Tooth Contact – HPSTC. The position of this spot depends on the basic geometical characteristics of the teeth (Fig.1) and may be determined on the basis of analytical calculations [1-4]. Contact initiates at point A, where the foot of the pinion gear touches the head of the coupled gear, and it ends at point B.

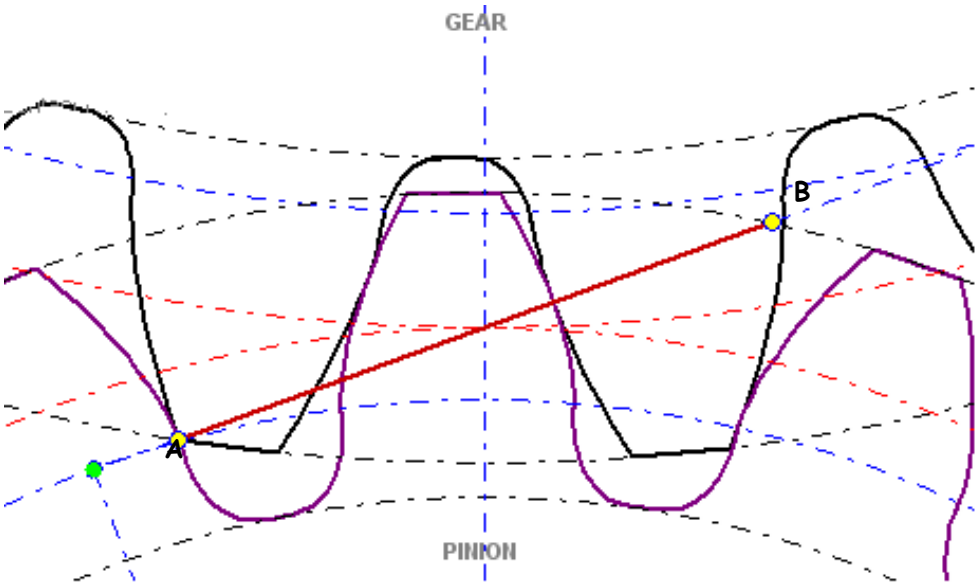

Figure 1. Schematic representation of the cooperation of two spur gears.

In order to experimentally study the strains in the vicinity of the loaded gear region a batch of specimens have been fabricated out of a metal sheet with nominal dimensions of 20 in x 20 in (508 mm x 508 mm) and thickness of 0.375 in (9.5 mm). The sheet had been doubly coated and annealed in order to extinguish any residual stress. The actual sheet thickness has been measured at various positions and found to be approximately 9.25 mm. In addition, four prismatic specimens with dimensions 120 x 20 x 9.25 mm^3 have been fabricated in order to be utilized for determining the elasticity modulus and the stress-optical constant of the material, as well as their variance within the material. To get a first estimation of the highest fringe area, a diffuse light polariscope has been

used, which has been illuminated by a natrium vapor gas lamp in order to produce monochromatic light.

The specimens have been subjected to point loading and the resulting fringes corresponding to maximum stresses have been acquired (Fig.2a) using a polariscope with white light source. The measurements were compared with numerical values derived by a finite element model of the loaded gear tooth in ANSYS (Fig.2b). These comparisons were used for indicating the effect of structural parameters on the measured and simulated tooth response.

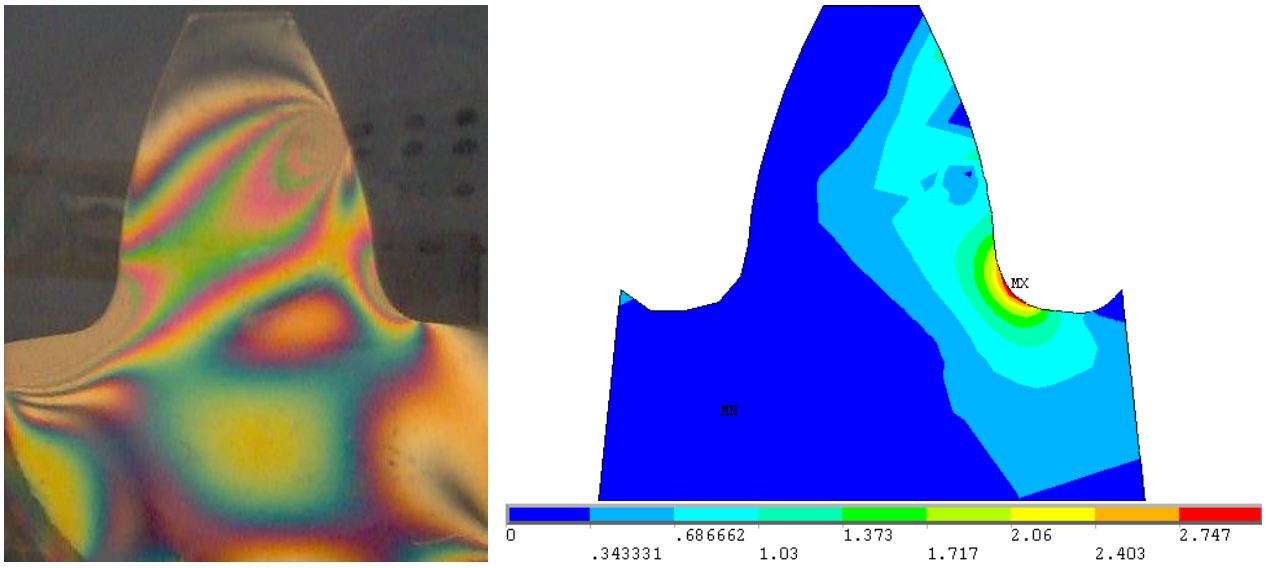

(a) (b)

Figure 2. Experimentally observed stress distribution in a loaded pinion gear (a) under white light and (b) The respective distribution according to the numerical model (ANSYS).

3. Concluding remarks

As far as the comparison between experimental and numerical results is concerned, it has been found that the deviations between measured and predicted maximum stress were in a range of [-1.56%, +1.73%]. These deviations were independent of the applied power (random or maximum) and the corresponding tangential force, for equal geometrical and material parameters. As far as the global stress distribution in the tooth area is concerned, it is expected that application of the load in a larger region instead of a point would lead to better correlation between predicted and experimentally observed values.

References

[1] J. Colbourne (1987). *The Geometry of Involute Gears*. Springer-Verlag, ISBN: 0-387-96522-X.
[2] T. Costopoulos and V. Spitas (2009). Reduction of gear fillet stresses by using asymmetric teeth, *J. Mechan. Mach. Theor*., **44**, 1524-1534.
[3] V. Spitas, V. T. Costopoulos and C. Spitas (2005). Increasing the strength of standard involute gear teeth with novel circular root fillet design, *Am. J. Applied Sci*., **2,** 1058-1064.
[4] V. Spitas, T. Costopoulos and C. Spitas (2007). Fast modeling of conjugate gear tooth profiles using discrete presentation by involute segments, *J. Mechan. Mach. Theor*., **42**, 751-762.

Corrosion and Degradation

CORROSION BEHAVIOUR OF 304L STAINLESS STEEL CONCRETE REINFORCEMENT IN ACID RAIN USING FLY ASH AS CORROSION INHIBITOR

S. Tsouli[1], A. G. Lekatou[1*], S. Kleftakis[1], T. E. Matikas[2] and P. T. Dalla[2]
[1] Laboratory of Applied Metallurgy, Department of Materials Science and Engineering, School of Engineering, University of Ioannina, Ioannina, Greece
[2] Mechanics, Smart Sensors & Nondestructive Evaluation Laboratory, Department of Materials Science and Engineering, School of Engineering, University of Ioannina, Ioannina, Greece

1. Introduction

Stainless steels and titanium are extensively employed in restoration works of ancient monuments. A typical example is the use of 316L stainless steel as steel reinforcement of ancient architectural members in the ancient theater of Dodona in Greece. Several works have shown that fly ash additions in the concrete may improve the corrosion resistance of structural steel [1, 2].

AISI 304 stainless steel is the most common austenitic stainless steel, while AISI 304L is widely used in engineering applications as an important structural material, in the aerospace industry, in architectural constructions etc. This is due to its good corrosion resistance, owing to the chromia-based passive film on the steel surface and the film stabilizing action of nickel, as well as formability [3, 4].

Reinforced concrete is nowadays the most common construction material [2, 5, 6]. Corrosion of steel reinforcement is a major factor responsible for the premature degradation of the structural integrity of reinforced concrete structures [1, 2, 5, 6]. The embedded (in the concrete) steel is protected by the passive oxide film formed on the surface of the steel, as a result of the high pH value of the concrete (pH ≈ 12.5 - 13.5) due to the presence of $Ca(OH)_2$. However, this protective film can be broken down due to either the presence of chloride ions or carbonation that can reduce the value of pH below 9 [2, 5, 6]. Consequently, rust products and oxides are formed, internal stresses appear and the concrete around steel reinforcement cracks [6].

Pollution has rapidly been increasing as a consequence of industrialization, burning of fossil fuels etc., leading to the formation of acid rain, which has a severe effect on metals and alloys and contributes to their deterioration [7]. Various methods have been developed in order to prevent steel corrosion, such as corrosion inhibitors addition, galvanization, coatings etc. [1, 2, 5, 6, 8]. Fly ash, namely the inorganic by-product of the combustion of lignite or subbituminous coal (Class C) or produced from burning anthracite or bituminous coal (Class F) in thermal power stations, can be employed as a corrosion inhibitor. Addition of fly ash into the concrete mixture may reduce the concrete porosity and limit the diffusion of CO_2 and Cl^- penetration, thus improving the resistance to deterioration of reinforced concrete, whilst at the same time increasing the compressive strength of the concrete [1,2,8].

2. The experimental protocol

In the present study, cyclic potentiodynamic polarization tests were conducted on concrete reinforcing rods of AISI 304L stainless steel of 6 mm diameter (three electrode cell, Ag/AgCl/3.5 M KCl, Pt, 4 h immersion under open circuit, room temperature, 10 mV/min scan rate). As electrolyte, an aerated aqueous saturated (s.) $Ca(OH)_2$ solution containing acid rain simulating solution and different fly ash contents was employed. This testing solution simulates concrete pore environments in urban and industrially polluted environmental conditions [7, 9]. Simultaneously, concrete reinforcing rods embedded in standard concrete cubes were subjected to salt spray testing for the period of four months. Furthermore, tensile testing was conducted before and after the salt spray test.

3. Results and conclusions

Cyclic polarization of AISI 304L concrete reinforcing rods in s. $Ca(OH)_2$ containing acid rain simulating solution and different amounts of fly ash revealed passivation and susceptibility to localized

* Corresponding author, alekatou@cc.uoi.gr

corrosion (Fig.1). Fly ash addition has led to less thermodynamic tendency for corrosion, slower corrosion kinetics and higher resistance to localized corrosion (negative hysteresis loops of smaller surface area or even positive hysteresis loops). The slowest corrosion kinetics has been exhibited by the 20% fly ash addition. However, 25 wt% fly ash addition in the concrete simulating solution led to a deterioration of the corrosion performance (both uniform and localized) as compared to the performance exhibited at 20 wt% fly ash, which is attributed to the agglomeration of the fly ash particles. Finally, salt spraying did not significantly affect the mechanical properties of the concrete reinforcement, with the exception of a slight decrease in the % elongation, which, although systematic, is within experimental error (Table 1). The present effort showed that 304L steel can replace 316L in the restoration of ancient works provided that fly ash is employed as a corrosion inhibitor.

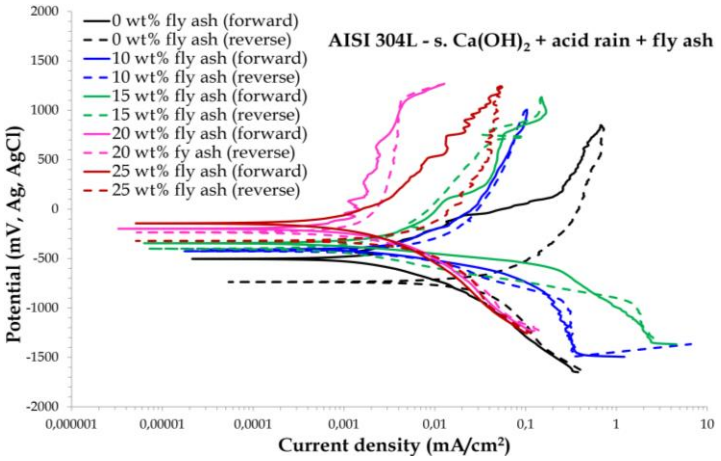

Figure 1. Cyclic voltammograms of 304L concrete reinforcing rods in s. Ca(OH)$_2$ containing acid rain simulating solution and different fly ash amounts.

Fly ash (wt%)	Duration (m)	σ_y 0.2% (MPa)	σ_y (MPa)	σ_t (MPa)	σ_f (MPa)	% EL
0	0	611±31	663±2	782±31	726±50	44±0
	2	605±50	663±23	776±58	720±57	42±1
15	0	619±30	660±9	790±27	732±3	43±1
	2	555±44	648±10	729±52	667±24	41±2
20	0	586±15	659±25	754±16	686±20	43±1
	2	594±19	653±8	771±18	735±4	40±2
25	0	592±8	664±1	753±11	669±1	42±1
	2	598±41	670±2	780±38	706±31	43±0

Table 1. Tensile properties of 304L concrete reinforcing rods embedded in concrete with different fly ash contents.

References

[1] N. Chousidis, I. Ioannou, E. Rakanta, C. Koutsodontis and G. Batis (2016). Effect of fly ash chemical composition on the reinforcement corrosion, thermal diffusion and strength of blended cement concretes, *Constr. Build. Mater.*, **126**, 86-97.
[2] M. Criado, I. Sobrados, J. M. Bastidas and J. Sanz (2016). Corrosion behaviour of coated steel rebars in carbonated andchloride-contaminated alkali-activated fly ash mortar, *Prog. Org. Coat.*, **99**, 11-22.
[3] A. Lekatou (2005). *Industrial alloys*, Papasotiriou Publication, Athens, 63-66 & 84.
[4] P. Wang, J. Zhang, Y. Zhang, H. Wang, W. Hu and D. Yu (2016). Preparation of high-performance ultrafine-grained AISI 304L stainless steel under high temperature and pressure, *Prog. Nat. Sci.: Mater. Int.*, **26(4)**, 404-410.
[5] N. Chousidis, E. Rakanta, I. Ioannou and G. Batis (2015). Anticorrosive effect of electrochemical manganese dioxide by-products in reinforced concrete, *J. Mater. Sci. Chem. Eng.*, **3**, 9-20.
[6] T. Zafeiropoulou, E. Rakanta and G. Batis (2011). Performance evaluation of organic coatings against corrosion in reinforced cement mortars, *Prog. Org. Coat.*, **72**, 175-180.
[7] H. Gerengi, G. Bereket and M. Kurtay (2016). A morphological and electrochemical comparison of the corrosion process of aluminum alloys under simulated acid rain conditions, *J. Taiwan Inst. Chem. E.*, **58**, 509-516.
[8] N. Chousidis, E. Rakanta, I. Ioannou and G. Batis (2015). Mechanical properties and durability performance of reinforced concrete containing fly ash, *Constr. Build. Mater.*, **101(1)**, 810-817.
[9] C. J. Kitowski and H. G. Wheat (1997). Effect of chlorides on reinforcing steel exposed to simulated concrete solutions, *Corros.*, **53(3)**, 216-226.

THE IMPACT OF CORROSION AND INELASTIC BUCKLING ON LOW CYCLE FATIGUE LIFE OF STEEL BARS

A. Apostolopoulos and T. E. Matikas
Department of Material Science and Engineering, University of Ioannina, Greece

1. Introduction

The effects of seismic action (seismic loads) are known to act on the load bearing elements of structures in the form of high strain reversals, which is commonly simulated as single axis Low Cycle Fatigue (LCF) [1]. In the current design practice, a displacement ductility coefficient is used even if it fails to account for the accumulated damage. This happens because it is implicitly assumed that structural damage occurs only due to the maximum response deformation and is independent of the number of non-peak inelastic cycles or strain energy dissipation [2]. However, all inelastic cycles must be considered as contributors to damage since they constitute the strain history observed in actual structures and their accumulation may become important depending on the characteristics of the ground motion [2].

During strong earthquakes, yielding structures are subjected to increased number of cycles into the inelastic range and the accumulated damage may significantly affect their overall performance. This type of damage may also evolve from multiple earthquakes, in this case, a series of pre or post shocks combined with the main shock may be treated as a single event of extended duration. There is an assessment of seismic damage which is usually assumed to be similar to metal fatigue under variable amplitude cyclic loading. On the other hand, relatively little attention has been devoted by the research community on the combined effect of corrosion and LCF on steel reinforcement since each one of these factors affects the rebar durability and performance and shortens the life expectancy of structures [3-8]. The analysis of the effective LCF (seismic) performance of steel reinforcing bars represents, nowadays, a problem of relevant importance in the widest framework of the investigation of the global ductile behavior of RC structures and remains, till now, partially unsolved [9].

The current experimental study examines the effect of corrosion damage and inelastic buckling on LCF life of reinforcing steel bars grade B500A and B500B, with nominal diameter 12 mm. In a total of 110 specimens, experiments were conducted before and after exposure in laboratory salt spray environment. Both tensile and low cycle fatigue tests were conducted.

2. Experimental procedure

In order to study the mechanical behavior of steel bars under conditions of corrosion damage and inelastic buckling on low cycle fatigue, a representative number of high strength steel specimens with B500A and B500B steel grades and 12 mm diameter were selected for experimental tensile tests and LCF tests. The above-mentioned specimens were sprayed in a salt spray fog corrosion chamber, according to ASTM B117 specification, for 45 and 90 days, with a 5% w.t. sodium chloride and 95% distilled water solution, pH range of 6.5 - 7.2, and temperature of 35 (+1.1–1.7 ^{o}C).

During the experimental procedure a digital measurement of pH monitored chamber's environment. A number of tensile tests were carried out on reference and corroded specimens to provide a general idea of the effects of corrosion on the tensile mechanical properties of the material. Tensile tests were carried out according to ISO 15630-1 [10]. The selected exposure times for the tensile tests were 0 and 90 days. Furthermore, a number of low cycle fatigue tests for each corrosion level were conducted for two different strain levels (imposed deformation) ± 2.5% and ± 4% (see Fig.1).

All mechanical tests were conducted at room temperature using an Instron dynamic servo-hydraulic system. All readings were recorded using a fully automated computer system. Tensile tests were performed at four specimens of each class A, B for grade B500 steel for different corrosion levels.

3. Results and discussions

The results of mechanical tensile tests confirmed that corrosion is a significant factor of degradation in mechanical properties of steel bars. The findings also suggest that the degradation of the mechanical performance of steel on seismic loads can be attributed to mechanism of inelastic buckling influenced by loading history with a combination of the presence of extensive porosity close to the surface of the steel bar. The effects on both steel types under conditions of laboratory salt spray corrosion and mass loss of 8.5% to 11.5%, showed an equivalent drop in strength properties, in contrast to ductility properties which recorded a dramatic drop.

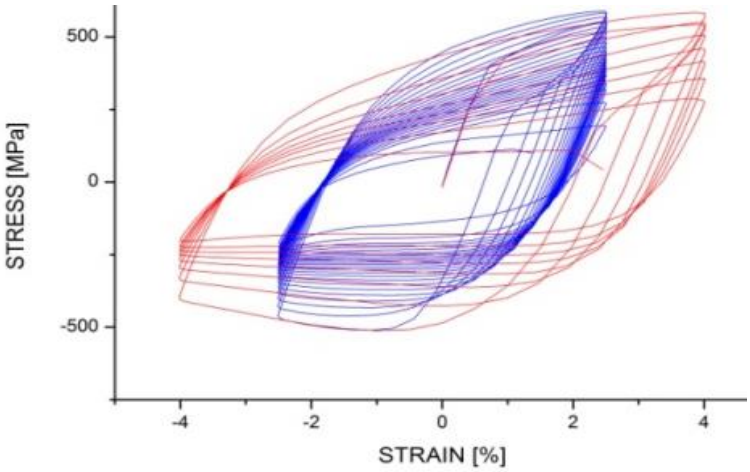

Figure 1. Hysteresis loops for two strain levels ± 2.5% (red) and ± 4% (blue color).

Generally, the lifetime (number of cycles) decreased with the increase of the level of imposed deformation and free length of the specimen. Increasing the free length reduces the mechanical performance of steel bar. This reduction is more unfavorable in case of corroded specimens where buckling phenomena are encouraged and the corroded bars have highly localized pitting corrosion. The negative effect of free length on the mechanical properties of steel bars is greater than the negative effect of corrosion, due to buckling phenomena which lead to premature unexpected failures.

References

[1] G. M. Sheng and S. H. Gong (1997). Investigation of low cycle fatigue behaviour of building structural steels under earthquake loading, *Acta Metallurgica Sinica*, **10**, 51-55.

[2] Y. H. Chai (2005). Incorporating low-cycle fatigue model into duration-dependent inelastic design spectra, *Earthquake Eng Struct. Dyn*., **34**, 83-92.

[3] S. Y. M. Ma, V. V. Bertero and E. P. Popov (1976). Experimental and analytical studies on the hysteretic behaviour of reinforced concrete rectangular and T-Beams. *Report No. EERC 76-2, Earthquake Engineering Research Center*, University of California, Berkeley, California, USA.

[4] T. Yoshaki (1983). *Proceedings of Academicals Lectures of JAS*. Tokyo, **606** (in Japanese).

[5] H. Shigeru (1995). Retrofitting of reinforced concrete moment resisting frames, *Research report, ISSN 0110-3326*.

[6] G. G. Clementa (2002). Testing of selected metallic reinforcing bars of extending the service life of future concrete bridges, *Final report of the Virginia Transportation Research Council*, Charlottesville, Virginia, VTRC 03-R7.

[7] H. Krawinkler (1987). Performance assessment of steel components, *Earthquake Spectra*, **3**, 27-41.

[8] I. Kasiraj and J. T. P. Yao (1969). Fatigue damage in seismic structures, *Journal of the Structural Division (ASCE)*, **95**, 1673-1692.

[9] C. Apostolopoulos, C. Ascanio, L. Bianco, A. Braconi, S. Caprili, G. Diamantogiannis, G. Ferreira Pimenta, M. Finetto, J. Moersch and W. Salvatore (2014). Effects of corrosion on low-cycle fatigue (seismic) behaviour of high strength steel reinforcing bars, *Final report of RFSR-CT-2009-00023 project*, European Commission, Brussels.

[10] ISO/FDIS 15630-1 (2002). International Standard. Steel for the reinforcement and prestressing of concrete - Test methods - Part 1: Reinforing bars, wire rod and wire [ISO/FDIS 15630-1 (2002)].

COMPARISON OF THE MECHANICAL RESPONSE OF A DUAL-PHASE AND A SINGLE-PHASE STEEL BAR CATEGORY

A. Drakakaki, A. Apostolopoulos and Ch. Apostolopoulos
Laboratory of Technology & Strength of Materials,
Department of Mechanical Engineering and Aeronautics, Patras, Greece

1. Introduction

In the present work, the effects of chloride-induced corrosion on a dual-face and a single-face reinforcing steels are evaluated in terms of corrosion resistance and mechanical characteristics before and after the corrosion process. Comparison of corrosion damage rates between the two types of steel, both of which have been used in existing structures, indicates that they demonstrate different resistance against the ascribed corrosion environments.

Three different corrosion procedures were imposed on the steel bar categories, in order to achieve a satisfying correlation with the environmental conditions. Initially, the simulation of exposure to harsh corrosive environment was achieved with the use of a salt spray fog chamber (Fig.1), under constant spraying with 5% w.t. NaCl solution. Secondarily, two sets of impressed current density corrosion tests were organized. The first set of tests was executed in constant wet conditions and the second in wet/dry cycles, making conditions more aggressive. Combining the above-mentioned methods, an effort was made to correlate the electrochemical corrosion system (Fig.2), to the natural environment, by exploiting the results taken from the salt spray fog chamber.

At the same time, the differences among the two steel bar categories are analyzed, and estimation is made concerning their degradation in reference to their exposure to the environmental conditions. Single-phase steel demonstrates higher corrosion resistance, in comparison to the dual-phase category. Vulnerability of dual-phase steel seems to be attributed to the existence of the martensite layer. Both, mechanical behavior and corrosion resistance of the two categories raise questions concerning the mechanical performance of existing structures as well.

The goal of the study was primarily to correlate artificial corrosion to environmental conditions and secondarily to highlight the differences among the two steel categories, given that they have been both used in existing civil engineering structures.

Figure 1. Salt spray fog chamber.

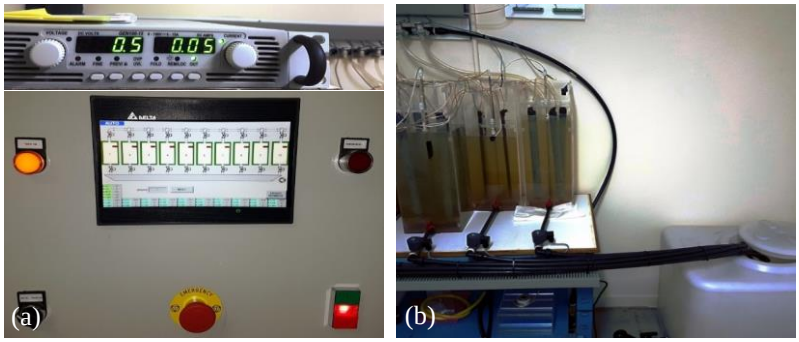

Figure 2. (a) Control System and (b) corrosion cells for the electrochemical corrosion tests.

2. Materials and methods

For the goals of the present study, material of two different steel reinforcement categories was used. Precisely, S500s dual phase [1-2] and S400 (StIII) single phase [3-5] steel bars were exposed to the corrosion process and they were mechanically tested in tensile and Low Cycle Fatigue (LCF) tests. Artificial corrosion tests were executed with the use of two methods, salt spray fog chamber (ac-

cording to ASTM B117 [6] specification) and electrochemical corrosion method. After removal from the corrosive conditions, the specimens were let to dry. The oxide layer formed was then removed from their surface according to ASTM G1 [7] specification. Afterwards, all mechanical tests were conducted at room temperature using an MTS 250 kN servo-hydraulic testing system. Three tests were performed for each case.

3. Results and discussion

Corrosion of steel reinforcement is a major problem for reinforced concrete structures, as far as durability is concerned [8]. Corrosion degradation is responsible for several issues, such as deterioration of both durability and service life of structures, resulting in premature failure. This scenario becomes even worse when the structures are located in earthquake prone areas. Cyclic loading, which is due to seismic activity, leads to a non- linear response of the structures that face durability issues.

Both dual and single-phase steel reinforcement have been used in existing structures. However, the different internal structure of the two types of steel attributes different mechanical characteristics to each category. Both different mechanical characteristics and corrosion resistance result in unlike response of the two materials in long term. Given the differences among the two materials examined in the present study, as far as yield stress and vulnerability to corrosion is concerned, it is difficult to make a common prediction for the deterioration of existing structures. An effort was made to correlate the results received from the laboratory tests, for each steel bar category, to the environmental conditions.

References

[1] Ch. Apostolopoulos (2007). Mechanical behavior of corroded reinforcing steel bars S500s tempcore under low cycle fatigue, *Construction and Building Materials*, **21**, 1447-1456.
[2] Ch. Apostolopoulos and C. A. Rodopoulos (2010). Inelastic cyclic behavior of as-received and pre-corroded S500s tempcore steel reinforcement, *International Journal of Structural Integrity*, **1**, 52-62.
[3] Ch. Apostolopoulos and M. P. Papadopoulos (2007). Tensile and low cycle fatigue behavior of corroded reinforcing steel bars S400, *Construction and Building Materials*, **21**, 855-864.
[4] Ch. Apostolopoulos, D. Michalopoulos and L. Dimitrov (2008). The impact of corrosion on the mechanical behavior of welded splices of reinforcing steel S400 and B500c, *Journal of Materials Engineering and Performance*, **17**, 70-79.
[5] Ch. Apostolopoulos and V. P. Pasialis (2010). Effects of corrosion and ribs on low cycle fatigue behavior of reinforcing steel bars S400, *Journal of Materials Engineering and Performance*, **19**, 385-394.
[6] ASTM B 117-94 (1995). Standard practice for operating salt (fog) testing apparatus. In: *Annual Book of ASTM standards, Section 3, Metal test methods and analytical procedures*. Philadelphia, USA: West Conshohocken, ASTM.
[7] ASTM G1-90 (1995). Standard practice for preparing, cleaning and evaluating corrosion test specimens. In: *Annual Book of ASTM standards, Section 3, Metal test methods and analytical procedures*. Philadelphia, USA: West Conshohocken, ASTM.
[8] A. A. Almusallam (2001). Effect of degree of corrosion on the properties of reinforcing steel bars, *Construction and Building Materials*, **15**, 361-368.

DEVELOPMENT OF NEW ENVIRONMENTALLY FRIENDLY ANTICORROSIVE SURFACE TREATMENTS FOR NEW AL-LI ALLOYS PROTECTION WITHIN THE FRAME OF CLEAN SKY2

A. Karanika[1], N. Vourdas[2], A. Makrikostas[1], R. Marini[1], Th. Plagianakos[1] and S. Kalogeropoulos[1]
[1] Hellenic Aerospace Industry S.A., Schimatari, Viotia, Greece
[2] Technological Educational Institute of Sterea Ellada, Psachna Campus, Evia, Greece

1. Introduction

Operational considerations, societal concerns and REACH regulations are creating a growing demand for the development of new effective and environmentally friendly technologies. From an operational point of view, materials used in manufacturing airframe components need to become lighter, more resistant in corrosion, cheaper and more eco-compliant [1]. These components will include the composite wing, the metallic or composite fuselage and the cockpit structure. From an environmental and societal point of view, it will be necessary to reduce the aviation footprint [2], through aircraft performance improvements (drag, weight and versatility) and an eco-friendly life cycle including a significant decrease of hazardous materials during the manufacturing phase. ACARE targets and REACH regulations should be also fulfilled.

Within the frame of all the above mentioned needs and targets, HAI is participating in Clean Sky2: ecoTECH seven years core project (2016-2022). Surface treatments anticorrosive technologies are under development and evaluation in ecoTECH project:

- New chromium free anodization surface treatments.
- Sprayable out-of bath surface treatments.

In this work, the current activities are presented in terms of surface treatments, mechanical characterization and formability performance on new Al alloys.

2. Experimental protocol

2.1 Exploitation of new Al alloys

The objective of this work is the investigation and characterization of high-strength aluminium-lithium alloys with improved mechanical properties, formability and corrosion resistance [3]. The investigated substrate materials are new Al-Li alloys from ARCONIC and Constellium. In more details, the investigated alloys are the following: (i) 2060 T8E30 by ARCONIC, (ii) 2198 T3 by Constellium. So far, Tensile (ASTM E8) and Fatigue properties (BS EN 6072) have been characterized in L direction of 2060 T8E30 specimens. Sheets of the above mentioned alloy have also subjected in rolling experiments in various radius in order to estimate the formability performance of the new alloy.

2.2 Candidate surface treatments

New Al-Li alloys exhibit better-off behavior against corrosion, thus allowing for less severe corrosion protection schemes. The objectives of this research activity are to investigate the effects of different surface treatments and anti-corrosion paints on new aluminium components. The investigated surface treatments are: (i) Thin Film Sulphuric Anodizing (TFSA) and (ii) sprayable application of Sol Gel (AC131). Both treatments are fully Chromium free and REACH compliant [4]. The process sequence for the surface preparation of the Al surfaces is the following: 1) Alkaline degreasing; 2) Rinsing; 3) Alkaline etching; 4) Rinsing; 5) Desmuting; 6) Final Rinsing. In Fig.1 the surface of Al2198 alloy is depicted with SEM, after surface preparation.

3. Results and discussion

The initial tensile and fatigue results on 2060 T8E30 alloy specimens have been compared with the related mechanical properties of conventional aeronautical 2024 Al alloy. Typical quasi-static flow

curves for AA2060 are shown in Fig. 2. Samples out of 2060-T8E30 sheets have been subjected in rolling experiments and for different rolling radius. No cracks were detected after rolling and FPI nondestructive testing even on smaller radius of rolling. The experimental results are further discussed explicitly in the article.

4. Conclusions

The research is in progress for both conventional and new alloys and surface treatments with encouraging technical results, in terms of mechanical properties and formability, while surface treatments are close to meet the technical specifications set for the current technologies.

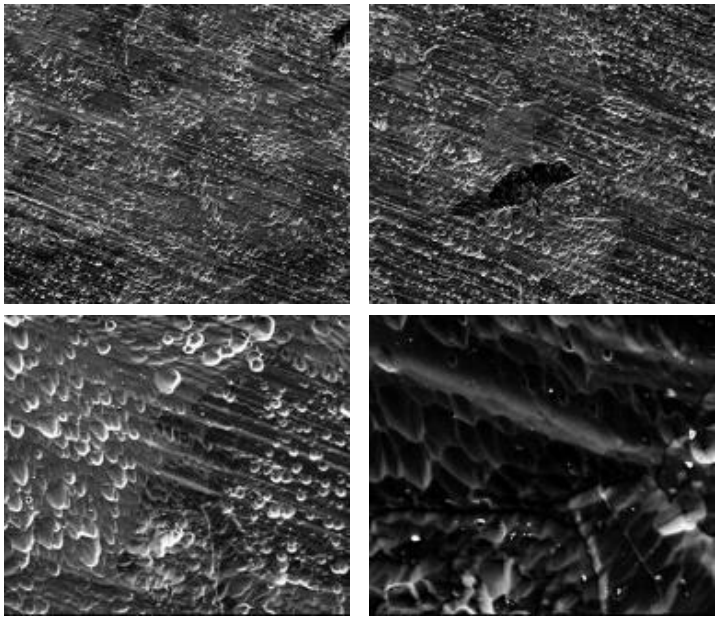

Figure 1. SEM images of the Al2198 after surface preparation and before anodization and/or Sol Gel.

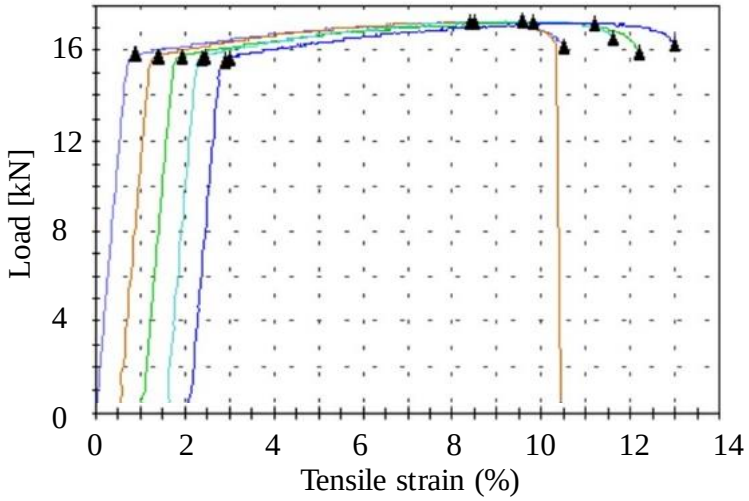

Figure 2. Tensile test results for five different specimens on 2060T8E30 along the L rolling direction.

Acknowledgements

This research at Hellenic Aerospace Industry S.A. was performed in cooperation with TEI of Sterea Ellada, in the framework of the JTI-CS2-AIR ecoTECH core project, funded by the Clean Sky Joint Technology Initiative.

References

[1] J. Montgomery (2007). Aircraft primary structure and materials, *Workshop on Revolutionary Aircraft for Quiet Communities. Hampton*, VA: National Institute of Aerospace.
[2] M. Price, S. Raghunathan and R. Curran (2006). An integrated systems engineering approach to aircraft design, *Progress in Aerospace Sciences*, **42**, 331-376.
[3] T. Dursun and C. Soutis (2014). Recent developments in advanced aircraft aluminium alloys, *Materials & Design*, **56**, 862-871.
[4] R. L. Twite and G. P. Bierwagen (1998). Review of alternatives to chromate for corrosion protection of aluminum aerospace alloys, *Progress in Organic Coatings*, **33**, 91-100.

EFFECT OF CORROSION EXPOSURE ON THE MECHANICAL PERFORMANCE OF 2024 ALUMINIUM ALLOY ELECTRON BEAM WELDED JOINTS

E. Dovletoglou[1], P. Skarvelis[2], V. Stergiou[3] and N. D. Alexopoulos[1]
[1] University of the Aegean, School of Engineering,
Department of Financial Engineering, 821 32 Chios, Greece
[2] National Technical University of Athens, School of Mining and Metallurgical Engineering,
7 Heroes Polytechniou Str., Athens, Greece157 73 Zografou, Greece
[3] Research and Product Design, Hellenic Aerospace Industry S.A.,
P.O. Box 23, Schimatari, Greece

1. Introduction

The last few decades, there is an increasing interest for altering the manufacturing processes in aircraft components. The conventional differential structures are being replaced by welded ones, mainly to reduce structural weight and increase structural safety. Several welding techniques are candidate for such a cause, mainly depending on their availability as well as their effectiveness when used in different metallic structures (i.e., structures made of steels, titanium and aluminium alloys, etc.). One of the most favorable and already applied process for welding metallic structures is the electron beam welding, where it utilizes a concentrated electron beam to produce essential narrow welded seams and for relatively high thickness structures.

Aluminium alloy 2024 is a high-strength aluminum alloy with improved mechanical properties, e.g. fatigue lifge, fracture toughness and resistance to corrosion [1, 2]. The low density of aluminium, its ability to resist the kind of progressive oxidization as well as corrosion by environmental factors and chemical or physical agents, are the most important characteristics which put aluminium in an advantageous position compared to other metals [3]. An extended research has been already implemented regarding the performance of welded joints of different aluminum alloys, such as 2024, 5005 and 6061 [4]. Previous research [2] on AA2024 sheet (10 cm x 15 cm) has concluded that EBWed AA2024 imposes lower overall metallurgical damage as compared to other welding processes, and hence, it appears worth investigating further its performance. Nevertheless, EBWed aluminum alloys present specific disadvantages such as a large degraded fusion zone [2, 3], solidification cracking during welding [5] and porosity in the weld [6]. The aim of the present study is to experimentally investigate the mechanical performance of electron beam welded AA2024 as well as the corrosion susceptibility of the welded joints.

2. Materials and methods

For the present investigation, the material used was AA2024 at T3 temper and of 3.2 mm nominal thickness. Rectangular sheets (100 mm x 200 mm) were exposed to different artificial ageing conditions, to simulate all ageing conditions, namely under- (UA), peak- (PA) and over-ageing (OA) at 170^{o}C. Electron beam welding was performed after the different artificial ageing conditions to assess the effect of artificial ageing on the resulting microstructure after the fusion process.

Tensile and fatigue specimens were machined along the longitudinal (L) rolling direction of the welded sheets and according to ASTM E8 and E466 specifications, respectively. The tensile and fatigue specimens have been machined from the welded sheets, with the welding seam being at the middle of the cross-section of the specimens. The tensile specimens were subjected to mechanical testing according to ASTM E8 specification in order to investigate the effect of the respective fusion welding on the tensile mechanical properties. A number of welded specimens was exposed to laboratory exfoliation corrosion environment (EXCO) up to 48 h, according to ASTM G34 specification. This test series aimed to assess the corrosion resistance of the welded joints and generally to compare their susceptibility to corrosion with non-welded specimens. A common corrosion exposure

time was selected to corrode all fatigue specimens so as to construct the S-N curve and compare it against the respective one of non-corroded welded specimens.

3. Results and discussions

Preliminary results show that the welding process essentially affects elongation at fracture; it is essentially decreased from approximately 12% (non-welded specimens) at around 3% (Fig.1). Ultimate tensile strength is not significantly decreased, showing that welded joints with high structural joining efficiency can be achieved. The effect of corrosion exposure on the welded joints is also analyzed and discussed on the article. The effect of short exposure time (e.g. 2 h) shows that similar tensile flow curves are obtained with the exception of lower ductility properties. Higher exposure time to corrosion solution (e.g. 4 h and so forth) essentially decreases the ultimate tensile strength of the specimens as well as elongation at fracture. In ref.[7] this large drop in strength properties was also observed and it was associated with decrease in the cross-sectional area of the specimens due to the formation of surface corrosion products, including micro-cracking. For exposure up to 24 h no significant strength drop is noticed, however an essential deterioration of the mechanical properties was noticed for extreme corrosion exposure; both, ultimate tensile strength and tensile elongation at fracture was essentially decreased at low levels. The results of the tensile tests will be further discussed along with microstructural investigation of the corroded specimens with light optical microscopy.

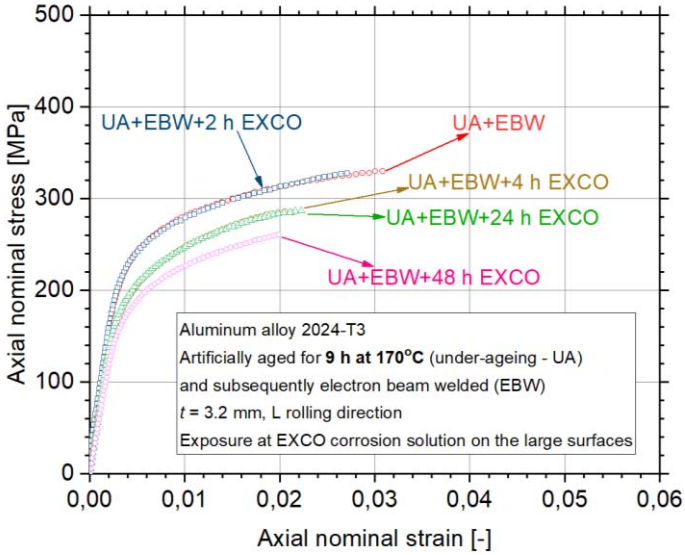

Figure 1. Typical tensile flow curves of corroded and non-corroded EBWed specimens.

The corrosion exposure was found to, also, decrease the fatigue life of the welded specimens. More than 30% decrease of the fatigue endurance limit was observed after the exposure of the specimens tested under fatigue to the corrosive environment.

References

[1] J. R. Davis (2001). *ASM Specialty Handbook: Aluminum and Aluminum Alloys*, ASM International, Ohaio, 351-416.
[2] F. Lefebvre, S. Wang, M. J. Starink and I. Sinclair. (2002). Microstructural features of fusion welded 2024-T351, in *Proceedings of 8th International Conference (ICAA8)*, July 2-5, Cambridge, UK.
[3] R. V. Preston, H. R. Shercliff, P. J. Withers and S. D. Smith (2003). Finite element modelling of tungsten inert gas welding of aluminium alloy 2024. *Sci. Tech. Weld. Join.*, **8**, 10-18.
[4] G. Çam, V. Ventzke, J. F. Dos Santos, M. Koçak, G. Jennequin and P. Gonthier-Maurin (2000). Characterisation of electron beam welded aluminium alloys, *Practical Metallography*, **37**, 59-89.
[5] S. Kou and Y. Le (1988). Welding parameters and the grain-structure of weld metal e a thermodynamic consideration, *Metal.Trans. A.*, **19,** 1075-1082.
[6] B. Hu and I. M. Richardson (2005). Autogenous laser keyhole welding of aluminum alloy 2024, *Journal of Laser Applications*, **17**, 70-80.
[7] N. D. Alexopoulos, Z. Velonaki, C. I. Stergiou, S. K. Kourkoulis (2016). The effect of artificial ageing heat treatments on the corrosion-induced hydrogen embrittlement of 2024 (Al-Cu) aluminium alloy, *Corros. Sci.*, **102**, 413-424.

EFFECT OF CORROSION EXPOSURE ON ALUMINUM ALLOY 2024 FOR DIFFERENT ARTIFICIAL AGEING CONDITIONS

N. Siskou[1], Ch. Charalampidou[1] and S. K. Kourkoulis[2]
[1] Department of Financial and Management Engineering, School of Engineering, University of the Aegean, Chios, Greece
[2] Department of Mechanics, Laboratory for Testing and Materials, National Technical University of Athens, Athens, Greece

1. Introduction

Corrosion exposure leads to mechanical properties degradation of aluminum alloys and consequently to the deterioration of the structural integrity of aircraft structures. Aluminum alloys, e.g. 2024, are commonly used in the aircraft industry due to their high specific strength and damage tolerance. However, they are susceptible to corrosion attack due to their microstructure (Cu content) and complex precipitation system [1-3]. The major strengthening precipitation system of AA2024 is the *S* (Al_2CuMg) and θ (Al_2CuMg) particles. Since the *S*-phase particles are preferentially cited at grain boundaries, copper depleted zones are formed adjacent to the boundaries that are anodic to the copper rich grain boundaries; hence, a micro-galvanic corrosion takes place leading to corrosion of the particle or the surrounding matrix [3]. The effect of corrosion on reference specimens from AA2024 at T3 temper is extensively studied in the literature. Corrosion exposure of AA2024-T3 in accelerated laboratory environments resulted in mechanical properties degradation mainly due to surface pitting, subsequent micro-cracking formation as well as hydrogen embrittlement [5]. It is acknowledged [6] that corrosion exposure has a negative effect on yield strength of AA2024-T3 mainly due to cross-section decrease at higher exposure times as well as on ductility due to combination of hydrogen embrittlement and cross-sectional decrease. Synergy of corrosion-induced surface microcracking and hydrogen embrittlement was found to decrease the tensile mechanical properties and essentially tensile ductility [7].

As the design life of a typical aircraft is about 25 years, the mechanical properties of the AA2024-T3 should vary during this period due to the microstructural changes coming from natural ageing of the alloy. Hence, a more realistic point of view is that the alloy should be exposed to the corrosive environment when first being natural (or artificially) aged to assess its true degradation due to the synergy of ageing and corrosion. It is generally reported [8] that the 2xxx aluminium alloys in T3 condition (under-ageing) have lower corrosion resistance than at the T6 and T8 (peak-ageing).

2. Material and experimental procedure

In this study, the effect of artificial ageing on the corrosion evolution and residual mechanical properties of AA2024 is investigated. Artificially aged tensile specimens were pre-exposed to exfoliation corrosion solution (EXCO) for different exposure times and then were mechanically tested to assess the effect of microstructural changes due to ageing on the corrosion evolution and damage.

Tensile specimens of AA2024-T3 (received in sheet form of 3.2 mm nominal thickness) were exposed for different artificial ageing heat-treatments in order to simulate natural ageing of the alloy. All specimens were artificially aged in the same temperature of 190°C for different times to simulate under-, peak- and over-ageing tempers. After artificial ageing heat-treatment specimens were covered on the side-surfaces (LT rolling direction) and immersed in exfoliation corrosion (EXCO) solution, according to ASTM G34. Afterwards, all the specimens were tensile tested according to ASTM E8.

3. Results and discussion

Fig.1a shows the tensile flow curves (grey circles) of the non-corroded specimens for (a) 2 h ageing time (under-ageing condition) and (b) 8 h ageing time (peak-ageing condition). Ageing time has a profound effect on the increase of yield stress; more than 100 MPa increase can be noticed on the

expense of tensile ductility (elongation at fracture) that exceeds 25% decrease. Figure 1a shows the tensile flow curves for different exposure times to corrosion solution in under-ageing condition. Essential decrease (exceeding 15%) in elongation at fracture is noticed after only 2 h corrosion exposure (green circles). For the case of 24 h exposure time (magenta circles) the flow curve is essentially decreased and a vertical drop of approximately 100 MPa is noticed for ultimate tensile strength. This was attributed in [6] as the outcome of the decrease of cross-section as well as of the local embrittlement due to hydrogen diffusion.

Fig.1b shows the respective flow curves of the same corrosion exposure times in the peak-aged specimens of AA2024. It can be easily noticed that the effect of corrosion exposure is definitely not the same as in the T3 temper. The effect of corrosion exposure (e.g. at 24 h exposure) is evident in the decrease of tensile elongation at fracture (approximately 20 %), when compared against the respective at the under-ageing condition (more than 45% was noticed). Such effects on the tensile mechanical properties as well as for other artificial ageing conditions are explicitly discussed in the article, supported by metallographic investigations to support the findings of the present work.

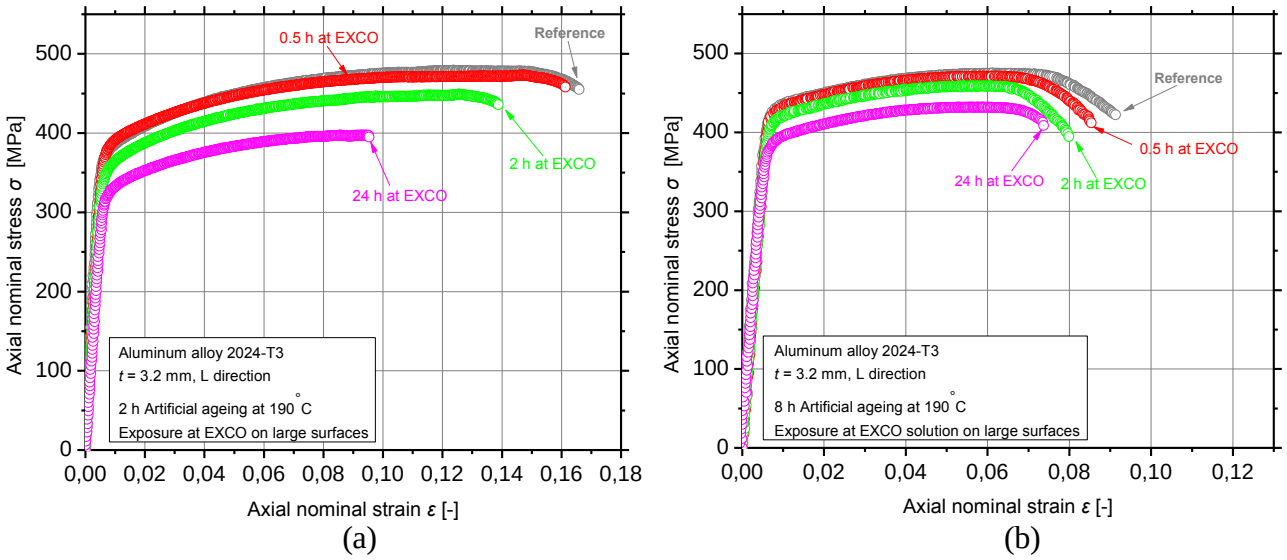

Figure 1. Typical tensile flow curves of corroded and non-corroded specimens for different artificial ageing heat treatment for (a) 2 h - under-ageing condition and (b) 8 h - peak-ageing condition.

References

[1] J. A. DeRose, J. Suter, T. Bałkowiec, A. Michalski, K. J. Kurzydlowski and P. Schmutz (2012). Localised corrosion initiation and microstructural characterisation of an Al2024 alloy with a higher Cu to Mg ratio, *Corros. Sci.*, **55**, 313-325.

[2] A. Boag, A. E. Hughes, A. M. Glenn, T. H. Muster and D. McCulloch (2011). Corrosion of AA2024-T3 part I: localised corrosion of isolated IM particles, *Corros. Sci.*, **53**, 17-26.

[3] V. Guillaumin and G. Mankowski (1999). Localized corrosion of 2024-T351 aluminum alloy in chloride media, *Corros. Sci.*, **41**, 421-438.

[4] A. E. Hughes, T. H. Muster, A. Boag, A. M. Glenn, C. Luo, X. Zhou, G. E. Thompson, D. McCulloch (2010). Co-operative corrosion phenomena, Corros. Sci. **52**, 665-668.

[5] H. Kamoutsi, G. N. Haidemenopoulos, V. Bontozoglou and Sp. G. Pantelakis (2006). Corrosion-induced hydrogen embrittlement in aluminum alloy 2024, *Corros. Sci.*, **48**, 1209-1224.

[6] N. D. Alexopoulos, C. J. Dalakouras, P. Skarvelis and S. K. Kourkoulis (2012). Accelerated corrosion exposure in ultra-thin sheets of 2024 aircraft aluminium alloy for GLARE applications, *Corros. Sci.*, **55**, 289-300.

[7] Al. Th. Kermanidis, P. V. Petroyiannis and Sp. G. Pantelakis (2005). Fatigue and damage tolerance behaviour of corroded 2024 T351 aircraft aluminum alloy, *Theor. Appl. Fract. Mech.*, **43**, 121-132.

[8] L. Korb and D. Olson (eds.) (1992). *ASM Handbook: Corrosion*, 9th ed., ASM International, Metals Park, OH, USA.

Posters

PULL-OUT OF TITANIUM BARS FROM RESTORED MARBLE ELEMENTS: A CONTRIBUTION TOWARDS ELIMINATION OF PARASITIC PHENOMENA

I. Dakanali
Laboratory for Testing and Materials, Department of Mechanics,
National Technical University of Athens, Theocaris Bld., Zografou Campus, 157 73, Athens, Greece

1. Introduction

According to the technique, in-situ developed by the scientific personnel working for the restoration of the Acropolis monuments, rejoining fragmented marble structural members is achieved by inserting threaded titanium bars into holes predrilled in the body of the members. The holes are then filled with a liquid cementitious material. The purpose of the present study is to investigate the extraction of the bars from the marble volume, known as pull-out. Understanding the mechanisms activated before and during this phenomenon is of paramount importance in order to properly describe the response of restored marble members [1, 2]. Several specimens' configurations have been already tested in order to simulate the exact mechanical behavior of the marble - cement paste - titanium bar interfaces. During the experiments several innovative techniques were used to monitor the response of the specimens (including the Acoustic Emissions (AEs) and the Pressure Stimulated Currents (PSCs) ones) in parallel with traditional sensing techniques [3, 4] for comparison/calibration reasons.

2. Experience from on-going research projects: The crucial role of the design of the specimens

The specimens were prepared by experienced technicians of the Acropolis work-site. Marble blocks with a through hole in the center of their cross section are filled with cement paste and a threaded titanium bar is driven into the hole. The reinforcement length is equal to half of the marble's block height. The main goal of the project is to eliminate any interaction of the examined area (marble - cement paste - bar interfaces) with the boundaries of the specimens. Initially, marble blocks of "Tau" configuration (Fig.1a) were used. The anchoring length is at the upper half of the block and its two flanges are restrained by two stiff metallic beams (Fig.1b). The titanium bar is gripped by the frame's jaw and is pulled-out from the marble's volume. Unfortunately, quite often, due to parasitic bending moments, some specimens failed due to marble fractured before activation of the pull-out (Figs.1c,d).

Another class of specimens, shaped according to the standards but of much larger dimensions, was tested (Fig.2a). The marble blocks were properly constrained by a rigid metallic plate with a hole at its center (Fig.2b). The advantage of the specific design is that the area of interest is relatively far from the marble volume compressed against the loading platen, reducing parasitic signals, which shadow the signals from the pull-out phenomenon itself. Interesting results were obtained for both the pull-out mechanisms and, also, for the capability of AE- and PSC-techniques to provide pre-failure indications [3, 4]. Nevertheless, the parasitic signals were not completely eliminated rendering further improvements necessary: The bar was in contact to the marble block at the lower edge of the block (Figs.2c,d). The configuration provided a clearer insight to the pull-out phenomenon itself. A

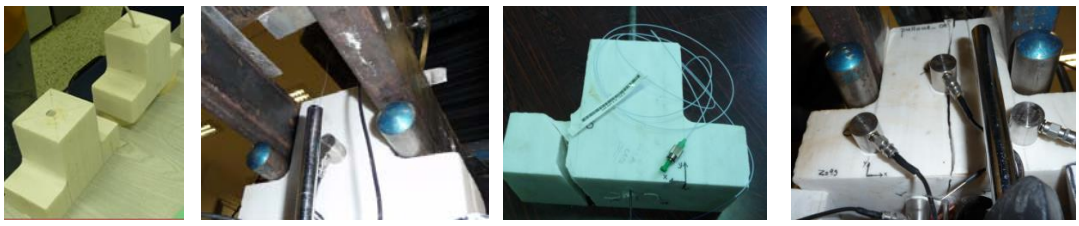

(a) (b) (c) (d)

Figure 1. "Tau" shaped specimens (a), their loading scheme (b) and failure modes (c, d).

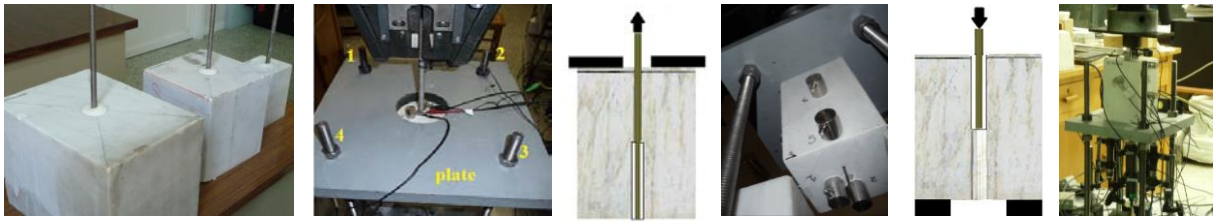

(a) (b) (c) (d) (e) (f)

Figure 2. Alternative configurations of specimens used to study the mechanisms leading to pull-out.

slightly modified configuration included specimens for which the anchoring length was again at the upper edge but the reinforcing bar was "pushed-in" rather than "pulled-out". (Figs.2e,f). Although relieved from parasitic effects due to marble-loading platen compression the outcomes of this configuration are more difficult to be properly interpreted due to the expansion of the bar.

3. Conclusions - The imperative need for alternative specimens' configurations

The experience gathered by the protocols described, definitely indicates the need for further improvements of the specimen's geometry, in the direction of completely eliminating parasitic effects and signals. In this context two alternative configurations are already tested in the frame of an on-going project, implemented in collaboration with the scientific personnel of the "Acropolis Restoration Service". The first one includes two marble blocks connected with a titanium bar, closely resembling the connection of restored fragments (Figs.3a,b). The lower block is restricted by a rigid metallic plate and the upper one is pulled upwards forcing the bar to slide through the hole (Figs.3c,d). The second configuration includes a single block with two holes. A titanium bar is inserted in each hole. The anchoring lengths in both edges are exactly the same. The upper and lower bars are gripped by the upper and lower jaws of the frame, respectively, without any contact of the marble block. (Fig. 3e). Preliminary results are encouraging indicating almost complete elimination of parasitic effects.

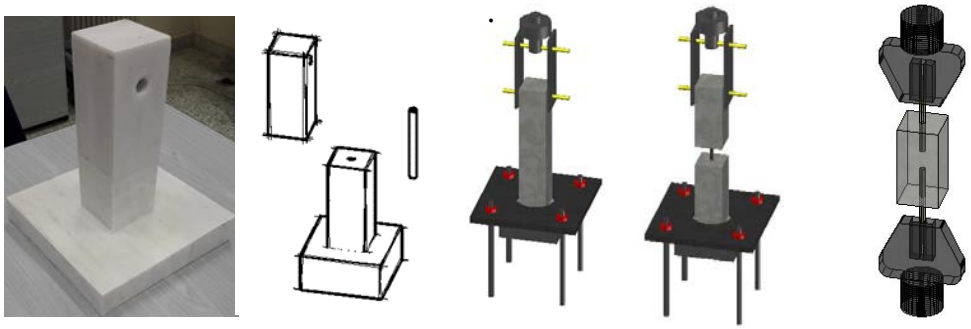

(a) (b) (c) (d) (e)

Figure 3. Two novel configurations in the direction of total elimination of parasitic signals.

References

[1] S. K. Kourkoulis, I. Dakanali, E. D. Pasiou, I. Stavrakas and D. Triantis (2017). AEs vs. PSCs during bending of restored marble epistyles: Preliminary results, *Fract. & Struct. Integrity*, **41**, 536-551.

[2] S. K. Kourkoulis and I. Dakanali (2017). Monitoring the mechanical response of asymmetrically fractured marble epistyles after restoring their structural integrity, *Proc. Struct. Integrity*, **3**, 316-325.

[3] S. K. Kourkoulis, A. Marinelli and I. Dakanali (2016). A combined experimental and numerical study of the pull-out mechanism of threaded titanium bars embedded in marble blocks, in *Proceedings 7th European Congress on Computational Methods in Applied Sciences & Engineering*, **3**, 5207-5218.

[4] I. Dakanali, I. Stavrakas, D. Triantis and S. K. Kourkoulis (2016). Pull-out of threaded reinforcing bars from marble blocks, *Proc. Struct. Integrity*, **2**, 2865-2872.

[5] S. K. Kourkoulis and I. Dakanali (2017). Pre-failure indicators detected by AEs: Alfas stone, cement-mortar, cement-paste specimens under 3-point bending, *Fract. & Struct. Integrity*, **40**, 74-84.

NON-DESTRUCTIVE MECHANICAL CHARACTERIZATION OF BRITTLE MATERIALS WITH PORTABLE DEVICES

G. Exadaktylos
Technical University Crete, Chania, Greece

1. Short introduction

One challenging problem in Rock Mechanics and Materials Science is the *in situ* characterization of mechanical parameters and damage of rocks and artificial quasi-brittle structural materials like concrete, high-performance concrete, shotcrete (in tunneling and geotechnical applications), ceramics, mortar etc. exposed in the action of various mechanical and environmental "loads" during their service time. This challenging task was pursued and accomplished at a certain degree some years ago [1] by developing an integrated portable system composed of drilling, indentation and acoustic tools. In this paper experimental results referring to the testing in the lab and on site of the integrated portable tool are presented. It is worth noting that these 3 tools could be used alone or in combinations of 2 or 3 also to test small specimens of brittle or quasi-brittle materials not only rocks or concretes but also other natural or artificial materials like bones, glasses, bricks etc.

2. Description and applications of the portable devices

The micro-rotary-drilling device shown in Fig.1a measures the normal force (or thrust force or weight-on-bit, WOB) necessary to drill the material under constant input penetration rate (5-80 mm/min) and constant rotation speed (ranges 150-1000 rpm). An example output graph of the WOB w.r.t. drilling depth on a rock showing the reproducibility of test results is shown in Fig.1b. This device is suitable for both laboratory and "in situ" tests. It records the force resistance profile along the penetration depth (up to 50 mm). Based on a model of rotary drilling resistance of materials linking the thrust force with uniaxial compressive strength and friction angle, the latter material parameters of brittle materials could be estimated with a back-analysis procedure. The portable indenter, shown in Fig.1c, employs spherical or flat indenters (of diameter 2-3 mm) and it is used for the measurement of Young's modulus of the material. Indentation forces could be up to 2000 N. It has a frictionless design in penetration force reading, a constant displacement rate and constant force rate. With this tool multiple loading/unloading cycles could be performed in a single test as is shown in Fig.1d. Lab tests could be also conducted on small size specimens ("matchbox" size). Moreover, it could be used to perform indentations at the end of drilled holes with the microdrilling tool. Young's modulus could be then found by using *Hertz's indentation theory* and a back-analysis procedure. Finally, the portable acoustic tool (Fig.1e) measures the emitted acoustic energy during drilling (Fig.1f), and the acoustic wave speed, as well as the dynamic Young's Modulus of materials. Thus DIAS (acronym from *Drilling-Indentation-Acoustic* tool) is a modular tool comprised from three independent portable light tools that may conduct in situ tests (e.g. Fig.1g) communicate between them through the same platform (Fig.1h) and with wireless connections.

3. Concluding remarks

The capabilities of the new portable modular system were demonstrated at five stone quarries and associated monuments constructed from these stones (Trondheim-Norwway, Tongeren-Belgium, Florence and Carrara-Italy, Parthenon, Athens and Aptera wall in Chania, Greece) comprising a flexible portable "light-weight laboratory". Standardization is a next indispensable step because potential end-users rely on "risk-free" standardized methods. Furthermore, the characterization of heterogeneous materials at larger depths behind exposed surfaces requires larger diameters and larger depths of drilling and indentation which are also challenging problems.

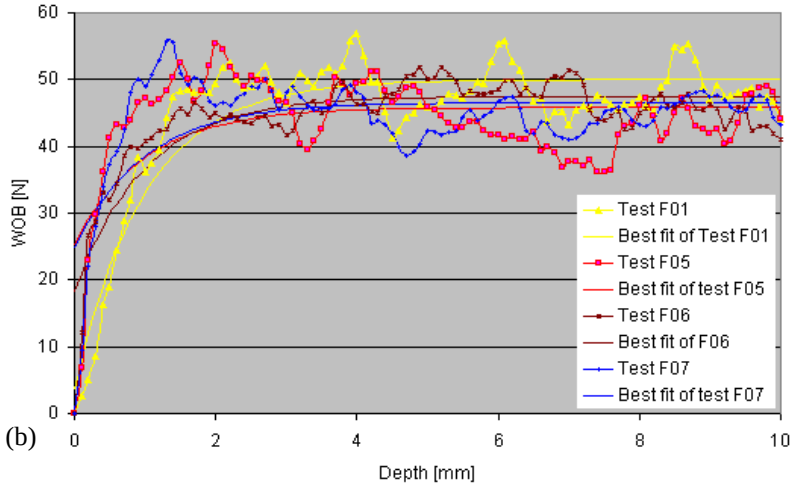

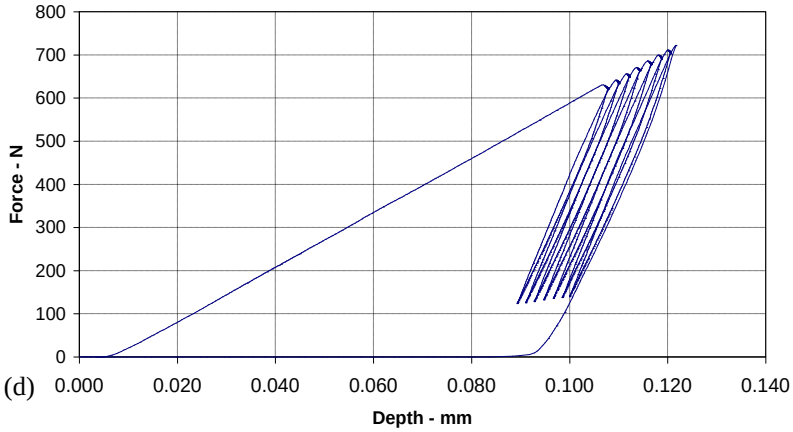

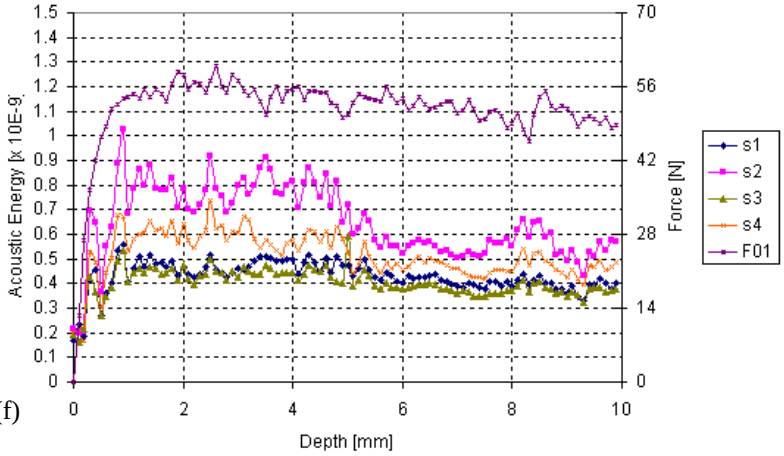

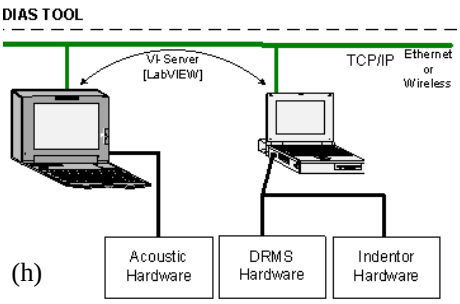

Figure 1. (a) Drilling tool in the suitcase, (b) repeatability of drilling force with drilling depth measurements, (c) indentor mounted on the wall of Duomo at Florence, (d) force-displacement diagram of an indentation test, (e) acoustic tool communicating input-output data in a wireless fashion to the laptop, (f) acoustic energy vs drilling depth from drilling tests at various locations in an underground stone quarry in Maastricht (Netherlands), (g) combined tests in the under-ground stone quarry, and (h) communication between the three modules for data transfer.

References

[1] http://minelab.mred.tuc.gr/dias/

COMPARATIVE STUDY OF PRINTING PATTERNS ON ADDITIVE MANUFACTURING

K. I. Giannakopoulos[1], V. D. Sagias[1], E. D. Pasiou[2] and C. Stergiou[1]
[1] Piraeus University of Applied Sciences, Egaleo-Athens, Greece
[2] National Technical University of Athens, Department of Mechanics, Athens, Greece

1. Introduction

Additive manufacturing (AM) matured within the last years from rapid prototyping towards rapid manufacturing. The evolution of materials and cellular structures, used in additive manufacturing, provide enhanced properties on mechanical parts for everyday use. Still, the research community has not fully resolved several issues as, for example, how to optimize the manufacturing process, in order to improve mechanical properties of the part for a specific use. In this work, an experimental comparative study for two different cellular solid structures is described, based on the Fused Deposition Modelling (FDM) additive manufacturing process, by using specimens made of PLA.

The main principle of AM technology is that a 3D model initially generated using Computer Aided Design software, can be manufactured directly utilizing digital data without the need for extensive process planning. Different manufacturing technologies require a detailed breakdown of the product geometry, to determine the order in which the various features can be fabricated, as well as the tools and processes needed or any additional setup. The basic feature that describes how Additive Manufacturing works is that parts are constructed by adding material in layers; each layer being a rudimentary cross-section of the part derived from the original CAD model. Obviously, each layer must have a finite thickness, and the resulting object will be an approximation of the original model. Smaller layer thickness results in greater resemblance to the original object and more smooth surfaces. Most commercially available AM machines use a layer-based approach.

All additive manufacturing techniques follow a common seven-step process:

- Creation of a digital CAD model or scanned object
- Conversion of the model to STL Format
- Transfer to AM machine and STL File Manipulation
- Machine Setup
- Build
- Removal of supports
- Post-processing

In the FDM technique, hot plastic material fibers exit from a head which moves along the XY plane. The head-nozzle deposits thin layers of plastic on a base, creating the first cross-section. The material comes in a filamentous form into a spool, which is fed to the back of the machine. The filament is pushed through heated edges into an extrusion nozzle as it moves and extruded. The nozzle melts the material and can be moved in a horizontal and vertical direction with an N.C. Controller.

Among other criteria, infill pattern's contribution to the manufactures part's mechanical properties is high, and therefore it is considered as the base for this comparative experimental study [1,2].

2. Experimental protocol

Honeycomb and the newly introduced cubic+octet geometric structures were selected for the needs of the present experimental protocol. Honeycomb was selected as a structural element based on its wide usage while the cubic+octet as a new and promising geometry, which has been previously investigated with the aid of the Finite Element Analysis (FEA) [3]. Both elements were produced adopting the FDM technology and Polylactic Acid (PLA) material and finally they were tested under uniaxial compression using an INSTRON servohdraulic frame of capacity 300 kN. The experi-

Figure 1. Typical specimens of the two classes of geometries during and after the experiments: Honeycomb (left) and Cubic+octet (right).

ments were implemented under displacement control mode at a rate equal to 0.2 mm/min, resembling a quasi-static loading scheme. Typical specimens, during and after the tests, are shown in Fig.1.

3. Results and discussion

Typical raw results are presented in Fig.2, in which the force applied is plotted versus the respective shortening of the specimens. The repeatability for specimens of the same class is remarkable. Ignoring inevitable bedding errors, the honeycomb specimens exhibit an almost perfectly linear region up to about 80 kN, which designates, also, the peak load undertaken. After this linear region, the load starts decreasing monotonously and the structure deforms until fracture. On the contrary, the respective curves for the cubic+octet specimens are characterized by strong non-linearity from relatively early loading steps. At a load level equal to about 30 kN the slope of the plots is almost zeroed and the structure deforms under almost constant external load. After a shortening equal to about 5 mm the force required for further shortening starts increasing indicating collapse of the internal structure. From a quantitative point of view, the honeycomb structure exhibits much higher stiffness compared to the cubic+octet structure, contrary to results based on numerical models.

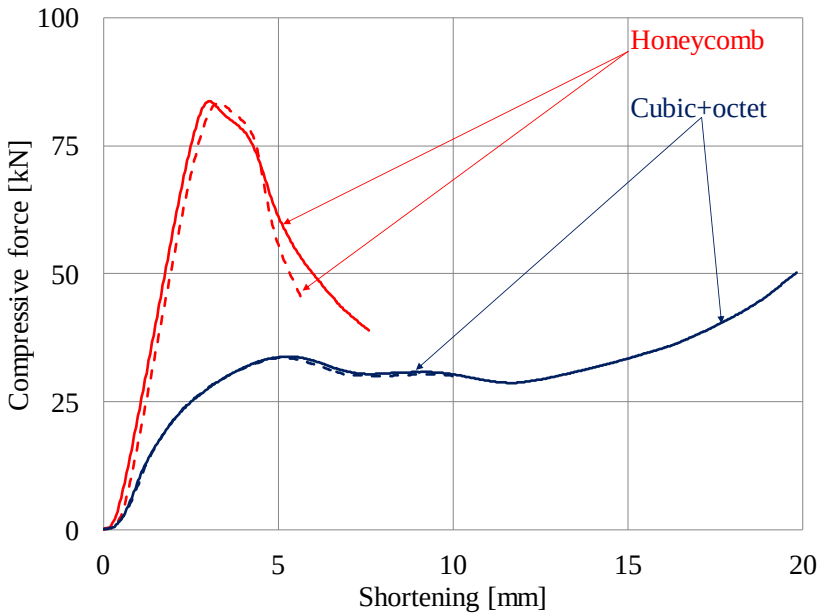

Figure 2. The compressive force applied versus the overall shortening of the specimens for typical specimens of the two classes of geometries.

References

[1] M. Fernandez-Vicente et al. (2016). Effect of infill parameters on tensile mechanical behavior in desktop 3D printing, *3D Printing and Additive Manufacturing*, **3**, 183-192.

[2] L. Baich and G. Manogharan (2015). Study of infill print parameters on mechanical strength and Production Cost-Time of 3D Printed ABS Parts, *Int. J. of Rapid Manufacturing*, **5**, 209-218.

[3] J. B. Berger, H. N. G. Wadley and R. M. McMeeking (2017). Mechanical metamaterials at the theoretical limit of isotropic elastic stiffness, *Int. J. of Science Nature*, **543**, 533-537.

PIEZO-RESISTIVE RESPONSE OF EMBEDDED PVA-CNT FIBERS IN GLASS FIBER REINFORCED POLYMER COMPOSITES UNDER QUASI-STATIC INCREMENTAL AND CYCLIC LOADINGS

A. Karayianni[1], P. Poulin[2], S. K. Kourkoulis[3] and N. D. Alexopoulos[1]
[1] University of the Aegean, School of Engineering, Dept. of Financial Engineering, Chios, Greece
[2] Université de Bordeaux, Centre de Recherche Paul Pascal - CNRS, Pessac, France
[3] National Technical University of Athens, Laboratory for Testing and Materials, Athens, Greece

1. Introduction

Composites are continuously increasing their share in engineering applications where strength and light-weight properties are of imperative importance. Despite their superior strength properties, their main disadvantage is their monitoring ability; due to the external applied loadings (fatigue or even impact) developed non-visible damage can be accumulated without being identified. Several monitoring/sensing techniques of the composites have been proposed in the literature [1]. Nevertheless, on-service load monitoring and damage detection sensors are required, to ensure structural integrity and thus maintain safety.

During the last decade, several embedded sensors were proposed [1-4]; however, each one exhibits individual limitations concerning high costs of fabrication, application and maintenance, resolution or clearness of the measured data, and decrease of the mechanical properties of the material. A very promising, in-service embedded damage monitoring sensor is the Polyvinyl Alcohol-Carbon Nanotubes (PVA-CNT) fiber. The utilization of these fibers as strain sensors for damage monitoring has been studied in the literature [5]. It has been shown that these conductive fibers can be embedded into non-conductive composite materials and successfully used to monitor internal damage by measuring their electrical resistance change under applied mechanical loading, without decreasing the material's mechanical performance [6]. The effect of pre-stretching the PVA-CNT fibers before embedding them into the composite material has also been investigated. Alexopoulos et al. [7] demonstrated that by increasing the fiber's pre-stretch ratio, the elastic modulus and the electrical resistance change values of the fiber increases, thus increasing the sensitivity of the fiber, and therefore a higher ERC value is correlated to the same applied mechanical strain.

2. Materials and experimental procedure

The effect of the electrical resistance change due to mechanical strain of the PVA-CNT fibers has been studied in various loading tests. Nevertheless, the response of the sensors under fatigue loading tests has not been thoroughly assessed although it is critical, since the aerospace structures are subjected to cyclic mechanical loadings. In the present work, PVA-CNT fibers, pre-stretched at different ratios, were embedded into glass fiber reinforced polymer (GFRP) specimens to in-situ measure their electrical resistance change during quasi-static incremental tensile and cyclic mechanical tests.

Glass-fiber reinforced polymer composite specimens with dimensions of length x width = 250 mm x 25 mm, embedded with a single axial, 50 mm in length PVA-CNT fiber, pre-stretched by 50%, 100% and 200%, as well as 0% for the untreated fiber, were tested in two different case studies: (a) incremental loading - unloading tests until final fracture, and (b) cyclic loadings up to 500 cycles.

3. Results and discussion

Fig.1a shows the experimental results of the progressive damage accumulation tests (incremental loading-unloading steps) of the composite under quasi-static loads. The results of residual axial strain after every unloading of four different coupons can be seen in Fig.1a; their difference lies on the embedded pre-stretched fiber. It is noticed that after each unloading branch, residual axial strain measurements were recorded and generally embedding of the different pre-stretched fiber does not essential-

ly change the mechanical behavior of the composite. Some slight variations in the residual strain values are within experimental error and more experimental results are discussed in the manuscript.

Fig.1b shows the electrical behavior of the embedded fiber for various pre-stretched levels. Residual resistance changes of the embedded fiber were recorded after each unloading branch, thus giving evidence that the embedded sensor mimics the response of residual axial strain values of the composite. Correlation of residual electrical resistance change values after each unloading with respective residual axial strain values of the composite is discussed in the article. The electro-mechanical behavior of the fiber under cyclic loading tests is also discussed in the article.

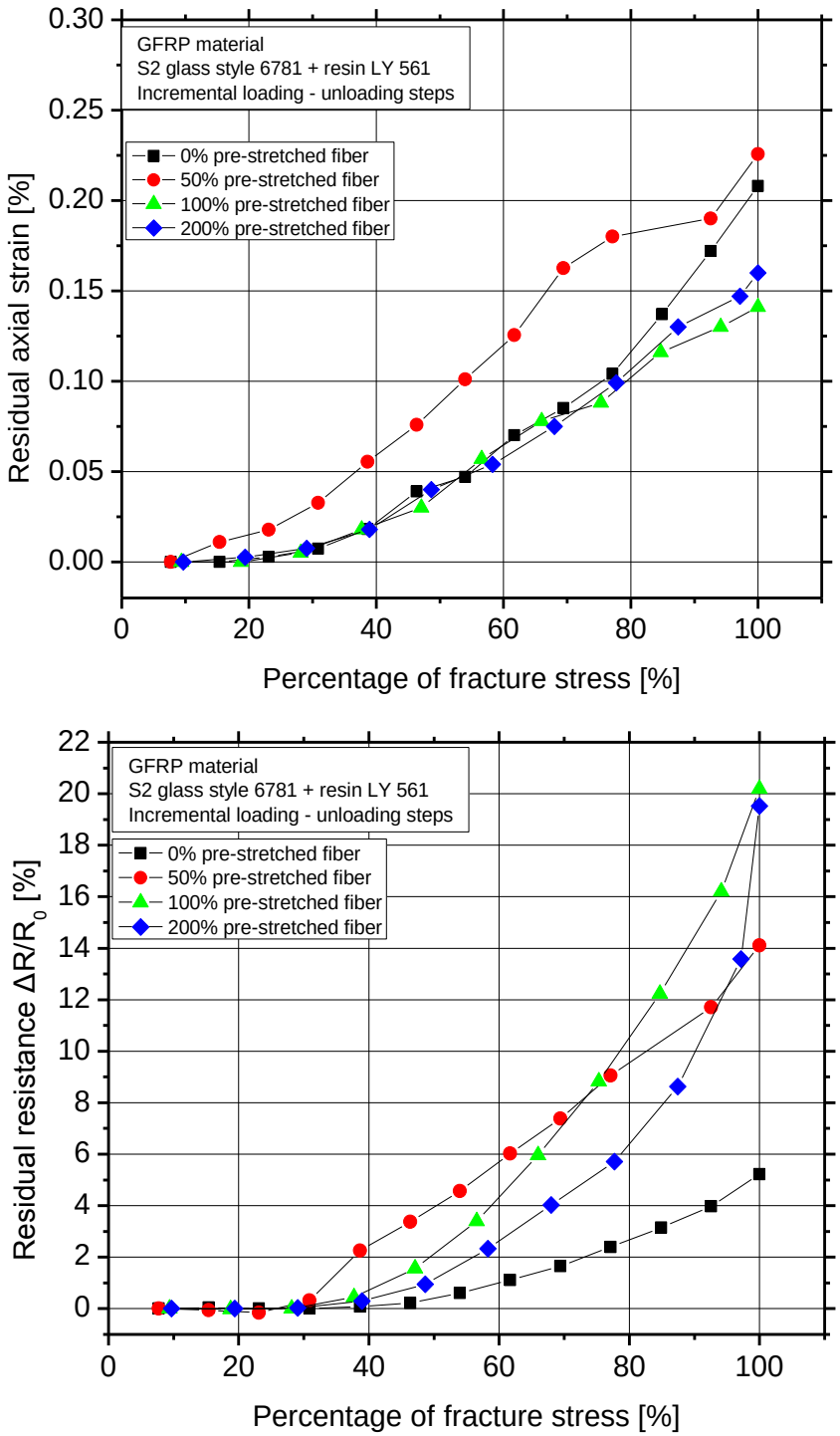

Figure 1. (a) Residual axial strains and (b) residual electrical resistance changes after each unloading step of the progressive damage tensile test for four different fiber pre-stretch ratios.

References

[1] S. Prashanth et al. (2017). Fiber reinforced composites, *J. Mat. Sci. & Eng.*, **6**, 345-357.

[2] A. Papantoniou, G. Rigas and N. D. Alexopoulos (2011). Assessment of the strain monitoring reliability of fiber Bragg grating sensor (FBGs) in advanced composite structures, *Comp. Struct.*, **93**, 2163-2172.

[3] S. Yaacoubi et al. (2017). Ultrasonic guided waves for reinforced plastics safety, *Reinforced Plastics*, **61**, 87-91.

[4] F. Dahmene et al. (2015). Acoustic emission of composites structures: Story, success, and challenges, *Physics Procedia*, **70**, 599-603.

[5] N. D. Alexopoulos et al. (2010). Damage detection of glass fiber reinforced composites using embedded PVA–carbon nanotube (CNT) fibers, *Comp. Sci. Technol.*, **70**, 1733-1741.

[6] N. D. Alexopoulos et al. (2010). Structural health monitoring of glass fiber reinforced composites using embedded carbon nanotube (CNT) fibers, *Comp. Sci. Technol.*, **70**, 260-271.

[7] N. D. Alexopoulos et al. (2013). Improved strain sensing performance of glass fiber polymer composites with embedded pre-stretched polyvinyl alcohol-carbon nanotube fibers, *Carbon*, **59**, 65-75.

MONITORING OF ACOUSTIC EMISSIONS ON THREE-POINT BENDING EXPERIMENTS IN CEMENT MORTAR BEAMS IN THE LIGHT OF NON-EXTENSIVE STATISTICAL PHYSICS

A. Kyriazopoulos[1], C. Anastasiadis[1], D. Triantis[1] and F. Vallianatos[2]
[1] Laboratory of Electronic Devices & Materials, Department of Electronic Engineering, Technological Educational Institution of Athens, Greece
[2] Technological Educational Institution of Crete, Chania, Greece

1. Introduction

This paper explores the possibility of utilizing statistical physics with Acoustic Emissions (AE) data, in order to obtain information about the proximity of cement mortar beams to the final stage of fracture when subjected to mechanical loading under three-point bending (3BP) conditions. In particular, a generalization of Boltzmann-Gibbs (BG) statistics, introduced by Tsallis, referred as Non-Extensive Statistical Physics (NESP) [1] and generalized by Tsekouras and Tsallis [2], is used to determine if the distribution of inter-event times of AEs obeys such statistics.

2. Description of the experimental protocol

Seven 3PB tests were performed with cement mortar beams, according to the following protocol: Load (L) initially increases at a constant rate (50 N/s approximately) to an L_i value, whereupon any further increase stops, and the load is kept constant at the above value for a sufficient time interval. L_i is selected different for each experiment, covering a range from 57% to 96% of the beam's strength (L_f). The L_f value estimation was performed after the completion of each experiment, progressively increasing the load up to failure. The specimens were prismatic beams of dimensions equal to 190 mm x 45 mm x 45 mm, made of cement mortar. The mixture of cement mortar contained Ordinary Portland Cement (OPC), sand of fine aggregates and water, at a ratio of 1: 3: 0.5, respectively. The size of the fine aggregates was small, varying from about 0.6 mm to about 1.8 mm, rendering the heterogeneity of the specimens relatively low. Detailed description of the specimens, the experimental setup, and the AE recording equipment can be found in a previous paper [3].

3. Results

Using the inter-event times ($\delta\tau$) of the consecutive acoustic hits, while the load remained constant at the L_i level, it was shown that the function of the normalized cumulative probability $P(>\delta\tau)$ follows for the middle ranged values of $\delta\tau$, the q-exponential relationship [4]:

$$P\left(>\delta\tau\right)=\exp_q\left(-\beta_q\cdot\delta\tau\right)=\left[1+\left(q-1\right)\cdot\beta_q\cdot\delta\tau\right]^{1/1-q} \quad (1)$$

where the q index expresses the degree of non-additivity and β_q is a generalized relaxation constant with inverse time dimension. The values obtained by the q index can provide valuable information on the organization and hierarchical structure of the time evolution of microcracking process. Quotient values of the index q approaching unity indicate that the microcrack array development process is less organized with an exponential statistical approach (q = 1). As far as the value of q deviates from unity and approaches 1.5, the growing microcracks seems to have a significant organization implying a long range interaction, consistent with irreversible damage.

For instance, Fig.1 depicts the function $P(>\delta\tau)$, its fitting based on Eq.1 and the resulting index value q, for one of the seven experiments implemented ($L_i = 0.85L_f$). It is obvious that for the larger

values of inter-event times, P(>δτ) deviates from the q-exponential law (Eq.1) and seems to obey a purely exponential law in accordance to Tsekouras and Tsallis [2] and Vallianatos et al. [5]. It was further concluded that the deviation becomes more intense as the L_i level approaches the fracture limit expressing an aging effect.

4. Conclusions

Studying the variation of q index in relation to L_i values, it was found that as one approaches higher load levels, there is a progressive increase of the q values (see Fig.2) till a critical load-level, where afterthen q decreases with load. This behavior implies that at low loading levels the growing micro-cracks have a weak organization mode, consistent with sweak short range interactions, while reaching levels of about 88% to 94% of the fracture limit, a value q≈1.4 results, indicating organization and hierarchy in crack's system. After a critical load, the q value decreases approaching fracture as a consequence of the uncontrolled growth scheme and of the progressive clustering of microcracks into macrocracks, resulting in the development and forming of the ultimate macrocrack leading to failure.

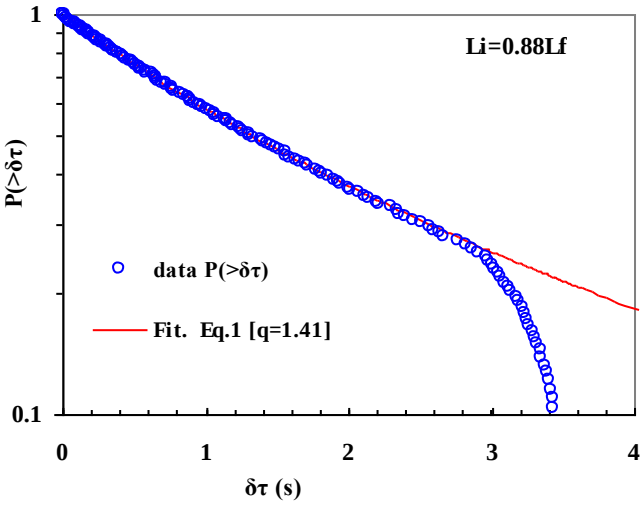

Figure 1. The function P (>δτ) vs. δτ and the fitting based on Eq.1.

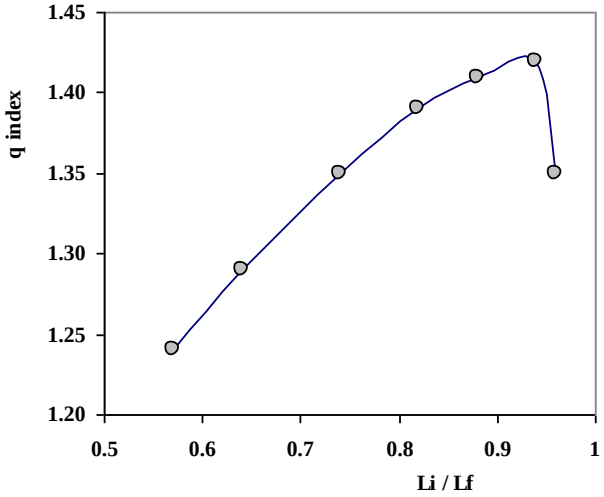

Figure 2. The q-index for various normalized load values.

References

[1] C. Tsallis (2009). *Introduction to nonextensive statistical mechanics: Approaching a complex world*, Springer, Berlin.

[2] G. A. Tsekouras and C. Tsallis (2005). Generalized entropy arising from a distribution of q indices, *Physical Review E*, **71(4)**, 046144.

[3] C. Stergiopoulos, I. Stavrakas, G. Hloupis, D. Triantis and F. Vallianatos (2013). Electrical and acoustic emissions in cement mortar beams subjected to mechanical loading up to fracture, *Engineering Failure Analysis*, **35**, 454-461.

[4] F. Vallianatos, P. Benson, P. Meredith and P. Sammonds (2012). Experimental evidence of a non-extensive statistical physics behavior of fracture in triaxially deformed Etna basalt using acoustic emissions, *EPL*, **97**, 58002.

[5] F. Vallianatos, G. Papadakis and G. Michas (2016). Generalized statistical mechanics approaches to earthquakes and tectonics, *Proc. R. Soc. A Math. Phys. Eng. Sci*., **472**, 20160497 (doi:10.1098/rspa. 2016.0497).

DETERMINING THE LIMITATIONS OF 2.3 GHz GPR SCANNING IN DETECTING OBJECTS OF SMALL GEOMETRICAL DIMENSIONS

I. Lampros, I. Christakis, D. Triantis and I. Stavrakas
Laboratory of Electronic Devices and Materials, Department of Electronics Engineering, Technological Educational Institute of Athens, 12210, Greece

1. Introduction

Among the various non-destructive geophysical methods applied for detecting subsurface imperfections and for determining the composition of the Earth's crust, the electromagnetic (utilized via Ground Penetrating Radar - GPR) is, perhaps, the one with the highest potential for tracking structures of limited dimensions [1, 2]. The present study attempts to test the possibility of detecting pre-installed targets of small geometrical dimensions, by employing a GPR instrument with very high frequency (2.3 GHz) wave emitting/receiving antennas. The novelty of this study is based on the fact that an apparatus primarily utilized on the field, can be employed in a more spatially confined environment to successfully track small size objects. Beneficial information can be derived from such an endeavor, pertaining to the capabilities of such an instrument, which could inspire its implementation in studies beyond the scope of geophysical surveys.

2. The materials and the experimental technique

The GPR system utilised in the present work comprised a MALA's ProEx control unit with an HF antenna module facilitating the wired tethering of an HF-2.3 GHz pulse-wave emitting/receiving antenna. The experimental setup consisted of stacked Expanded Polystyrene Sheets (EPS), on the upper surface of which the antenna was moving during each sweep using a guideline grid (Fig.1). The targets chosen, cylindrical shaped metallic (aluminium, iron) objects (of diameter, δ, equal to 2 cm, 1 cm and 0.1 cm and length, L, equal to 2 cm, 10 cm and 40 cm), were placed at vertical distances, d, equal to 13 cm to15 cm from the antenna, such that the scanning course bisected the length of each object perpendicularly. The setup of the GPR system parameters and the acquisition of scanning data were performed using the software tool MALA-GroundVision. The results of this study were derived from signal conditioning methods applied on the collected data and are presented in graphical form (B-scans) in the next section. The adopted elaboration methods provided by the software are primarily filtering and amplification algorithms.

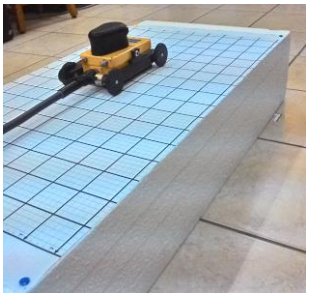

Figure 1. GPR system (MALA HF antenna) on experimental setup of EPS with guide grid.

3. Results and discussion

GPR antenna transmits a 2.3 GHz electromagnetic pulse in the medium under test and the reflection of this pulse is detected and properly analyzed. In order to obtain best results and successfully detect a target object, a sufficient contrast in the dielectric properties of the target and the surrounding environment should exist. The experimental procedure described in the above section was designed according to the above requirement. The contrast of dielectric properties between EPS and the surrounding air is negligible, so interference in the form of reverberations from surrounding objects (near-by chair, user's leg etc.) rendered raw data B-scans not suitable for the specific purpose [1, 3].

In order to discern the reflections produced by the pre-installed targets, the use of algorithms such as "*DC adjustment*" (dewow filter), *"Delete mean trace"* (suppression of patterns repeated on a horizontal progression) and contrast adjustment with GroundVision, became essential for data

processing. This resulted in GPR profiles (see Figs.2(b, c, d)) showcasing parabolic shapes (albeit slightly distorted) that adhere to the spatial coordinates of the metallic objects placed for detection in the experimental setup [1, 3].

It can be observed that the detection of the smallest object, iron wire of L=2 cm and δ=0.1 cm at d=15 cm, is not feasible (Fig.2b). Reflections for objects of the next size level (aluminum tubes of L=2 cm and δ=1 cm, and even more for the case of δ=2 cm) are different from surrounding interference with some attenuation (see Figs.2(b, c)). Changing the length of the objects to L=10 cm or L=40 cm for all cases of δ and d, boosts the reflection originating from the aforementioned targets substantially, thus rendering them clearly detectable (see Figs.2(b, c, d)).

Further studies and experimentation need to be conducted, in order to determine the possibility of small size targets detection under alternative conditions, e.g. different medium (cement, marble, sand), scan profiles parallel to targets lengthwise and objects of different material composition.

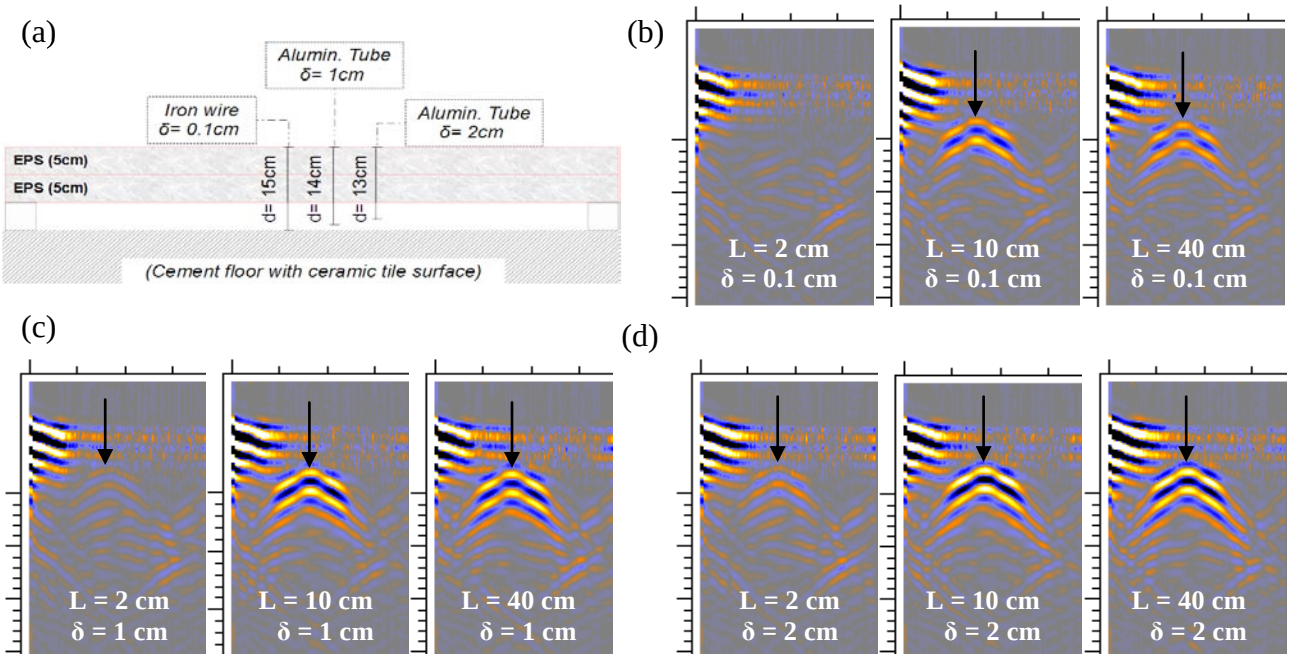

Figure 2. (a) Lengthwise profile of experimental set up for individual placement of target, B-scans for: (b) Iron wire of δ=0.1 cm at d=15 cm, (c) Aluminium tube of δ=1 cm at d=14 cm, (d) Aluminium tube of δ=2 cm at d=13 cm (each arrow pointing a hyperbola peak indicates the location of target).

References

[1] I. Stavrakas, E. D. Pasiou, G. Hloupis, D. Triantis and S. K. Kourkoulis (2015). Mechanical status fingerprint investigation of marble blocks using GPR field measurements, in *Proceedings of the 8th National Conference of Non-destructive Testing*, Athens, 8-9 May 2015, 58-60.

[2] L. Topczewski, F. M. Fernandes, P. J. S. Cruz and P. B. Lourenço (2007). Practical implications of GPR investigation using 3D data reconstruction and transmission tomography, *Journal of Building Appraisal*, **3**, 59-76.

[3] M. Szymczyk and P. Szymczyk (2014). Preprocessing of GPR data, *Image Processing & Communication*, **18(2-3)**, 83-90.

STRUCTURAL INTERVENTION OF THE ARCHITRAVES OF THE PARTHENON'S NORTH COLONNADE

M. Mentzini
Ministry of Culture and Sports, Athens, Greece

1. Introduction

The extended damages observed on the restored (by the engineer N. Balanos in the eve of the 20th century) architraves of Parthenon's North Colonnade were caused by a combination of catastrophic factors. Among the most serious ones, stand the problems aroused by the aforementioned intervention (thoughtless use of iron elements, which after oxidization expand making the beginning of a destructive process whereby the surrounding marble is fractured further) (Fig.1). The aim of the restoration of N. Balanos was to recover the results of the explosion during the siege of the Acropolis by Morosini's Venetians (1687 A.D.) and despite the problems caused, he succeeded to give to the Temple its most characteristic and recognizable view.

2. The on-going restoration project of the monuments of the Acropolis of Athens

From the early seventies a pioneer method has been developed for the structural restoration of the monuments of the Acropolis of Athens, according to which the joining of their fragments with or without supplements of new marble, is achieved by using titanium bars in combination with suitable cement mortar [1]. A new era, the contemporary phase of restoration of the Acropolis monuments, began at 2000 (by Acropolis Restoration Service (YSMA)), introducing new innovative methods, nowadays recognized and used all over the world [2]. Especially the restoration of Parthenon's North Colonnade was an enormous work plan to be carried out. As a result implementation of the restoration project as a whole is very difficult, unless it is divided into parts of similar members.

3. Restoring the architraves of the Parthenon Temple

In the present paper the tactic, complexity and difficulty of the steps' sequence for the structural intervention on the architraves are presented with the aid of some characteristic examples followed by an evaluation of the areas where a severe stress field has been developed [3, 4].

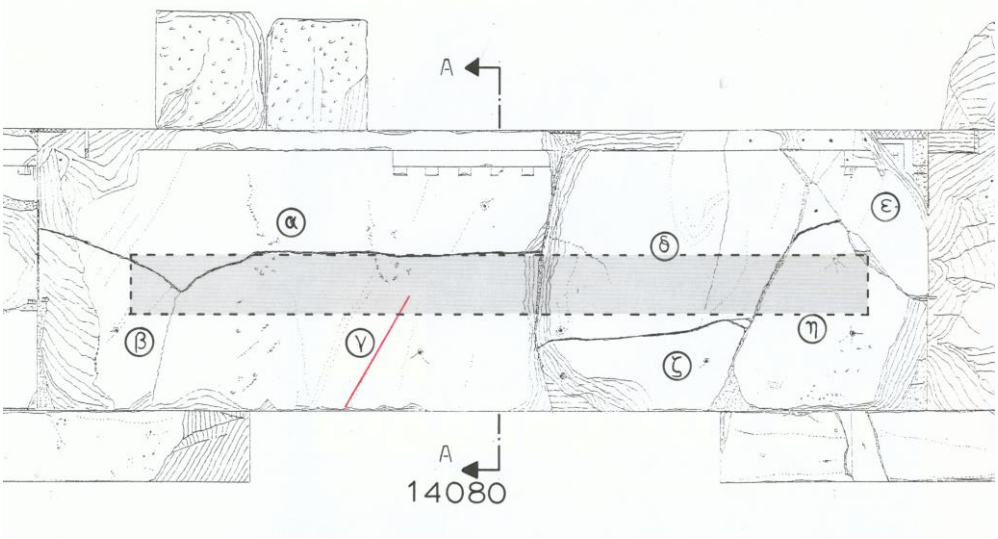

Figure 1. Front view (north side) of the 14080 architrave. The main fragments are discernible. Dotted lines correspond to the contour of the iron,"I"- shaped beam placed in a carved cavity on the back side of the architrave, during N. Balanos' restoration. Red line indicates the direction of the stratification of the material.

The determination of the reinforcement required for joining together the multi-fragmented architraves of Parthenon's North Colonnade, is a prerequisite in order to restore them in the direction of behaving as intact members and also to prevent further failures.

Due to the irregular shape of the ancient fragments it is difficult to join them (or to join ancient fragments with supplements of new marble). Moreover it is very difficult to accurately determine the direction along which reinforcing is to be placed. Quite often the theoretical approach of the intervention has to be redesigning in situ. Attention should be paid to avoid crossing of the reinforcement coming from different directions. For example, two types of reinforcing bars are considered: (i) Bending reinforcement, which corresponds to the titanium bars required for the architrave in order to recover the strength level dictated by the expected maximum external loading, and (ii) Shape restoration reinforcement which corresponds to the titanium bars required for the restoration of the shape integrity of the architrave. It is calculated from simple equilibrium concepts prohibiting the overturning of the overlying fragments (in case friction forces are not sufficient) and/or ensuring the successful suspension of the underlying pieces (Fig.2).

The architraves are here denoted by the unique code assigned to them during their dismantling from the Temple, while it is clarified the initial and the final (after the intervention) exact position (recall that N. Balanos changed the original position of many architraves on the monument).

Finally the detailed in-situ observation and the data gathered succeeded to identify and verify the conclusions of previous numerical and experimental analyses [4], in order to understand the behavior of the architraves as structural members and provide valuable information about the locations more susceptible to fail.

Figure 2. Joining together the ancient fragments ε and ζ (see Fig.1) and new supplements (on the left). The aforementioned complex is joined to the rest, already restored, eastern part (on the right).

References

[1] C. Zambas, M. Ioannidou and A. Papanikolaou (1986). The use of titanium reinforcements for the restoration of marble architectural members of Acropolis Monuments, in *Proc. IIC Congress on Case Studies in the Conservation of Stone and Wall Paintings*, Bologna: The International Institute for Conservation of Historic and Artistic Works, 138-143.

[2] M. Mentzini (2002). Joining together architraves and drums of Parthenon using titanium: A new approach, in *Proc. 5th Int. Symp. for the Restoration of Acropolis Monuments*, Athens: Committee for the Conservation of the Acropolis Monuments, 233-242.

[3] M. Mentzini (2013). 4.3.3.1. Columns and architraves: The process of structural intervention, Interventions on the Acropolis monuments 2000-2012, The completed programs, 4. The Parthenon's project, 4.3 Parthenon's North Colonnade restoration, 4.3.3. The project realization, *Proc. 6th Int. Symp. for Restoration of Acropolis Monuments*, Athens: Committee for the Conservation of the Acropolis Monuments, 1-24.

[4] M. Mentzini (2018). *Report of the project of the Parthenon's North Colonnade restoration. Ancient members' structural intervention: Columns and architraves. The architraves, vol. C,* Archives of the General Direction of Antiquities and Cultural Heritage, Ministry of Culture and Sports, unpublished.

THE POTENTIALITY OF DIGITAL IMAGE CORRELATION TO BIOMECHANICALLY ASSESS OSTEOSYNTHESES OF INTERTROCHANTERIC FRACTURES

M. Papasimakopoulos[1], E. D. Pasiou[1], G. Kyriakopoulos[2], L. Oikonomou[2], A. Panagopoulos[3] and G. Anastopoulos[2]

[1] National Technical University of Athens, Department of Mechanics, Athens, Greece
[2] 1st Department of Trauma and Orthopaedics General Hospital of Athens "G. Gennimatas", Greece
[3] Department of Shoulder & Elbow Surgery, Patras University Hospital,26504 Rio-Patras, Greece

1. Introduction

Fractures of the proximal femur, place a heavy burden on health systems worldwide. For example, it is estimated that in the UK about 100.000 patients annually will require surgical treatment for a hip fracture by 2020 [1]. Currently, hip fractures lead to more than 300.000 hospitalizations in the US [2] and this number is expected to rise due to increased life spans and an aging baby boom generation. Intertrochanteric hip fractures account for 50% of all hip fractures within the US population [3]. The vast majority of these fractures require surgical repair to withstand early mobilization and weight bearing, which prevents complications due to prolonged bed rest and aids in fracture healing. The consequences for hip fractures in elderly individuals are significant in terms of lives lost and the associated negative impacts on hip fracture patients" functioning and quality of life. Usually the consequences of mechanical failure are dire in terms of morbidity and mortality.

2. The difficulties of the biomechanical assessment of surgical treatments: The DIC technique

The standard practice in surgical treatment of intertrochanteric hip fractures has been the sliding hip screw (Fig.1a), in use since the 1960"s, allowing for controlled impaction of the fracture. In unstable fractures, however, the results have not been as good, despite the use of trochanteric support plates, derotational screws and other auxiliary devices. Consequently, intramedullary devices (Fig.1b), as for example trochanteric nails, have been used for unstable fracture configurations.

The increased complexity of the proximal femoral geometry, poses significant difficulties in the biomechanical assessment of the techniques used for fixing the respective fractures. This is clearly enlightened by considering that data are to be obtained from the body of fixation elements while they are within the fractured bone. Finite element models appear as a unique tool that could offer some solutions to the problem. However, numerical models must be validated/calibrated on the basis of data, even from a small number of experiments. In this direction, an experimental protocol is here described aiming to quantify the relative potentialities of a novel technique, i.e., the 3-Dimensional Digital Image Correlation (3D-DIC).

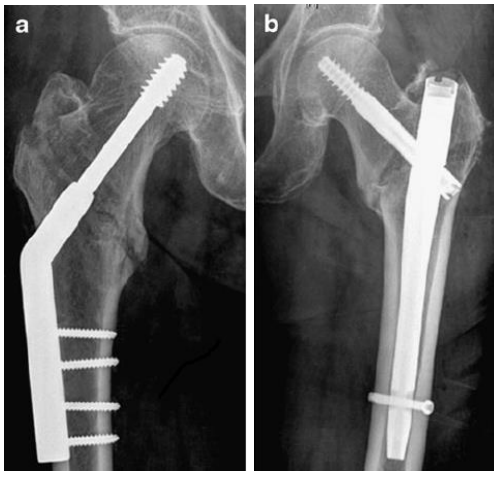

Figure 1. Sliding hip screw- (a) and intramedullary nail-fixation (b) of intertrochanteric fractures.

DIC is a full-field image analysis technique, based on a sequence of digital images. It permits determination of the displacement field of any point of the surface of a mechanically loaded object in three dimensions. The object is observed from different directions by two cameras and the position of each point is assigned to a specific pixel in the camera plane. During loading, the system takes digital images of the object comparing them against the image of the undeformed object. Nowadays, 3D-DIC is extensively applied in many scientific fields. Its main advantage is that it permits isolation of rigid body translations and rotations and, also, it offers „unlimited" number of „virtual gauges" chosen even „post-mortem".

3. Materials and methods

Artificial intertrochanteric fractures, on "adult" sawbone femurs, fixated by the gamma nail osteosynthesis (Stryker) technique were considered (Fig.2a). The fixated constructs were clamped and loaded, simulating single-foot stance. The load was applied with the aid of an MTS Insight 10 kN electromechanical loading frame. The displacement field was determined using a 3D-DIC system (Limess), controlled by Istra4D software (Fig.2b). Single electrical strain gauges, properly attached at strategic loci of the constructs (both at the external surface of the sawbones and also on the body of the nails) provided data for strains, mainly for calibration reasons. In addition, Acoustic Emission sensors were used to detect signals related to mechanical damage processes within the body of the construct. The tests were terminated either upon fracture of the construct or upon exceeding a predefined load level equal to 2.5 kN. All experiments were implemented under displacement-control mode, at a rate ensuring quasi-static conditions.

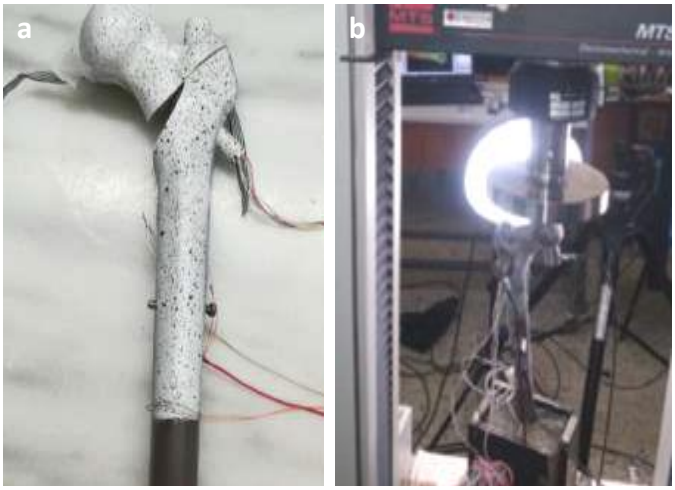

Figure 2. (a) A typical construct before being tested (the dots pattern required by the DIC technique is clearly visible) and (b) The experimental set-up.

4. Results and concluding remarks

Analysis of the experimental results concerning the full-field displacement components (Fig.3) revealed that the data provided by the DIC technique are in excellent agreement with those of the electrical strain gauges (at least at the points where the latter are attached). It was, also, indicated that quite a few parasitic factors influence the experiments. These factors are mainly related to rigid body rotations and translations due to the degrees of freedom of the construct (and especially the head of the femur), which should not be completely restricted, in order for the tests to simulate conditions of clinical relevance.

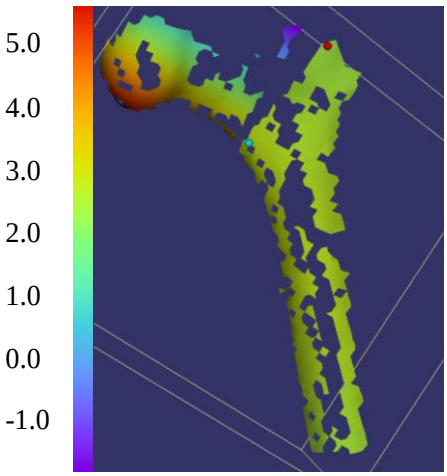

Figure 3. The displacement along an axis normal to the fracture plane at a load equal to 2.3 kN.

From the clinical point of view it was concluded that the results obtained exhibit significant scattering, not only between the two classes of constructs considered (stable and unstable fractures) but, also, for constructs of the same class, indicating increased variability. It was also, revealed that the role of the screw stabilizing the nail is of critical importance (not only concerning its placement details but also its actual contact conditions with the body of the nail) since it restricts some degrees of freedom. Finally, critical conclusions were drawn concerning improvements of the clamping-loading conditions that could minimize parasitic phenomena without struggling from clinical reality.

References

[1] S. M. White and R. Griffiths (2011). Projected incidence of proximal femoral fracture in England: A report from the NHS Hip Fracture Anaesthesia Network (HIPFAN), *Injury*, **42(11)**, 1230-1233.
[2] R. Cornwall, M. S. Gilbert et al. (2004). Functional outcomes and mortality vary among different types of hip fractures: a function of patient characteristics, *Clin Orthop Relat R*, **425**, 64-71.
[3] J. D. Michelson, A. Myers, R. Jinnah et al. (1995). Epidemiology of hip fractures among the elderly. Risk factors for fracture type, *Clin Orthop Relat R*, **311**, 129-135.

EXPERIMENTAL STUDY OF THE BIOMECHANICAL BEHAVIOR OF THE KEY BRANCHES OF HUMAN BEARING AORTAS

S. K. Pomakidou[1] and D. P. Sokolis[2]
[1] National Technical University of Athens, Laboratory for Testing and Materials, Department of Mechanics, School of Applied Mathematical and Physical Sciences, Athens, Greece
[2] Biomedical Research Foundation of the Academy of Athens, Athens, Greece

1. Introduction

The biomechanical properties of peripheral elastic arteries are studied in the present paper, which is the outcome of an experimental project in progress, implemented by the Biomechanics Unit of the Department of Mechanics of the National Technical University of Athens and the Biomedical Research Foundation of the Academy of Athens. Regional elastic arteries have both similarities and differences with the main body of the abdominal aorta. The properties of each type of artery differ depending on location, the purpose served by each artery type, its structure and its composition.

2. State of the art

Concerning the mechanical response of bearing aortas, relatively few studies have been performed on rats and other laboratory animals [1-4] worldwide, and even fewer in human tissues [5, 6]. Therefore, it appears quite challenging to carry out experimental protocols that could provide data about the stress and strain fields developed in the specific tissues, in the direction of deriving the respective mechanical properties. The assumptions, usually adopted, are related to the cylindrical geometry of the tested samples (described in terms of cylindrical coordinates in the regional, axial and radial direction), the material symmetry, the heterogeneity and the incompressibility [7, 8]. The mechanical properties under biaxial loading schemes have been recently studied in laboratory animals [9].

3. Materials and methods

The goal of the present study is to determine stress and strain states using data from inflation-extension tests in order to detect certain properties of the elastic arteries. Hence, the determination of the physiological state may help to find fault causes and ways of dealing with pathogens.

Samples were taken from 18 persons, and 8 different types of artery were cut off from the abdominal aorta (left renal, right renal, left external iliac, right outer external iliac, left internal iliac, right internal iliac, inferior mesenteric artery and superior mesenteric artery). Then the samples were subjected to inflation and extension tests and data for force, pressure and external diameter were taken. Typical raw data concerning the dependence of the aortas' external diameter on the lumen pressure are shown in Fig.1). Processing properly the as above raw data and using equations of continuum mechanics, provides stress and strain data for all three directions mentioned previously.

4. Results and discussion

Typical results concerning the dependence of the difference between the residual strains at the outer and the inner layers are plotted in Fig.2 versus the age of the persons. The results of the experimental protocol showed that as the tissue ages it becomes stiffer, thicker in the outer side and releases higher stresses, unless it develops layers of atherosclerotic plaque and so the release of the residual stresses is not allowed. Also the collagen fibers that are responsible for the elasticity of the tissue appeared to be axially oriented (as it was indicated by the σ-ε plots along the longitudinal and the circumferential directions) facilitating the normal operation of the elastic arteries.

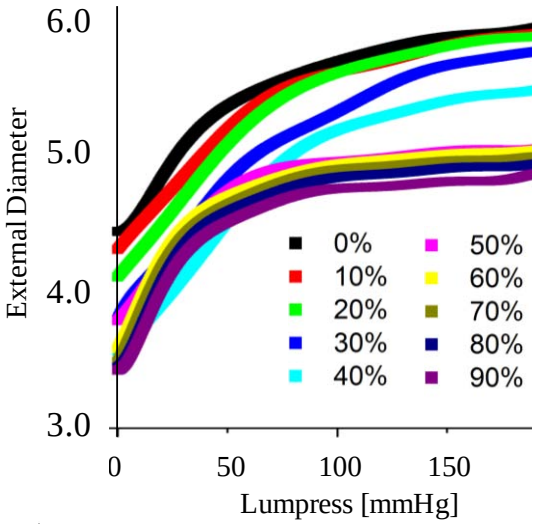

Figure 1. Characteristic plots of lumen pressure versus external diameter of the inferior mesenteric of a person male 24 years old.

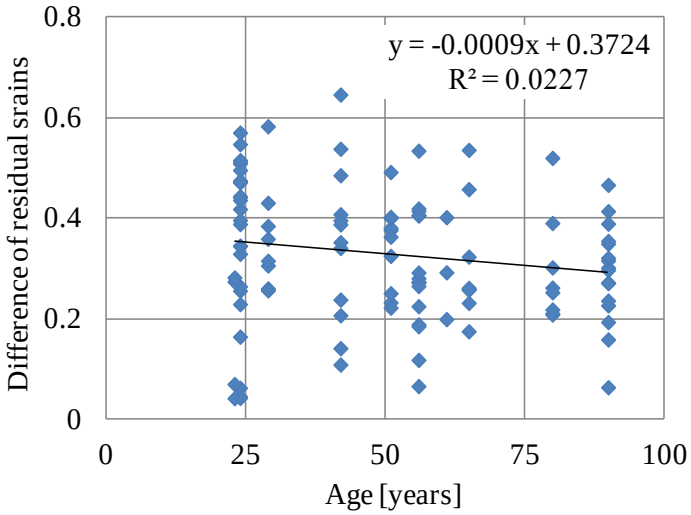

Figure 2. Correlation graph of the difference of the residual strains of the inner and outer layers of the aorta versus the age of the person.

For the sake of completeness of the experimental project described here, it would be desirable to submit samples of all types of arteries considered, also, to histological examination, so as to determine the correlation between elastin or collagen and the age of the persons, the regions of appearance of the elastin or collagen in relation to the age and the gender of the samples and, of course, the directions along which the above substances are distributed. Moreover, interesting conclusions, complementary to the ones of the present study, would result from the implementation of uniaxial stretching along the longitudinal direction of the tissues.

References

[1] P. H. Chew, F. C. Yin and S. L. Zeger (1986). Biaxial stress-strain properties of canine pericardium, *Journal of Molecular and Cellular Cardiology*, **18**, 567-578.
[2] C. J. Chuong and Y. C. Fung (1986). *On residual stress in arteries*, *ASME J. Biomech. Eng.*, **108**, 189-192.
[3] Y. C. Fung (1993). *Biomechanics: Mechanical Properties of Living Tissues*, Springer Science & Business Media, New York.
[4] Y. C. Fung (1973). Biorheology of soft tissues, *Biorheology*, **10**, 139-155.
[5] R. H. Cox (1974). Three-dimensional mechanics of arterial segments in vitro: methods, *J. Appl. Physiol.*, **36**, 381-384.
[6] Y. C. Fung and S. Q. Liu (1989). Change of residual strains in arteries due to hypertrophy caused by aortic constriction, *Circulation Research*, **65**, 1340–1349.
[7] Y. C. Fung (1994). *A first course in Continuum Mechanics*, 3rd ed. Englewood Cliffs, New Jersey: Prentice Hall.
[8] T. C. Gasser, R. W. Ogden and G. A. Holzapfel (2006). Hyperelastic modelling of arterial layers with distributed collagen fibre orientations, *Journal of Royal Society Interface*, **3**, 15-35.
[9] X. Guo,Y. Kono, R. Mattrey and G. S. Kassab (2002). Morphometry and strain distribution of the C57BL/6 mouse aorta, *American Journal of Physiology - Heart and Circulatory Physiology*, **283**, H1829 - H1837.

MECHANICAL PROPERTIES OF 3D PRINTED POLYMER SPECIMENS

V. D. Sagias, K. I. Giannakopoulos and C. Stergiou
School of Engineering, Department of Mechanical Engineering
Piraeus University of Applied Sciences,
Egaleo-Athens, Greece

1. Introduction

The procedure of manufacturing objects by sequentially depositing layers of material, based on 3D digital models, is called Additive Manufacturing (AM) or 3D-printing [1]. The first steps, in this revolutionary new technology, took place in 1980 in research centers and nowadays is rapidly gaining consumer acceptance. The main innovation in this technology, is the ability of constructing complex structures, which cannot be manufactured by using traditional processes.

Fused Disposition Modeling (FDM) technology along with the ABS (Acrylonitrile Butadiene Styrene) material are widely used in additive manufacturing. Through this method the material is heated and placed on a plate, layer by layer, until the part is manufactured. The material is heated slightly above the melting point and solidifies as soon as it comes out of the nozzle.

2. The experimental protocol

In this work a novel approach is presented on how parts can be manufactured (printed) to achieve improved mechanical properties, by using affordable 3D printers. The methodology is based on an experimental procedure through which the optimum combination of manufacturing parameters and their values can be obtained, in order to achieve the goal. The Taguchi methodology was selected as an optimization tool towards the goal of improving the part's mechanical properties [2].

The manufacturing parameters, used in the present work, for setting up the AM manufacturing process, are [3]:

- Layer resolution. The thickness value of each layer can be 70 um, 200 um or 300 um.
- Print pattern. The pattern used for the AM process (Cross, Diamonds or Honeycomb).
- Print strength. Material quantity used to infill the part (Hollow, Strong or Solid).
- Placement of specimen on table, during AM process (Horizontally, Perpendicular or 45°).

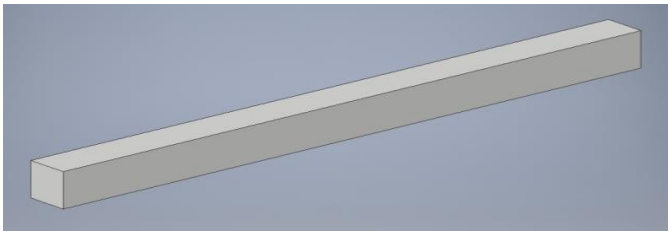

Figure 1. CAD model of a typical specimen.

The mechanical strength of the 3D printed specimens was measured using a Galdabini QUASAR 100 tensile machine. The strain rate was constant for all experiments (1 mm/min) and all specimens were prismatic with rectangular cross section.

3. Results and conclusions

According to the findings of the present study, the factors' significance according to their influence on the mechanical properties of the specimens is ordered as follows:

1. Layer resolution.

2. Print strength.
3. Print pattern.
4. Placement of specimen on table.

Instead of eighty-one (81) experiments that were assumed to be required, only nine (9) experiments were actually needed to be conducted, based on the Taguchi method approach. The optimum combination of the manufacturing parameters resulting to the specimen with the highest ultimate tensile strength (UTS) was the following:

- Layer resolution: 70 um
- Print strength: Solid
- Print pattern: Honeycomb
- Placement of specimen on table: 45°

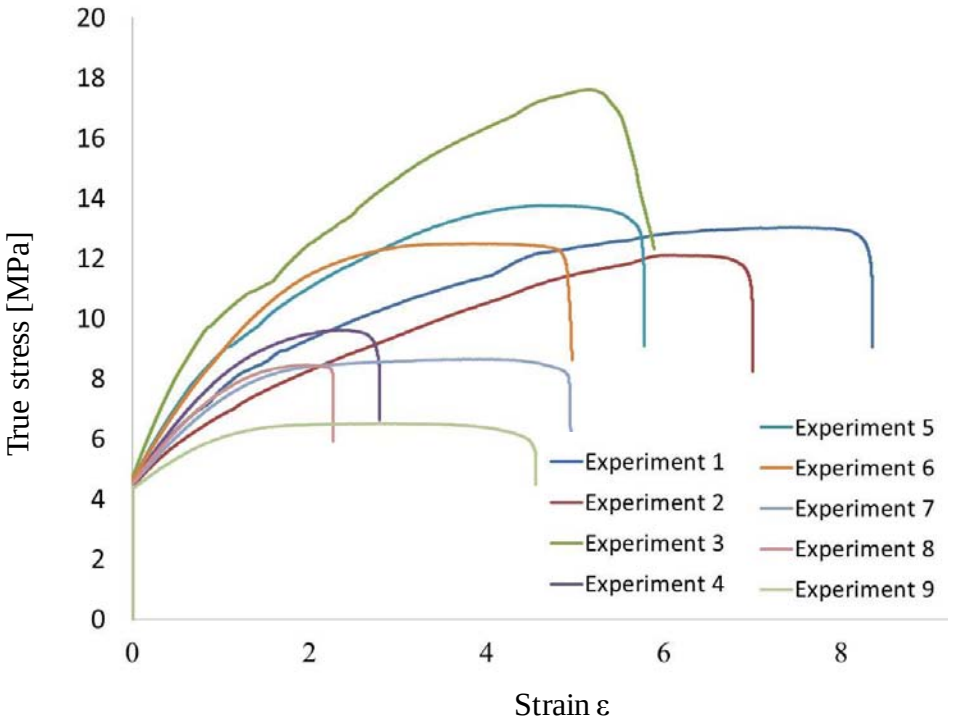

Figure 2. Stress-Strain diagrams.

Regarding the mechanical behaviour of the 3D printed specimens with the various parameters of printing, it was found that the maximum UTS was about 18 MPa in addition to the fact that all specimens were plastically deformed before their fracture.

The methodology presented here can be extended as a pre-processing approach aiming to optimize any part's mechanical properties according to its use.

References

[1] A. Bandybadhay and S. Bose (2016). *Additive Manufacturing*. 1st ed. London New York: CRC Press.
[2] R. K. Roy (1990). *A primer on the Taguchi method*, 1st ed., Society of Manufacturing Engineers.
[3] M. Vaezi and C. Chua (2010). Effects of layer thickness and binder saturation level parameters on 3D printing process, *The Int. J. of Adv. Manufacturing Technology*, **53**, 275-284.

THERMOMECHANICAL RESPONSE OF Fe_3O_4/PVDF NANOCOMPOSITES

A. Sanida[1], Th. G. Velmachos[1], S. G. Stavropoulos[1], G. C. Psarras[1],
C. Tsonos[2], A. Kanapitsas[2], N. Soin[3] and E. Siores[3]
[1] Smart Materials & Nanodielectrics Laboratory, Department of Materials Science,
School of Natural Sciences, University of Patras, Patras 26504, Greece
[2] Electronics Engineering Department,
Technological Education Institute (TEI) of Sterea Ellada, 35100 Lamia, Greece
[3] Institute for Materials Research and Innovation (IMRI), University of Bolton,
Deane Road, BL3 5AB Bolton, UK

1. Abstract

Polyvinyledene fluoride (PVDF) is a semi-crystalline thermoplastic polymer used in various technological applications due to its enhanced thermal stability and good chemical resistance [1]. Polymer matrix nanocomposites represent a novel and rapidly growing field of engineering materials due to their improved thermomechanical, electrical and magnetic performance [2]. In the present study the thermomechanical behaviour of Fe_3O_4/PVDF nanocomposites is investigated by varying the content of the reinforcing phase.

2. The experimental protocol

Nanocomposites were prepared by employing commercially available constituents. In particular, PVDF SOLEF 1008 was supplied by Solvay Solexis, while Fe_3O_4 nanoparticles were obtained from Sigma-Aldrich, with average size less than 50 nm. Nanocomposites were manufactured by employing a lab scale twin screw compounder (Thermo Scientific) with counter running screws. Details for the preparation procedure can be found in ref. [3]. Filler's content in the prepared samples was 0, 5, 10, and 15% w/w. Dynamic mechanical analysis (DMA) on all prepared specimens was conducted via a TA Q800 device provided by TA Instruments, in the temperature range from 30 ^oC to 100 ^oC at a heating rate equal to 5 ^oC/min. The DMA experiments were carried out under three-point bending configuration using suitable rectangular shaped specimens at f =1 Hz. Static tensile mechanical tests were made by employing an Instron 5582 device operating at a displacement rate of 5 mm/min. Specimens' thermal response was examined by means of Differential Scanning Calorimetry (DSC), using a TA Q200 device. Samples from all examined systems were put into aluminum crucibles, and an empty one was serving as reference. In the thermal cycles applied, temperature was varied from -40 ^oC to 200 ^oC and backwards with the heating/cooling rate being equal to 10 ^oC. Each sample was subjected to two successive thermal cycles.

3. Results and discussion

The dynamic mechanical response of PVDF and the Fe_3O_4/PVDF nanocomposites is depicted in Fig.1. The reinforcement of Fe_3O_4 is evident in the storage modulus curves in the whole temperature range. The vanishing values of storage modulus in all specimens with rising temperature are attributed to a transition/relaxation which is associated with molecular motion of amorphous parts restricted within the crystalline region or various defect types in crystals and in the crystalline/amorphous interface. In the loss modulus spectra the recorded curves indicate this transition.

Results from quasi-static mechanical tests are shown in Fig.2. Young's modulus increases with filler content, although at the highest content a leveling off is observed, indicating that the optimum static mechanical performance does not coincide with the maximum filler content. Tensile strength varies with filler content because nanoinclusions can prohibit yielding of the specimen and at the same they act as stress raisers.

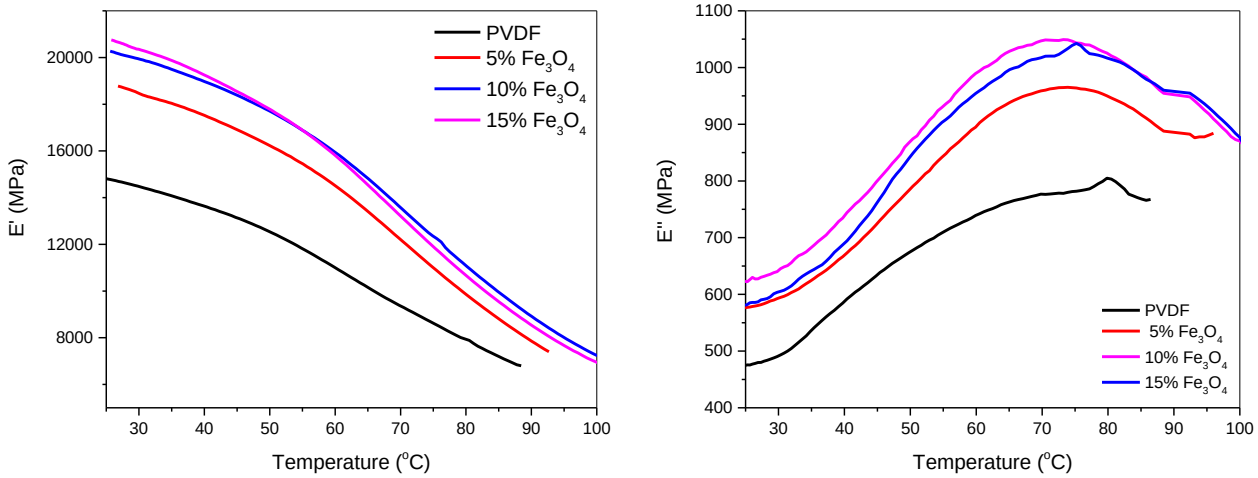

Figure 1. Storage modulus (left) and loss modulus (right) of all studied systems, as a function of temperature at f=1 Hz.

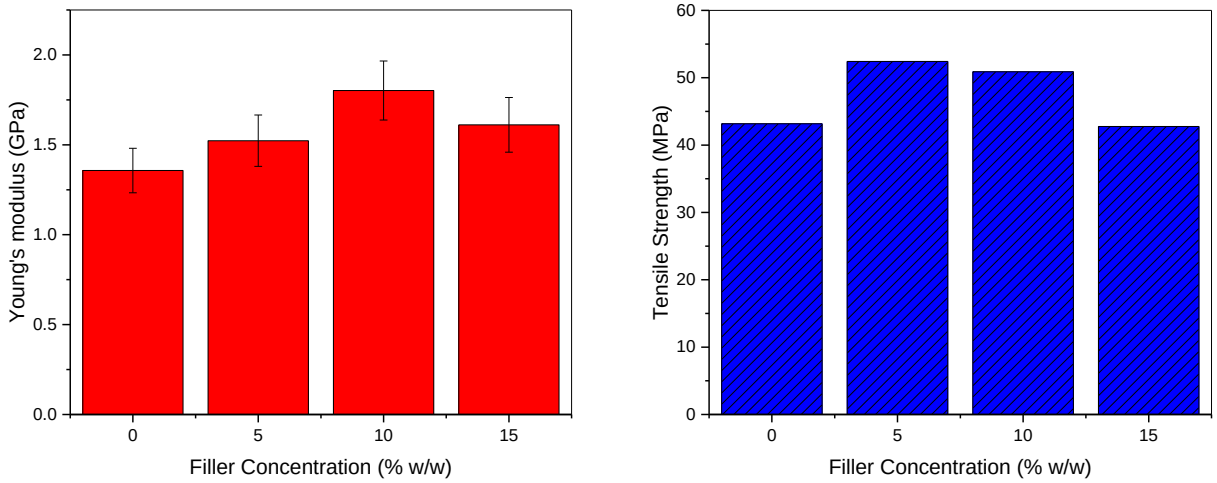

Figure 2. Young's modulus (left) and tensile strength (right) of all studied systems, as a function of filler content.

4. Conclusions

In the present study Fe_3O_4/PVDF nanocomposites were prepared and studied varying the reinforcing phase content. Storage modulus was found to increase systematically with filler content in the whole temperature range of the tests. The peak position of the broad peaks recorded in the loss modulus spectra indicate the transition associated with molecular motion of amorphous parts restricted within the crystalline region or various defect types in crystals and in the crystalline/ amorphous interface, which seems not to be significantly affected by the presence of nanofiller. Finally, Young's modulus increases, in general, with the concentration of Fe_3O_4 while the tensile strength initially increases and consequently decreases with increasing filler concentration.

References

[1] V. Sencadas, V. M. Moreira, S. Lanceros-Mendez, A. S. Pouzada and R. Gregorio (2006). α- to β transformation on PVDF films obtained by uniaxial stretch, *Mater. Sci. Forum*, **514–516**, 872-876.

[2] C. Tsonos, N. Soin, G. Tomara, B. Yang, G. C. Psarras, A. Kanapitsas and E. Siores (2016). Electromagnetic wave absorption properties of ternary poly(vinylidene fluoride)/magnetite nanocomposites with carbon nanotubes and graphene, *RSC Adv.*, **6**, 1919-1924.

CORROSION-INDUCED SURFACE MICRO-CRACKING AND CALCULATION OF THE STRESS INTENSITY FACTOR IN ULTRA-THIN SHEETS OF ALUMINUM ALLOY 2024

***P. Skarvelis*[1] and *Ch. Charalampidou*[2]**
[1] *School of Mining and Metallurgical Engineering, National Technical University of Athens, Athens, Greece*
[2] *Department of Financial and Management Engineering, School of Engineering, University of the Aegean, Chios, Greece*

1. Introduction

Corrosion damage may appear in aircraft structures in the form of pits, intergranular as well as exfoliation corrosion. The main damage mechanism on the corroded surface is the formation of pits and the subsequent initiation of surface micro-cracking [1]. Environmentally assisted cracking leads to catastrophic failure of the material. Cracks nucleate at a point along the perimeter of a pit where microstructural discontinuities as well as stress concentration, that is quantified by the stress intensity factor K, exist [2]. When the local mechanical condition is adequate, rapid crack growth takes place that results in the fracture of specimen/structure. This critical condition that defines the onset of the unstable crack growth is the critical stress intensity factor or threshold stress intensity factor K_{th} [3]. In structural applications it is critical to calculate the maximum mechanical load or the critical length of discontinuities in order to prevent material fracture ($K<K_{th}$) and generally to maintain the structural integrity [4]. The detrimental effects of corrosion damage on the structural integrity of AA2024 are qualitatively acknowledged, however, to date there are few articles in the open literature trying to quantify these properties. Jones et al. [5] acknowledged that the critical crack in its early stages ($\Delta K < 5$ MPa$\sqrt{m}$) interacts with adjacent corrosion pits and material microstructure and therefore low crack growth rates were observed. A semi-elliptical surface crack grows up to a critical size leading to rapid failure of the specimen. Pit depth was found to increase with increasing polarization time and a linear relationship between critical pit depth and stress intensity factor was observed [6].

In the present work, the effect of corrosion-induced micro-cracking on the structural integrity of ultra-thin (t <0.4 mm) AA2024-T3 is investigated. Pre-corroded specimens, exposed for different times to exfoliation corrosion solution were investigated in terms of corrosion-induced surface crack density in order to be correlated with the already available tensile mechanical tests [7].

2. Material and experimental procedure

Material used was a wrought aluminum alloy 2024-T3, received in sheet form of 0.4 mm nominal thickness. Rectangular flat specimens (10 x 20 mm^2) were machined from the sheets for metallographic investigation after the exposure to exfoliation corrosion solution according to ASTM G34 specification. The machined side surfaces were ground on SiC papers up to1200 grit and then they were polished with diamond pastes down to 0.25 μm. Specimens were machined in both, longitudinal (L) and transverse (T) sheet rolling direction. All depths of attack measurements per different corrosion case were inserted in the Origin® software for the statistical analysis of the results.

3. Results and discussion

The distribution of K values for the different cases of exposure time and sheet rolling direction can be seen in Fig.1. The calculated values were inserted in the Easyfit® software to calculate the best-fit of one-dimensional distribution according to Kolmogorov-Smirnov (KS) goodness-of-fit test [8]. For the case of both-sided corroded specimens, two different groups can be identified; for short cracks (t<1.33 h) the best fitting distribution is the Normal while for long cracks (t>1.33 h) the best fitting

distribution is the Lognormal. As expected, the stress intensity factor distribution shifts to higher values with increasing exposure time for all investigated cases, since depth of attack α increases with exposure time. Lower K values were calculated for the longitudinal L rolling direction when compared with the respective exposure times of the transverse T rolling direction. Higher possibility percentage for the K factor to exceed the threshold value of K>3.2 MPa√m, according to literature [9] was observed for the T than the L rolling direction. Probability to exceed the threshold value K_{th}=3.2 MPa√m exceeded 50% after only 4 h exposure time.

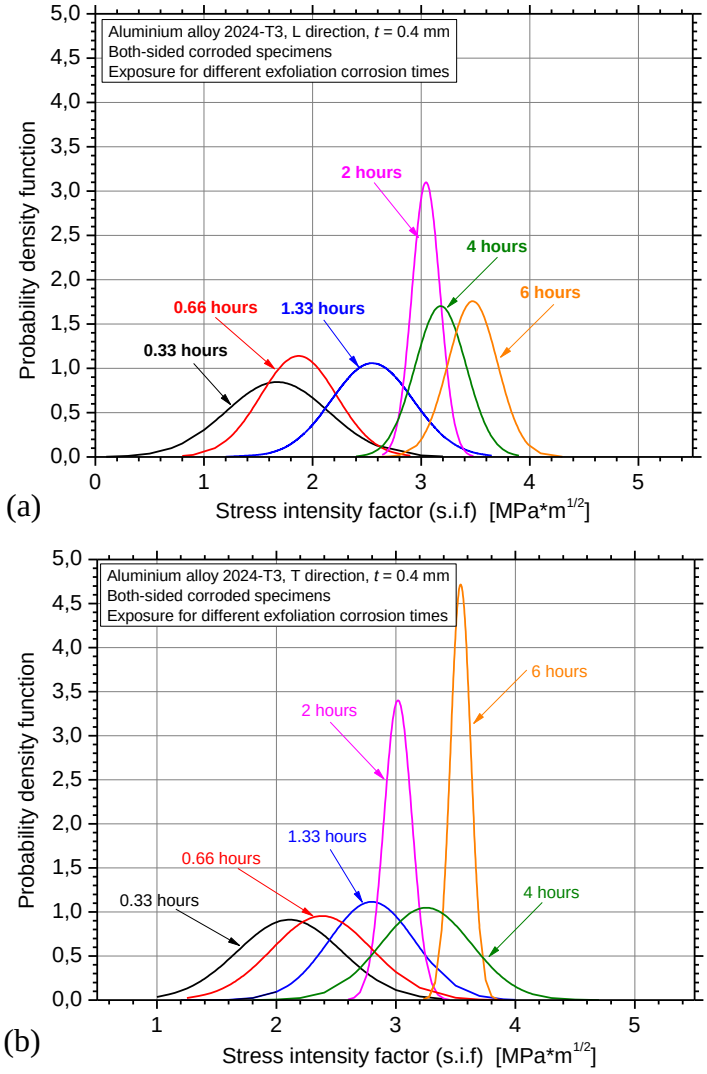

Figure 1. Distribution of stress intensity factor K for different times to exfoliation corrosion solution for both-sided corroded specimens for (a) L and (b) T rolling directions, respectively.

References

[1] Z. Szklarska-Smialowska (1999). Pitting corrosion of aluminum, *Corrosion Science*, **411**, 743-767.

[2] K. van der Walde and B. M. Hillberry (2007). Initiation and shape development of corrosion-nucleated fatigue cracking, *International Journal of Fatigue*, **29**, 1269-1281.

[3] G. S. Chen, K. C. Wan, M. Gao, R. P. Wei and T. H. Flournoy (1996). Transition from pitting to fatigue crack growth modeling of corrosion fatigue crack nucleation in a 2024-T3 aluminum alloy, *Materials Science and Engineering A*, **219**, 126-132.

[4] S. G. Pantelakis, A. N. Chamos and D. Setsika (2012). Tolerable corrosion damage on aircraft aluminum structures: local cladding patterns, *Theoretical and Applied Fracture Mechanics*, **58**, 55-64.

[5] K. Jones, S. R. Shinde, P. N. Clark and D. W. Hoeppner (2008). Effect of prior corrosion on short crack behavior in 2024 -T3 aluminum alloy, *Corrosion Science*, **50**, 2588-2595.

[6] M. Khobaib, T. Matikas and M. S. Donley (2003). Fatigue behavior of crack initiating from corrosion damage, *Journal of Advanced Materials*, **35**, 3-8.

[7] N. D. Alexopoulos, C. J. Dalakouras, P. Skarvelis and S. K. Kourkoulis (2012). Accelerated corrosion exposure in ultra-thin sheets of 2024 aircraft aluminium alloy for GLARE applications, *Corrosion Science*, **55**, 289-300.

[8] G. E. Noether (1978). A brief survey of nonparametric statistics, in *Studies in Statistics*, (R. V. Hogg, ed.), Mathematical Association America, 39-65.

[9] A. K. Vasudevan and S. Suresh (1982). Influence of corrosion deposits on near-threshold fatigue crack growth behavior in 2xxx and 7xxx series aluminum alloy, *Metallurgical Transactions A*, **12**, 2271-2280.

TSALLIS ENTROPY MODELING OF PRESSURE STIMULATED CURRENTS WHEN CEMENT-BASED MATERIALS ARE SUBJECTED TO ABRUPT REPETITIVE BENDING LOADINGS

I. Stavrakas and A. Kyriazopoulos
Laboratory of Electronic Devices and Materials, Department of Electronics Engineering, Technological Educational Institute of Athens, 12210, Greece.

1. Introduction

Weak electrical current emissions when a brittle material is subjected to mechanical loading are properly supported theoretically and verified experimentally. These electrical currents are known in literature as Pressure Stimulated Currents (PSCs) [1]. In this work, cement mortar specimens are subjected to 5 repetitive Three Point Bending (3PB) loading/unloading tests. It was verified that the PSC values during each next loading/unloading process were lower. The PSC relaxation during the time interval for which the mechanical load was maintained constant at its high level followed a q-exponential decrease, according to the Non Extensive Statistical Physics (NESP) Tsallis' entropy [2]. Similar experiments have been conducted on marble and amphibolite specimens, involving other loading protocols and clearly show compatible results [3].

2. Materials and the experimental protocol

The specimens used were prismatic cement mortar beams of square cross section 40 mm x 40 mm and length 100 mm. Series of preliminary 3PB tests were conducted and the bending strength was found to be 4.5 kN approximately. The detailed experimental apparatus is presented in a previous paper [4]. A pair of electrodes was installed at the middle of the lower edge of the specimen, enabling the collection of the PSC close to the potential damage initiation.

3. Results and discussion

The specimens were subjected to a specific loading scheme: An initial relatively low load of 1.8 kN was applied and it was kept constant for a long time interval in order for the PSC to relax. Afterwards, the load was increased from 1.8 kN to 4.2 kN approximately (i.e., in the immediate vicinity of 3PB strength) at a rate of 0.1 kN/s. Then the mechanical load was again kept practically constant for a relatively long time interval in order for the PSC to relax back to a background value. Finally, the mechanical load was reduced back to the level of 1.8 kN. The above pattern was repeated 5 times and the PSC behavior was concurrently recorded.

Fig.1 shows a typical curve of the applied mechanical load (grey line) during the above patterns. The corresponding behavior of the PSC emissions is also presented, using common time scale, for all five repetitions of the loading pattern. The time scale was synchronized according to the time (t_m) where the mechanical load reached the value of 4.2 kN and then it was kept constant. Observing the PSC emission curves it can be easily seen that during each next loading cycle the values of the recorded PSC become lower, a fact that is in full agreement with the expected PSC behaviour. The application of each new compressive stress cycle of the same characteristics causes the removal of the micro-crack edges to new excitation positions, resulting in a smaller number of new micro-cracks, to which the smaller peak values of PSC may be attributed. At the same time, some of the existing dislocations within the material sample are replaced by partially grown neighbouring dislocations corresponding to smaller energy values, so as to meet the requirements of thermodynamics.

The relaxation of the PSC emissions when the applied mechanical load is kept constant at the high level of 4.2 kN is studied under the frame of NESP. Specifically, Tsallis' entropy modeling [2], that was previously used to interpret experimental results with marble and amphibolite specimens [3], is also adopted herein. For all five PSC relaxation processes, the function:

$$\xi(t) = \frac{PSC(t)}{PSC(t_m)}, \text{ for } t > t_m \quad (1)$$

where $PSC(t_m)$ corresponds to the PSC maximum value that is reached during t_m, may be fitted by the following generalized q-exponential function:

$$\xi(t) = \left[1 + (q-1)\cdot\beta_q \cdot t\right]^{1/1-q} \quad (2)$$

The q-exponent and the β_q parameter were calculated after performing fitting for each of the 5 PSC relaxations according to Eq.2 and the corresponding values are plotted in Fig.2.

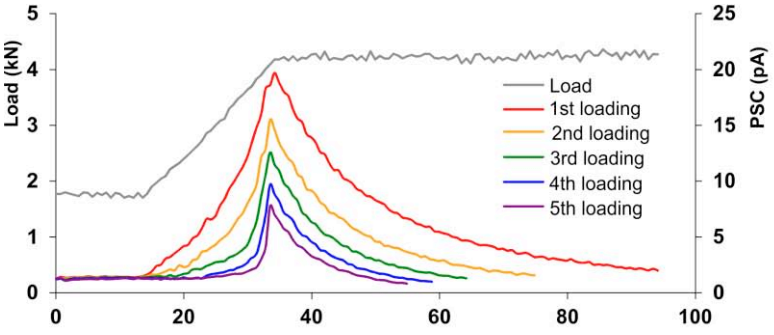

Figure 1. A typical temporal variation of the mechanical load and the corresponding behaviour of the PSCs depicted in common time scale.

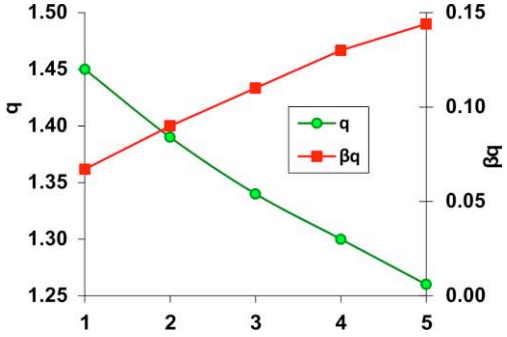

Figure 2. The values of the q-exponent and β_q parameter for the 5 relaxation processes.

4. Conclusions

In this work PSC relaxations are studied under the frame of Tsallis' entropy for cement mortar beams subjected to 3PB repetitive load/unload loops. The results are clearly compatible to already published ones indicating similar PSC relaxations when marble and amphibolite specimens were subjected to repetitive loading/unloading loops.

It is concluded that the NESP framework may offer a new perspective to the description of damage evolution. During the initial loading/unloading process the micro-cracks grow solely by propagation of their tips, because they soon start to interact with others creating a damage network. As the population of the damages self-organizes, they begin to coalesce, shifting the main process of growth from propagation to coalescence. This process is projected through the reduction of the q-exponent near the critical limit value of 1.25.

References

[1] I. Stavrakas, D. Triantis, Z. Agioutantis, S. Maurigiannakis, V. Saltas, F. Vallianatos and M. Clarke (2004). Pressure stimulated currents in rocks and their correlation with mechanical properties, *Natural Hazards and Earth System Sciences*, **4**, 563-567.

[2] C. Tsallis (2009). *Introduction to nonextensive statistical mechanics: Approaching a complex world*, Springer, Berlin.

[3] F. Vallianatos and D. Triantis (2012). Is pressure stimulated current relaxation in amphibolite a case of non-extensivity?, *EPL (Europhysics Letters)*, **99(1)**, 18006.

[4] C. Stergiopoulos, I. Stavrakas, G. Hloupis, D. Triantis and F. Vallianatos (2013). Electrical and acoustic emissions in cement mortar beams subjected to mechanical loading up to fracture, *Engineering Failure Analysis*, **35**, 454-461.

ACOUSTIC EMISSION MONITORING OF MARBLE SPECIMENS UNDER UNIAXIAL COMPRESSION: PRECURSOR PHENOMENA IN THE NEAR-FAILURE PHASE

D. Triantis
Laboratory of Electronic Devices & Materials, Department of Electronic Engineering, Technological Educational Institution of Athens, Athens, Greece

1. Introduction

In this work, attention is paid to the time variation of key Acoustic Emission (AE) parameters, such as the b-value, the RA (Rise Time/Amplitude) and the AF (Average Frequency), in case quasi-brittle materials as marble, are subjected to uniaxial compression. Emphasis is given on the AEs recorded near failure, when different types of AE signals with varying frequency ranges and amplitudes are observed.

2. The experimental protocol

Prismatic samples of Dionysos marble, of dimensions 40 mm x 40 mm x 100 mm were used. Detailed characteristics of the material can be found in ref. [1]. As a first step, the compression strength of the material was determined, during a preliminary experimental protocol. The respective value was found ranging between 62 MPa and 65 MPa. The main experimental protocol included axial compression loading of the specimens according to the following scheme of four distinct stages until failure: During the first stage (A), the stress increased at a constant rate of 0.44 MPa/s up to a value of 60.5 MPa. A second loading stage (B) of more than 100 s followed, during which the stress remained constant at 60.5 MPa. Given that at the end of stage B the AE activity was very limited, a slight increase of the stress equal to about 3 MPa was imposed (stage C), at the same rate (0.44 MPa/s). Finally, during the last stage (D), the stress was kept constant at 63.5 MPa. The samples failed after a time interval of about 60 s. An acoustic sensor recording the AE hits was attached at the center of the side surface of the samples. Mistras Group Inc equipment and software were used.

3. Results

Various AE statistical parameters were used including: The I_b-values (based on the amplitude distribution) [2] and the average frequency (AF) and the RA (Rise Time/Amplitude), which is necessary in order to identify the failure modes [3]. The I_b-values were calculated for N=100 successive AE hits. Accordingly, the average values of AF and RA of each hundred of successive AE hits, denoted as <AF> and <RA>, were calculated.

In Fig.1 the time evolution of the I_b-value is depicted for all four stages. During stage A, the I_b-value reaches, initially, relatively high values, exceeding 2. A slight drop is observed for t>95 s when the stress exceeds 44 MPa, which corresponds to about 70% of the materials' compressive strength. On approaching failure (>57 MPa), a strong decrease occurs and a minimum value ($I_b \approx 1$) is recorded for t=137 s, upon completion of stage A. It should be noted that the value of 1 is generally considered as the threshold beyond which serious damage has already occurred. In stage B, the I_b-values rise continuously and after 35 s the values are stabilized - with some fluctuations - between 3.0 and 3.3. A similar pattern is also observed in stages C and D, except that in stage D, for t>290 s, instead of a further increase of the I_b-value, a gradual reduction appears, indicative of the upcoming macroscopic failure.

The time evolution of the average frequency <AF> of the AE hits exhibits a similar behavior with that of the I_b-values. A sharp drop is observed (see Fig.2), when the stress in stage A exceeds 57 MPa, as well as while entering stage C, whereas, in stage D, 30 s prior to the final failure, the values start decreasing. During the last 3 s, the <AF> values decrease rapidly from 20 to 10 kHz.

Taking into consideration that low AF values indicate shear type of cracking, it can be concluded that while microcracks cluster to create macrocracks, frictional phenomena appear. Finally, the time evolution of the <RA> values (Fig.2) reveals strong peaks while approaching fracture, indicating, also, shear activity.

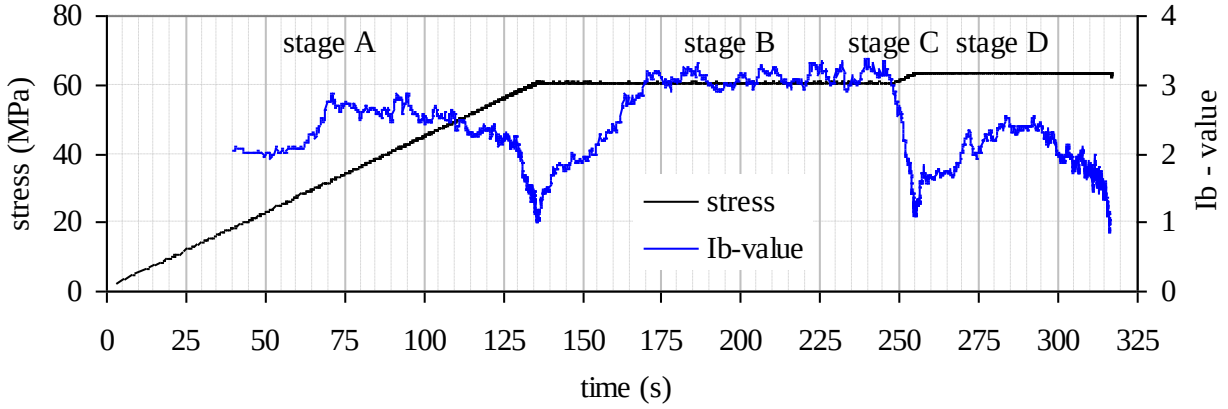

Figure 1. The time variation of axial stress in juxtaposition to that of the I_b-values.

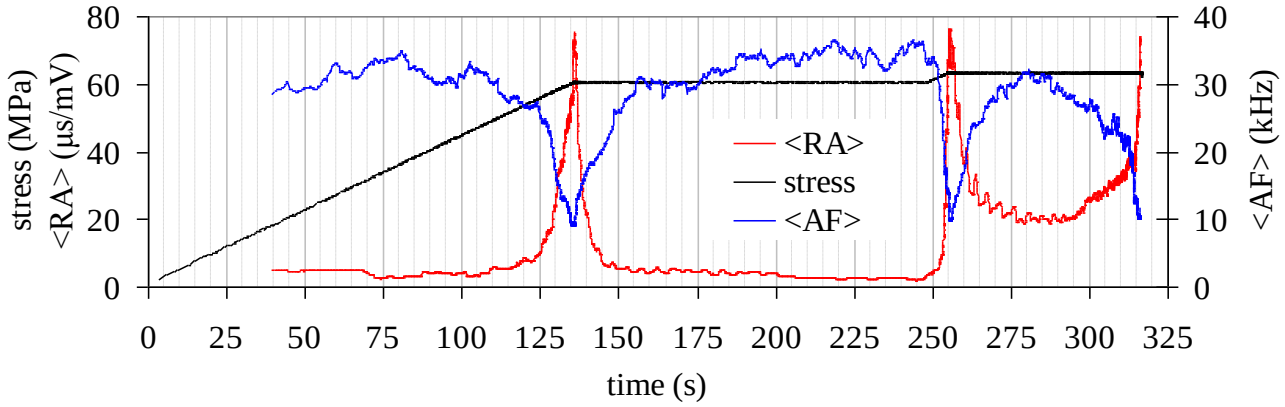

Figure 2. The time variation of axial stress in juxtaposition to these of <RA> and <AF>.

4. Conclusions

The observed sudden drop of the I_b-value, especially while approaching values close to 1, is a serious warning of upcoming failure. The shift of <AF> to lower values and the shift of <RA> to higher ones are connected to the failure mechanism, related to frictional phenomena. Following the initial development of the main network of cracks, and at time instants close to the sample failure, shear mode of AEs prevails, attributed to frictional phenomena among the macrocracks, which formulate the main fracture.

References

[1] E. D. Pasiou and D. Triantis (2017). Correlation between the electric and acoustic signals emitted during compression of brittle materials, *Fracture and Structural Integrity*, **40**, 41-51.
[2] T. Shiotani, M. Ohtsu and K. Ikeda (2001). Detection and evaluation of AE waves due to rock deformation, *Construction and Building Materials*, **15**, 235-246.
[3] D. G. Aggelis, D. V. Soulioti, N. Sapouridis, N. M. Barkoula, A. S. Paipetis and T. E. Matikas (2001). Acoustic emission characterization of the fracture process in fibre reinforced concrete, *Construction and Building Materials*, **25**, 4126-4131.

Rock Mechanics

MICROSTRUCTURAL AND MECHANICAL CHARACTERIZATION OF TWO MARBLES IN A FOLDED GEOLOGICAL SETTING

G. Exadaktylos, G. Alevizos, P. Liolios and S. Mavrigiannakis
Technical University Crete, Chania, Greece

1. Introductory comments

For the design of the room-and-pillar underground exploitation of a white dolomitic marble deposit in Northern Greece (Drama) the primary tasks are: (1) the characterization of microstructure, elasticity and strength parameters of rock samples in the lab and (2) the estimation of in situ stresses. The two metamorphic marbles belong to the Rhodope geologic zone and the Pageon Mt. tectonic unit with the white dolomitic marble to be older than the grey calcitic marble. Due to significant past folding of the formations of this zone by the action of significant horizontal thrust stresses during a past orogenetic process, the dolomitic marble overlies in some places the calcitic marble as is shown in the cross-section and the photo of Fig.1. The underground exploitation of the white dolomitic marble will be done inevitably in regions where the two marble formations are both present, therefore the design of rooms and pillars should be based on the characterization of both formations.

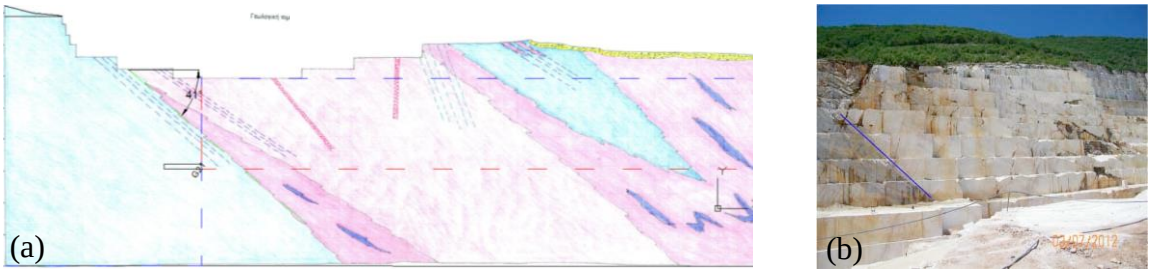

Figure 1. Folded calcitic and dolomitic marble formations tectonic setting; (a) vertical section along the dip of marble formations (calcitic: blue color, dolomitic: pink), and (b) photo of the same section of the two marble formations (contact of the marble formations is indicated with the blue line).

2. Experimental results

The mineralogical composition of the white marble found from XRD analysis is dolomitic i.e., 98% $CaMg(CO_3)_2$ (Dolomite) and 2% $CaCO_3$ (Calcite), while the composition of the grey marble is calcitic that is 70% calcite, 28% dolomite, 1% quartz and 1% muscovite. The microstructure of the two marbles is displayed in the optical microscopy photos of Fig.2. Uniaxial (unconfined) compression tests were conducted on cylindrical specimens of 80 mm diameter and height:diameter ratio equal to 2 extracted from vertical drill cored boreholes, for the characterization of the elasticity and uniaxial compression strength (UCS) of the two marble types. Brazilian tests were also conducted to infer the tensile strength (TS) of the marbles. Electrical strain gauges and two acoustic emissions (AE) sensors were employed during the compression tests. The AE sensors were used to infer the previous most recent vertical stress experienced by the marbles based on the "Kaiser effect", namely for a specimen containing microcracks, such as brittle rock, uniaxial loading is aseismic until a stress threshold is reached characteristic of the earlier stress magnitude it experienced [1]. From Table 1 it may be observed that the dolomitic marble exhibits higher compression strength compared to the calcitic marble that could be explained by the smaller size of crystals of this marble inferred from optical microscopy observations (Fig.2). However, the dolomitic marble exhibits more nonlinear behavior and smaller Young's modulus and Poisson's ratio compared to the calcitic marble. The evolution of AE hits with axial stress during the compression tests of two marble specimens are shown in Fig.3. In the same plots the evolution of the volumetric strain is also shown.

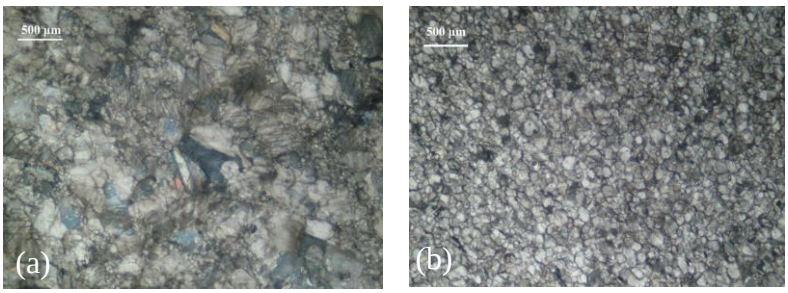

Figure 2. Optical microscopy photos of the two marbles with light transmission in crossed-Nicols scheme; (a) Coarse-grained calcitic marble exhibiting twinning, and (b) dolomitic marble.

Marble type	E [GPa]	Poisson's ratio	UCS [MPa]	TS [MPa]
Dolomitic	10-40	0.2	80	6
Calcitic	50	0.3	55	7

Table 1. Typical mechanical properties of the two marble types.

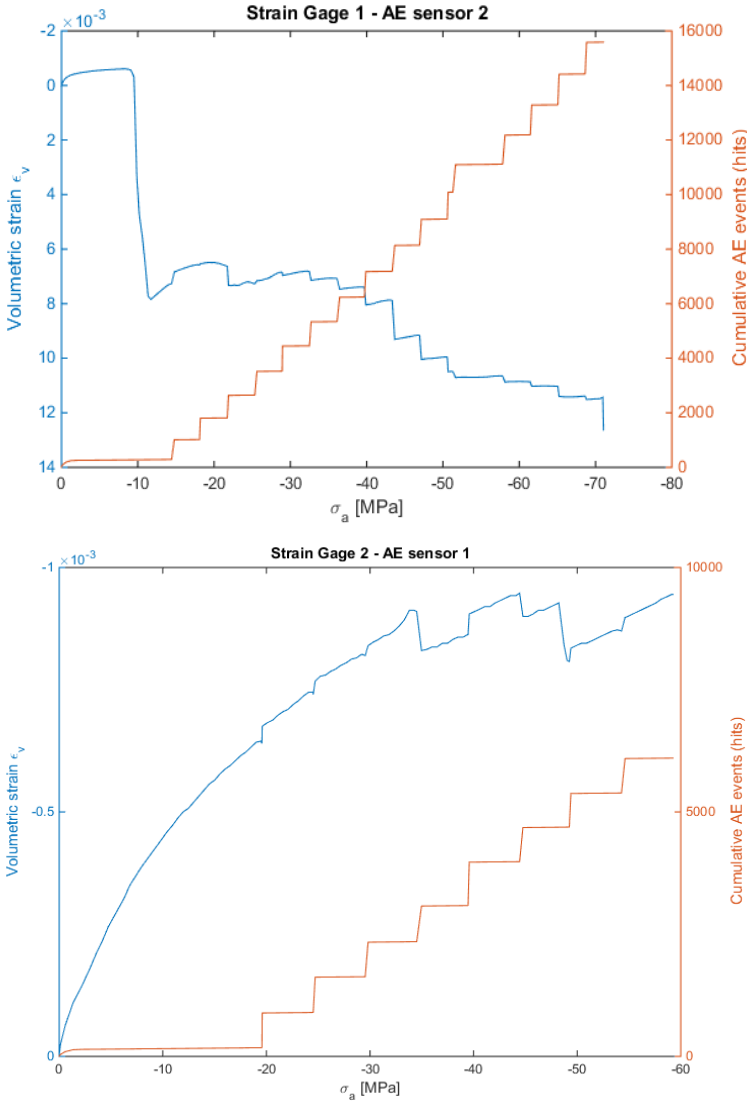

Figure 3. Evolution of AE hits and volumetric strain with the axial compression stress; (a) dolomitic marble, and (b) calcitic marble.

3. Conclusions

From Fig.3a it may be seen that, for the dolomitic marble, significant number of AE hits are only recorded after a level of the axial stress equal to about 15 MPa. The respective level for the "harder" calcitic marble is equal to about 20 MPa, as it can be seen from Fig.3b. Assuming that the Kaiser principle is valid, it seems that the most recent vertical stress experienced by these specimens are those inferred from tests, for the "softer" dolomitic and "harder" calcitic marble, respectively.

It should be noted here, that the vertical stress that could be inferred from the dead load gravity loading of these marbles with 150 m height of overburden, would be of the order of 4÷5 MPa.

This difference is quite significant, so in situ stress determination tests should be conducted to confirm or not the above mentioned observations.

References

[1] E. Villaescusa, M. Seto and G. Baird (2002). Stress measurements from oriented core, *Int. J. Rock Mech. in. Sci.*, **39**, 603-615.

INVESTIGATING THE FRACTURE BEHAVIOR OF PORTLAND LIMESTONE: AN EXPERIMENTAL STUDY

A. Marinelli and M. R. Stewart
School of Engineering and the Built Environment,
Edinburgh Napier University, Scotland

1. Introduction

Edinburgh gave itself the title "Athens of the North" to express its growing importance and sense of achievement. The fashion of classical architecture grew throughout the 1700s and ancient Greek styles came to influence the city's public buildings and monuments, forming what remains and develops as an excellent showcase of natural building stone's use as a construction material.

For the purpose of definition of failure criteria for natural building stones used in new as well as restoration projects in Edinburgh, the mechanical behavior and fracture characteristics of Portland Limestone and Corsehill sandstone were experimentally investigated. This paper focuses on the influence of specimen shape and size on the behavior of Portland Limestone, as observed when subjected to a suitable experimental programme.

The possibility of introducing alternative criteria, beyond the conventional ones based on the ultimate strength of materials, is examined on the basis of linear fracture mechanics concepts. In addition, existing data are used for verification and comparison as well as extension of conclusions.

2. Available data

A previous comparative study of the fracture properties of natural building stones used in Edinburgh [1] provided an insight into the nature and mechanical behavior of Portland Limestone, observing - among others - the effect of the presence of machined notches of varying lengths on the flexural strength of the stone specimens, when subjected to three- and four-point bending tests.

Consideration of relevant studies on marble [2, 3] and porous stone of Kefalonia [4] has paved the way for this particular investigation on Portland Limestone, seeking to investigate further the effect of specimen size and shape on flexural strength, deflection at mid-span, crack mouth opening displacement (CMOD) and fracture energy.

3. Methodology

Adopting principles used in studies of fracture energy for concrete samples [5, 6] and following methodologies described in RILEM TC50-FMC (1985) and BS EN 12372:2006, the "Grove Whitbed" Portland Limestone was experimentally studied within the Heavy Structures Lab facilities at Edinburgh Napier University.

The experimental protocol involved performing three-point bending tests on specimens with span/height ratios of 5/2, 4 and 6, bearing a machined notch at their mid-span for 1/3 of their height. For each span/height ratio, three different sizes of specimen (span length = 200 mm, 400 mm and 800 mm) were tested, with four repetitions each, in order to observe the influence of size as well as shape on flexural strength, deflection at mid-span, CMOD and fracture energy.

The bending load was applied uniformly along the thickness of the specimens with the aid of a steel roller and was controlled by the displacement of hydraulic jack, increasing at a rate equal to 0.1 mm/minute. CMOD was measured with a clip gauge supported by a pair of machined knife edges. Load-deflection (mid-span) and Load-CMOD curves were obtained for each experiment.

4. Experimental results

A selection of average test results from three-point bending tests is shown in Table 1.

Span/Height	Span [mm]	Flexural strength [MPa]	Fracture energy [Nm/m^2]
5/2	200	1.89	67.46
	400	1.76	95.30
4	200	2.37	36.45
	400	1.84	40.12
6	200	3.18	37.78
	400	1.82	49.27

Table 1. Average results from three-point bending tests.

For all span/height ratios, flexural strength on average decreases gradually as test specimen size increases. Fracture energy increases with test specimen size, following a bilinear law for span/depth ratios of 5/2 and 4, which suggests that there may be a critical size of test specimen at which the relationship between fracture energy and size is significantly altered.

5. Discussion

This research aims at contributing to the effort of assessing fracture behavior of full size structural members made of natural building stone. The scattering of results is significant but this is common for all aspects of the mechanical behavior of most brittle geomaterials. A wider range of specimen geometries/sizes is required to fully verify the trends observed, regarding: (a) the negative correlation between the flexural strength of Portland Limestone test specimens and their span lengths for all three shapes and (b) the positive correlation between fracture energy and specimen size.

References

[1] M. R. Stewart (2016). Comparative study of the fracture properties of natural building stones used in Edinburgh, *MEng Civil Engineering Honours Project*, School of Engineering and the Built Environment, Edinburgh Napier University.

[2] I. Vayas, A. Marinelli, S. K. Kourkoulis and S.-A. Papanicolopulos (2009). Investigating the fracture behavior of Dionysos marble: An experimental study, in *"Protection of Historical Buildings"*, Vol. II, Mazzolani FM (ed.), A. Balkema Book, Boca Raton, 1699-1704.

[3] S. K. Kourkoulis, G. E. Exadaktylos and I. Vardoulakis (2002). The influence of notch geometry and non-linearity on the SIF in case of 3P-B marble specimens, in *Proceedings of 14th European Conference on Fracture*, September 8-13, Krakow, Poland.

[4] S. K. Kourkoulis and E. Ganniari-Papageorgiou (2010). Experimental study of the size and shape effects of natural building stones, *Construction and Building Materials*, **24(5)**, 803-810.

[5] R. K. Navalurkar, C. T. Hsu, S. K. Kim and M. Wecharatana (1999). True fracture energy of concrete, *ACI Materials Journal*, **96(2)**, 213-225.

[6] J. Malvar and G. Warren (1988). Fracture energy for three-point bend tests in single-edge notched beams, in *NCEL Technical Report*, Naval Civil Engineering Laboratory, California.

MULTISTAGE TRIAXIAL TESTING OF VARIOUS ROCK TYPES: A CASE STUDY FROM EAST ATTICA PREFECTURE

D. Kotsanis, P. P. Nomikos, D. Rozos and A. I. Sofianos
School of Mining and Metallurgical Engineering
National Technical University of Athens, Greece

1. Introduction

The conventional triaxial test has been used for many years in order to gain an insight into the mechanical behaviour of rock subjected to a three - dimensional state of stress. In such type of test, a rock specimen is subjected to a compressive stress state in which the maximum principal stress is constantly increasing and the other two principal stresses are of equal magnitude, i.e., $\sigma_1 > \sigma_2 = \sigma_3 > 0$, where positive stresses indicate compression. Although such a stress field is not particularly common in the subsurface [1], it is commonly used in rock mechanics laboratories due to necessity which results from restriction of the experimental set up. From the results of this test a number of failure criteria have been developed and important mechanical parameters have been calculated [2].

According to the recommendations of the International Society for Rock Mechanics [3] there are three ways to conduct a conventional triaxial test such as:

(a) the single stage triaxial test (type I),
(b) the multiple failure state triaxial test (type II) and
(c) the continuous failure stage test (type III).

With the single stage test, several triaxial tests are required in order to predict the strength envelope of a rock sample with satisfactory accuracy, over the required range of confining pressures, where the actual number of specimens needed depends on the intrinsic variability of the rock and the scatter of the data. As an alternative to the above, a methodology was proposed [4], called the multiple failure state triaxial test (or simply the "multi-stage triaxial test"), in the content of which, by using only one specimen, the complete failure envelope of the tested material can be obtained.

In the present study, a number of multi-stage triaxial tests were performed on representative specimens from Alpine (marbles, limestones and schists) and Post Alpine formations (sandstones, microbreccia and limestones) from East Attica Prefecture. The peak and the residual strength envelopes of these specimens were obtained and their strength parameters were found.

2. Experimental configuration

A servo-hydraulic driven loading frame of 5000 kN capacity was used for the application and measuring of the axial load in the rock specimen. A Hoek-Franklin triaxial cell [5] was used in order to apply the confining pressure ($\sigma_2 = \sigma_3 = p$) to the specimens. The preparation of the specimens was in accordance with the recommendations of the ISRM [3] and the slenderness ratio was 2:1, with diameter equal to 54.5 mm. For each test, a number of 4 to 6 loading stages were achieved where, in the case of the hard rocks, the final confining stress never exceeded 30 MPa. At each stage the axial load was increased under a constant axial displacement rate, while the confining stress was kept constant until the imminent failure point was reached. The confining stress was then increased, in one step, to the desired level. This step was accompanied by an axial load increase until the next imminent point of failure was reached. This procedure was repeated until the maximum desirable confining pressure was achieved. Then, the axial displacement was increased until the peak strength of the specimen, where the complete failure envelope had been obtained. Loading of the specimen was continued until the axial load was reduced to its residual value for the maximum confining pressure. After the residual strength is reached, the confining stress is progressively reduced with a constant rate until the specimen is completely unloaded. From this final stage the residual strength envelope can be obtained.

3. Results and discussion

Through the results of these tests, it was evident that the shear manner of failure was the dominant one, but in the case of marbles and alpine limestones, ductile mechanisms were also present, even under medium confinement [6, 7].

Two strength models, for the peak and residual strength, were fitted, e.g., the Mohr - Coulomb criterion and the Hoek - Brown criterion. In the case of the peak strength envelope both models fit well the experimental data and the results were consistent with those in the literature for rock types of similar origin. In the residual state of stress, the cohesion was reduced dramatically, as it was expected, and the friction angle was increased. The latter result seems to be reasonable because the contribution of friction to rock strength increases after intense micro-cracking and the formation of macroscopic fracture planes.

References

[1] J. C. Jaeger, N. G. W. Cook and R. W. Zimmerman (2007). *Fundamentals of Rock Mechanics*, 4th ed. Blackwell Publishing Ltd, 150-152.

[2] M. S. Paterson and T-f. Wong (2005). *Experimental Rock Deformation –The Brittle Field*, 2nd ed. Springer - Verlag, Berlin Heidelberg, 17-44.

[3] K. Kovari, A. Tisa, H. H. Einstein and J. A. Franklin (1983). Suggested methods for determining the strength of rock materials in triaxial compression: Revised version, *Int. J. Rock. Mech. Min. Sci*., **206**, 283-290.

[4] K. Kovari and A. Tisa (1975). Multiple failure state and strain controlled triaxial tests, *Rock. Mech. Rock. Eng*., **71**, 17-33.

[5] E. Hoek and J. A. Franklin (1968). A simple triaxial cell for field and laboratory testing of rock, *Trans. Instn. Min. Metall.*, **77**, A22-26.

[6] F. J. Turner, D. T. Griggs and H. C. Heard (1954). Experimental deformation of calcite crystals, *Geol. Soc. Am. Bull*., **65**, 883-934.

[7] J. T. Fredrich, B. Evans and T-f. Wong (1989). Micromechanics of the brittle to plastic transition in Carrara marble, *J. Geophys. Res*., **94**, 4129-4145.

AE HIT-FREQUENCY VARIATIONS AS PRE-FAILURE INDICATORS DURING COMPRESSIVE LOADING ON MARBLE SPECIMENS

D. K. Tsaousi, I. Stavrakas and D. Triantis
Laboratory of Electronic Devices and Materials, Department of Electronics Engineering, Technological Educational Institute of Athens, 12210, Greece

1. Introduction

The Acoustic Emissions (AE) experimental technique is widely used to detect from micro-fracture states up to macro-fracture events that take place in the bulk of a material when subjected to mechanical loading. In this work the AE technique is employed in order to monitor damage evolution within Dionysos marble specimens, subjected to uniaxial compression until fracture. The novelty of the study is that the AE hit-frequency variations are studied during the loading of the specimens and pre-failure indications are detected. To this end, four acoustic sensors are placed in various positions on the specimen under study, in order to determine the variability of the AE hit frequency.

2. Materials and experimental technique

The material used for the preparation of the specimens of the experimental protocol is Dionysos marble. The specimens were orthogonal parallelepipeds of square cross section 45 x 45 x 100 mm^3. The load was imposed at a constant rate equal to 0.2 MPa/sec. The detailed experimental apparatus was presented in a previous work [1] and only essential information will be presented herein. Concerning the recording of the AE signals, four R6α sensors were attached on the specimen's surface (Fig.1). An electrical strain gauge was used for recording the strain during the experiment concurrently to the AE measurements. Failure of the specimens occurred at a stress level equal to about 57 MPa. The strain-time relation follows a linear law up to about 53 MPa, and the Young modulus was calculated to be 40 GPa.

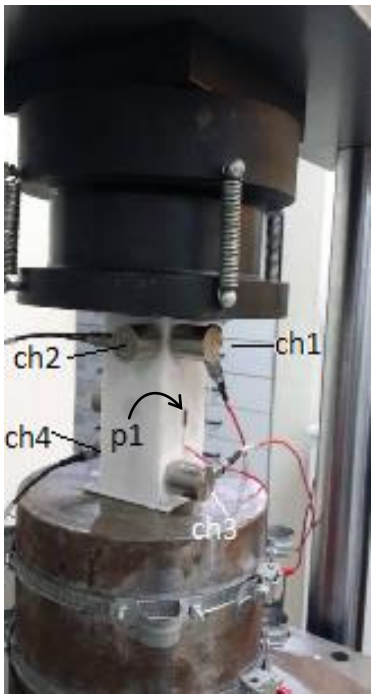

Figure 1. A photo of the experimental installation showing the 4 AE sensors (ch1-ch4) and the strain sensor (p1).

3. Results and discussion

The AE activity is studied through a new methodology for the analysis of the AE data, and, in particular, with the use of the function F which stands for the mean frequency of the AE hits [2]. The F-function calculation is performed using the inter-event times ($\Delta t=t_{i+1}-t_i$), of a group that contains a sufficient number of sequential hits (e.g. n=50). After calculating the mean value $<\Delta t>_i$ of each group, the resulting value is inverted. This defines the mean frequency F of the AE hits appearance in a time lapse beginning from t_{i-n} until t_i. Each F value corresponds to a mean time instance τ between t_{i-n} until t_i.

The function F(τ) provides a continuous representation of the acoustic activity, instead of the standard calculation of hits per second. More particularly, one obtains a detailed representation of the stage close to the failure of the specimens.

The F function, that was calculated from the AE data of the four sensors, is presented in Fig.2 in logarithmic scale (t_f-τ), where t_f corresponds to the time of failure. Additionally, the corresponding behavior of the strain is plotted. The dotted line indicates the linear fitting of the strain. A deviation

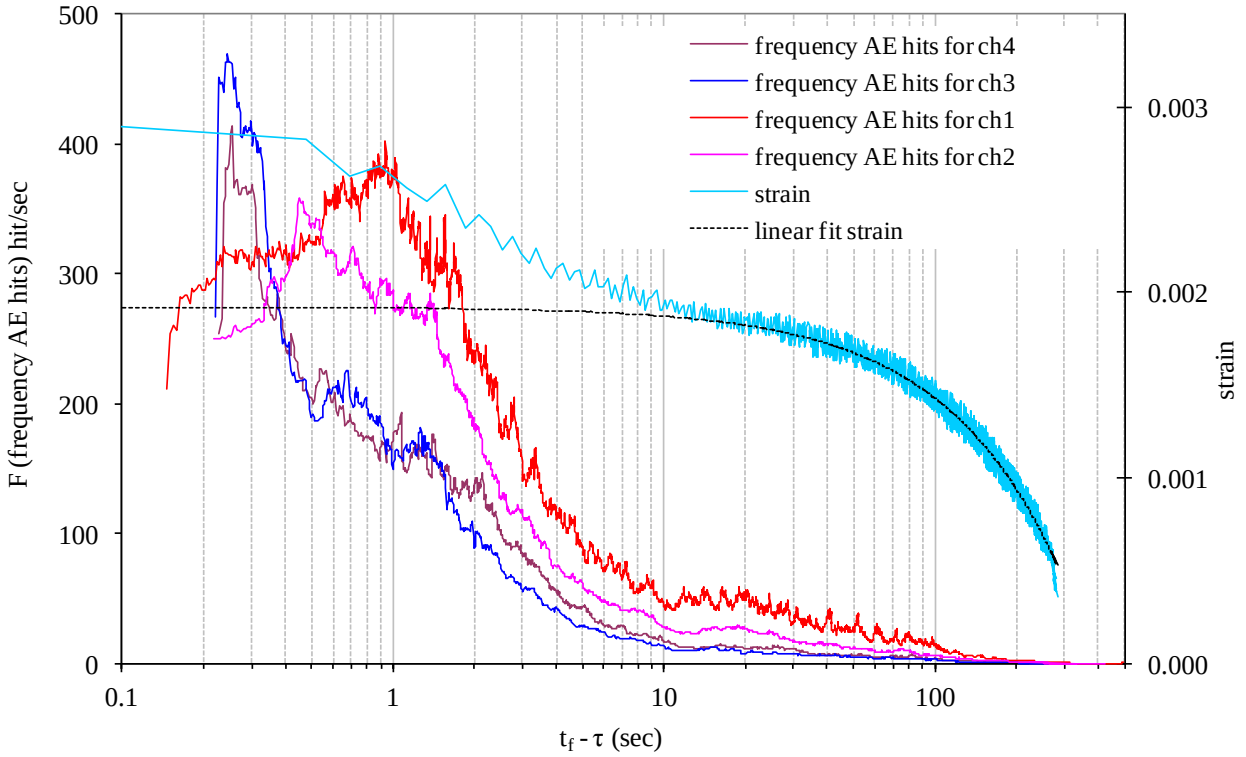

Figure 2. The F-function versus the parameter (t_f-τ) (where t_f is the failure time), for all the AE channels and the corresponding mechanical strain.

from linearity is observed at approximately (t_f-τ)=30 s, when the AE activity starts to increase rapidly, depending on the position of each sensor. It is worth noting that channels 1 and 2, that are located at the upper side of the specimen, show intense AE activity earlier with respect to the other two channels (i.e. channels 3 and 4). It must be noted that after the specimen's failure it was observed that extensive damages and fractures were located at the top side of the specimen. The above is supported by that fact that the F function that concerns channels 1 and 2 shows a peak in higher values of (t_f -τ), compared to channels 3 and 4.

Another interesting observation is that a steep decrease of the AE activity is observed a short time before fracture at all the AE channels. This is attributed to the increased duration of the AE hits slightly before fracture, since these hits are attributed to the coalescence of the created damages. Thus the AE event duration is longer and stronger overlapping all the rest of the AE activity.

References

[1] I. Stavrakas (2017). Acoustic emissions and Pressure Stimulated Currents experimental techniques used to verify Kaiser effect during compression tests of Dionysos marble, *Fracture and Structural Integrity*, **40**, 32-40.

[2] D. Triantis and S. K. Kourkoulis (2018). An alternative approach for representing the data provided by the acoustic emission technique (submitted).

EXPERIMENTAL STUDY OF PARTICLE SHAPE EFFECT ON FLOW CHARACTERISTICS OF GRANULAR MATERIALS

B. Soltanbeigi[1,2], S.-A. Papanicolopulos[2], H. Zetzener[1], J. Y. Ooi[2] and A. Kwade[1]
[1] Institut für Partikeltechnik (IPAT), Technische Universität Braunschweig, Volkmaroderstraße 5, 38104 Braunschweig, Germany
[2] Institute for Infrastructure and Environment, School of Engineering, University of Edinburgh, EH9 3JL, Edinburgh, UK

1. Abstract

Particulate materials exist in large quantity in nature, and it is also estimated that over 75% of all raw materials dealt with in industry are particulate in structure. The flowability of particulate materials is a crucial factor in bulk material handling processes, since it directly affects the efficiency of the production line and the consistency of the final product. The current study focuses on the influence of particle-scale properties on the bulk response of particulate systems.

An important factor that governs the interaction of individual particles is the shape complexity. In this regard, a multiscale study is considered to characterize the influence of shape on the bulk response.

2. A 1 g silo discharge test

A flat-bottom silo is used for investigating the particle shape effect on the flow kinematics at earth gravity. The silo has transparent walls and allows visualization of the flow during the discharge. A high-speed camera is utilized to capture successive images at all the stages of the test (Fig.1a). Later, using Particle Image Velocimetry (PIV), the displacement field is tracked and plotted as vectors (Fig. 1b). This allows comparing the flow channel geometry for spherical and cylindrical particles (Fig.1c). It is clear that the flow profiles are following different trends: for spheres, it is seen that there is a wider flow channel and particles from near the walls (near the surface) are contributing to flow, while cylindrical particles are only discharging along the height of the channel and a larger stagnant zone emerges. This is due to higher interlocking among cylinders which hinders the motion of the particles and leads to the creation of an unstable rathole. The formed heaps at the end of discharge suggest the particle shape effect on the angle of repose for granular assemblies (i.e. higher interlocking of cylindrical particles provides a higher angle of repose).

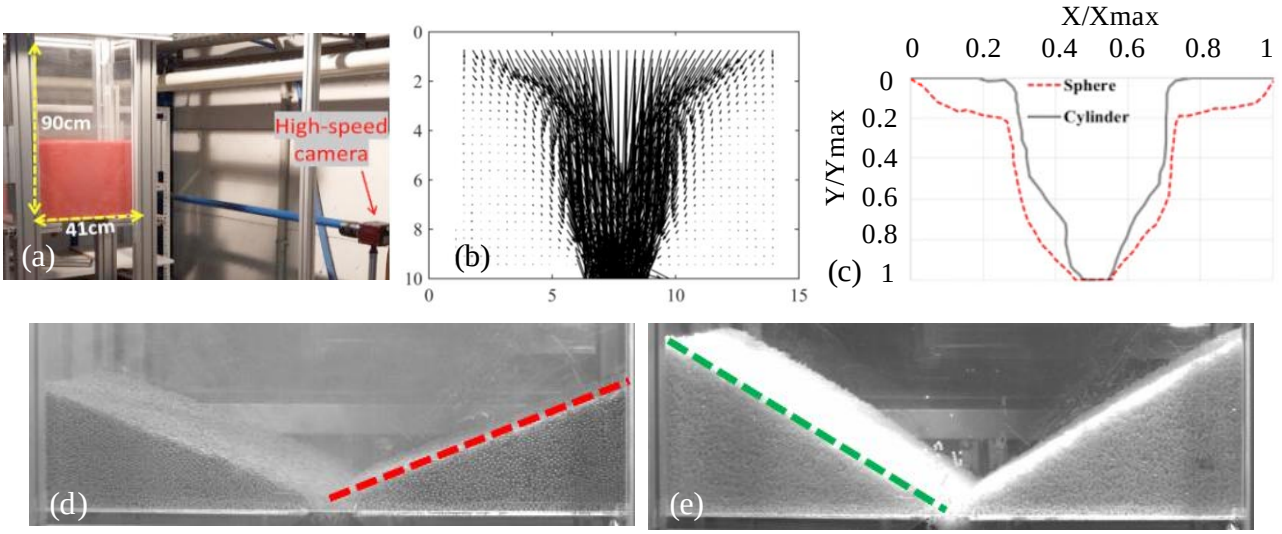

Figure 1. Silo discharge at 1g: (a) test set-up; (b) a sample of vector field (at M_D =10 % for spheres); (c) flow channel geometry; (d) dead-zone at the end of discharge (sphere); (e) dead-zone at the end of discharge (cylinder).

3. Silo centrifuge test

Characterizing the flow of the granular material at reduced scale (in the laboratory) can lead to inaccurate estimation of the wall stresses in large-size prototypes. This is because of the size effect that arises from the difference in pressure level and ratio between the mean particle dimension and silo size [1]. This effect can be more intense for material with complex shapes (e.g. flaky or rod-shapes), since the amount of interlocking and accordingly the bulk solid strength could highly be dependent on the magnitude of stress. An alternative way to simulate higher stress state in pilot-scale tests is to introduce centrifugal forces [2]. A silo centrifuge device, with transparent walls, is used for the current study. A load cell (connected to the collecting bin) and a high-speed camera make it possible to measure the discharge rate of particles over time and also visualize the flow profiles.

The increase in mass discharge rate between two identical silos at different gravities is calculated by considering Beverloo's [3] correlation for the silo discharge rate:

$$W = C\rho_b \sqrt{g}\left(D - kd\right)^{5/2} \tag{1}$$

$$\frac{W_1}{W_2} = \sqrt{\frac{g_1}{g_2}} \tag{2}$$

where, W is the mass discharge rate, *C* is a dimensionless constant related to the material properties, ρ_b is the bulk density, *g* is the gravitational acceleration, *D* is the dimension of the outlet, *k* is a factor that is related to particle shape and *d* is the particle dimension. We have already studied the validation of the proposed approach by Beverloo numerically, using Discrete Element Modelling (DEM). On the other hand, several experiments have been conducted in various accelerations with spheres and cylinders. The preliminary results suggest that the experimental observations have approximately 20% deviation from Beverloo's correlation. Accordingly, our first objective is to validate experimentally this analytical approach. Secondly, visualizing flow profiles, the influence of the shape parameter on flow characteristics of non-spherical particles is studied (under higher stresses). Finally, we revisit the conventional scaling rules for centrifuge tests and evaluate if these rules are independent of the shape factor.

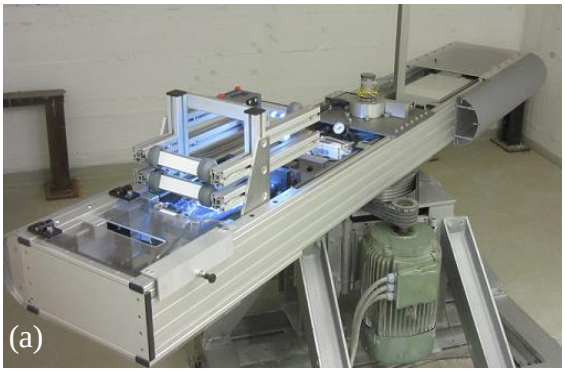

Figure 2. Modified silo centrifuge device (a) test set-up and (b) visualization enabled for the device.

References

[1] J. Tejchman (2013). *Confined granular flow in silos: experimental and numerical investigations*. Springer Science & Business Media.

[2] T. Ittershagen, H. Zetzener, J. Schwedes and A. Kwade (2013). Anisotropic behaviour of bulk solids and its effect on silo design, *Powder Technology*, **247**, 260-264.

[3] W. A. Beverloo, H. A. Leniger and J. Van de Velde (1961). The flow of granular solids through orifices, *Chemical Engineering Science*, **15(3-4)**, 260-269.

FIRST ORDER RELIABILITY METHOD ON SOIL STRENGTH PARAMETERS ESTIMATION AND STABILITY ANALYSIS

G. Belokas
Technological Educational Institute of Athens
Department of Civil Engineering and Surveying & Geoinformatics Engineering

1. Introduction

Modern codes of practice for the analysis and the design of geotechnical works (e.g. Eurocode 7 - EC7), provide an alternative of performing probabilistic (non-deterministic) analyses by application of reliability theory principles. Such an analysis, applicable to geotechnical engineering limit states analysis, is the First Order Reliability Method (FORM) [1-3], which is used for the estimation of error propagation, such as the uncertainty of the experimental results from laboratory tests (e.g. GUM: 1995, see ISO/IEC Guide 98-3:2008 [4]), and applies directly to cases where a closed form analytical solution exists.

Under the framework of EC7, the reliability analysis (uncertainty calculation) for a limit equilibrium problem can be performed with respect to the safety margin (SM), which, for a certain level of confidence, requires the knowledge of the uncertainty of the parameters that affect the value of SM, including strength constants. The best estimate of cohesion (c) and angle of shearing resistance (υ) and the corresponding variations (or uncertainties) may be calculated directly via statistical methods (e.g. Direct Shear Test), or the FORM may be applied for the error propagation in order to calculate the variations (e.g. Typical Triaxial Shear Test).

2. The two-variable linear model

The present work explores the application of the FORM for the statistical evaluation of the strength parameters and for the slope stability analytical solution of a wedge failure mechanism. Issues with respect to the design and characteristic strength are also discussed, as well as the application of the FORM to a general limit equilibrium slope stability problem.

The two-variable linear Mohr-Coulomb failure criterion (Eq.(1)), which is commonly used in geotechnical engineering practice, includes two constants (cohesion, c, and angle of shearing resistance, υ) and two variables (normal stress, σ_n, and shear stress, τ), which correspond to a two dimensional sample ($x=\sigma_n$, $y=\tau$, Fig.1).

$$\tau = c_m + \sigma_n (\tan\upsilon)_m \tag{1}$$

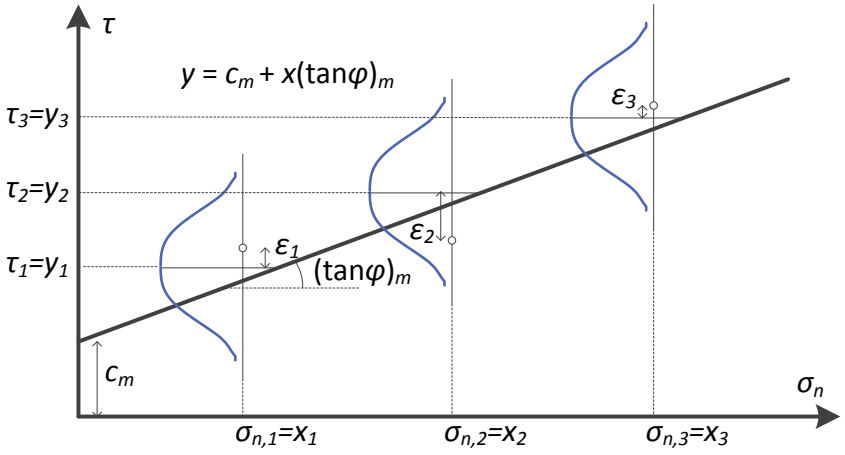

Figure 1. Graphical representation of the regression model.

Assuming that: a) x_i is an accurate observation, b) each x_i is an independent observation, c) the error ε_i has a constant variation for each x_i and d) the uncertainties of the y_i observations are equivalent (otherwise weight coefficients are required), then the estimators for the linear regression coefficients can be determined using the least square method. The standard error estimators $SE_{tan\upsilon}$ and SE_c are given by the following Eqs.(2), which apply to Direct Shear Test.

$$SE_b = \sqrt{\sum_{i=1}^{n}\varepsilon_i^2 \Big/ \left[(n-2)\sum_{i=1}^{n}\left(x_i-\bar{x}\right)^2\right]},\ SE_a = SE_b\sqrt{\frac{1}{n}\sum_{i=1}^{n}x_i^2} \tag{2}$$

Concerning the Typical Triaxial test, since $\sigma_3=\sigma_c$ (cell pressure) is the applied magnitude and $\sigma_1=\sigma_a$ (axial stress) is the measured one, in order to estimate the standard errors of c_m and $(tan\upsilon)_m$ an error propagation method is required. FORM makes use of the second moment statistics (i.e., the mean and the standard deviation) of the random variables and assumes a linearized form of the performance function (e.g. $z=g(X_1,\ldots, X_n)$) at the mean values of the random variables and independency between all variables, which approximates the standard error by the following Eq.(3):

$$SE_{d,z} \approx \sqrt{\sum_{i=1}^{n}\left(\partial g/\partial X_i\right)^2\left(SE_{X_i}\right)^2} \tag{3}$$

The above were applied to experimental data for the estimation of the characteristic values according to EN1997 requirements and were compared with respective approaches of common civil engineering practice and, also, to a planar wedge failure mechanism.

3. Conclusions

The determination of the best estimates, the uncertainties and the characteristic values for the two-variable linear model is not that straightforward as for the case of a single variable model. For the Typical Triaxial Test the FORM can provide all the required statistical quantities to be used for a probabilistic analysis. The comparison of FORM with common practice approaches applied to experimental data, for which the σ_c of each test specimen could be considered an independent observation, revealed that the FORM yielded a lower uncertainty. This is due to the fact that the FORM considers a larger sample size with respect to other methods. Finally, in probabilistic analyses a sensitivity analysis should always be performed in order to observe the influence of each uncertainty separately. For slopes it seems that the most influential uncertainty is the cohesion.

References

[1] G. Baecher and J. Christian (2003). *Reliability and Statistics in Geotechnical Engineering*. Wiley, 618.
[2] P. Nomikos, S. Christodoulopoulou and A. Sofianos (2009). Simplified probabilistic tunnel design, *6th Panhellenic Conference on Geotechnical and Geoenvironmental Engineering*,Volos, Greece.
[3] T. Orr and D. Breysse (2008). Eurocode 7 and reliability-based design. Reliability-Based Design in Geotechnical Engineering. *Computations and Applications*, Kok-Kwang Phoon (ed.), Taylor & Francis, 298-343.
[4] ISO/IEC Guide 98-3:2008. *Uncertainty of measurement – Part 3: Guide to the expression of uncertainty in measurement* (GUM: 1995).

Concrete and Mortar

ON THE EXPERIMENTAL INVESTIGATION OF POZZOLANIC LIME MORTAR STRESS-STRAIN BEHAVIOR AND DEFORMATION CHARACTERISTICS WHEN SUBJECTED TO CYCLIC LOADING

K. Kaklis[1], Z. Agioutantis[2], S. Mavrigiannakis[1] and P. Maravelaki-Kalaitzaki[3]
[1] School of Mineral Resources Engineering, Technical University of Crete, Chania, Greece
[2] Department of Mining Engineering, University of Kentucky, Lexington, Kentucky, USA
[3] School of Architectural Engineering, Technical University of Crete, Chania, Greece

1. Introduction

A previous research study [1] experimentally investigated the mechanical properties of a pozzolanic lime mortar consisting of carbonate sand, hydrated lime and metakaolin. This mortar is often utilized as a filler material in restoration projects by infilling joint fragments of historic structures where shear stresses develop along the mortar-stone interface. In addition to using mortars for joining broken stone fragments, they can also be used for filling up grooves carved in stone for inserting metallic connectors. An example application is the metallic "I" shaped connectors placed in sculptured grooves during the restoration process of the Parthenon in Athens, Greece [2]. The overarching goal of this work is to allow metakaolin lime (ML) mortars to be considered as a potential substitute to cement-based mortars commonly employed in such applications in order to minimize salt induced decay and incompatibility due to the cement present in such mortars.

Mortar behavior involves more than selecting appropriate elastic constants and strength parameters and inserting them into equations of continuum mechanics or numerical modeling. Inelastic or plastic deformations are, in fact, often of major significance in determining the stability and long term satisfactory behavior of mortar applications. Triaxial testing results [1] clearly show that specimens predominantly exhibit a plastic behavior, which may be beneficial for using this material as filler between metallic connectors and marble blocks in conditions of high shear stresses. In this study, two series of uniaxial and triaxial compression tests with loading-unloading cycles were executed in order to examine the stress-strain behavior and the deformation characteristics of the pozzolanic lime mortar.

2. Material and methods

The pozzolanic mortar mix consisted of 50% carbonate sand, 30% hydrated lime (purchased from CaO Hellas), and 20% metakaolin (Metastar 501 marketed by Imerys) (w/w). All mix designs tested are based on a water-binder (lime and metakaolin) (W/B) ratio of 0.92. The weight ratio between the hydrated lime and metakaolin is 1.5 for all tests to ensure a full pozzolanic reaction.

Cylindrical specimens were utilized for the uniaxial and triaxial compression tests. Mortar specimens were cast in prismatic molds constructed out of melamine furniture boards. The cylinders were cored out of these blocks by using a typical laboratory coring apparatus following recommendations in the relevant literature for rock mechanics tests. The height to diameter ratio (*h/D*) for the uniaxial and triaxial compression tests remained constant and equal to 2:1.

These tests were performed using a stiff 1600 kN MTS hydraulic testing frame (model 815) for the axial load and a Wykeham Farrance triaxial testing chamber with a maximum pressure capacity of 14 MPa for the lateral load.

3. The experimental setup

Triaxial compression tests are employed to determine the mechanical properties of materials under multiaxial loading conditions. This test provides a quantitative measure of the compressive strength of a material under confinement as well as the corresponding stress-strain behavior of the specimen under

such conditions. In rock or soil mechanics, triaxial testing is commonly used to estimate the in-situ material strength by simulating the corresponding confining (geostatic) pressures.

In preparing specimens for this test, each sample is covered with a thin rubber membrane and subsequently placed inside a pressure vessel. The pressure vessel is used to apply the desired confining pressure. In triaxial tests, following the ISRM suggested methods, specimens are initially loaded hydrostatically to the desired confining pressure using a lateral pressure controller. The lateral stress is then kept constant, while the axial stress increases until failure.

4. Experimental results

Fig.1a presents a typical stress-strain curve under a conventional triaxial compression test with four cycles under a confining pressure of 3.96 MPa. The narrow loop circumscribed by the unloading - reloading branches may be approximately substituted by a straight line (Fig.1b) and its slope can be taken as the mean Young's modulus [3].

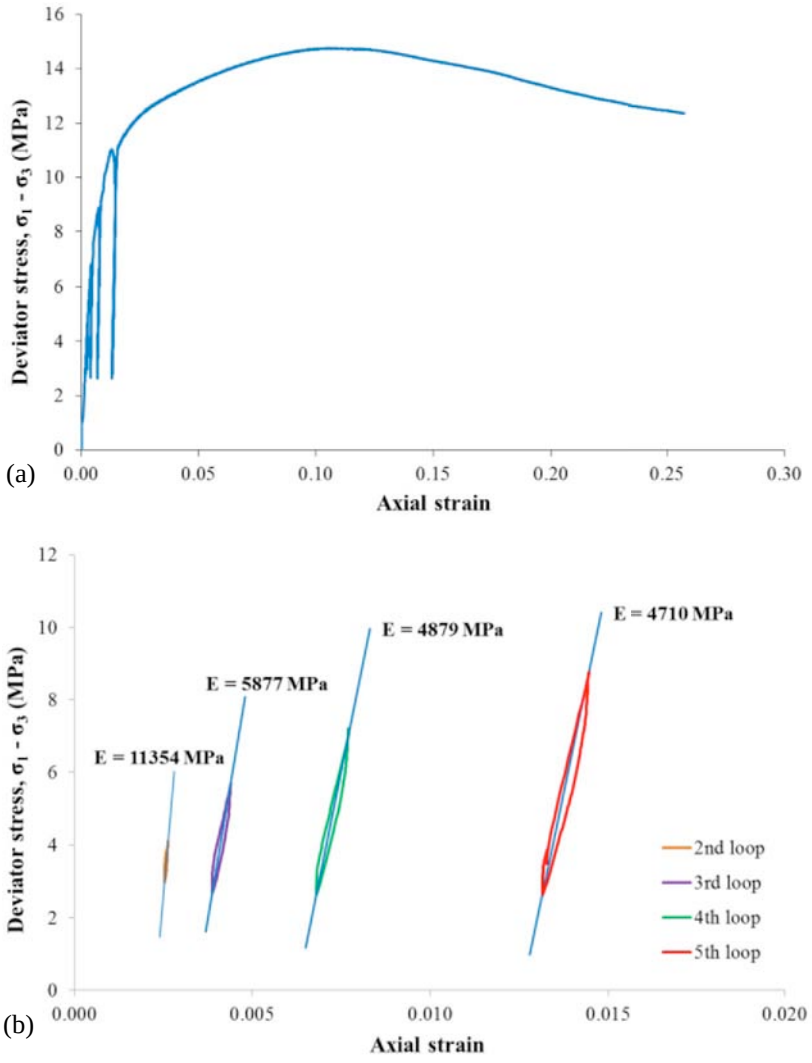

Figure 1. (a) The complete deviator stress-strain curve for pozzolanic mortar specimen tested in triaxial cyclic loading under a confining pressure of 3.96 MPa. (b) The mean Young's modulus for each loop of the cyclic loading.

Acknowledgements

This research has been co-financed by the European Union (European Social Fund-ESF) and Greek national funds through the Operational Program "Education and Lifelong Learning" of the National Strategic Reference Framework (NSRF) - Research Funding Program: THALES: Reinforcement of the interdisciplinary and/or inter-institutional research and innovation.

References

[1] K. N. Kaklis, S. P. Maurigiannakis, Z. G. Agioutantis and P. Maravelaki-Kalaitzaki (2018). Characterization of pozzolanic lime mortars used as filling material in shaped grooves for restoring member connections in ancient monuments, *International Journal of Architectural Heritage*, **12(1)**, 75-90.

[2] S. K. Kourkoulis and E. D. Pasiou (2015). Interconnected epistyles of marble monuments under axial loads, *International Journal of Architectural Heritage*, **9(3)**, 177-194.

[3] K. Mogi (2007). *Experimental Rock Mechanics*, Geomechanics Research Series 3, Balkema proceedings and monographs in engineering, water and earth sciences, Taylor & Francis / Balkema, The Netherlands, 122-131.

INFLUENCE OF ANISOTROPY ON THE RESULTS OF THE BRAZILIAN-DISC TEST

E. Ganniari-Papageorgiou[1], P. Chatzistergos[1] and Ch. F. Markides[2]
[1] Staffordshire University, Stoke on Trent, UK
[2] National Technical University of Athens, Department of Mechanics, Athens, Greece

1. Introduction

By all accounts the Brazilian-disc test is perhaps the most popular alternative of the direct tension test for the determination of the tensile strength of rocks. It is the anisotropic nature of the latter, however, which, in general, undermines the reliability of the relative analytic solutions describing the stress field in the disc, since they are based on the assumption that due to symmetry only normal principal stresses exist at the centre of the disc. Indeed, in the case of transverse isotropy considered here, the degree of anisotropy (in conjunction with an arbitrary orientation of the externally applied load with respect to the layers of isotropy) causes additional shear stresses at the disc's centre, complicating further the determination of the stress field and the crack initiation point. In this direction, a combined numerical and analytical study is described here, aiming to the description of the stress field in a transversely isotropic disc during the implementation of the Brazilian-disc test according to the standard of the International Society for Rock Mechanics [1]. The study is a part of an ongoing project quantifying the role of anisotropy in the validity of the test and the failure of rock-like materials.

2. Methods

2.1 Finite element modeling

A 2D finite element (FE) model of the Brazilian-disc test was designed using ANSYS 16.0 (Fig.1). The model comprises a disc of radius, R=50 mm and thickness, w=10 mm and rigid curved compression plates [1]. The disc's material is simulated as linearly elastic, transversely isotropic with $E_x=E_z=E_1$, $E_y=E_2$. Frictionless contact is assumed between the disc and the compression plates. The stress field in the disc was determined considering materials with different degrees of anisotropy and for different relative angles between loading and the material's planes of elastic symmetry (φ_0). Two natural and one fictitious transversely isotropic materials with increasing degrees of anisotropy were included in this study, as follows: (1) Dionysos Marble (DM, E_1=74 GPa, E_2=45 GPa, ν_1= 0.35, ν_2=0.29), (2) Serpentinous Schist (SSc, E_1=58 GPa, E_2=27 GPa, ν_1=0.34, ν_2=0.12), (3) Fictitious Material (FM, E_1=100 GPa, E_2=30 GPa, ν_1=0.21, ν_2=0.15). An isotropic material was also examined as reference (PMMA, E=3.19 GPa, ν=0.36). The value of the first principal stress at the centre of the disc was determined for φ_0 angles varying in the (0^o - 90^o) range.

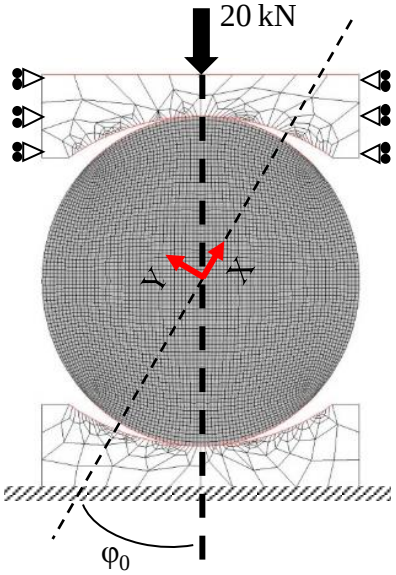

Figure 1. The FE model of the Brazilian-disc test.

2.2 Analytic solution

Confronting the above problem as a first fundamental one of plane linear elasticity, the stresses are obtained on the disc's cross-section employing Lekhnitskii's complex potentials [2] of the two complicated complex variables $z_1=x+\mu_1 y$ and $z_2=x+\mu_2 y$, with $\mu_{1,2}$ being the solution of the characteristic equation associated with the so-called "generalized" biharmonic equation. Namely, assuming a parabolic distribution for the externally applied load:

$$\sigma_r = -P(\theta) = -P_c\left[1-\sin^2(\phi_o-\theta)/\sin^2\omega_o\right],\ (P_c=P(\theta)_{max}>0,\ \theta \text{ anticlockwise from x-axis}), \quad (1)$$

over two symmetric arcs of the disc's periphery of varying length, $2R\omega_o$, each, according to the load level, load orientation and elastic parameters [3], the stress components are obtained in series form as:

$$\sigma_x = (\bar{b}_1 - b_1)/Ri + 2\Re\left[\mu_1^2 \sum_{n=3,5,...} A_n P_{1n}'(z_1) + \mu_2^2 \sum_{n=3,5,...} B_n P_{2n}'(z_2)\right] \quad (2)$$

$$\sigma_y = (a_1 + \bar{a}_1)/R + 2\Re\left[\sum_{n=3,5,...} A_n P_{1n}'(z_1) + \sum_{n=3,5,...} B_n P_{2n}'(z_2)\right] \quad (3)$$

$$\tau_{xy} = (a_1 - \bar{a}_1)/Ri - 2\Re\left[\mu_1 \sum_{n=3,5,...} A_n P_{1n}'(z_1) + \mu_2 \sum_{n=3,5,...} B_n P_{2n}'(z_2)\right] \quad (4)$$

where i denotes the imaginary unit, over-bar the complex conjugate, $\Re$ the real part and prime indicates the first derivative, while all constants appear they can be found in [3]. In addition, for the results plotted in Fig.2 the following, well-known transformation formula, was used:

$$\sigma_\theta = (\sigma_x + \sigma_y)/2 - (\sigma_x - \sigma_y)\cos 2\theta/2 - \tau_{xy}\sin 2\theta \quad (5)$$

whereas for calculating ω_o, it was assumed that $G_2 \cong E_1E_2/\left[E_1(1+2\nu_2)+E_2\right]$.

3. Results and conclusions

The average absolute difference between analytical and numerical calculations was only 0.33%, 2.7%, 1.6% and 3.1% for PMMA, DM, SSc and FM respectively. In transversely isotropic materials, for a given external force and φ_0-value, different 1st principal stresses are generated at the disc's center. The difference between the stress for $\varphi_0=0^o$ and $\varphi_0=90^o$ for DM, SSc and FM was 22%, 31% and 43%, respectively. The 1st principal stress is significantly affected by the degree of anisotropy. Indicatively, when $\varphi_0=0^o$ its value for DM (E_1/E_2=1.6), SSc (E_1/E_2=2.1) and FC (E_1/E_2=3.3) is equal to 10.6 MPa, 9.8 MPa and 8.1 MPa, respectively. For comparison, the same value for an isotropic material is 12.4 MPa.

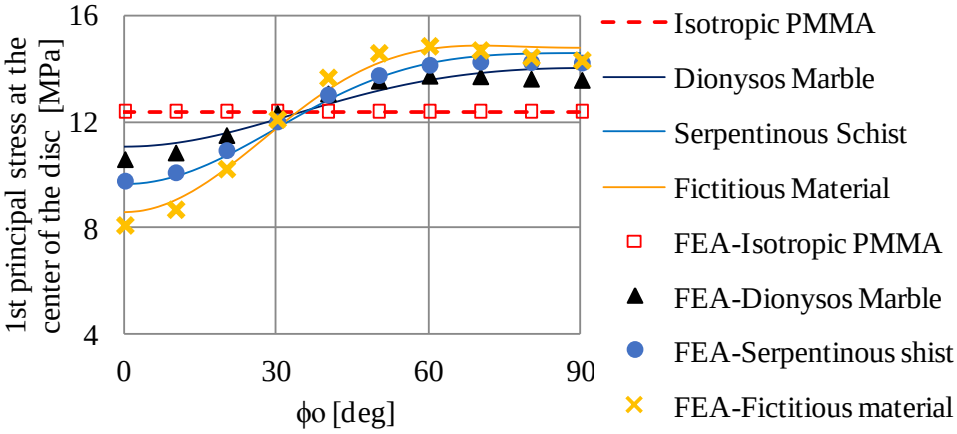

Figure 2. The 1st principal stress at the disc's center.

Concluding, it was clearly shown, by both the analytical and the numerical results, that the outcome of the Brazilian-disc test is significantly affected by anisotropy, as it was quantified, for example, for the magnitude of the 1st principal stress at the centre of the disc. Therefore, it can be said, that determination of the tensile strength of anisotropic materials, by means of the standardized Brazilian-disc test, provides erroneous results, in case the role of anisotropy on the stress field of the disc is ignored.

References

[1] ISRM (1978). Suggested methods for determining tensile strength of rock materials, *Int. J. Rock Mech. Mining Sci. & Geomech. Abs.*, **15(3)**, 99-103.
[2] S. G. Lekhnitskii (1968). *Anisotropic Plates*, Gordon and Breach, New York.
[3] Ch. F. Markides and S. K. Kourkoulis (2016). Anisotropic discs loaded by parabolically distributed pressure, *Procedia Structural Integrity*, **2**, 2659-2666.

MULTIFACTORIAL EXPERIMENTAL ANALYSIS OF CONCRETE COMPRESSIVE STRENGTH AS A FUNCTION OF TIME AND WATER TO CEMENT RATIO

S. Gavela, N. Nikoloutsopoulos, G. Papadakos, D. Passa and A. Sotiropoulou
School of Pedagogical and Technological Education,
Department of Civil Engineering Educators, Athens Greece

1. Area of interest

The compressive strength of concrete is typically determined for fixed nominal values of curing age. Corresponding measurements, even if performed by multiple specimens testing, cannot figure the dispersion of the results attributed to all the significant effective error parameters. Efforts have been made to model the effect of specimen curing age [1, 2], the geometrical deteriorations of the specimen [3], the water to cement ratio value [4-8], the curing temperature [5, 9-10] and the relative humidity where the specimens are exposed during the curing procedure [11], for a given mix of selected qualitative characteristics of constituting materials in the form of a strictly defined specimen geometry, according to EN 12390-1.

All these parameters are studied and corresponding values are selected prior to the testing in order not to alter the definition of the testing result. If these parameters are accurately followed, the definitional error is minimal, so the results of the testing are trustworthy. Still, essential questions remain; to what extent do all these parameters correlate to each other and to the result of the test procedure? Are the results of the testing procedure valid if these parameters fail to be accurately followed? For example, should a testing result be put aside if the curing age of the specimen deviates by a few days from the typical nominal 28-days value?

Studying the effect of all the above parameters of the test procedure in one experiment for various levels of parameters set values would lead to an enormous specimens' population. This study is part of a long, multistage experimental process aiming at the creation of a function that correlates the expected testing result of the compressive strength of concrete specimens to all of the above parameters that will be finally assessed as significant to incorporate. Based on the use of such a multifactorial function, results retrieved from more loosely defined testing procedures would be corrected accordingly, compatible with the strict definition of the testing procedure. Also, the integration of various similar experiments of such a protocol could lead to the standardization of a semi-empirical model on the relation of concrete compressive strength as a function of a great number of testing parameters and mix materials characteristics [12].

More specifically, the present study aims at the experimental investigation of: (a) the correlation of compressive strength testing results with the parameters of curing age and water-to-cement ratio through sensitivity analysis and (b) the significance of the cross-correlation between these two parameters.

2. Basic assumptions and method used

The testing procedure followed for the realization of the experiment is exactly the one described in the European Standard EN 12390-3:2009. The apparatus used for the tests is a uniaxial compressive strength machine calibrated according to the requirements of the International Standard ISO 7500-1.

The essential contribution of this study lies in the experimental design for the combination of curing ages and the parameter of water-to-cement mass ratio. Specimen curing age values at the time of compressive strength testing were selected to include the typical value of 28-days. Water-to-cement ratio values were selected to be separated by equivalent intervals. At the same time, superplasticizer's mix proportions were kept the same, except from the mixture with the less water-

to-cement ratio. In this mixture a small increase of superplasticizer's mix proportion was needed in order for the mixture to become workable. Multiple molds were used randomly, so the effect of any specimens' geometrical deteriorations has been incorporated in the result. All other test procedure or mix characteristics were kept constant, as possible.

The above mentioned experimental results were used into a multifactorial regression analysis procedure leading to a sigmoidal - by time - equation. Sensitivity analysis and application of the law of propagation of uncertainty was performed according to the ISO GUM procedure.

3. Results and conclusions

The basic result of this study is a multifactorial regression function incorporating both the parameters of the curing age and the water-to-cement ratio for given qualitative characteristics of the constituents. Despite the fact that this regression function corresponds to these qualitative characteristics of the constituents, the sensitivity analysis of this study is expected to have a more global validity.

Such semi-empirical models, especially if completed with all the significant parameters, are expected to be useful, among others, for accredited testing laboratories in order to perform their internal quality control program.

References

[1] R. Féret (1892). On the compactness of the mortars, *Annales des Ponts et Chaussées*, **7(4)**, 5-164.
[2] D. A. Abrams (1927). Water-cement ratio as a basis of concrete quality, *ACI Structural Journal, Proceedings*, **23(2)**, 452-457.
[3] M. K. Abd and Z. D. Habeeb (2014). Effect of specimen size and shape on compressive strength of self-compacting concrete, *DJES*, **7(2)**, 16-29.
[4] F. Aslani, L. Maia and J. Santos (2017). Effect of specimen geometry and specimen preparation on the concrete compressive strength test, *Struct Eng Mech*, **62(1)**, 97-106.
[5] P. Freiesleben Hansen and J. Pedersen (1985). Curing of concrete structures, *CEB Information Bulletin*, **166**, 42.
[6] N. J. Carino and H. S. Lew (1983). Temperature effects on strength-maturity relations of mortar, *ACI Structural Journal, Proceedings*, **80(3)**, 177-182.
[7] C. Yeh (2006). Generalization of strength versus water–cementitious ratio relationship to age, *Cem. Concr. Res.*, **36**, 1865-1873.
[8] Metwally abd allah Abd elaty (2014). Compressive strength prediction of Portland cement concrete with age using a new model, *HBRC Journal*, **10**, 145-155.
[9] A. Sotiropoulou, S. Gavela, N. Nikoloutsopoulos, D. Passa and G. Papadakos (2017). Experimental study of wood shaving addition in mortar and statistical modeling on selected effects, *Journal of the Mechanical Behaviour of Materials*, **26(1-2)**, DOI: https://doi.org/10.1515/jmbm-2017-0013.
[10] J.-K. Kim, Y.-H. Moon and S.-H. Eo (1998). Compressive strength development of concrete with different curing time and temperature, *Cem. Concr. Res.*, **28(12)**, 1761-1773.
[11] H. Un and B. Baradan (2011). The effect of curing temperature and relative humidity on the strength development of Portland cement mortar, *SRE*, **6(12)**, 2504-2511.
[12] S. Gavela, G. Papadakos and V. Kaselouri – Rigopoulou (2017). A suggestion for standardizing a traceable process for the determination of the mechanical properties of concrete containing thermoplastic polymers as aggregates, in *Thermoplastic Composites – Emerging Technology, Uses and Prospects*, Materials Science and Technologies NOVA publications book, ISBN: 978-1-53610-727-2.

COMPARISON OF SHEAR STRENGTHENING TECHNIQUES OF REINFORCED CONCRETE BEAMS WITH CARBON FIBER REINFORCED POLYMERS (CFRPs)

N. Nikoloutsopoulos, D. Passa, S. Gavela and A. Sotiropoulou
School of Pedagogical and Technological Education,
Department of Civil Engineering Educators, Athens Greece

1. Introduction

Intensive research has been focused on strengthening of old reinforced concrete constructions, especially in brittle failures. Strengthening of shear-critical reinforced concrete beams using externally epoxy-bonded fiber reinforced polymers (FRPs) is a promising and extensively studied technique. The most common method of amplification is the in situ wet application of carbon fiber fabrics or strips, impregnated with resin and wrapped around the beams in the direction of the main vertical axis fibers of the axle beam [1].

However, premature debonding failure governs in flanged beams with U-strengthening technique since the slab usually prevents the wrapping around the cross section or/and the proper end anchorage of the externally applied FRP [2]. For more efficient shear strengthening of beams with carbon fiber strips, each of them is anchored with carbon fiber rope. In this way, the fewer perforations in the existing carrier are assured, compared with the reinforcement of continuous fabrics and quadriclateral strips [3].

In this study, the effectiveness of a new strengthening technique for upgrading the behavior of shear reinforced concrete beams using carbon FRP with no drillings operations is experimentally studied.

2. Experimental procedure

In the context of this research, strength class C30/37 reinforced concrete beams were produced to be strengthened in shear. The beams' dimensions were 15x15x70cm with bending reinforcement 3Ø10 and without shear reinforcement. The specimens were strengthened in different schemes and tested in two point bending test for studying the shear failure. The investigated strengthening schemes are presented in Table 1.

Beams were strengthened with Carbon Fiber Reinforced Polymers (CFRPs) and epoxy based resin, which were sponsored by Sika Hellas A.B.E.E. SikaWrap®-230C was used for strips, Sika-Wrap®FX-50C for rope, Sikadur®-330 for boxing the rope in a notch and bonding the FRP with concrete and Sikadur®-300 for impregnating the rope.

3. Results and conclusions

It is noted that the experimental results of each strengthening technique are very close to the results of the theoretical calculations. In particular, the experimental results are greater than the results of the theoretical calculations because the latter involve safety factors. The shear strength that is taken up by the composite marginally approximates the required value.

With different combinations of placement of composite materials on the beam, but also with different forms of composite materials (rope, strip, jacket), the required strengthening can be achieved with the fewest drilling operations to the slab.

Strengthening technique F (Rope in two sided notch at 45^o), which is new and does not need any drilling operations, produces results comparable to strengthening technique D (Rope in perimeter notch at 90^o) which includes drilling operations when applied in practice for the strengthening of reinforced concrete constructions.

Code	Strengthening Technique groups	Code	Strengthening Techniques
Ref	With no strengthening	-	-
A	Four-sided strips or four-sided continuous jacket	A.1	Four-sided single strip
		A.2	Four- sided double strips
		A.3	Four-sided single continuous jacket
B	Three-sided strips or three-sided continuous jacket	B.1	Three-sided single strip
		B.2	Three-sided double strips
		B.3	Three-sided single jacket
		B.4	Three-sided double jacket
C	Three-sided strips & three-sided continuous jacket with rope anchorage	C.1	Three-sided single strip with rope anchorage
		C.2	Three-sided double strips with rope anchorage
		C.3	Three-sided single jacket with rope anchorage
D	Rope in perimeter notch at 90^o	D.1	Single rope in perimeter notch at 90^o
		D.2	Double rope in perimeter notch at 90^o
E	Rope in two sided notch at 90^o with two different axial distances between stripes	E.1	Single rope in two sided notch at 90^o
		E.2	Double rope in two sided notch at 90^o
F	Rope in two sided notch at 45^o	F.1	Single rope in two sided notch at 45^o
		F.2	Double rope in two sided notch at 45^o

Table 1. Strengthening techniques.

References

[1] C. E. Chalioris, N. A. Papadopoulos, T. A. Panagiotopoulos and P. K. Kosmidou (2017). Shear strengthening of reinforced concrete deep beams without stirrups using carbon fibre rope as transverse link reinforcement, in *25th International Conference on Composites/Nano Engineering (ICCE 25)*, July 16-22, Rome, Italy.

[2] G. M. Chen , S. W. Li , D. Fernando , P. C. Liu and J. F. Chen (2017). Full-range FRP failure behaviour in RC beams shear-strengthened with FRP wraps, *International Journal of Solids and Structures*, **125**, 1-21.

[3] K. Yang, G. Kim and H.Yang (2011). Shear behavior of continuous reinforced concrete T-beams using wire rope as internal shear reinforcement, *Construction and Building Materials*, **25**, 911-918.

EXPERIMENTAL AND NUMERICAL SIMULATION OF CURVED FRAME STRUCTURES

C. B. Demakos[1], A. Kyriazopoulos[2], N. Pnevmatikos[2] and D. Drivas[1]
[1]Piraeus University of Applied Sciences, Reinforced Concrete Lab,
[2]Athens University of Applied Sciences

1. Introduction

Curved geometry is a tool for optimization of structures, since for designing a modern and cost consuming arch structure it is necessary to decrease the material used and simultaneously the frame structure to attain a sufficient flexural capacity. This is possible by transforming all stresses inside the structure to mainly compressive ones approaching the respective strength of the material. Experimental results obtained in this paper for cement mortar arches under external bending and variously distributed loadings revealed that the load carrying capacity of thin arches attains values close to the compression strength of the mortar used. In addition, numerical simulation, using non-linear analysis with finite shell elements, verified the experimental findings for the curved frames.

An important question, automatically generated, is the one concerning the appropriate equation describing this curved geometry. Galileo [1] postulated that this shape is a parabola and Euler proved in 1744 that the catenary is the curve which, when rotated about the x-axis, gives the surface of minimum area (the catenoid) for the given bounding circles. Finally, Fuss (1796) provided equations describing the equilibrium of a chain under any force. It is noted that the geometry of the catenary is not a parabola but a cosine-hyperbola. This method was used by Gaudi to determine the optimal geometry and build the famous "*Basílica i Temple Expiatori de la Sagrada Família Church*". Since then, engineers develop empirical methods for structures mainly in stone bridges, which always are under compression. Catenary arches are often used in the construction of kilns and bridges [2].

2. The experiment setup

An experimental protocol was implemented in the Laboratory of Reinforced Concrete of Piraeus University [3] including experiments with three curved arches tested under bending. The dimensions of the specimens were L=70 cm (span) and h= 30 cm (height) resembling the following parabola:

$$y = 4\,h\,[\,(x/L) - (x/L)^2\,] \quad (1)$$

keeping the height to span ratio equal to $h/L=\sqrt{3}/4$. A tested specimen is shown in Fig.1. The cement frame section was 8 mm thick and 10 cm wide. The compression strength of the cement mortar was equal to 50 MPa. The specimen was placed inside a box, filled with sand over the arch, in order to load it uniformly in bending. A force was then applied over the surface of the sand, using a wooden plate (Fig.1b).

Figure 1. Front view of a specimen (up) and a specimen inside the box (down).

3. Modeling of structure, analysis results and discussions

The specimens tested were numerically modeled and the numerical results were compared against the experimental ones. The model's geometry is exactly that of the tested specimens. The material was cement mortar of compressive strength equal to about 50 MPa. Two levels of simulation were implemented, to model the curved frame, one with linear- and one with shell-elements (see Fig.2).

The loading of the arch structure consists of two parts. One is the own-weight of the sand inside the box and the second is the force from the loading frame. In order to simulate the load of the

sand, the weight of a sand column (Fig.3a) above each element was calculated and applied to this element providing an overall load distribution as it is shown in Fig.3b. Applying a progressively increasing load, the stress distribution was calculated as it is shown in Fig.4a.

Fig.4b shows the failure pattern of an arch submitted to the previously referred bending loading. The variation of the vertical load versus the displacment was calculated at the midle of the arch structure model and it is plotted in Fig.5 in comparison to the respective experimental one. A good agreement is revealed and this is apparent, also, by the crack pattern of the fractured specimen. The experimental values for the load are slightly higher than the numerical ones, obviously, due to the own-weight of the sand. Furthermore, the numerical aproach provides lower upper bending force and more ductile deformation for the same level of stresses compared to the experimental results.

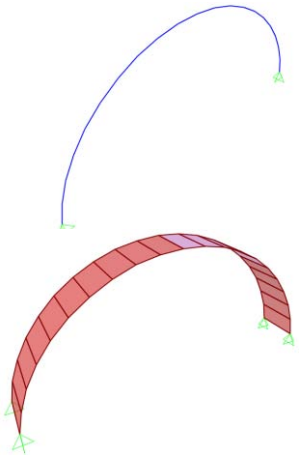

Figure 2. A curved frame model with linear- (up) and shell- finite elements (down).

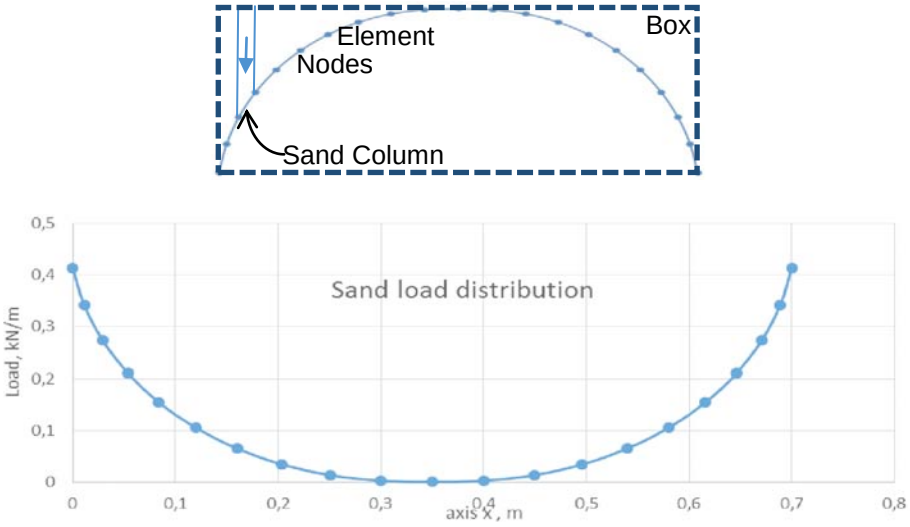

Figure 3. Arch structure with sand loading (left) and loading variation curve on the structure (below).

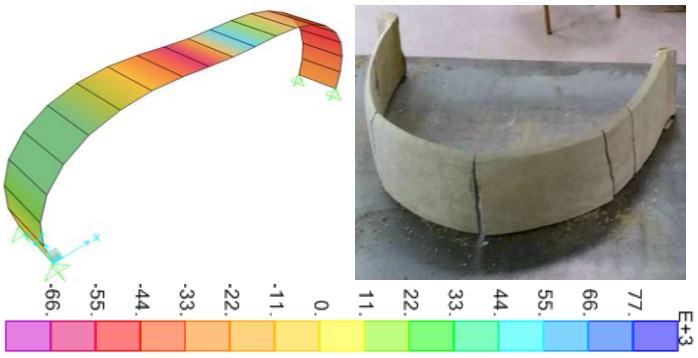

Figure 4. Stress distribution in (a) the deformed curved model and (b) the fractured specimen.

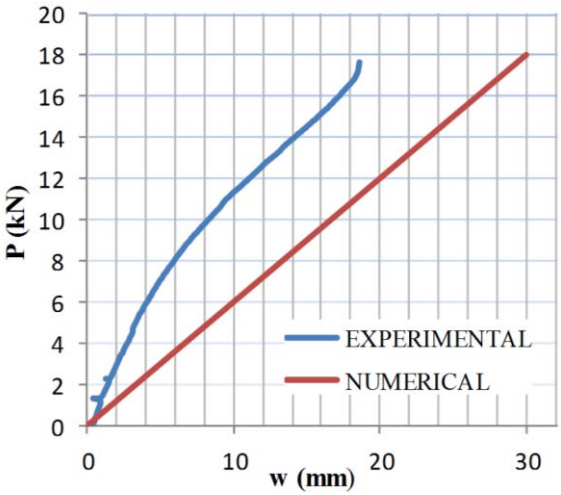

Figure 5. Loading vs. displacement variation curves from numerical approach and tests for arch structures.

References

[1] G. Galileo (1638). *Two New Sciences*, The MacMillan Co, New York, 1914.

[2] O. Sigmund (2003). *Topology Optimization, State-of-the-Art and Future Perspectives*, Copenhagen: Technical University of Denmark (DTU).

[3] A. Liberis (2017). Seismic and energy retrofit of structures and sustainable development (in Greek). *Master thesis, Postgraduate Program (MSc)*, Piraeus University of Applied Sciences, Greece.

WORKABILITY IN 3D PRINTING CONCRETE

M. Papachristoforou, V. Mitsopoulos and M. Stefanidou
Aristotle University of Thessaloniki, Thessaloniki, Greece

1. Introduction

3D concrete printing is an innovative construction method that promises to be highly advantageous in the construction field in terms of optimizing construction time, cost, design flexibility, error reduction, and environmental aspects. Concrete is extruded through a nozzle to build structural components layer-by-layer without the use of formwork or any subsequent vibration. In the present abstract a new method is introduced for high performance concrete that checks workability and printability windows for 3D printing concrete.

2. Challenges

Some of the challenges that need to be taken into account include the workability of the matrix inside the mixer so that it is fluid enough to pour through the nozzle of the mechanism without blocking it, especially in the last phases of the printing procedure when the mixture would lose some of its flowability. Three requirements are proposed with respect to print quality, namely, surface quality, squared edges and dimension conformity and consistency. Next, buildability (shape stability) of a mixture must be examined and relevant adjustments should be made accordingly. However, acceptance or rejection decision must be based on layer settlement experiment, where concrete layers are printed on top of each other with the same extrusion mechanism as the full-scale concrete printer. No visible deformations should occur when target interlayer time gap is used. The third step in laboratory testing of a printing mixture refers to printability window of a mixture, where printability limit (the longest time when a mixture can be printed with acceptable print quality) should be measured and reported for a specific mixture.

3. Workability

It is essential to comprehend that the workability of the mixture and the time it needs to set are important to the characterization of a mixture as printable or not. In the international bibliography some of the methods used include using a flow table (ASTM C1437-15) where initially a mold is filled with mortar and compacted. Then the mold is lifted and the table is immediately dropped 25 times in 15 s. The flow is the average base diameter of the mortar mass, expressed as a percentage of the original base diameter. Also, the compressive strength is measured according to ASTM C109. Relevant to shape quality, cylinder stability test is proposed for rapid evaluation and comparison of influence of different materials (additives or admixtures) on shape stability. “Cylinder stability” test was developed as another test method for shape stability evaluation of different mixtures [1].

In the present study the workability is measured through various tests that include a rheometer (ICAR Rheometer), flow table test (EN 1015-3:1999 and ASTM C1437-15) and Vicat needle test (ASTM C191-13). All these are conducted into 0, 15 and 30 min time lapses in order to determine the rate of which the workability is lost for the given 3D printing system. The rheometer test was conducted to determine the viscosity characteristics of the mixtures and how these are correlated to the flow table measures and finally, to printability. In Fig.1a, the correlation between maximum torque and flow table is presented, along with the printable area (blue part of the chart). Buildability was estimated by the number of layers of the printing specimen that can be achieved without collapse (Fig.1b). In other studies, 5 layers were considered to be the target and the same number of layers without collapsing was succeeded [2]. In addition, the print quality, namely surface quality and dimensional conformity/consistency, when using a specific printing mixture, has also been

studied and compared to other studies in order to check the consistency and accuracy of the results. Based on proposed criteria, the mixtures were considered acceptable or not for printing.

Also, in this study, the specimens used in compressive- and bending-strength tests, are formed by 40 x 40 x 160 mm prismatic specimens that are left 24 hours in the mould and then they were cured for 28 days in the humidity chamber to gain full strength (EN-1926). Moreover, the shrinkage of some mixtures is measured, in order to define some minimum limits about the width of each printed layer (ASTM D-955). This is essential since shrinkage problems can be severe in real-life scenarios-3D printing procedures.

4. Materials and printing

Extrudability and flowability are related to the concrete extrusion, flow, and workability, as the aim is to reach a continuous easy-flowing paste from the source to the printing nozzle. Aggregates of a maximum size of 1 mm were selected as the diameter of the printing nozzle is relatively small (~2 cm). Other dry constituents include cement type II, 52.5, blast furnace slag and silica fume. Also, a mixture including quartz was studied for its workability and strength properties in order to be used as 3D printing material. Apart from these, limestone filler was also used to ensure that no segregation occurred and to test the compressive strength. Also, a superplasticizer (Viscocrete) is used to ultimately increase the workability of the concrete and compensate for the low water-cement ratio. In some cases VMA was also added to ensure better cohesion. An appropriate balance of all the constituents had to be reached to ensure proper function of the mix. Several experiments were performed to determine a base structure for printable mixtures. Even though in this study the segregation problem was significant due to the high W/C ratio, the results gained from the compressive strength tests were within the range of other similar studies using similar aggregates (from 16 to 45 MPa).

A prototype system was introduced to print and check all the latter parameters in small scale experiments. The system includes the nozzle for extrusion as well as the base where the nozzle prints the layers of the mixtures, which in each turn is also able to move in x-y-z axis. Regarding the 3D printing machine, a 2 cm nozzle was selected with smooth end and a screw-kind extrusion system was selected for the extrusion process due to some of the advantages and ease it offers relevant to other extrusion methods (syringe extrusion). Compared to implementing a full-size printer, the main advantages of using such a laboratory-scale printing machine include savings in time, cost, and material.

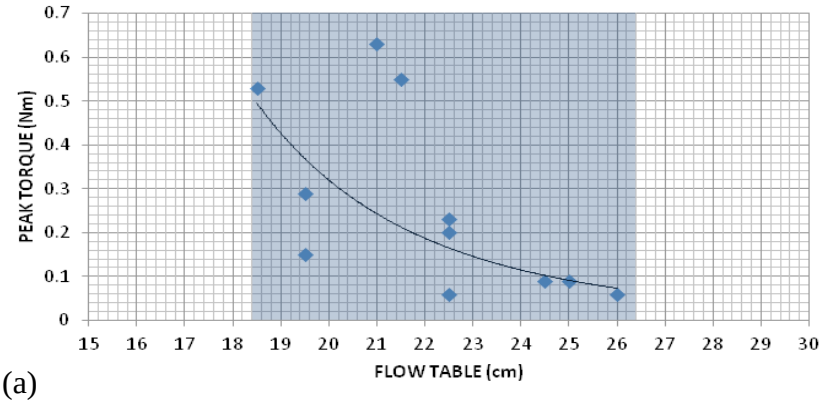

(a)

(b)

Figure 1. (a) Peak torque versus flow table values and (b) Buildability of different mixtures.

References

[1] A. Kazemian, X. Yuan, E. Cochran and B. Khoshnevis (2017). Cementitious materials for construction-scale 3D printing: Laboratory testing of fresh printing mixture, *Constr. Build. Mat.*, **145**, 639-647.

[2] Z. Malaeb, H. Hachem, A. Tourbah, T. Maalouf, N. El Zarwi and F. Hamzeh (2015). 3D Concrete Printing: Machine and Mix Design, *Int. J. Civil. Eng.and Tech*, **6(6)**, 14-22.

In memory of Professor
Pericles S. Theocaris

ON THE QUEST OF PROPER FORMING OF FAILURE CRITERIA

N. P. Andrianopoulos
National Technical University of Athens, School of Applied Mathematical and Physical Sciences, Dept. of Mechanics, Laboratory of Testing and Materials, Theocaris Bld., Zografou, 157 73, Greece

1. General

A few comments are presented concerning the desired properties of a criterion of failure of materials. These comments may be proven useful for an improved prediction of critical behavior of structural members. An easy and common approach is to perform a series of experiments for various loading systems (and perhaps specimen geometries) and plot critical failure points in a suitable "space" of stresses, strains etc. Then an interpolation function can be obtained to serve as "failure criterion" for the material. This is by no means enough or, even, permittable. For a given range of experimental critical points, numerical interpolation usually results in many almost equivalent equations, which may divert considerably outside the range of experimental points (definition domain). Which equation is the correct outside the initial domain? To choose one of them we must perform a, let say, *conceptional extrapolation* [1].

2. Deductive versus inductive approach in explaining natural phenomena

In our *deterministic* Newtonian world an order/explanation to phenomena must be put by either: (a) introducing an axiomatic hypothesis governing a class of them and concluding, in a *deductive* manner (top down), their observed behavior or (b) comparing many similar cases to locate behavioral similarities allowing for the extraction of a rule in an *inductive* way (down top). Both methods are almost equivalent but in case of induction it is not clear whether or not *causality* is satisfied. All measured parameters may not play role in the phenomenon, being in fact side-effects. A dilemma concerning the "*space*" of description of the experimental data arises, namely the selection of parameters causally connected, the remaining being simply "present". A classic example of a wrong "space" is fatigue where a purely linear elastic parameter (stress intensity factor K_I) is used to describe a purely nonlinear elastic/plastic phenomenon. Causality and proper space are vital to exclude irrelevant *Correlation* "incidents".

On the other hand, deductive approaches fail to predict *exactly* experimental results, showing, however, an acceptable agreement with them. In any case, they are free from the dangerous and unpredictable conceptual extrapolation and, with a proper safety factor, can cover a wide range (if not all) of similar phenomena. In other words, deductive approaches serve as the thin main line passing smoothly through experimental data. This way, axiomatic-deductive approaches can be considered as "*Laws*", although inductive-conclusive ones may be called "*Rules*".

3. A typical example: The constitutive equations

The space of description of a class of similar phenomena may be wrong but, also, it may be "*incomplete*". The dimensions of such spaces are fewer than the number of independent physical parameters being causally involved. Constitutive equations are a typical example. Namely, equivalent von Mises stress-strain curves are used to characterize the mechanical behavior of a material, the area under this curve representing the strain energy density (SED) stored into the material. Under equal hydrostatic pressure this area is zero, although SED is, obviously, stored into the material. Thus, a second constitutive equation is required, connecting pressure with volume expansion as shown in Fig.1 for the completeness of space. There, the two experimental constitutive equations are plotted for a mild steel. Areas in red mark the available strain energy density for distortion (SED_D) and for dilatation (SED_V), respectively.

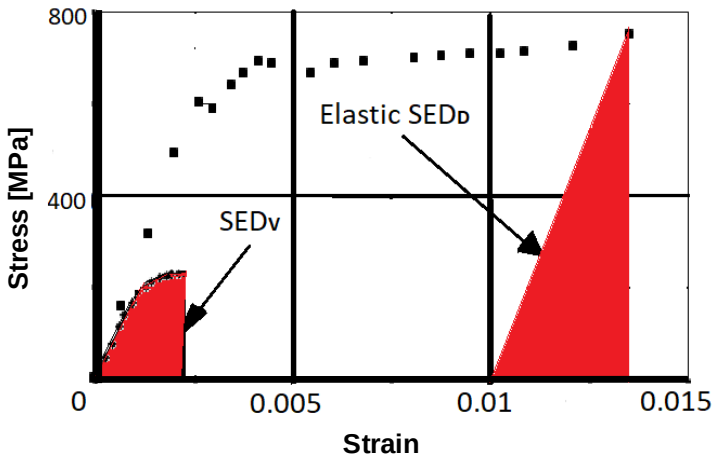

Figure 1. The two constitutive equations (σ_{eq}-ε_{eq} and p-Θ) for a typical mild steel. Areas in red represent SED_V for volume and SED_D for shape changes.

4. Discussion and conclusions

At this point some conclusions are worth: (1) It is desirable for failure criteria to be based on *all* stresses and strains, i.e. strain energy density SED. (2) Causality demands the presence of an *available cause* for failure, namely *elastic* SED. (3) Plastic work is elastic SED already transformed to "work". So, plastic work is a result not a cause of failure. It is an un-integrated failure. (4) Cracks and other geometrical singularities must solely be understood as modulators of the stress/strain fields and nothing more. Thus, it is not clear to us the distinction between criteria suitable for either "Fracture Mechanics" or "Strength of Materials". (5) The reaction of a material to external loads is *geometrical*, materialized through shape and/or volume changes implying that a distinction must be made between SED for distortion (say SED_D) and for volume changes (say SED_V).

An example of independent action of SED_D and SED_V is the classical "cup-cone" mixed failure of a cylindrical ductile specimen under tension where failure starts as brittle cleavage (SED_V dominance) in the core of the specimen and integrates as plastic collapse (SED_D dominance) according to the varying geometry of the specimen, i.e. the varying ratio of (normal/shear) stresses and strains. So, the behavior of SED_D and SED_V is independent to each-other (competitive) and the physical meaning of the algebraic sum SED_D+SED_V is questionable.

The as above comments drove to the introduction of the so-called T-criterion which resulted in satisfactory predictions in linear isotropic [2, 3] or anisotropic [4] and non-linear elastoplastic [5] materials under static, dynamic [6] and fatigue [7] loads.

References

[1] P. S. Theocaris (1989). Variations on a theme of fracture criteria, *Engng. Fract. Mech*., **33**, 205-214.
[2] P. S. Theocaris and N. P. Andrianopoulos (1982). The Mises elastic-plastic boundary as the core region in fracture criteria, *Engng. Fract. Mech*., **16**, 425-432.
[3] N. P. Andrianopoulos and P. S.Theocaris (1985). The Griffith-Orowan fracture theory revisited: The T-criterion, *Int. J. Mech. Sciences*, **27**, 793-801.
[4] N. P. Andrianopoulos and I. T. Dernikas (2013). An attempt to separate elastic strain energy density of linear elastic anisotropic materials based on strains considerations, *Acta Mechanica*, **224**, 1879-1885.
[5] N. P. Andrianopoulos and V. M. Manolopoulos (2012). Can Coulomb criterion be generalized in case of ductile materials? An application to Bridgman experiments, *Inter. J. of Mech. Sciences*, **54**, 241-248.
[6] P. S. Theocaris, N. P. Andrianopoulos and S. K. Kourkoulis (1992). The "Twin-Crack" model and the T-criterion in predicting dynamic instability for asymmetric cracks, *Engng. Fract. Mech*., **43**, 137-146.
[7] N. P. Andrianopoulos and A. Pikrakis (2017). On the effect of hydrostatic stress on fatigue crack propagation, *International Journal of Structural Integrity*, **8**, 240-255.

THE OPTICAL METHOD OF CAUSTICS IN THE LAST 50 YEARS

G. A. Papadopoulos
National Technical University of Athens, Department of Mechanics,
Laboratory for Testing and Materials, Zografou campus, GR-157 73, Athens, Greece

1. Introduction

The experimental method of transmitted caustics was developed first by Manogg [1] while, the experimental method of reflected caustics was developed by Theocaris [2]. It is based on the laws of geometrical optics and transforms the stress singularity into an optical singularity. This optical singularity provides valuable information for the respective stress field. According to the method of caustics, a coherent light beam from a laser impinges normally on the specimen in the vicinity of the crack tip, and the reflected rays are received on a reference screen at some distance from the specimen. When a certain load is applied to the specimen the reflected light rays in the vicinity of the crack tip (where an abrupt thickness variation appears due to the existence of a singularity) are scattered and when projected on a reference screen placed at some distance from the specimen are concentrated along a curve, the so-called caustic [3]. The method of reflected caustics, as it has been developed during the last fifty years, was extensively applied to various elastic problems containing singularities and especially to problems with cracked plates made of either isotropic or birefringent materials, to contact problems, and to problems of multi-wedges (composite materials) by Theocaris and coworkers [4-6]. The method of caustics works equally well in elastic problems with any type of stress concentration, not necessarily including singularities. In such cases the caustic is generated from a deformed boundary instead of a singular curve in the interior of the specimen (initial curve). For these applications the reader is referred to the review paper of ref. [7].

2. The method of reflected caustics

The optical method of caustics transforms the stress singularity into an optical singularity, using the reflection laws of geometric. For divergent light beam the reflected light rays from the front (f) and the rear (r) faces of the plate form two caustics, the (f) and (r) caustics, respectively. For a cracked isotropic elastic specimen, the parametric equations of the two caustics are [2, 3]:

$$X_{r,f} = \lambda_m r_o(\cos\theta \pm \frac{2}{3}\cos\frac{3\theta}{2}), \quad Y_{r,f} = \lambda_m r_o(\sin\theta \pm \frac{2}{3}\sin\frac{3\theta}{2}) \tag{1}$$

where r_o is the radius of initial curve of the caustics. This radius is given as:

$$r_o = \left(\frac{3}{2}C_{r,f}\right)^{2/5},\ C_{r,f} = \frac{\varepsilon z_o d c_{r,f} K_I}{\lambda_m\sqrt{2\pi}},\ \lambda_m = \frac{z_o \pm z_i}{z_i} \tag{2}$$

z_o is the distance between the specimen and the reference plane, d the specimen's thickness, λ_m the magnification ratio of the experimental set-up, z_i the distance between the specimen and the light beam focus, and K_I the mode-I stress intensity factor. It holds that $\varepsilon=2$ for the (r) caustic and $\varepsilon=1$for the (f) one. Finally, c_r, c_f are the material's stress-optical constants. It holds that $c_f=\nu/E$ (ν is Poisson's ratio and E is Young's modulus). The experimental stress intensity factor K_I is estimated as [2, 3]:

$$K_I = \frac{2\sqrt{2\pi}}{3\varepsilon z_o d\lambda_m^{3/2} c_{r,f}}\left(\frac{D_{t,l}}{\delta_{t,l}}\right)^{5/2} = 1.67C\left(\frac{D_{t,l}}{\delta_{t,l}}\right)^{5/2},\ C = \frac{1}{\varepsilon z_o d\lambda_m^{3/2} c_{r,f}} \tag{3}$$

where $D_{t,l}$ are the maximum diameters of the caustics (D_t is the transverse one and D_l the longitudinal one) and $\delta_{t,l}$ are correction factors with $\delta_t=3.1702$ and $\delta_l=3.00$. As it can be seen from

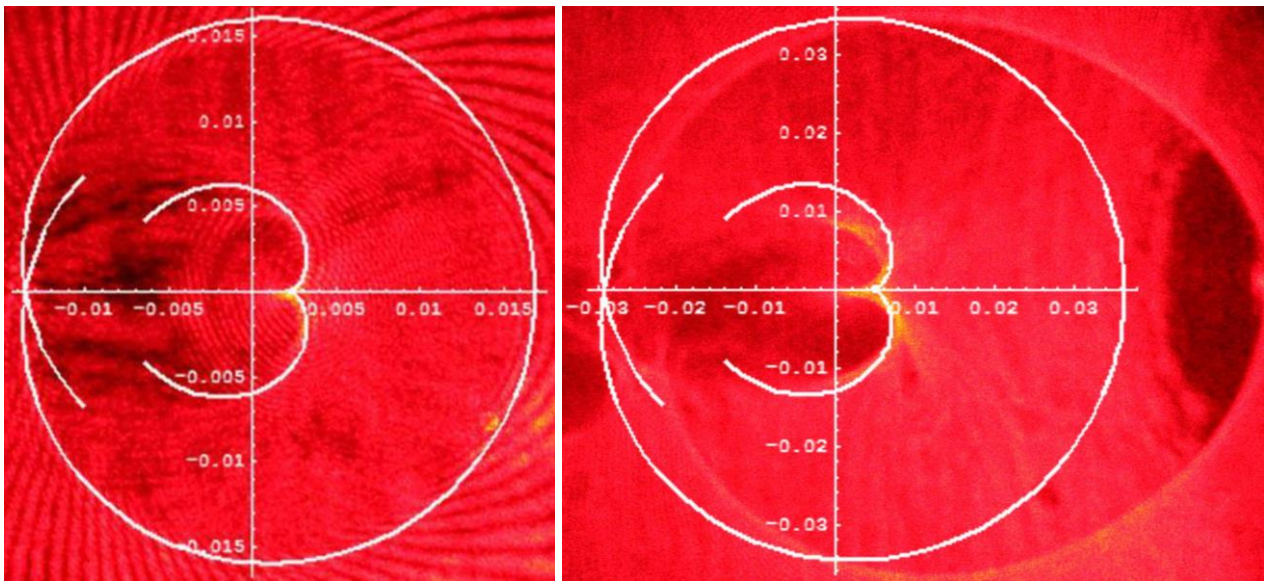

Figure 1. Experimental and theoretical caustics in Lexan (PCBA) specimens for a stress level equal to σ=2.42 MPa and crack length (a) α=2.8 cm and (b) α=6.9 cm.

Fig.1, where theoretical and experimental caustics are presented, their shape is almost elliptic. As a result, their area (A) can be, also, used for the experimental estimation of the stress intensity factor K_I instead of their diameters as follows [8]:

$$K_I=0.1358CA^{5/4},\ C=\frac{1}{\varepsilon z_o d\lambda_m^{3/2}c_{r,f}} \qquad (4)$$

3. Future applications

The method of caustics (both transmitted and reflected) is nowadays widely applied for the solution of various engineering problems worldwide. For example, it was recently applied for the estimation of the stress intensity factor in cracked marble specimens using the so called parallel-springs model (Fig.2), described in details in the extended version of the manuscript and also in ref. [9].

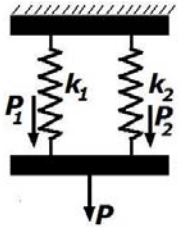

Figure 2. Parallel-springs model.

References

[1] P. Manogg (1964). Anwendung der Schattenoptik zur Untersuchung des Zerreissvorgangs von Platten, *Dissertation 4/64*, Universitaet Freiburg, Germany.
[2] P. S. Theocaris (1970). Local Yielding Around a Crack-Tip in Plexiglas, *Journal of Applied Mechanics, Trans. ASME*, **37**, 409-415.
[3] G. A. Papadopoulos (1993). Fracture mechanics: The experimental method of caustics and the Det.-criterion of fracture, Springer-Verlag, London.
[4] P. S. Theocaris and E. E. Gdoutos (1972). An optical method for determining opening-mode and edge sliding-mode stress intensity factors, *Journal of Applied Mechanics, Trans. ASME*, **39**, 91-97.
[5] P. S. Theocaris and G. A. Papadopoulos (1981). Stress intensity factor from reflected caustics in bire-fringent plates with crack, *Journal of Strain Analysis*, **16**, 29-36.
[6] P. S. Theocaris (1981). Elastic stress intensity factors evaluated by caustics, in *Mechanics of Fracture*, (ed. G. C. Sih), Martinus Nijhoff Publishers, **7**, 189-252.
[7] P. S. Theocaris (1978). The method of caustics applied to elastic problems, in *Developments of stress analysis-1*, (ed. G. Holister), Applied Sciences Publishers, London, England, Chapt. 2: 27-63.
[8] G. A. Papadopoulos (2011). New Formula of experimental stress intensity factor evaluation by caustics, *Intrnational Journal of Fracture*, **171**, 79-84.
[9] J. Generalis (2018). A study of the stress intensity factors in metal and marbles by the method of caustics (in Greek), Postgraduate Diploma Thesis, NTUA, Athens, Greece.

CONTACT LENGTH IN DISCS AND RINGS BY REFLECTED CAUSTICS METHOD

Ch. F. Markides
Laboratory for Testing and Materials, Department of Mechanics, School of Applied Mathematical and Physical Sciences, National Technical University of Athens, 157 73, Athens, Greece

1. Introduction

Caustics are for over a half century a well-known experimental method most noted for its effectiveness in numerous engineering applications, as the study of static and dynamic stress intensity around cracks, impact, contact and fatigue problems, concerning isotropic, anisotropic or even graded and composite materials. Introduced by Manogg [1] as transmitted ones then extended by Theocaris [2] to the reflected caustics, the technique is still in use [3] due to its high sensitivity and accuracy in detecting the slightest stress/strain gradients on the tested specimen. Easy to use, it requires a He-Ne laser, two lenses, a semi-reflector, a reference screen, a (high-speed) camera and a face-polished specimen regarding the reflected caustics studied here (Fig.1). Namely, red light emerging from the laser tube, opens through a pin hole, becomes a bundle of parallel rays passing through the first lens, closes with the aid of the second lens and directed through the semi-reflector impinges on the specimen as a divergent (here) bundle with its focus in front of the specimen (Fig.2). Then, the reflected light from the front or even back face of the specimen impinges onto the semi-reflector, reflected further on the reference screen on which is photographed; light from areas of strong specimen thickness, the so-called initial curves, due geometric singularities, contact etc., received on the screen on strongly illuminated curves the caustics. Constructing the parametric equations of caustics, correlating their features (e.g., diameters) with critical characteristics of the stress field, one has just to insert the experimental measurements into the theoretic equations in order to obtain the stress intensity, the contact length etc. In the present study, the classic equations of initial curves and caustics [4], improved by taking into account also the in plane deformation [5], are considered determining the contact length in the Brazilian disc-test (or the ring-test) as standardized by the International Society for Rock Mechanics (ISRM) [6] (Fig.3).

Figure 1. Reflected caustics' experimental set-up.

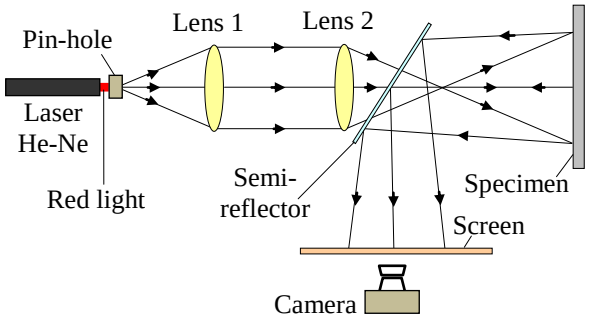

Figure 2. Sketch of experimental procedure.

2. Experimental protocol and results

Intact and circularly perforated cylindrical discs of radius R= 50 mm and thickness 10 mm made of plexiglass were tested. Preliminary uniaxial tension tests with orthogonal plates (250 x 20 x 2 mm^3) of the same batch of material yield E=3.2 GPa and ν=0.38, resulting to an optical constant c_f=1.18x10^{-10} m^2/N, required for reflected caustics formulae [4,5]. The specimens were squeezed between the curved ISRM's jaws mounted at an electromechanical INSTRON 1125 loading frame of 50 kN capacity. With the lower jaw fixed, the upper jaw compressed the cylinders under a displacement control mode at a rate of 0.1 mm/min. For the intact discs the overall applied load reached a level of 40 kN inducing a tensile stress of about 25 MPa at the disc's centre, below the yield stress of

the material, while for the ring-shaped ones (of internal radius 0.4R) the load was 5 kN, ensuring that the linearity limit is not exceeded. In both cases the contact length generated between the disc/ring and the ISRM's jaw was measured using the caustics method, by introducing the experimentally measured characteristic distance $2W_{x'}$ (Fig.4) into the appropriate formula [4, 5]. In this context, the initial curves, the respective caustics and the corresponding contact lengths between the uniform disc and the ISRM jaw are shown for three different load levels in Fig.5; initial curve's splitting tendency for increasing loading requires further investigation.

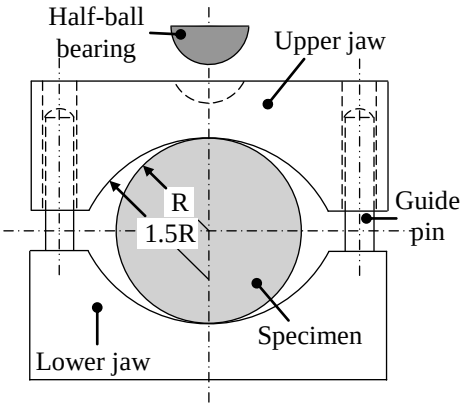

Figure 3. ISRM's apparatus.

3. Discussion

The contact length between a disc/ring and the curved jaw of the ISRM's apparatus for the implementation of the Brazilian-disc test was obtained by the method of caustics. Though one of the oldest optical methods, caustics were [7,8] and still are open to discussion, further improvement and standardization, in order to become the powerful tool required by researchers demanding the highest accuracy and effectiveness in their experimental and analytical results.

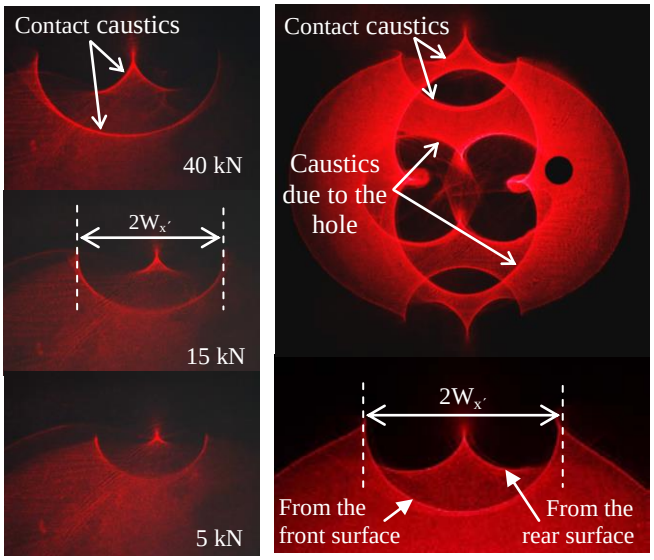

Figure 4. Intact disc (left) and ring (right).

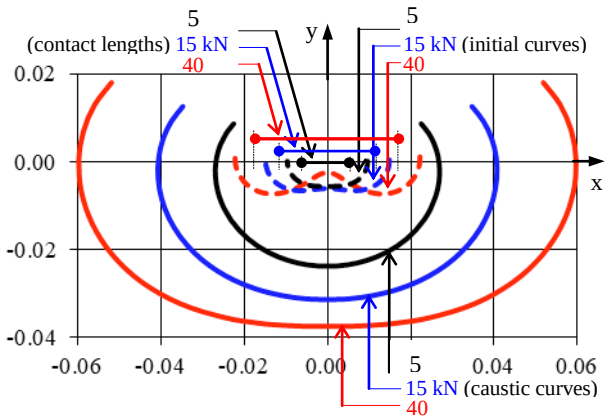

Figure 5. Contact length (intact disc).

References

[1] P. Manogg (1964). Schattenoptische Messung der spezifischen Bruchenergie waehrend des Bruchvorgangs bei Plexiglas, in *Proceedings of the International Conference on Physics of Noncrystalline Solids*, J. A. Prins, (ed), Delft, The Netherlands, 481-490.

[2] P. S. Theocaris (1970). Local yielding around a crack-tip in plexiglas, *J. Appl. Mech.*, **37**, 409-415.

[3] G. A. Papadopoulos (2011). New formula of experimental stress intensity factor evaluation by caustics, *Int. J. Fract.*, **171**, 79-84.

[4] P. S. Theocaris and C. A. Stassinakis (1978). The elastic contact of two disks by the method of caustics, *Exp. Mech*., **18(11)**, 409-415.

[5] Ch. F. Markides and S. K. Kourkoulis (2013). Revisiting the reflected caustics method: The accurate shape of the "initial curve", *Engng. Trans.*, **61(4)**, 265-287.

[6] ISRM (1978). Suggested methods for determining tensile strength of rock materials, *Int. J.. Rock Mech. Min. Sci*., **15(3)**, 99-103.

[7] P. S. Theocaris and C. Razem (1981). Error analysis in evaluating SIFs by reflected caustics, *Int. J. Mech. Sci.*, **23**, 275-284.

[8] A. J. Rosakis and A. T. Zehnder (1985). On the method of caustics: An exact analysis based on geometrical optics, *J. Elasticity*, **15**, 347-367.

RECENT ADVANCES IN STRUCTURAL HEALTH MONITORING OF RESTORED ELEMENTS OF MARBLE MONUMENTS

S. K. Kourkoulis
National Technical University of Athens, School of Applied Mathematical and Physical Sciences,
Department of Mechanics, Laboratory for Testing and Materials,
Theocaris Building, Zografou Campus, 157 73, Greece

1. Introduction

The mechanical response of restored structural members to external excitations, at load levels close to those causing failure, is among the critical issues confronted by engineers working in projects related to the restoration and conservation of ancient monuments of classical cultural heritage. The specific issue is just another aspect of the classical question related to the remaining load carrying capacity of any structural element, and constitutes the very heart of Fracture Mechanics in case the element is already cracked or notched, as it happens with restored elements of ancient marble monuments. Alternatively, the question can be formulated as follows: *Is it possible to predict the instant at which a pre-existing defect, either in the form of a crack or a notch, is going to start propagating leading the structural member to catastrophic failure*? In general, the answer is negative, due to quite a few practical restrictions of the restoration praxis, which make the problem extremely complicated. Indeed, the actual load level induced on a monument's structural member is not a-priori known, rendering application of standard crack initiation criteria impossible, while, on the other hand, the building materials of ancient marble monuments is usually characterized by inhomogeneity and anisotropy. As a result, restored members should be continuously monitored in the direction of detecting even the slightest changes in the status of their internal damage.

2. Structural Health Monitoring (SHM) of restored elements of ancient marble monuments

Most ancient Greek temples were constructed using natural building stones, usually quarried from the near vicinity of the place of the temple. The monuments of the Acropolis of Athens were an exception of the above rule: they were built using marble quarried from mount Pentelicus, almost 30 km away from the Acropolis hill. It is a fine-grained white marble consisting of calcite (~98%) and very small amounts of muscovite, sericite, quartz and chlorite. Pentelic marble is characterized by bimodularity, slight nonlinearity and anisotropy, usually modelled as transverse isotropy [1]. Given that quite a few structural elements of these monuments are damaged, an ambitious, world-wide renowned, restoration project is implemented by the "*Acropolis Restoration Service*".

The technique, nowadays adopted, for restoring fragmented members of the Acropolis monuments (in-situ developed by the scientific personnel of the project) is based, in principle, on the use of titanium elements, placed either in holes drilled in the marble body or in grooves sculptured on their surface. Holes and grooves are then filled with a cement-based material [2]. The specific approach generates a three-material complex (marble-cement-titanium) with two interfaces (marble-to-cement and cement-to-titanium). Recent studies revealed that damage mechanisms are firstly activated along these interfaces [3]. As a result, monitoring the status of restored elements needs data from these "hidden" interfaces. Moreover, the data required must be obtained with the aid of reliable, inexpensive and very small sensors that safeguard the aesthetic splendor of the monuments.

In the direction of somehow contributing to the solution of these open problems, series of experimental protocols are implemented in the Laboratory for Testing and Materials of the National Technical University of Athens. During the implementation of these protocols both traditional and innovative sensing techniques are used in a combined manner, in order to properly calibrate the outcomes of the novel techniques, given that in most cases the data provided by them are of qualitative rather than quantitative nature.

As an example, results from two ongoing projects, related to monitoring the response of marble elements, are here discussed. In both projects, the state of the specimens is monitored using the Acoustic Emission (AE) technique in combination with that of Pressure Stimulated Currents (PSC) [4]. The first protocol describes the damage accumulation in prismatic notched marble specimens under 3-point bending. Characteristic results are plotted in Fig.1a, in which the normalized value of the electric currents (PSC) and the Ib-value of the AEs are plotted versus the (t_f-t) parameter (i.e., according to an inverse time arrow, in an attempt to enlighten the very last loading steps) in logarithmic scale. It is seen that almost ten seconds before fracture the PSC plot exhibits a characteristic slope change while at exactly the same time instant, the Ib-value of the AEs starts decreasing to values lower than 1, a behaviour designating entrance of the system (specimen) to its "critical stage".

The second protocol deals with the pull-out phenomenon, i.e., the gradual or abrupt detachment of the reinforcing bars from the marble body. Results of this protocol, regarding the time evolution of the axial force induced and that of the PSC recorded, are shown in Fig.1b. It is observed that well before the load drop (corresponding to the onset of relative slip of the bar with respect to marble) the PSC exhibits an abrupt change that can be considered as a well distinguishable pre-failure sign.

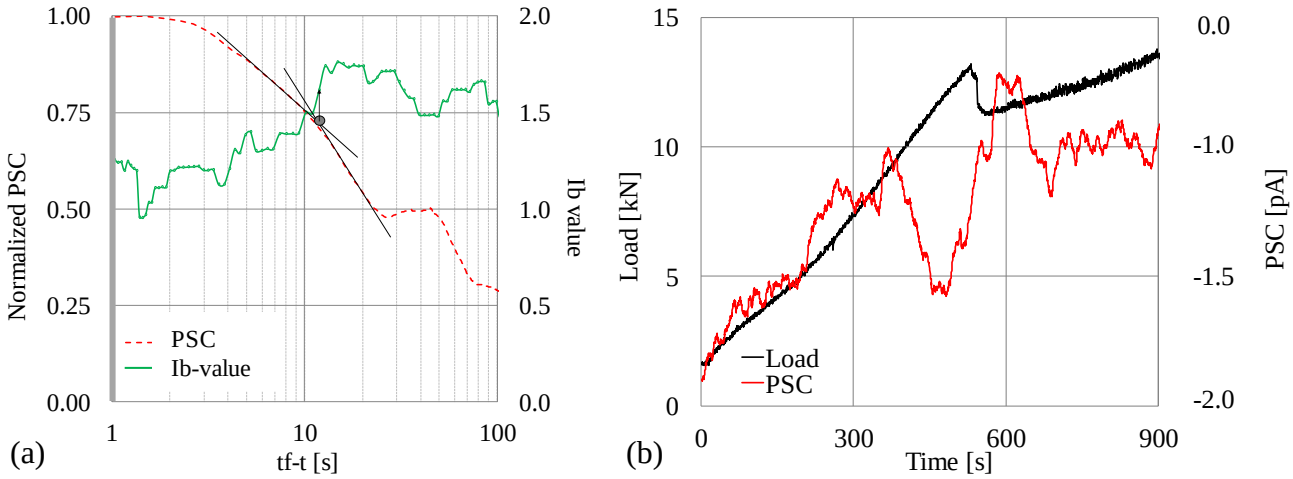

Figure 1. (a) The PSC and the Ib-value versus the (t_f-t) parameter in a 3-point bending test; (b) The time evolution of the PSC and the load induced during a pull-out test.

3. Concluding remarks

The conclusions drawn from the above protocols, and also from additional ones in progress [5], indicate that the data of the AE- and PSC-techniques are in good mutual agreement. Moreover, it is shown that both techniques provide early signs concerning the entrance of the system to its "critical stage", i.e., warnings of upcoming failure. Taking into account this agreement, the fact that the AE technique is nowadays considered a mature sensing system (and, thus, a reliable calibration tool for the PSC technique) and finally the low cost and small size of the PSC sensors, it appears that the latter could become a very attractive alternative for SHM of restored elements of ancient monuments.

References

[1] S. K. Kourkoulis, G. E. Exadaktylos and I. Vardoulakis (1999). U-notched Dionysos-Pentelicon marble in 3-point bending: The effect of nonlinearity, anisotropy and microstructure, *Int. J. Fract.*, **98**, 369-92.
[2] M. Korres and Ch. Bouras (1983). *Study for the Parthenon's restoration*. Athens: Ministry of Culture.
[3] S. K. Kourkoulis and E. D. Pasiou (2015). Interconnected epistyles of marble monuments under axial loads, *Int. J. Architectural Heritage*, **9(3)**,177-194.
[4] D. Triantis, I. Stavrakas, A. Kyriazopoulos, G. Hloupis and Z. Agioutantis (2012). Pressure stimulated electrical emissions from cement mortar used as failure predictors, *Int. J. Fract.*, **175**, 53-61.
[5] S. K. Kourkoulis, I. Dakanali, E. D. Pasiou, I. Stavrakas and D. Triantis (2017). Acoustic Emissions versus PSCs during bending of restored marble epistyles: Preliminary results, *Fract. Struct. Integrity*, **41**, 536-551.

Environmental Aspects

EXPERIMENTAL ANALYSIS OF WATER SALINITY IMPACT ON THE ENERGY CONSUMPTION OF SMALL DESALINATION PLANTS

K. Christopoulos[1], N. Pospotikis[1], Em. Kostopoulos[1], E. Kondili[2] and J. K. Kaldellis[1]
[1]Soft Energy Applications & Environmental Protection Laboratory,
Piraeus University of Applied Sciences, Athens, Greece
[2]Optimization of Production Systems Laboratory, Mechanical Engineering Department,
Piraeus University of Applied Sciences, Athens, Greece

1. Introduction

Water shortage has emerged as one of the most crucial resources problem, especially in areas with specific geographical characteristics, e.g. island regions. The general problem of clean water shortage is gradually increasing, as economic growth, irrigation needs, declining precipitation levels and overexploitation of groundwater are factors that increase the water balance deficit. One of the most popular solutions in order to face the water shortage is the sea water desalination.

Among the various desalination technologies reverse osmosis is a challenging alternative, exhibiting very attractive characteristics, like the small area demand, the modularity, the insignificant - compared to other technologies- environmental impacts, providing several advantages and being available for a wide range of water demand values. In Fig.1 it is obvious that reverse osmosis technology has clearly surpassed the rest desalination technologies over the last 20 years.

The vast majority of remote Greek islands faces a severe water shortage problem, especially during summer [2]. In order to solve this problem the idea of developing reverse osmosis desalination plants has been vastly adopted by the regional authorities providing very high quality of clean water and securing the supply especially during periods of high demand. However, one of the major problems arising when implementing this solution, on top of the well known environmental impacts, is the significant energy consumption of the desalination units.

2. The experimental protocol

In order to examine the real energy consumption of small desalination units, the experimental installation of the Soft Energy Applications & Environmental Protection Laboratory (SEA & ENVIPRO Lab) is used. This specific desalination unit (Fig.2) has been funded by the Piraeus University of Applied Science (PUAS) in the context of Excellence-II (Aristia) research program of General Secretariat of Research and Technology (GSRT) and can be used in order to measure the real elec-

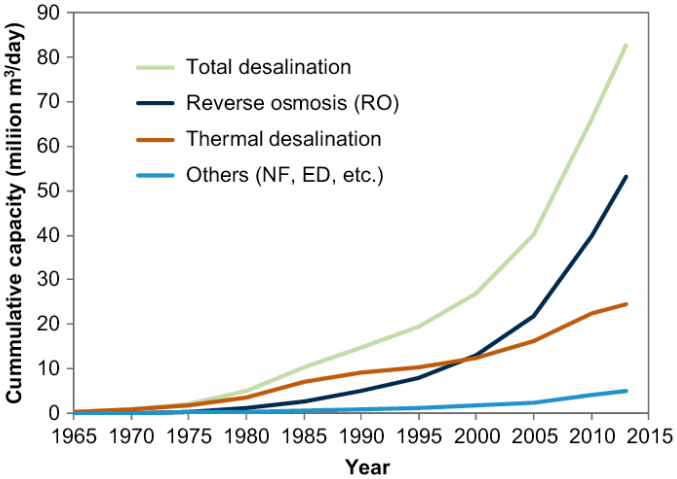

Figure 1. Cumulative installed worldwide desalination capacity in terms of applied technology [1].

Figure 2. Small experimental desalination unit.

tricity consumption of a small desalination unit at different water salinity values and variable operational conditions.

In this context the current work investigates the power demand (kW) and the specific energy consumption per unit volume of desalinated water (kWh/m^3) produced for variable operational conditions of the installation (e.g. variable pressure of feed pump). Moreover, the impact of water salinity (using realistic values concerning the sea water salinity) has been examined and the corresponding specific energy consumption is estimated.

3. Results and conclusions

According to the preliminary indicative (for water salinity equal to 55600 μS) results obtained, the curve in Fig.3 represents a significant and almost linear power demand increase from 2.5 to 3.1 kW$_e$ while the feed pump pressure increases from 45 bar to 60 bar.

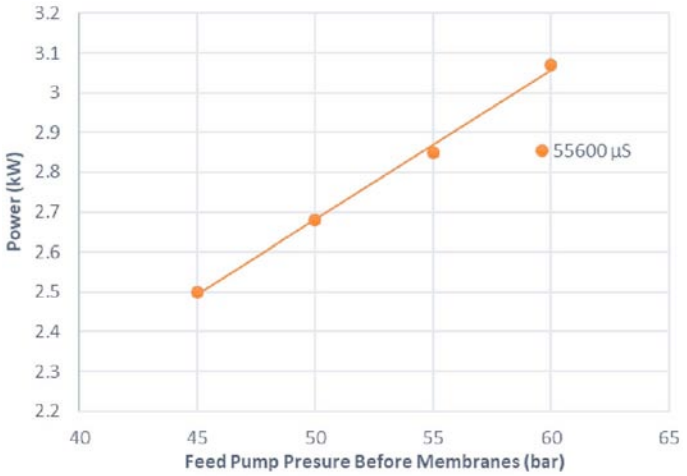

Figure 3. Feed water pressure impact on the desalination unit power demand.

It is also very interesting to estimate the corresponding electrical energy consumption per m^3 of desalinated (clean) water production given in Fig.4. According to the measurements taken a gradual energy consumption decrease is encountered vs. the clean water production, while the values obtained are relatively high (i.e. ranging between 10 and 25 kWh$_e$/m^3) for various reasons, including the small size of the installation and the absence of energy recovery procedure.

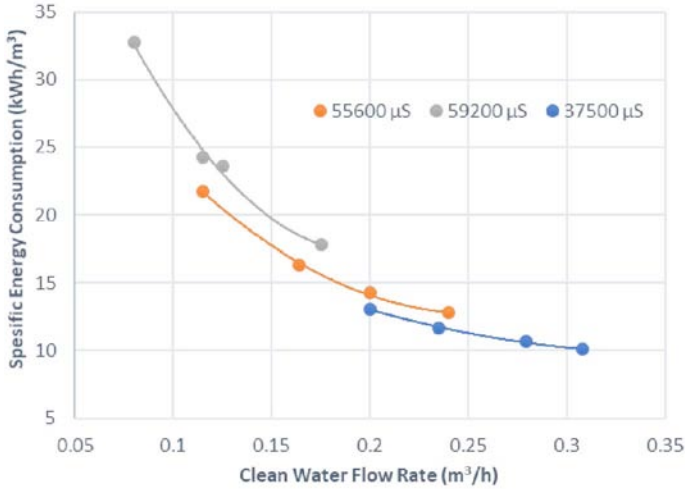

Figure 4. Specific energy consumption variation with the clean water volume flow rate.

Finally, the corresponding energy demand is related with the necessary energy production of the existing hybrid power station (based on a wind turbine and a photovoltaic generator) in order to underline the opportunity of covering the water demand problems of remote Greek islands on the basis of clean-green energy production technologies.

References

[1] L. O. Villacorte, S. A. A. Tabatabai, N. Dhakal, G. Amy, J. C. Schippers and M. D. Kennedy (2014). Algal blooms: an emerging threat to seawater reverse osmosis desalination, *Journal of Desalination and Water Treatment*, **55**, 2601-2611.

[2] J. K. Kaldellis, K. A. Kavadias and E. Kondili (2004). Renewable energy desalination plants for the Greek islands, technical and economic considerations, *Desalination Journal*, **170(2)**, 187-203.

ORBAN GUN BALLISTICS AND ASSESSMENT OF HISTORICAL EVIDENCE CONCERNING THE BOMBARDMENT OF CONSTANTINOPLE WALLS IN 1453

***A. Kakaliagos*[1] *and N. Ninis*[2]**
[1] *Senior Structural Engineer, Consultant*
[2] *Civil Engineer, Greek Ministry of Culture and Sports, Athens, Greece*

1. Introduction

In this paper, the bombardment of the Constantinople Theodosian Walls by the great cannon of Orban is treated as a full scale experiment and is numerically reproduced deploying Structural Mechanics. A scenario has been selected in order to check Orban's gun bombarding effect on Constantinople Inner Walls on April 24, 1453 [1]. Overall gun dimensions were assessed based on historical reports, whereby, the gunpowder charge p was estimated at 177 kg (Fig.1) [2, 3, 4]. The gun was placed at a distance of 500 m from the Inner Walls, outside the range of Justinianni's Genoese Crossbowen, which was estimated at 400 yards from the Outer Wall ramparts (Fig.2a).

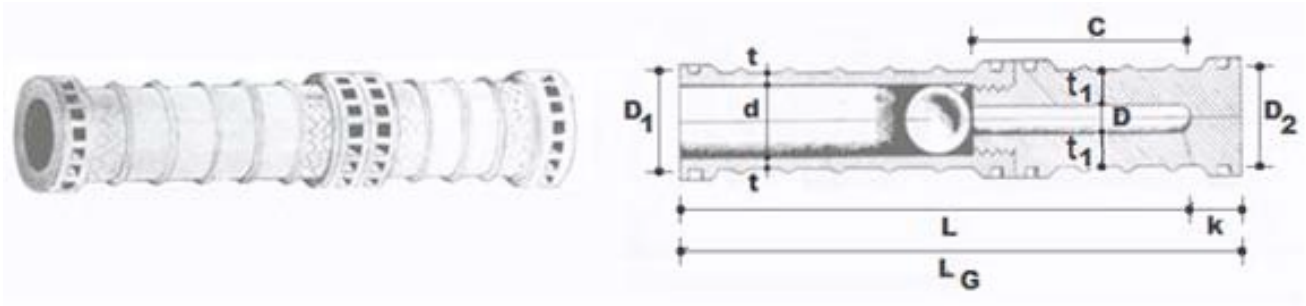

L_G	L	c	B	p	d	D	D_1	D_2	t	t_1	k
[mm]	[mm]	[mm]	[kg]	[kg]	[mm]	[mm]	[mm]	[mm]	[mm]	[mm]	[mm]
9200	8552	2752	600	117	752	248	1152	1544	200	648	648

Figure 1. Schematic representation of Orban's Bombard and numerical values of its geometrical parameters.

2. The analytical model

An analytical model was developed for muzzle velocity in units m/sec (Eq.(1)). Herein, R is a factor to consider the efffect of hot gunpowder expanding gases after ignition inside the gunpowder chamber [5, 6]. This factor captures the initial ratio of gunpowder chamber hot gas pressure to atmospheric pressure, with the atmospheric pressure set at 101.3 kPa. The dimensionless factor ψ equals 6.13 for granite cannon balls.

$$v = 26\sqrt{\frac{R}{\frac{\alpha}{\beta}\psi\lambda^2+1}\ln\alpha},\ \text{where}\ \alpha=\frac{L}{c},\ \lambda=\frac{d}{D}\ \text{and}\ \beta=\frac{L}{d}\ (\text{gun caliber}) \quad (1)$$

Considering the gun chamber as thick cylinder under internal pressure with R set at 1000, the von Mises combined stress at the intersection of gunpowder chamber internal surface to cannon breech yields 210 MPa. This result is relatively close to typical bronze yield and tensile strength at 220 MPa and 240 MPa, respectively. Consequently, the rise of atmospheric pressure in the gun powder chamber could be set at a maximum value of R equal to 1000 approximately. Based on the

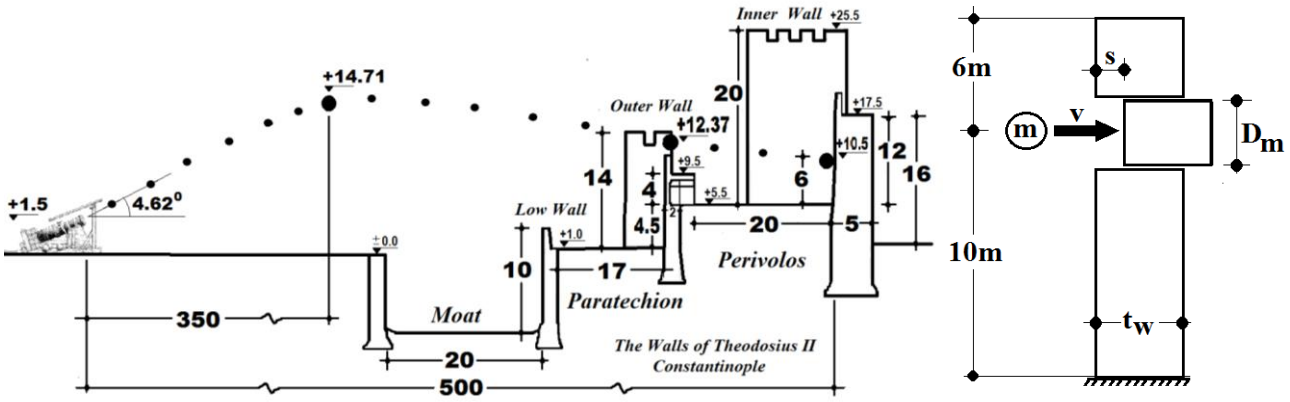

(a) (b)

Figure 2. Bombardment of the Inner Walls:
(a) Cannonball trajectory; (b) Punching shear cylinder.

above muzzle velocity was subsonic at 216 m/sec. The cannonball trajectory after leaving the barrel was expressed by Newton's equations of motion. Given the muzzle velocity, the initial position of the gun and the inclination of the barrel, the trajectory of the cannonball has been evaluated numerically, using a linear step by step numerical procedure with a time integration step of 0.001 s. It was assumed that the projectile would impose a punching shear failure mechanism into the Inner Wall masonry. Considering energy equilibrium during cannonball impact on the wall, analytical expressions were produced to calculate the required setback s of punching shear cylinder (Fig.2b). This setback s is function of cannonball weight B, acceleration of gravity g, impact velocity v and initial punching shear resistance V_m.

3. Results and discussion

It was calculated, that the first shot delivered a required setback s at 1.67 m, whereby, the second shot created a breach in the wall. With wall collapse triggered after the second shot due to wall punching shear failure, the length of the breach measured from the ramparts was equal to 8.88 m and confirmed historical reports for a total length of the breach at 5 fathoms (9.15 m) [5]. Additionally, the cannon ball penetration into soil was evaluated.

Finally, a numerical effort was made to assess the sound pressure level inside Constantinople during bombardment. The peak blast overpressure corresponding to the rise of atmospheric pressure inside the gun was converted to an equivalent sound pressure measured in dB. The resulting sound pressure at St. Romanus Gate and at the Mesotechion portion of the Theodosian Walls was at 120 dB. Based on this result the tremendous psychological effect of the Cannon's blast on the City's population, mentioned in historical records, is confirmed [2, 7].

References

[1] N. Iskanter (1998). *The Tale of Constantinople of its Origin and Capture by the Turks in the Year 1453,* W. K. Hanak and M. Philippides (eds.), A. D. Caratzas, Athens, Greece.
[2] P. V. Nicolò Barbaro (1856). *Giornale dell'assedio di Costantinopoli 1453, corredato di note e documenti di Enrico Cornet,* Libreria Tendler & Comp, Vienna.
[3] L. Chalkondyles (1996). *A Translation and Commentary of the Demonstrations of Histories, H΄ (320B [201P] - 403B [214P]* (translation Nikolaos Nikoloudis), Athens.
[4] Michail Critovoulos (1983). *Critobuli Imbriotae Historiae, A΄ (17.1 – 72.3),* D.R. Reinsch (ed.), Corpus Fontium Historiae Byzantinae 22, Berlin – New York.
[5] B. Robins (1742). *New Principles of Gunnery,* London, Library of the University of Michigan.
[6] A. R. Collins, *Smooth Bore Canon Balistics,* www.arc.id.au.
[7] G. Phrantzes (1838). *The Siege of Constandinople,* in *Annales Georgii Phrantzae Protovestiarii,* Bonn.

RE-EXAMING THE URBAN EXPERIMENT: VARIABLE GEOMETRIES OF SPATIAL INTELLIGENCE

N. Kourniatis[1] and I. Fakiri[2]
[1]Post-doc, Dept. of Informatics and Telecommunications, NKUA, Dr Architect NTUA, Athens, Greece
[2]PhD Candidate, School of Architecture NTUA, Athens, Greece

1. General

This research is being conducted at a time when the focus of architectural activity shifts from its perception as a form or [and] operational organization, which responds to a given architectural program, to its perception as composition of use material entities, properties and relationships. This concern, a result of the emergence of digital technologies and convergence of different scientific disciplines, is based on the ability of design tools to support and reinforce the discussion on urban landscape as an open process for action. The term "smart city", has been linked with digital applications, sensors, and software to define the city of the future. However, the real challenge is to develop a "smart city" that is based on the city of today and enables the integration of smart practices that may reform the spatial structure of the city. To this end the research focuses on the ways in which specific key concepts, present a dynamic intervention tool, leading to an instrumental and performative construction of a "smarter city". Our goal, in an effort to manage the cities anew, or better yet, the "smarter cities", is the introduction of an experimental tool, which participates and supports the urban metabolism. This particular dynamic tool can act, in our opinion, as a filter, which does not only receive information but, also, checks if this information can be modified, while producing connections supported by algorithmic programs. At this level, this paper presents a method for approaching three-dimensional (3D) models for n-dimensional hypercubes through polar zonohedra. The paper then goes on to present certain sections of the solids in question and the creation of tessellations on the plane, in order to contribute to urban metabolism. Thus, a key element of this mechanism is the production of an IT infrastructure, which through distributed computing systems and networks may gather information, while taking into account the temporality of change evolution, thus adapting this information to the passage of time.

2. Research framework

Before tackling the main issue of the research presented in this paper, it is necessary to present the broader context of this research, as this constitutes the basis, which feeds the research interests, produces general questions and directs research methods. In this framework, according to N. Leach [1] for some time now, new technologies have had a substantial impact on architectural design. From the use of standard drafting packages to the more experimental use of design tools, new technologies have come to play a major role in architectural production. But the question then arises as to how these digital tools can be used at a larger scale to generate and model cities. Back in 2002 A. Gillespie [2] was forced to comment: "*We are left to conclude that planners have yet to develop the awareness, let alone the expertise or appropriate policy intervention mechanisms that would enable them to influence the spatial development of city*".

3. Tools and strategies towards smarter cities

In this section we attempt to define a methodology in which the urban landscape is shaped through a complex diagrammatic entity capable of operating through feedback. The methodology concerns the Empirical Documentation investigating the establishment of the urban landscape through a composite diagrammatic entity, capable of operating with feedback and shaping a wider scope than that of the active metabolic factors. Therefore, the present study will formulate a new dynamic tool, which incorporates the concepts of dynamic planning processes towards the re-management of the

cityscape. Along this policy lines, the first level regards the data configuration. Specifically, all data - parameters derived from the reading of the landscape are identified, recorded and assessed, as well as feed the system and affect its evolutionary path. The data collected are classified into three categories, which will be constituted as "tanks". The data entered in these tanks involve the reading of the landscape as a surface, as a system and as a body. Specifically, the last tank relates to data which arise from human perception. Researches have shown that a space can easily affect humans' behaviour either in a pleasant or unpleasant way. Human brains have specific neurons that help to create an "internal" construction of the outside world.

Summarizing, the landscape as a surface, the landscape as a system and the landscape as a human perception contribute to the development of operational strategies aimed at the management of the landscape as a whole. The establishment of the three tanks is the first piece of the methodological tool. The objective of this phase is to collect data, and to transform them into appropriate forms, vector objects, so as to be used as data of the next phase (syntaxis). At this level, as mentioned before, this paper presents a method for approaching 3D models for n-dimensional hypercubes through polar zonohedra. The paper then goes on to present certain sections of the solids in question and the creation of tessellations on the plane in order to contribute to urban metabolism. The process of constructing zonohedra and the tessellations that will be presented lead to the conclusion that the polar zonohedra, which constitute Euclidean models of hypercubes in 3D space, can fill space and subsequently create planar tessellations, depending on the composition of the initial spatial pattern, which is repeated, thus filling the space. The method followed shows an approach to the geometric structure of tessellation, which intertwines regular n-gons with projections of solids in order to achieve a plane, in a way that they have never been associated with the urban metabolism before now. The handling of the landscape as a combined surface, system and body may actively contribute to the dynamics of the city and aims to develop operational strategies towards the city redefinition.

At the second stage, the term conduit is introduced, that conveys fluxes through it, always assigned to vector objects belonging to the first tank. The second phase of the methodological tool introduces specific standards called "indicators". These "indicators" are quantified data that meet specific conditions (simplicity, power, data availability over time, sensitivity to small changes, validity) and allow the system to legislate and monitor the quality of the variables managed. At the point where the "indicators" check the validity of the previous level's data, the conduit is charged with a plus or minus sign.

At the level of the switching, the movement of the duct is double, as mentioned above, depending on the sign of the vector objects located therein, since the vector objects with negative sign (-) are considered those whose size deviation from the permissible limits is the highest, as indicated by the indices. At the point where the entire conductor is positively charged, all data and actions that have occurred are completed and the system is stabilized, otherwise the process is repeated to achieve a universal positive charge. The dynamic structure then remains constant until the change of the data contained in the tanks. That is, until the chart that feeds data to the tanks perceives a change in the specific field.

To sum up, if today the cultural consideration changes looking for a smarter city, then design strategies should move to manufacturing techniques that manage change through ecological evolving and developing platforms. In an effort to form a smarter city, natural landscape should not be a backdrop on which the urban articulation will be placed, but a dynamic field of study, management and recovery of the urban fabric. On this basis, the research presented in this paper is a first conceptual approach to a mechanism that may monitor the transformation of natural space, fed with data obtained from its analysis, in order to compose them and redefine the urban space.

References

[1] A. Gillespie (2002). Digital lifestyles and the future city, in: N. Leach (ed.) Designing for a Digital World, John Wiley & Sons, Chichester, UK.
[2] N. Leach (2009). Digital cities, *Architectural Design*, **79(4)**, 6-13.

FATIGUE ASSESSMENT OF STEEL FRAMES SUBJECTED TO A NUMBER OF EARTHQUAKE EXCITATIONS

N. G. Pnevmatikos[1], G. A. Papagiannopoulos[2] and G. Hatzigeorgiou[2]
[1] Technological Educational Institution of Athens,
Department of Civil Engineering, Surveying and Geoinformatics
[2] Greek Open University, Director of Post-Graduate Program: Engineering Project Management

1. Introduction

It is well known that fatigue is a reason for structural failure in steel structures. Connections in steel bridges and in steel building frames can fail due to fatigue. This paper focuses on the fatigue assessment of steel frames subjected to earthquake loads. Adapting the theory of high and low cycle fatigue, a procedure for estimating a fatigue damage limit state for earthquake design is proposed. The method can be applied for damage assessment of the existing structure to past earthquakes excitations. Results of linear and nonlinear analysis are combined with fatigue-damage design curves to predict failure or the remaining useful life after a scenario of earthquakes. A three-storey moment resistant steel frame is examined. The frame is solved under seismic actions with linear and non-linear time history analysis. Various loading scenarios are considered and the fatigue life and damage index are estimated.

2. State of the art

Fatigue design is, nowadays, not only of theoretical importance but it is also imprinted to the respective codes, such as Eurocode [1] and, also, British and American standards. During the last decades, a lot of research in low cycle fatigue due to earthquake loads has been done. Vayas et al. [2] performed fatigue analysis of moment resisting steel frames subjected to earthquake excitations. Campbell et al. [3] proposed a method for calculating the fatigue damage in steel moment frames. They combine the results of nonlinear analysis with experimentally obtained fatigue-damage curves in order to predict failure or the remaining useful life after an earthquake. Applications of the above methods are presented in a recent paper by Koutsomichali [4]. Furthermore, Castiglioni et al. [5] work on constant and variable amplitude cyclic behavior of welded steel beam-to-column connections. In the present work a methodology for fatigue assessment of steel frame subjected to a number of earthquake excitations is presented.

3. Methodology

The procedure of the fatigue damage assessment to a steel frame subjected to earthquake excitation consists of four basic steps:

- Determine the time history load sequences representing an estimated upper limit of all operating loads expected to occur during design life. Perform linear and nonlinear time-history analysis of the structure subjected to time history loads.
- Extract the time history response quantities of interest, such as bending moment, axial forces, tensile stresses, plastic beam rotations, storey drift, etc. Convert the time history response to an equivalent number of loading cycles, for instance, reservoir method.
- Create a stress or plastic rotation spectrum in the detail region of interested that must be determined by classifying the stress or plastic rotations and the corresponding number of cycles in descending order.
- For each range of stresses calculate the degree of existing (cumulative) damage from the S-N curve. Calculate the fatigue damage of the equivalent cyclic responses and combine individual contributions using appropriate rule.

The above methodology can be applied in two ways. The first one includes calculation of stresses from linear time history analysis, creation of stresses spectrum, find the number of cycles to the cor-

responding stresses from EC3 design chart, find the damage index and fatigue life applying the miner's low for a specific detail category. The second way consists of the extraction of plastic rotation with non-linear analysis. Calculate the number of deformation cycles from low cycle model, assess the damage index and fatigue life applying the miner's low for a specific detail category.

4. Case study-analysis, results and discussion

Linear and non-linear analyses were executed in a two bay of 4 m span and two-storey of 3 m height steel moment frame. The material was of grade S235. The beams and columns sections are IPE330 and HEB240, respectively. The vertical loads cause bending moment at the beam equal to 40% of the yield moment. The fatigue load will be the Aigio, 1995, earthquake excitation.

A linear time history analysis with 1/3 of earthquake excitation was performed. The spectrum stresses at the beam-column connection were obtained. A mean number per year of small earthquakes was assumed to happen in the region. Using the fatigue chart from EC3 part 1-9 for a detail category 80 and 90 and applying the miner's law, the fatigue damage index and the fatigue life were calculated and shown in Fig.1a.

As a second step, a non-linear time history analysis, with twice the Aigio earthquake excitation, was performed. The spectrum of plastic rotation at the connections was obtained. A model for low cycle fatigue is applied and the damage index and the fatigue life are, again, calculated for various slopes of the fatigue curve, m, and shown in figure 1(b).

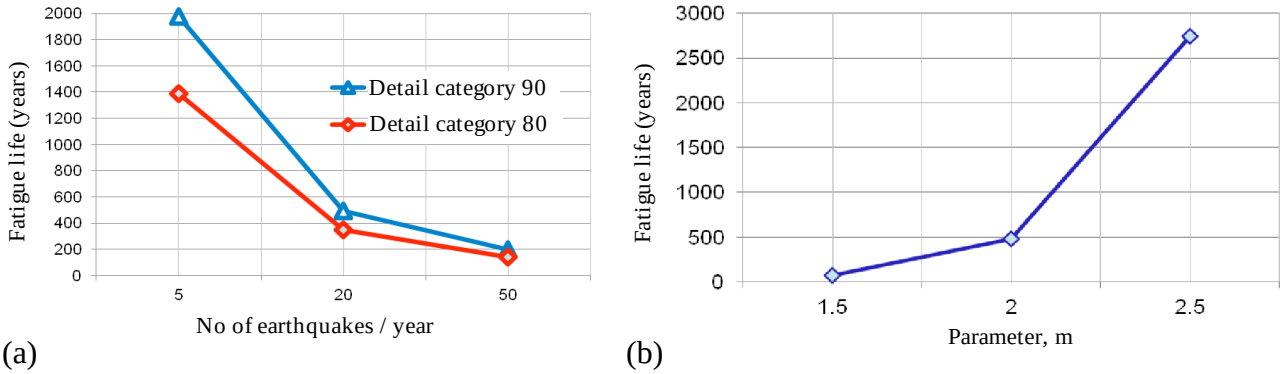

(a) (b)

Figure 1. (a) Fatigue life versus the number of earthquakes per year. (b) Fatigue life versus parameter m for low-cycle fatigue.

5. Conclusions

A fatigue analysis for steel moment resistance frame subjected to earthquake load was performed. It can be concluded that several minor earthquakes per year shorten the fatigue life due to earthquake. If fatigue due to other loads is also taken into account, the fatigue life is considerably reduced.

References

[1] Eurocode 3, EN1993-1-9. *Desisign of steel structures, Part 1-9: Fatigue*.

[2] I. Vayas, A. Sophokleous and F. Dinu (2003). Fatigue analysis of moment resisting steel frames, *Journal of Earthquake Engineering*, **7**, 637-654.

[3] S. D. Campbell, R. M. Richard and J. E. Partridge (2008). Steel moment frame damage predictions using low-cycle fatigue, in *Proceedings of the 14th World Conference Earthquake Engineering*, October 12-17, Beijing, China.

[4] N. Koustomichali (2012). Application of fatique methods in structures subjected to earthquake actions, Master thesis, *Greek Open University, Post-Graduate Program: Earthquake Engineering and Seismic Design of Structures*, Supervisor: N. Pnevmatikos.

[5] C. A. Castiglioni, H. P. Mouzakis and P. G. Carydis (2007). Constant and variable amplitude cyclic behavior of welded steel beam-to-column connections, *Journal of Earthquake Engineering*, **11**, 876-902.

SOLAR ENERGY CONTRIBUTION TO AN ELECTRIC VEHICLE NEEDS ON THE BASIS OF LONG-TERM MEASUREMENTS

Em. Kostopoulos, G. Dimas, K. Christopoulos, G. Spyropoulos and J. K. Kaldellis
Soft Energy Applications & Environmental Protection Laboratory
Piraeus University of Applied Sciences (PUAS), Athens, Greece

1. Introduction

Transportation sector is of utmost importance for the continuous development of the current globalized economy. To this end, transportation sector is heavily dependent on fossil fuels [1] and it is responsible for almost 14% of global CO_2 emissions [2]. More specifically, according to the latest data available [3], the transportation sector absorbs more than 30% of the EU-28 final energy consumption, while it is responsible for emitting more than 1000Mtn of carbon dioxide equivalent annually, i.e., 20% of the entire CO_2 production of the EU. Apart from CO_2, an abundance of air pollutants are emitted due to transportations; namely NO_x, PM, O_3, SO_x etc. [4].

The systematic introduction of non-fossil fuelled vehicles and more specifically electric vehicles (EVs), may significantly contribute on reducing the corresponding oil consumption and limiting of air pollutants' emissions, especially in the urban environment. More than 750,000 EVs have been sold during 2017 (Fig.1), while global electric car stock surpassed 2.5 million vehicles by the end of 2017 [5]. During the last five years global sales of EVs have increased very rapidly (Fig.1).

2. The necessity to use clean energy and the present protocol

At this point is important to mention the necessity to use clean energy for charging the batteries of the EVs, otherwise the environmental footprint of the proposed solution (in case of using fossil fuels) is quite questionable, if one takes into account the energy storage loss [4].

In order to contribute and support the clean-green transportation activities the present work investigates -on the basis of systematic measurements- the real world energy balance of selected commercial vehicles. For this purpose the pilot solar-based Electric Vehicle Charging Station (Fig.2) created by the Soft Energy Applications & Environmental Protection Laboratory of the Piraeus University of Applied Sciences (PUAS) has been used in order to experimentally analyze the main technical characteristics and the energy performance of a solar-based charging procedure.

Fig.3 presents a typical view of the PV energy yield as shown on the existing web platform in comparison with the charging voltage. The solar energy production variation due to the solar irradiance fluctuations along with the voltage profile at the electric vehicle charging point as a function of

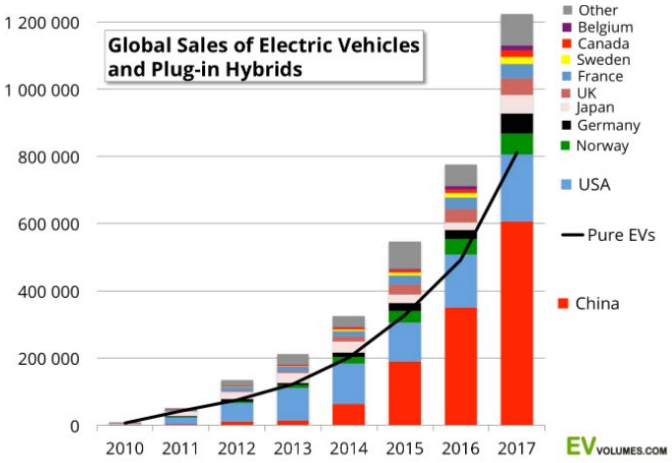

Figure 1. Global sales of EVs [5].

Figure 2. Experimental solar-based Electric Vehicle Charging Station (SEA Lab).

Figure 3. A typical data analysis for the PV production, on a selected date, as shown on web.

time, for an entire summer day is given. It is to be noted that the existence of the battery bank guarantees constant charging voltage although the photovoltaic generator's power output is quite variable.

3. Results and discussion

One of the most interesting findings during our long-term measurements is the impact of charging mode on the energy consumption of the EVs as well as the time required in order to meet the necessary state of charge, Figs.(4, 5). In this context, one may see the by 15% higher energy consumption during the charging phase when using the fast charging mode. Moreover, the final energy absorbed by the electric vehicle is by approximately 20% higher in comparison with the pure electrical vehicle energy consumption due to charging loss.

Finally, in Fig.5 rapid charging power decrease as the EV's battery state of charge (SOC) approaches 85% is observed. Thus considerable charging time is required to cover the SOC=85% to 100% interval, something perhaps not necessary in all cases.

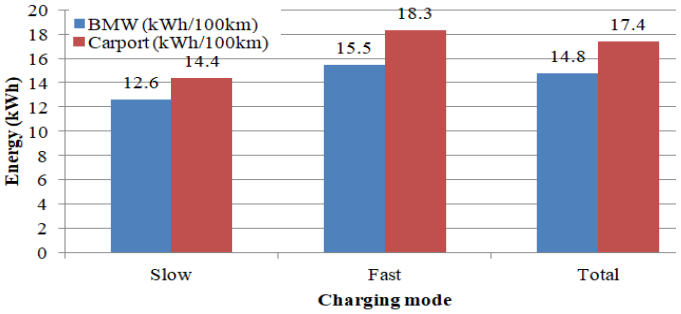

Figure 4. BMW-i3 energy consumption comparison, between vehicle's display and carport's values for slow and fast charging.

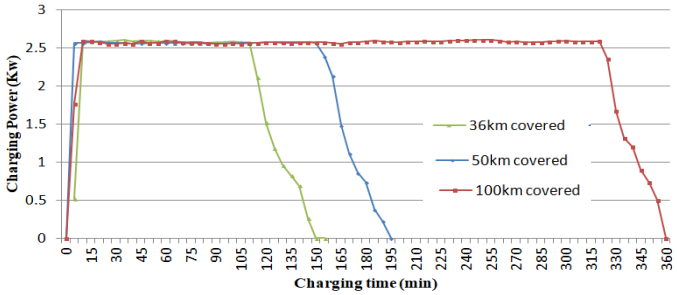

Figure 5. BMW-i3 slow charging profile after 36, 50 and 100 km have been covered.

References

[1] International Energy Agency, (IEA), https://www.iea.org/statistics/.
[2] Center for Climate and Energy Solutions, (C2ES). Available at: https://www.c2es.org/.
[3] Eurostat, http://ec.europa.eu/eurostat/statistics-explained/index.php/Main_Page.
[4] J. K. Kaldellis, G. Spyropoulos and St. Liaros (2015). Supporting Electro-mobility in Smart Cities using solar EV charging stations, in *3rd Mediterranean Green Buildings and Renewable Energy Forum (MED-GREEN 2015)*, Florence, Italy, pp. 501-513, Springer International Publishing).
[5] The Electric Vehicle World Sales Database, http://www.ev-volumes.com/.

Mechanical Properties and Simulation of Archaeological Materials

STUDIES ON MATERIALS & COMPOSITIONS FOR THE CONSOLIDATION, REPAIR & STRENGTHENING OF HERITAGE STRUCTURES

El.-E. Toumbakari
Directorate for Restoration of Ancient Monuments,
Hellenic Ministry of Culture, Athens, Greece

1. Introduction & definitions

In the introduction, the notion of "materials' compatibility" will first be presented following charters, resolutions and declarations of international institutions.

A second notion will be subsequently discussed, i.e. the notion of "bearing structure" or simply "structure" in terms of structural engineering, with the aim to highlight the difference, as well as the connection, between structural behaviour and building materials. It will be argued that the design of materials for applications in structures must take into account, not only parameters at a micro-level (this of the material) but, and maybe more important, at a macro-level (this of the structure). However, this relationship is far from being linear. To this purpose, mathematical formulae which are utilized for the prediction of masonry mechanical properties on the basis of the mechanical properties of its individual components (stone, mortars) will be recalled and the crucial role played by mortars will be shown.

Finally, a third notion will be introduced, namely the historic materials' technologies, whose understanding and preservation is one, among other, duties of the workers in the field of cultural heritage preservation. A short overview of the basic technologies in Greece will be made, focusing on binders and filling materials rather than stones and bricks, as they provide the framework, within which material design ought to develop in a critical, rather than imitative, manner.

2. Review of recommendations regarding material design for historic masonry

The first attempt to study historic mortars and discuss the issue of designing repair materials can be traced back to the Symposium organized by ICCROM in 1982 [1]. Since then, research was carried out following two axes, materials and structures.

In this paragraph, a short overview of the corresponding literature will be made, which will show that, if materials' research was much developed, on the contrary, research on the material parameters affecting masonry behaviour was until recently limited. In this context, the work that has been carried out in the framework of the International Union of Laboratories and Experts on Construction Materials, Structural Systems & Structures (RILEM) [2, 3] will also be presented.

Subsequently, researches on the effect of mortars and grouts on structural behaviour will be subsequently presented. To this purpose, focus will be made on research on structural grouts, which has shown that the parameter governing the response of masonry, and which is therefore important to grout design, is bond strength. With this work, grout design for historic masonry moved towards the use of lower strength mixtures, even if the use of Portland cement in limited quantities is considered necessary.

3. Case-studies

Finally, examples of materials' design will be presented, covering the aspects of material and "historical" compatibility [4-6].

Concerning the material compatibility, examples of lime-pozzolan-cement compositions will be discussed and put in the context of research on hydraulic binders. The history of research on the development of lime-pozzolan-cement compositions in Greece will be outlined. Moreover, it will be

shown that those compositions can cover a variety of requirements, and are therefore a good and flexible solution for historic masonries.

Concerning "historical" compatibility, examples of mortar design will be given and emphasis will be put on the use of earth-based ones for prehistoric masonry. It is well-known earth-based binders were used extensively in the construction of prehistoric structures. Consequently, compatibility as well as "authenticity" issues call for the re-use of earth for the conservation of these structures. Earth binders are known to be vulnerable to environmental exposure, therefore stabilised-earth mortars were specifically designed in order to be compatible to the historic fabric and at the same time sufficient from a safety and durability point of view.

References

[1] ICCROM (1982). *Mortars, cements and grouts used in the conservation of historic buildings*, International Centre for the Study of the Preservation and the Restoration of Cultural Property, Proceedings of the International Symposium, 3-6 November 1981, Rome, Italy.

[2] RILEM TC 167-COM (2004*). Characterisation of old mortars with respect to their repair - Final report*, C. Groot, G. Ashall and J. Hughes (eds), RILEM Publications.

[3] RILEM TC 203-RHM (Main author: John J. Hughes) (2012). Repair mortars for historic masonry. The role of mortar in masonry: an introduction to requirements for the design of repair mortars, *Materials and Structures*, **45(9)**, 1287-1294.

[4] E.-E Toumbakari, M. Kaipanou, A. Ntziouni and V. Kasselouri-Rigopoulou (2010). Mechanical properties and durability of cement-stabilized earth mortars for application in prehistoric monuments, in *Proceedings of 8th International Symposium on the Conservation of Monuments in the Mediterranean Basin ,* May 31-June 2, Patras, Greece.

[5] K. Van Balen, E.-E. Toumbakari, M.-T. Blanco, J. Aguilera, F. Puertas A. Palomo, S. Sabbioni, G. Zappia, C. Riontino and G. Gobbi (1999). Procedure for mortar identification: a proposal, in *International RILEM Workshop on "Historic Mortars: Characteristics and Tests"*, P. J. M. Bartos, C.Groot and J.Hughes (eds), Paisley, Scotland, RILEM Publ. PRO12, 61-70.

[6] E. Vintzileou (2001). The effect of deep rejointing on the compressive strength of brick masonry, *Masonry International*, **15(1)**, 8-12.

HYDRAULIC MORTARS FOR JOINING ARCHAEOLOGICAL STONE FRAGMENTS - A METHODOLOGICAL APPROACH

I. Karatasios, M. Amenta and V. Kilikoglou
Institute of Nanoscience and Nanotechnology, N.C.S.R. "Demokritos",
Agia Paraskevi, 15310 Athens, Greece

1. Introduction

This work presents the methodological approach followed for the selection of compatible repair mortars, for joining stone fragments of marl limestones of the archaeological site of Zea theater, in Piraeus-Greece. The work focuses on the evaluation of the stone - repair mortar interface, based on the interpretation of mechanical properties of both individual stone and mortar specimens as well as, on joined stone specimens with different types of mortar mixtures.

Stone blocks used in archaeological monuments can be either homogeneous or heterogenous materials, depending on the stone lithology (e.g. marble, sandstone, marls etc) and their subsequent microstructure, with distinct mechanical properties. The selection of appropriate mortar mixtures for joining fragmented stone blocks, especially without reinforcement, is a complex process, since the mechanical behavior of the two materials should be matched while, mortar joints act a weakness zone for the composite mechanical behavior of stone units.

The main selection criteria encompass performance characteristics such as, enhanced adhesion and lower strength than the stone substrate - for avoiding failure of original stone, elevated surface area values, good workability and rheology as well as sort setting and hardening time. Moreover, a critical parameter for successful joining interventions is the prevention of crack development during setting.

The development and selection of compatible mortars for joining archaeological stone fragments requires therefore an in-depth study of mechanical and microstructural properties of both stone substrate and mortar mixtures. In theory the properties of stone and mortar should be fully matched, but in practice it is impossible, leading to several studies on the complex behavior of stone-mortar interface under mechanical load [1-3]. Based on the above context, the methodology described below was developed.

2. Methodology

Stone types were categorized in three groups, according to their strength level. Accordingly, five (5) types of mortar mixtures were designed according to the tensile strength of the stones, as this was determined by three point bending test. The cementing material used in the five different mixtures was: Type II 52.5 white cement, NHL5 hydraulic lime and lime-metakaoline mixed binder. The binders were further modified with metakaoline to adjust hydraulicity and the level of mechanical strength. Fine quartz sand (0/0.5 mm) was used in all mixtures for avoiding shrinkage cracking.

The mechanical properties and the adhesion ability of mortar mixtures were tested after curing for 28 days. Although there are several norms and standards for testing individual mortar properties, the methodology for evaluating the adhesion strength on stone-mortar interface is not clear. For instance, some researchers propose the use of pull-off tests for evaluating adhesion strength. However, in practice the basic failure modes that occur at the level of stone–mortar interface are two [4]: tensile failure (mode I), associated to stresses acting to joints, and shear failure (mode II) corresponding to a sliding mechanism of the mortar joint. The preponderance or the combination of various failure modes is related to the orientation of the joints with respect to the principal stresses and to the ratio between the principal stresses.

In this work, the selection of compatible repair mortars was based on the interpretation of mechanical properties of both individual stone and mortar specimens subjected to unconfined com-

pression and three-points bending stress as well as, on joined stone specimens with different types of mortar mixtures under four point bending stress. In the later case, the joins were parallel to the direction of the load.

3. Results and discussion

Stone lithotypes were categorized in three groups according to their compressive strength values, namely: low (<20 MPa), moderate (20-50 MPa) and high (>50 MPa), exhibiting average porosity values between 8-25%. The bond strength between mortar and stone was primary depended on the binder composition. NHL binder failed to provide good adhesion to the stone substrate during application, leading to increased number of failed specimens. In contrast, the use of lime-pozzolan mixtures exhibited increased workability and reduced water demand for standard consistency at 16 cm. However, lime-based mixtures had quite high porosity values (~40%), leading to low bond strength. Finally, the use of ternary mixtures with cement-lime-metakaolin exhibited compatible porosity and strength values (Fig.1), both in three-point and four-point bending tests.

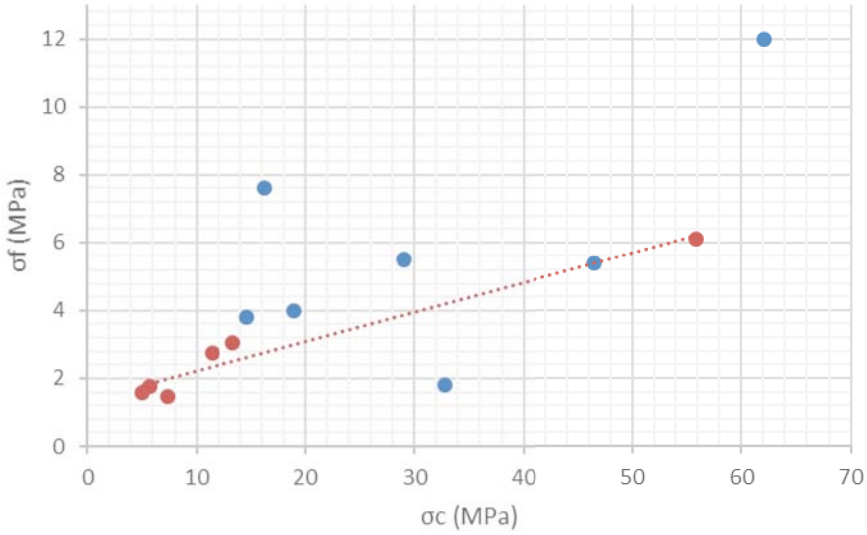

Figure 1. Compressive versus three-point bending strength values of stone specimens (blue) and adhesive mortar mixtures (red).

Overall, the interpretation of microstructural and mechanical properties results highlighted the essential role of four-point bending for assessing the bond strength of stone-mortar interface, as well as the predominant role of composition, physical and chemical characteristics of the binder on the development of the adhesion properties of repair mortars.

References

[1] J. E. Lindqvist (2009). Repair mortars for historic masonry. Testing of hardened mortars, a process of questioning and interpreting, *Mater. Struct.*, **42**, 853-865.
[2] A. Isebaert, L. van Parys and V. Cnudde (2014). Composition and compatibility requirements of mineral repair mortars for stone: a review, *Constr. Build. Mater.*, **59**, 39-50.
[3] B. Szemerey-Kiss and A. Torok (2017). Failure mechanisms of repair mortar stone interface assessed by pull-off strength tests, *Bull. Eng. Geol. Environ.*, **76**, 159-167.
[4] G. Vasconcelos and P. B. Lourenco (2009). Experimental characterization of stone masonry in shear and compression, *Constr. Build. Mater.*, **23**, 3337-3345.

MULTI-WALLED CARBON NANOTUBE WHITE CEMENT-BASED MORTARS FOR THE RESTORATION OF CULTURAL HERITAGE MONUMENTS

Z. S. Metaxa[1] and S. Boutsioukou[2]
[1] National Technical University of Athens,
Department of Mechanics, Laboratory for Testing and Materials, Athens, Greece
[2] University of the Aegean, Department of Financial Engineering, 82132 Chios, Greece

1. Abstract

Multi-wall carbon nanotubes (MWCNTs) were added as a reinforcement in mortars that are currently used for the restoration of cultural heritage monuments. The main goal of the study was to investigate the influence of several parameters, such as the surfactant type and concentration, on the dispersion of the MWCNTs. These parameters were examined by studying the mortar nano-composites' mechanical performance (compressive, flexural strength and modulus of elasticity) and electrical resistivity. Initially, an ionic and non-ionic surfactant, typically used for the dispersion of CNTs in polymers, were adopted to prepare / modify the surface of the MWCNTs with non-covalent functionalization and to improve their dispersion state and bonding with the surrounding mortar matrix. According to the results, the exploitation of these surfactants to disperse MWCNTs for cement-based materials should be avoided as they are not compatible with the cementitious matrix. As an alternative dispersion agent, a water reducing admixture was used. The results have showed that the dispersion agent concentration plays an important role on the uniform distribution of the MWCNTs. In general, the optimum MWCNT dispersion is directly related to the observed reduction of the nanocomposite mortars' electrical resistivity as well as the enhancement of their mechanical properties.

2. Introduction

Several studies have shown that the introduction of carbon nanotubes in cementitious materials made from Ordinary Portland Cement (OPC) improves the mechanical performance of the matrix [1, 2]. The extend of this improvement is strongly related to the nanomaterials' distribution state inside the matrix. That is whether the MWCNTs are uniformly dispersed or they form agglomerates. In addition, besides the improvement of the mechanical performance, the incorporation of MWCNTs at concentrations above the percolation threshold could provide the material with monitoring capabilities [3]. This is a key concept for their wide-spread use, as currently the traditional approaches for structural health monitoring of Historical Monument components is largely based on strain gauges that are applied on the outer material's surface and therefore cannot detect any strain changes or induced damage inside the material / structure [4]. The addition of electrically conductive carbon nanotubes, is expected to improve the mechanical performance of the cementitious materials used for the restoration of cultural heritage monuments and supply them with improved sensing characteristics.

In this study, the incorporation of MWCNTs in mortar samples made from white cement was investigated. It should be noted that current research has mainly focused on using CNTs as a reinforcement for OPC. Their addition in white cement matrices is still at a preliminary stage. Therefore, this study focuses on the first step that is the MWCNTs successful implementation.

3. Results and conclusions

MWCNTs, Aalborg white CEM I 52.5R, coarse and fine quartz sand and three different types of surfactants were used in this study. Initially, several aqueous MWCNTs/surfactant solutions were prepared and ultrasonicated using a titanium probe. The MWCNTs/surfactant solutions were mixed with the cement and sand following the respective ASTM specifications. Compression and three-

point bending tests were performed on intact and notched specimens, respectively. During the mechanical experiments, time, force, and displacement were continuously monitored and recorded. A multimeter was used to record in situ the electrical resistance of the nanocomposites over time using the four-point measurement set-up (direct current).

The results indicated that surfactants typically used for MWCNTs dispersion in polymers are possibly not suitable for use in cementitious materials as they downgrade the material's mechanical performance even at low concentrations (0.05 wt% of cement). The influence of the water reducing agent concentration on both the electrical resistivity and flexural stress of mortars reinforced with 0.2 wt% MWCNTs is presented in Fig.1. It is observed that there is an optimum water reducing agent amount (close to 0.8 wt%) for which the nanocomposites demonstrate both low electrical resistivity and maximum flexural strength. The dispersing agent concentration plays an important role on the uniform distribution of the MWCNTs. Similar results were obtained from the compression test indicating that the electrical and mechanical properties of the MWCNT mortar nanocomposites could be used to study the dispersion state of the MWCNTs inside the matrix.

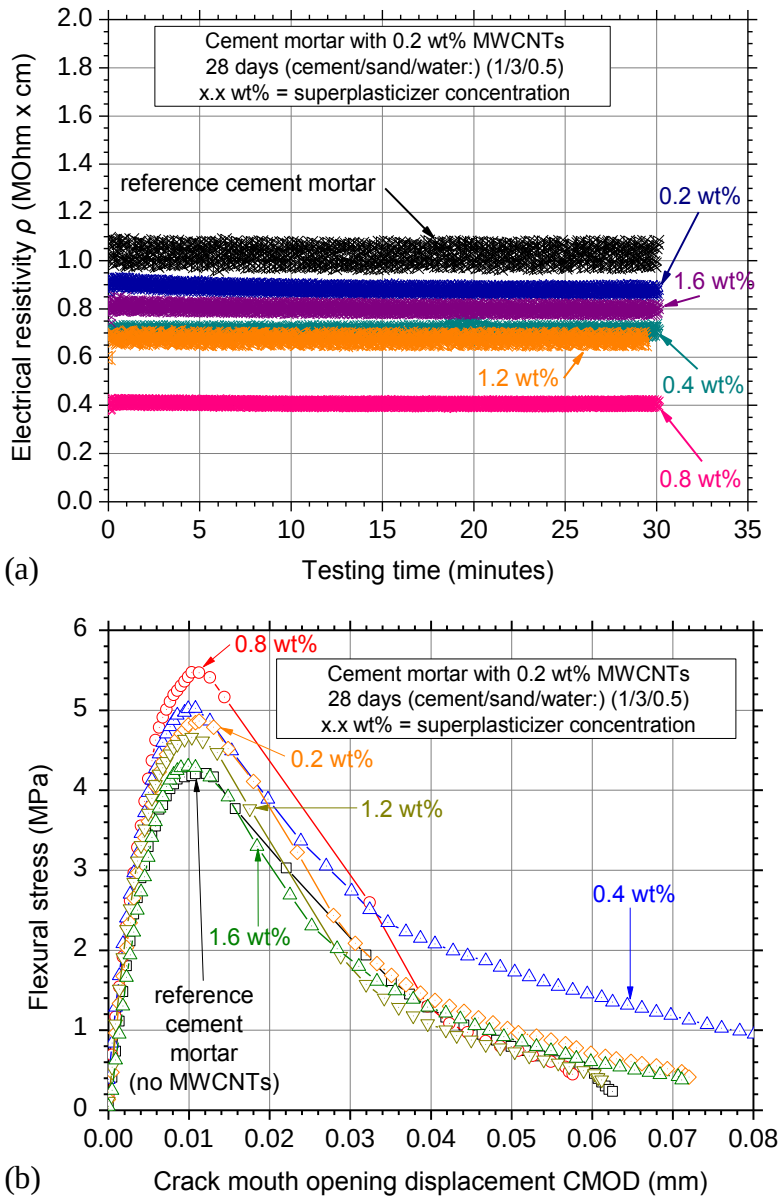

Figure 1. Effect of water reducing agent concentration on: (a) electrical resistivity versus testing time and (b) flexural strength versus crack mouth opening displacement of the investigated nanoreinforced white cement mortars.

References

[1] M. S. Konsta-Gdoutos, Z. S. Metaxa and S. P. Shah (2010). Multi-scale mechanical and fracture characteristics and early-age strain capacity of high performance carbon nanotube/cement nanocomposites, *Cem. Concr. Compos.*, **32**, 110-115.

[2] Z. S. Metaxa, J. W. T Seo, M. S. Konsta-Gdoutos, M. C. Hersam and S. P. Shah (2012). Highly concentrated carbon nanotube admixture for nano-fiber reinforced cementitious materials, *Cem. Concr. Compos.*, **34**, 612–617.

[3] Z. S. Metaxa, E. D. Pasiou, I. Dakanali, I. Stavrakas, D. Triantis and S. K. Kourkoulis (2016). Carbon nanotube reinforced mortar as a sensor to monitor the structural integrity of restored marble epistyles under shear, *Procedia Structural Integrity*, **2**, 2833–2840.

[4] S. K. Kourkoulis, M. Mentzini and E. Ganniari-Papageorgiou (2013). Restored marble epistyles under bending: A combined experimental and numerical study. *Int. J. Architectural Heritage*, **7**, 89–115.

MODELING OF THE MICROSTRUCTURE OF ANCIENT FUNCTIONAL CERAMICS AND ASSESSMENT OF THEIR PERFORMANCE

A. Hein and V. Kilikoglou
Institute of Nanoscience and Nanotechnology, N.C.S.R. "Demokritos",
Agia Paraskevi, 15310 Athens, Greece

1. Introduction

Ceramics were among the first materials processed by people, deployed as quasi universal materials serving diverse functions, such as cooking, metalworking, storage, transport, or construction. This versatility was related to various conditions. The raw materials, such as clays or tempers, were ubiquitously available and objects of any shape could be moulded from the unfired clay paste. Probably most importantly, though, after firing the ceramics exhibited sufficient resistance of the ceramics against thermo-mechanical loads. However, different functions required different material properties and the production process was accordingly adapted, which can be observed in studies of ceramics fulfilling different functions.

Apart from their composition, the material properties of the ceramics depended on their micromorphology and microstructure, in terms of pore structure, non-plastic inclusions and vitrification.

Material performance under load can be tested with specimens cut from the ancient ceramics or with laboratory specimens replicating the basic characteristics observed in archaeological samples. Alternatively, the relation between microstructure and material performance can be investigated by generating 3-dimensional computer models which can be evaluated by using the finite element method (FEM). In the present paper the modeling approach will be demonstrated with focus on characteristic pore structures which can be found in ancient pyrotechnical ceramics.

2. Pore structure of pyrotechnical ceramics: Archaeological evidence

Pyrotechnical ceramics used in antiquity were not as refractory as modern materials. While actual fireclays were used on a large scale only from the Roman Period onwards, until then raw materials for ceramic tools, fabricated for use in metallurgy or glass production, were basically the same as for the fabrication of common pottery. Sufficient heat resistance was rather achieved through the application of thick walls and tempering with non-plastic materials reducing thermal stresses and stabilizing the structures. Particularly the thick walls, though, reduced essentially heat transfer during use so that for example crucibles had to be heated primarily from inside. Heat transfer was additionally reduced by a highly porous ceramics' microstructure. This was achieved typically by adding organic materials to the clay paste, which burned out during pre-firing or use. A preference for the use of different kinds of organic fibres can be observed leaving extended pores oriented commonly parallel to the surfaces (Fig.1) [1]. Fibrous pore structure and orientation proved to reduce heat transfer additionally [2].

3. Modeling pore structure and material performance

In order to study the material performance in relation to pore structure micro-images of the ceramics (Fig.1) can be transferred to two-dimensional two phase models which can be evaluated using FEM [3]. Three-dimensional models can be generated for example on the basis of microCT scanning. Alternatively numerical models of pore structures can be generated considering observations and additional assumptions [4]. Numerical modeling allows for assessing specific parameters of the microstructure in a more systematic way and for identifying their particular effect on the materials performance under simulated thermal or mechanical loads. In the present paper heat transfer and elasticity of three-dimensional models considering different pore shapes will be investigated using FEM (Fig.2).

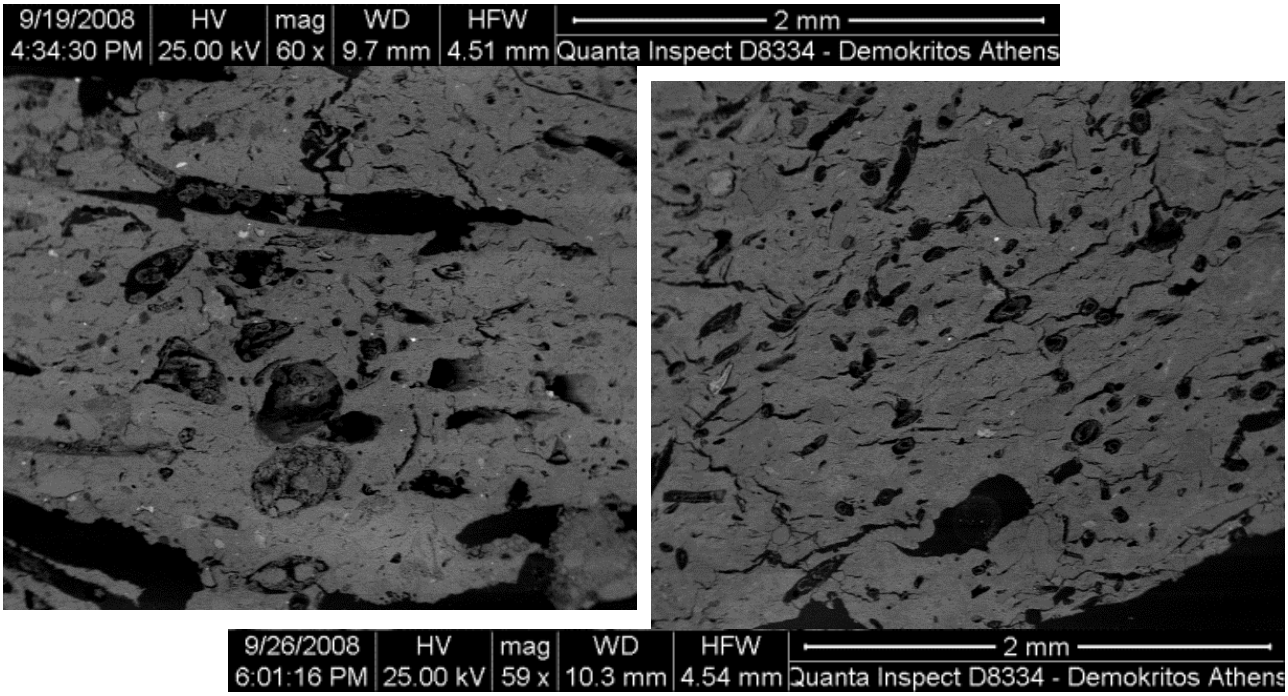

Figure 1. SEM micrographs of Late Minoan crucibles tempered with straw or and animal hair.

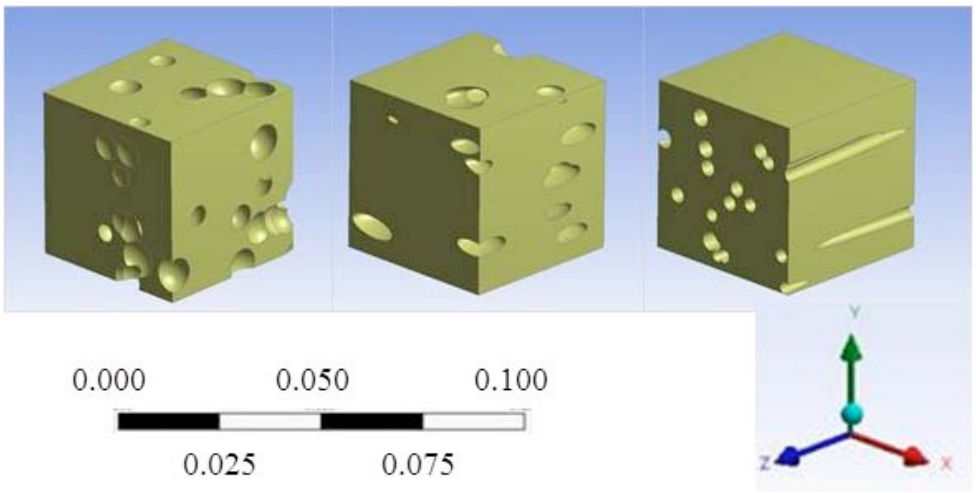

Figure 2. Modeled pore structures: spherical, ellipsoidal and fibrous pores.

References

[1] D. Evely, A. Hein and E. Nodarou (2012). Crucibles from Palaikastro, East Crete: Insights into Metallurgical Technology in the Aegean Late Bronze Age, *J. Archaeological Sci.*, **39**, 1821-1836.

[2] A. Hein, I. Karatasios, N. S. Müller and V. Kilikoglou (2013). Heat transfer properties of pyrotechnical ceramics used in ancient metallurgy, *Thermochimica Acta* **573**, 87-94.

[3] A. Hein and V. Kilikoglou (2007). Modeling of Thermal Behavior of Ancient Metallurgical Ceramics, *J. American Ceramic Soc.*, **90**, 878-884.

[4] A. P. Roberts and E. J. Garboczi (2000). Elastic Properties of Model Porous Ceramics, *J. American Ceramic Soc.*, **83**, 3041-3048.

ASSESSING WOOD ADHESIVES USED IN CONSERVATION VIA SHEAR BY COMPRESSION LOADING

E. Tsetsekou, A. Platanianaki and A. Pournou
Department of Conservation of Antiquities and Works of Art,
Technological Educational Institute of Athens,
Athens, Greece

1. Introduction

The selection of the appropriate adhesive is always important and a significant issue, especially when applied to conservation of wooden artefacts of Cultural Heritage. A poor adhesive can cause further and sometimes irreversible damage, both aesthetically and mechanically, to an already deteriorated object. Hence, the conservator has to be aware of the properties of the adhesive to be used such as their mechanical strength and aging behaviour over time.

In this work the suitability of five adhesives, commonly used in conservation of dry wood, is studied comparatively Three natural adhesives (casein, rabbit glue and fish glue) and two synthetic ones (a methacrylate resin, i.e., Paraloid B-72 and a polyvinyl acetate glue, i.e., Ravemul M18 Vinavil) were tested for their performance with respect to two different species of wood, *Abies alba* L. (fir) και *Acer pseudoplatanus* L (maple).

The adhesives were evaluated for their performance, before and after accelerating ageing, in relation to: (a) bond strength under shear stress, (b) reversibility, (c) reversibility via solvents, and (d) colour stability through time.

2. Methods

The application of the adhesives on the wooden samples (Fig.1) was implemented according to the ASTM D905 standard [1]. Four replicates were used for each adhesive. In total 120 pairs were prepared, 60 for each species. Pressure was then applied onto assembled samples for 72 hours. Post-cure conditioning was undertaken in a climate chamber (Binder KBF P 720) for 7 days under constant conditions (T= 23± 2 ^{o}C, RH=55% ± 2).

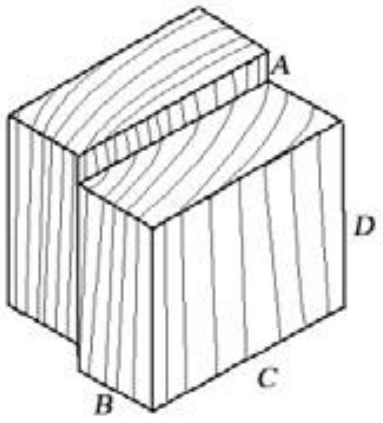

Dimensions	A	B	C	D
mm	6.3	19	44.4	50.8

Figure 1. The geometry and the dimensions of the specimens.

After curing, one group of 20 samples was aged under a XENON Arc lamp with a window glass filter, in an Atlas Suntest XLS+ chamber at irradiance level of 350 W/m^2. The samples remained in the chamber according to the ASTM G151 standard [2], until a distinct change in colour was produced. This change was observed after 98 hours, when samples have been exposed to a total of 120960 kJ/m^2.

A second group of 20 samples was subjected to ageing, with two different cycles of RH and temperature, in a climate chamber Binder KBF P 720, based on the ASTM 1183 [3]. The duration of the first (T: 23± 2 ^{o}C and RH: 78% ± 2) and the second cycle (T: 48.5± 2 ^{o}C and RH: 23 ± 2) was initially 24 hours. Then the first cycle was repeated for 72 hours and upon completion was followed by the second cycle conditions for 48 hours. This alternation of the first and second cycle was repeated for one more week. A last group of 20 samples was kept without being subjected to ageing, as control.

The bond strength was assessed on aged samples and controls by shear stress testing on an INSTRON 3300 machine with continuous motion of the movable head, at a rate of 5 mm/min, to failure of bond, based on the ASTM D905 standard [1]. All measurements taken were elaborated with the Blue Hill software.

Colour stability under UV exposure in the Atlas chamber, was evaluated by a Lovibond RT Series SP60 colorimeter, according to the European Standard EN 15886 [4].

Performance of glues was also evaluated based on the extent of wood damage produced during bond failure and based on their reversibility before and after aging with the use of solvents.

3. Results and discussion

Fish glue demonstrated the highest bond strength followed by Paraloid B72, rabbit glue, Vinavil and lastly casein. No wood failures were observed.

Concerning reversibility, Paraloid B72 was the easiest to remove from wood surface, before and after accelerated ageing, followed by casein, fish glue, rabbit glue and Vinavil. Accelerated ageing under the XENON arc lamp made Vinavil harder to remove. Changes in the solubility of rabbit glue were also observed in the samples subjected to temperature and RH cycles.

Vinavil was found to be the most colour stable adhesive followed by fish glue, rabbit glue, Paraloid B72 and lastly casein.

Taking into consideration all the above, Paraloid B72 and fish glue demonstrated the best performance as adhesives for wooden artifacts of Cultural Heritage.

References

[1] ASTM D905 (2003). *Standard test method for strength properties of adhesive bonds in shear by compression loading.*
[2] ASTM G151 (2010). *Standard practice for exposing nonmetallic materials in accelerated test devices that use laboratory light sources.*
[3] ASTM 1183 (2011). *Standard practices for resistance of adhesives to cyclic laboratory aging conditions.*
[4] European Standard EN 15886 (2011). *Conservation of cultural property - Test methods - Colour measurement of surfaces.*

Metals Processing

EXPERIMENTAL STUDY OF MACHINING AISI O1 WORKSTEEL WITH EDM PROCESS

E. L. Papazoglou, A. P. Markopoulos and D. E. Manolakos
National Technical University of Athens,
School of Mechanical Engineering, Section of Manufacturing Technology,
Heroon Polytechniou 9, 15780, Athens, Greece

1. General

Electrical Discharge Machining (EDM) is one of the earliest and most widely used non-conventional machining processes, with basic and major advantage the capability of machining any electrically conductive material, regardless of the material's hardness, strength, and other mechanical properties. Additionally, EDM is capable of machining parts and components with complex geometries, and high level of maintaining dimensional accuracy and surface finish. The main objective of this paper is to investigate the influence of EDM parameters, such as current intensity, I_P and pulse on time T_{on}, on the material removal ratio (MRR), and the surface quality and roughness.

Material removal ratio is a typical performance measure for the erosion rate of the workpiece, commonly expressed by the unit [mm^3/min], and is used as an indication of machining speed. The quality of the machined surface (SQ) is a broad and extremely important factor of the EDM process, including aspects as surface roughness (SR), extend of heat affected zone (HAZ), recast layer thickness (WL), and micro cracking density. The above mentioned measures - properties are in strong dependence on the amount of the released energy during machining [1-3].

2. Experimental procedure

A series of experiments were carried out, 12 in total, using AISI O1 work steel as workpiece material, and a rectangle copper electrode. The chemical composition of AISI O1 is given in Table 1. The selected machining conditions were: straight polarity, using hydrocarbon oil as dielectric fluid, with constant voltage 100 V, current intensity from 12 to 27 A, and pulse on time from 75 to 500 μsec (Table 2).

Element	C	Mn	Cr	W	V
Content [%]	0.95	1.1	0.45	0.45	0.1

Table 1. Chemical Composition of AISI O1.

#	**1**	**2**	**3**	**4**	**5**	**6**	**7**	**8**	**9**	**10**	**11**	**12**
I_P [A]	27	24	21	18	27	18	15	12	21	15	12	8
T_{on} [μsec]	100	100	100	100	300	300	300	300	500	500	500	75

Table 2. EDM experimental parameters.

3. Data and analysis of the results

Before, during and after each experiment, the necessary data such as the workpiece weight before and after machining, the average current intensity $\overline{I_p}$, machining efficiency and time, were transcribed for subsequent calculations, evaluation and analysis. Furthermore the maximum and average surface roughness (Ra, Rt) were measured as the mean from measurements made at five points on each

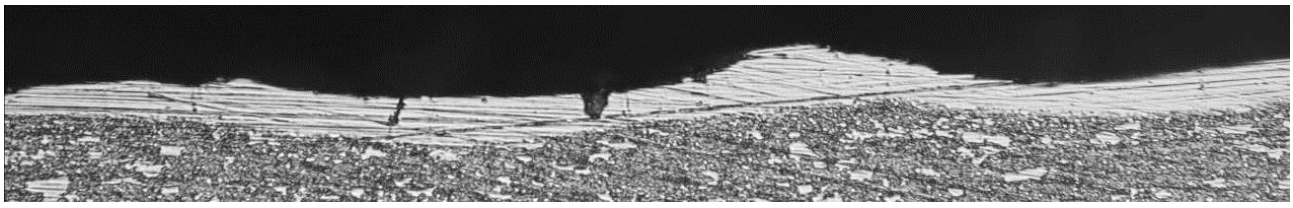

Figure 1. Microscope image of recast layer thickness on workpiece.

machined surface. At the end, four specimens were grinded, polished and chemical attacked with Nital (10%) for evaluation of the recast layer thickness through microscope observation (Fig.1).

As a general conclusion of the above described experimental procedure, the strong dependence of MRR, SR and WL thickness on the machining conditions should be mentioned. In some cases, the correlation is almost linear (Fig.2a), but in other ones the relation is more complicated and uncertain (Fig. 2b).

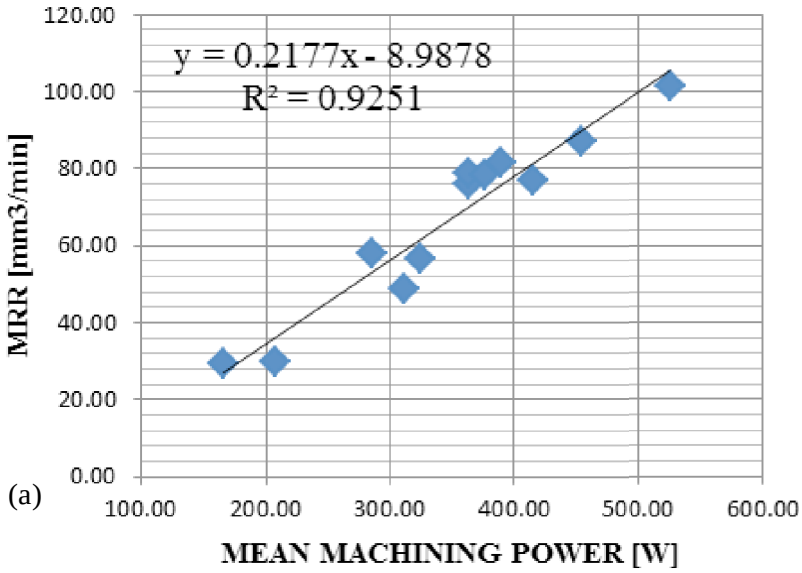

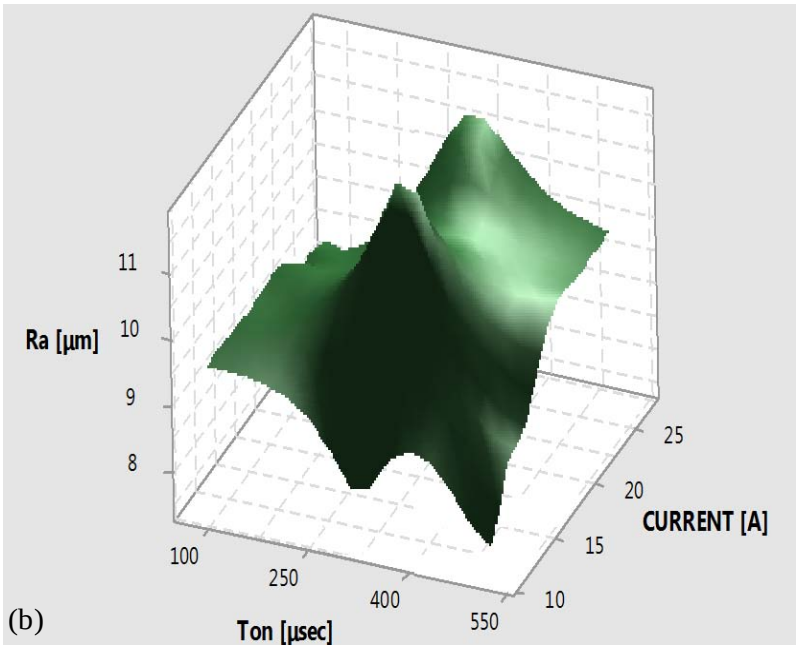

Figure 2. (a) MRR vs. mean machining power and (b) Average roughness vs. current intensity and pulse on time.

References

[1] M. P. Jahan (2015). *Electrical Discharge Machining*, Nova Science Publishers, New York.

[2] S. K. Choudhary and R. S. Jadoun (2014). Current advanced research development of Electric Discharge Machining (EDM): A review, *International Journal of Research in Advent Technology*, **2**, 273-297.

[3] M. Gostimirovic, P. Kovac, M. Sekulic and B. Skoric, (2012). Influence of discharge energy on machining characteristics in EDM, *Journal of Mechanical Science and Technology*, **26**, 173-179.

IDENTIFICATION OF APPROPRIATE AUTOGENOUS LASER WELDING PARAMETERS FOR Al-Li 2198 ALLOY

T. N. Examilioti[1,2,3], N. Kashaev[1], S. Riekehr[1], J. Enz[1], B. Klusemann[1,3] and N. D. Alexopoulos[2]
[1] Institute of Materials Research, Materials Mechanics, Helmholtz-Zentrum Geesthacht, D-21502 Geesthacht, Germany
[2] Department of Financial Engineering and Management, School of Engineering, University of the Aegean, Kountourioti 41, 82 132 Chios, Greece
[3] Institute of Product and Process Innovation, Leuphana University of Lüneburg, D-21339 Lüneburg, Germany

1. Abstract

The effect of laser beam welding process parameters on porosity formation and solidification cracking is examined for 5.0 mm thick Al-Li 2198 aluminum alloy specimens. Welding process parameters, like laser power, welding speed and the resulted linear heat-input, play a key role in the quality of laser beam welded joints. Therefore, the main objective of the present work is to identify the process window to produce autogenous (no filler wire used) welded joints with absence of cracks and pores. The effect of the welding parameters on microstructure in the welded zone was investigated using optical and scanning electron microscopy. The results showed that full penetration was not achieved when welding was performed at resulted linear heat inputs below 50 J/mm. The mechanical behavior of welded butt joints was investigated by hardness measurements and tensile and tests.

2. Introduction

Innovative Al-Li alloys have been recently developed and are supposed to replace conventional Al alloys, such as AA2024, in aerospace industry applications in the near future [1, 2]. Third generation Al-Li alloys such as AA2198 show a good balance between improved mechanical properties and damage tolerance capability [3]. These good mechanical properties are quite often associated with their tailored Li-concentration. New joining concepts have also been developed to lower structural weight and manufacturing cost. Laser beam welding (LBW) of AA2198 is a very promising method for joining aircraft structures. Replacing rivets of aluminum alloys with laser beam welded joints is an ongoing topic in the aerospace industry, which has been particularly realized for skin-stringer joints (e.g. Airbus A380, A318 and A340) [4, 5]. The main advantage of this joining technique is the input of high energy in a relatively small area. Additionally, high welding velocity and high degree of flexibility of the laser beam tool are some other advantages of this process. However, literature review on the optimization of LBW process parameters for third generation Al-Li alloys remains still rather limited.

3. Materials and experimental methods

AA2198 sheet material in T3 heat treatment condition was used in the present work. The weight percentage chemical composition of this alloy is <0.08% Si, 0.1% Fe, 2.9-3.5% Cu, <0.5% Mn, 0.25-0.8% Mg, 0.8-1.1% Li, 0.35% Zn, 0.04-0.18% Zr and Al remainder. The sheets had a 5.0 mm nominal thickness and were autogenously laser beam welded (without filler wire).

An Yb:YAG fiber laser (IPG YLS 8000) with maximum laser power of 8 kW was used for performing the welds. The LBW process was performed using the following process parameters:

- Laser power in the range between 5 kW and 8 kW;
- Laser beam welding in focus position (without defocusing);
- The welding speed in the range between 4m/min and 8 m/min.

To describe the effects of the LBW process parameter variations on the performance of the welds, the linear heat input (J/mm) is defined as the quotient from the used laser beam power (kW) and the welding speed (m/mm). Before welding, the plates were surface grinded and subsequently cleaned with alcohol to avoid hydrogen induced porosity that can degrade the quality of welded joints. Argon was used as a shielding gas with a gas flow rate of 5 l/min for all welding experiments. LBW was conducted parallel to the rolling direction of the sheet material.

4. Results and discussion

Radiography and optical microscopy were performed to investigate the effect of LBW process parameters on the resulting microstructure and appearance of the welding seams. Full penetration was achieved at linear heat inputs above 60 J/mm. Welds with the lowest porosity level were obtained at 8 kW laser power (Fig.1a). It was shown, that with increasing laser power, from 5 kW up to 8 kW and keeping the heat input at a constant value of 70 J/mm, the porosity level decreased but solidification cracks appeared (Fig.1b).

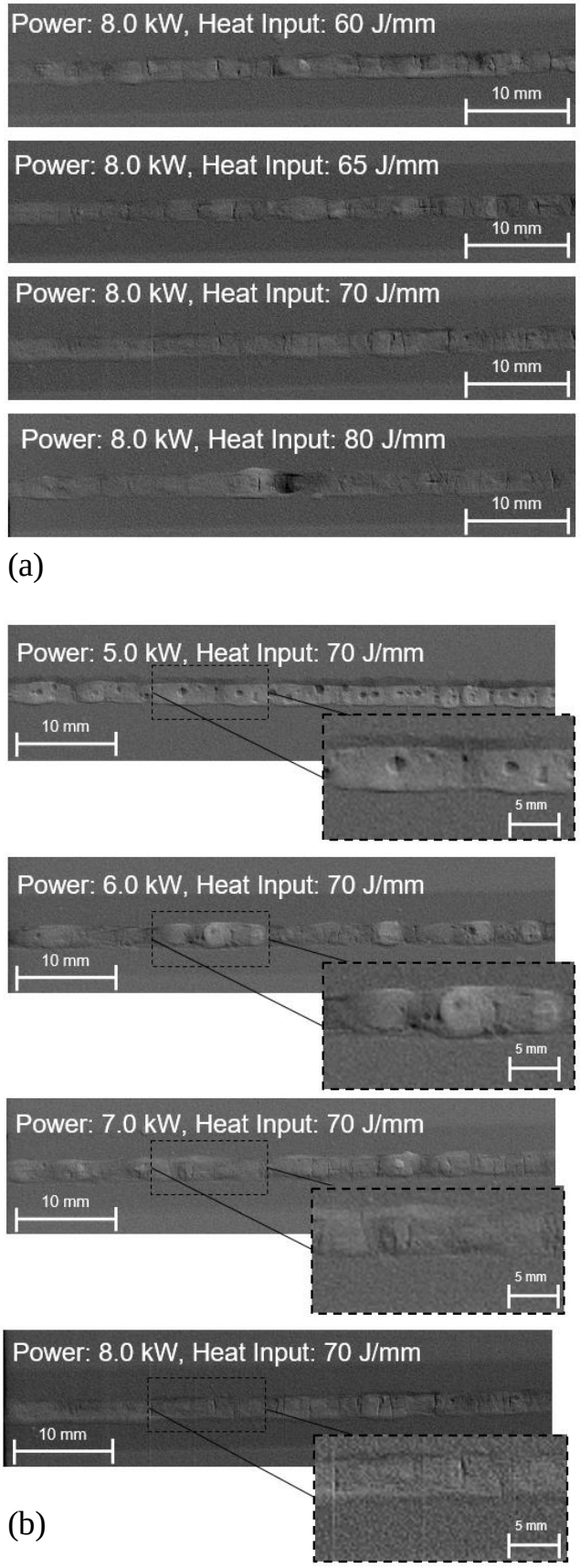

Figure 1. Radiographs with different laser beam welded parameters.

References

[1] N. D. Alexopoulos, E. Migklis, A. Stylianos, and D. P. Myriounis (2013). Fatigue behavior of the aeronautical Al-Li (2198) aluminum alloy under constant amplitude loading, *International Journal of Fatigue*, **56**, 95-105.

[2] R. J. Rioja and J. Liu (2012). The evolution of Al-Li base products for aerospace and space applications, *Metallurgical & Materials Transactions A*, **43(9)**, 3325-3337.

[3] T. Dursun and C. Soutis (2014). Recent developments in advanced aircraft aluminum alloys, *Materials and Design*, **56**, 862-871.

[4] J. Enz, S. Riekehr, V. Ventzke and N. Kashaev (2012). Influence of the local chemical composition on the mechanical properties of laser beam welded Al-Li alloys, *Physics Procedia*, **39**, 51-58.

[5] N. Kashaev, J. Enz, M. Horstmann, A. Groth, V. Ventzke, S. Riekehr and N. Huber (2013). Quality assessment of laser beam welded AA2198 integral structures, *27th Symposium of International Committee on Aeronautical Fatigue (ICAF)*, June 5-7, Jerusalem, Israel.

EXPERIMENTAL INVESTIGATION ON MACHINABILITY PARAMETERS IN TURNING OF CuZn39Pb3 BRASS ALLOY

N. M. Vaxevanidis[1], N. A. Fountas[1], A. Koutsomichalis[2] and J. D. Kechagias[3]
[1] School of Pedagogical and Technological Education (ASPETE), Department of Mechanical Engineering, Laboratory of Manufacturing Processes and Machine Tools (LMProMaT), ASPETE Campus, GR 14121, N. Heraklion, Greece
[2] Hellenic Air-Force Academy (HAFA), Faculty of Aerospace Studies, Dekelia Air Force Base, GR 19005, Greece
[3] Technological Educational Institute (TEI) of Thessaly, Mechanical Engineering Department, TEI Campus, GR 41110, Larissa, Greece

1. Introduction

Machinability of engineering materials is crucial for industrial manufacturing processes since it affects all the essential aspects involved, including workload, resources, surface integrity and part quality. Two basic machinability parameters are the surface texture, which is closely associated with the functional and the tribological performance of components and the cutting forces acting on the tool. Knowledge of the cutting forces is needed for estimation of power requirements and for the design of machine tool elements, tool-holders and fixtures, adequately rigid and free from vibration [1, 2].

Turning is the primary operation in metalworking industry for producing axisymmetric components. These components, typically, possesses critical features that require specific surface finish and the best possible functional behavior. The proper selection of cutting tools and process parameters for achieving high cutting performance in a turning operation is a critical task. An arc chain surface pattern is typical for turning but significant deviations appear due to irregular chip formation phenomena, such as built-up edge, discontinuous chip, very low feed rates, chatter and intense tool flank wear [2, 3].

The various manufacturing processes applied in industry produce the desired shapes of the components within prescribed dimensional tolerances and surface quality requirements. Therefore, any proposed description of a technological surface should take into account the features of the profile imparted by the machining process performed. In common industrial practice surface roughness is evaluated by profile amplitude parameters such as R_a (mean surface roughness) and R_t (maximum surface roughness) [4, 5].

The estimation of cutting force component magnitudes (with emphasis to the main cutting force) is of major importance for the metal cutting theory as well. A great number of interrelated parameters affect the cutting forces (i.e., operational parameters, cutting tool geometrical characteristics, coatings, etc), therefore the statistical analysis for proper modeling is an essential task [2, 6].

2. The experimental protocol

The work presented here investigates the influence of cutting conditions when longitudinally turning a brass alloy, on machinability indicators such as main cutting force F_c and surface roughness parameters R_a and R_t. Moreover, statistical regression models were developed, when possible, to express the correlation of the machining conditions with the imparted machinability characteristics.

An L18 mixed-level Taguchi Orthogonal Array experimental design was selected in order to study the effect of machining conditions, i.e., cutting speed (v), feed rate (s) and depth of cut (a) on surface roughness parameters; R_a and R_t, as well as on main cutting force component; F_c, when turning CuZn39Pb3 (CW614 - brass 583) alloy and to generate full quadratic prediction models. Note that studies concerning the microstructure and machinability of CuZn39Pb3 alloy have been already reported [7]. The surface roughness analysis was performed using a Rank Taylor-Hobson® Surtronic 3 profilometer equipped with the Talyprof® software whilst cutting force components were measured using a KISTLER® three-component dynamometer.

3. Results and conclusions

Indicative experimental results referring to the main cutting force, F_c and the surface roughness parameters R_a and R_t, are illustrated in Fig.1. Statistical analysis was performed in order to examine the variation of cutting conditions upon the selected surface roughness parameters and the main cutting force. MINITAB® 17 software was employed to perform the analysis and to obtain the necessary outputs for results interpretation. The main effects plots for parameters were produced to examine the influence of independent variables (cutting conditions) on the responses (F_c, R_a and R_t). More accurate results concerning the effects of machining parameters on the selected responses were obtained by conducting ANOVA analysis.

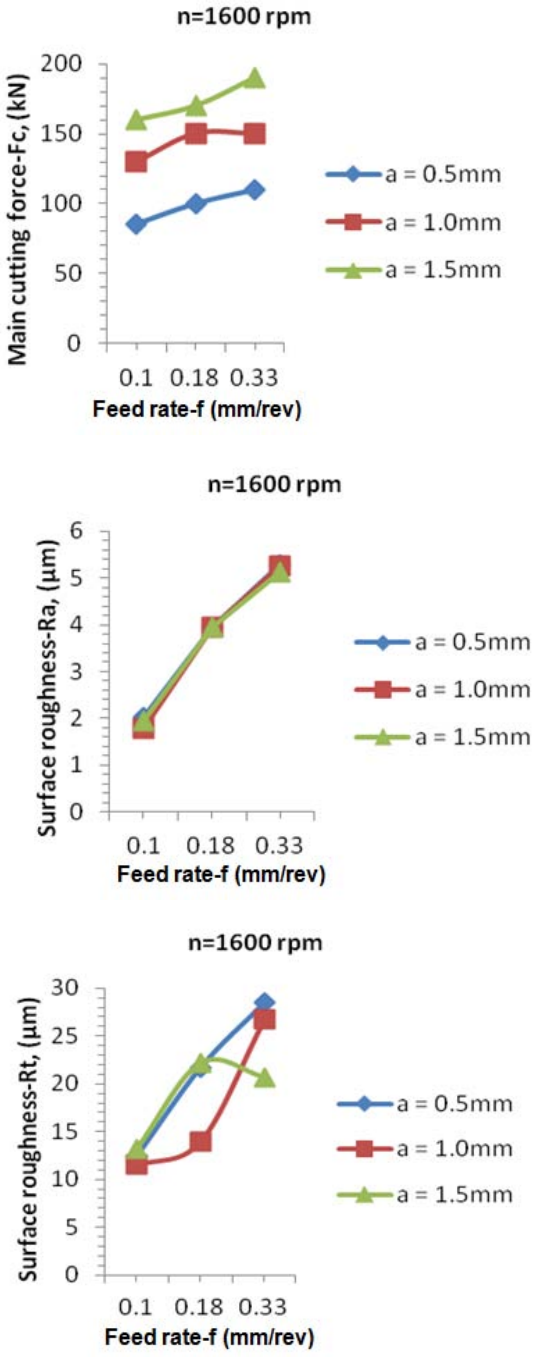

Figure 1. Variation of the main cutting force and the surface roughness in relation to the machining parameters.

Acknowledgements

The presentation of this work in the *1st International Conference of the GSEMM* was supported from the Special Account for Research of ASPETE through the funding program "Strengthening research of ASPETE faculty members".

References

[1] G. P. Petropoulos, C. N. Pandazaras and J. P. Davim (2010). Surface texture characterization and evaluation related to machining, in *Surface Integrity in Machining*, J. P. Davim (ed.), Springer, London, 37-66.

[2] N. M. Vaxevanidis, J. D. Kechagias, N. A. Fountas and D. E. Manolakos (2014). Evaluation of machinability in turning of engineering alloys by applying artificial neural networks, *Open Constr. & Building Technol. J.*, **8**, 389-399.

[3] W. Grzesik, B. Kruszynski and A. Ruszaj (2010). Surface integrity of machined surfaces, in *Surface Integrity in Machining*, J. P. Davim (ed.), Springer, London, 143-179.

[4] N. M. Vaxevanidis, N. Galanis, G. P. Petropoulos, N. Karalis, P. Vasilakakos and J. Sideris (2010). Surface roughness analysis in high speed-dry turning of tool steel, in *Proceedings of ESDA 2010: 10th Biennial ASME Conference on Engineering Systems Design and Analysis*, July 12-14, Istanbul, Turkey.

[5] G. P. Petropoulos, C. N. Pandazaras, N. M. Vaxevanidis and A. Antoniadis (2006). Multi-parameter identification and control of turned surface textures, *Int. J. Adv. Manuf. Technol.*, **29**, 118-128.

[6] N. M. Vaxevanidis, N. A. Fountas, J. Kechagias and D. E. Manolakos (2014). Estimation of main cutting force and surface roughness in turning of Ti-6Al-4V titanium alloy using design of experiments and artificial neural networks, in *Proceedings of the International Conference on Engineering and Applied Sciences Optimization (OPT-i)*, June 4-6, Kos, Greece.

[7] A. I. Toulfatzis, G. A. Pantazopoulos and A. S. Paipetis (2014). Fracture behavior and characterization of lead-free brass alloys for machining applications, *J. Mat. Eng. Perform.*, **23**, 3193-3206.

POWDER METALLURGY ROUTE ALUMINIUM FOAMS: A STUDY OF THE EFFECT OF POWDER MORPHOLOGY, COMPACTION PRESSURE AND FOAMING TEMPERATURE ON THE POROUS STRUCTURE

I. G. Papantoniou[1], D. I. Pantelis[2] and D. E. Manolakos[1]
[1] School of Mechanical Engineering, Manufacturing Technology Section,
National Technical University of Athens, Greece
[2] School of Naval Architecture and Marine Engineering,
Shipbuilding Technology Laboratory, National Technical University of Athens, Greece

1. General

The modern world needs new advanced materials with unique combination of properties that allow for new applications. Microcellular materials are among this new class of materials. Microcellular materials and specifically metallic foams have attracted the attention of scientific community because of their advanced combination of particular properties that they offer, compared to conventional solid metals. Such unique properties are their high strength to weight ratio, high energy absorption capacity, large specific surface, high gas and liquid permeability, and low thermal conductivity [1, 2].

Metal foams find many applications in areas such as the naval industry, aerospace, mechanical or chemical engineering and can be used as energy or sound absorbers, heat exchangers, filters and implants in medicine. The use of metal foams depends on their basic characteristics such as relative density, cell structure, wall thickness, strut integrity and cell morphology homogeneity. The most common type of metallic foam is the aluminium foam which is widely preferred due to its important mechanical and natural properties, high recyclability and non-toxicity [3, 4].

2. The experimental protocol

There is a significant number of ongoing research projects around the world aiming at cheaper and more standardized production of metal foams with high standards, because of their ever-increasing applications. The subject of this particular research is the production of metal foams using powder metallurgy route in order to further study and analyze the effect of different parameters in the foams final porosity and internal structure. In powder metallurgy route, metallic powder is mixed with a blowing agent and it is compacted to form a foamable precursor. Then the precursor is heated and formed in a furnace [5]. The advantage of this route is that the precursor can expand in a heated mould and the foam with a complicated shape can be made by mould filling [6].

In the present experimental procedure, the base material used were fine aluminium powder (Alfa Aesar, -325 mesh, 99.5%), coarse aluminium powder (Alfa Aesar, -40+325 mesh, 99.8%) and aluminium flakes (Alfa Aesar, APS 11 micron, 99.7%). Commercially available titanium hydride powder (with particle diameter < 45μm) was used as a blowing agent (Titanium(II) hydride, -325 mesh, 99%). Each aluminium powder was mixed with 0.6 w/w TiH_2 for one hour in a powder mixer. Ten grams of each mixture was then inserted carefully into a cylindrical stainless steel die, followed by a cold compaction, by the use of a mechanical press. For each mixture, five different compaction pressures were used in order to examine the effect of the compaction pressure combined with the morphology of the aluminium powder to the final porous structure after the foaming stage.

The precursor samples produced were led then to a furnace, so as the foaming procedure to take place under high temperatures. For each combination of aluminium powder and compaction pressure four discrete foaming temperatures were used: 650 °C, 700 °C, 750 °C and 800 °C. In all the experiments the foaming process was being monitored by a camera, connected to a computer for recording images (at a rate of 60 frames per second). Using the open-source image processing software ImageJ and the data from the camera the *porosity-time* (P_f - *t)* diagrams for each specimen were

created. The foaming time was 10 minutes, in order to observe all the foaming stages (nucleation, growth, peak, coarsening and decay).

3. Conclusions

From the analysis of the experimental results, the following concluding remarks can be drawn: Firstly, it should be noted that all the precursors with the aluminium flakes were collapsed just after the extrusion from the die. Hence, the specimens with the aluminium flakes were rejected from the following foaming stage. The maximum porosity - compaction pressure diagrams (resulted from the P_f - t diagrams) depicted that the porosity tends to grow by increasing the compaction pressure but stays stable for pressures higher than 700 MPa. The maximum porosity - foaming temperature diagram illustrated that by increasing the foaming temperature the final porosity scales up. Specifically, for sintering temperatures below the aluminium melting point, a minor foaming stage was observed. The maximum foaming was observed for 750 ^{o}C and 800 ^{o}C.

Additionally, all the foamed specimens with the fine aluminium powder presented 15-25% higher maximum porosity from the corresponding ones with the coarse aluminium powder.

Finally, additional specimens with the optimum parameters (fine aluminium, 700 MPa compaction pressure and 800 ^{o}C foaming temperature) were prepared and foamed at a holding time which corresponded to the maximum porosity (≈160 seconds). Compression tests were performed on those foamed specimens in order to investigate their s-e response. The curves were characterized by the typical initial elastic response, followed by a deformation plateau with a positive slope and finally a transition to densification. From the experimental s-e results of the foamed specimens, average compressive strength and density were calculated and presented for comparison with existing literature results [2] on periodic and stochastic metal foams.

References

[1] L. G. Gibson and M. F. Ashby (1997). *Cellular Solids, Structure and Properties*, 2nd ed. Cambridge University Press, Cambridge, UK.
[2] M. F. Ashby, A. G. Evans, N. A. Fleck, L. J. Gibson, J. W. Hutchinson and H. N. G. Wadley (2000). *Metal Foams: A Design Guide*. Butterworth-Heinemann, USA.
[3] J. Banhart (2001). Manufacture, characterization and application of cellular metals and metal foams, *Progr. Mater. Sci*., **46**, 559-632.
[4] A. Salimon, Y. Brechet, M. Ashby and A. Greer (2005). Potential applications for steel and titanium metal foams, *J. Mater. Sci*., **40**, 5793-5799.
[5] B. C. Allen and A. M. Sabroff (1963). *Method of making foamed metal*, US Patent 3,087,807.
[6] F. Baumgärtner, I. Duart and J. Banhart (2000). Industrialization of powder compact foaming process, *Adv. Eng. Mater*., **2**, 168-174.

EFFECT OF HEAT TREATMENT ON THE MECHANICAL BEHAVIOR OF ELECTRON BEAM WELDED Al-Mg-Si ALLOY SPECIMENS

V. Stergiou[1] and T. N. Examilioti[2]
[1] Special Processes & Laboratories Department,
Hellenic Aerospace Industry, 320 09 Schimatari, Greece
[2] Department of Financial Engineering and Management,
School of Engineering, University of the Aegean, Kountourioti 41, 82 132 Chios, Greece

1. Introduction

Aluminum alloys from 6xxx series are already applied in lower fuselage panels and processed with the welding process [1]. Aluminum alloys from 6xxx series, like AA6056 and AA6061, are widely used in the bottom of fuselage shell of the aircraft where strength and damage-tolerance properties are required. However, AA6056 did not meet the design criteria due to the low tolerance to damage, and therefore an improved variety of the alloy was developed. Innovative aluminum alloy 6156, due to the high damage tolerance capabilities, in comparison to its predecessor, is already applied to the bottom of the fuselage shell in different aircraft types, e.g. Airbus A380 [1]. The use of aluminum alloy with good weldability such as 6156 can reduce the weight of aircraft structures, by avoiding the traditional riveted joints in order to achieve a long-term increase in aircraft payload and also a lighter and stronger integral structure.

So far the literature review on aluminum alloy 6156 remains rather limited. The effect of ageing treatments on microstructure and hardness are reported by Lin et al. [2], Jin et al. [3] and Zhang et al. [4], while the effects of Ag addition on the long thermal stability of this alloy was reported by Zhang et al. [5].

In the present work, the effect of artificial ageing heat treatment before and after the welding process on the mechanical properties of (Al-Mg-Si) 6156-T4 aluminum alloy was investigated. Artificial ageing was performed under different conditions, namely to include all possible heat treatment conditions, like under-ageing (UA), peak-ageing (PA) and over-ageing (OA).

2. Materials and experimental methods

The material used for the present investigation was AA6156, which was received in T4 heat treatment condition with nominal thickness of 3.6 mm. The weight percentage chemical composition of this alloy is: 0.7-1.3% Si, 0.6-1.2% Mg, 0.7-1.1% Cu, 0.4-0.7%, <0.2% Fe, <0.25% Cr, 0.1-0.7% Zn and Al rem. No filler wire material was used for all investigated welding seams. Some specimens were artificially aged before the welding process (Before Welding Heat Treatment-BWHT) and some specimens were artificially aged post to the welding process (Post Welding Heat Treatment-PWHT). Artificial ageing conditions were performed at 170 ^{o}C and for different ageing times. The artificial ageing times were selected from the literature [6] so as to artificially age the material at all available ageing conditions, including under-ageing (UA), peak-ageing (PA) and over-ageing (OA) conditions.

3. Results and discussion

It is well known that the artificial ageing on such precipitation-hardened aluminum alloys has a profound effect on microstructural changes (precipitation of β'' particles), their size and population being directly related to the ageing conditions. Such second-phase precipitates (Mg_2Si), is well-known that have an impact on strength and ductility of the material, while it is also related with the capability of the material to resist fracture (fracture toughness). Fig.1a shows some representative tensile stress-strain curves for non-welded (reference) and welded specimens for various artificial

ageing conditions before welding (hereafter will be called as BWHT). Applying BWHT at 170 ^{o}C and for different ageing times, it was observed that the elongation at fracture shows a slight increase, when compared to the respective one without any heat treatment (welding at T4 condition).

Fig.1b shows representative load-crack mouth opening displacement (CMOD) plots of the resistance to fracture tests. The specimens without welding present essentially higher peak loads with increasing artificial ageing. On the contrary, BWHT specimens attain the same maximum load (around 4.7 kN). Moreover, it was shown that they have similar fracture toughness values.

All the results are explicitly discussed in the article and a correlation with resulting microstructure is attempted to assess their effect on the mechanical properties. Summing up, the results showed that the BWHT increases the tensile ductility and also presents higher decrease in fracture toughness. On the contrary, PWHT significantly increases the strength properties of the welded joints.

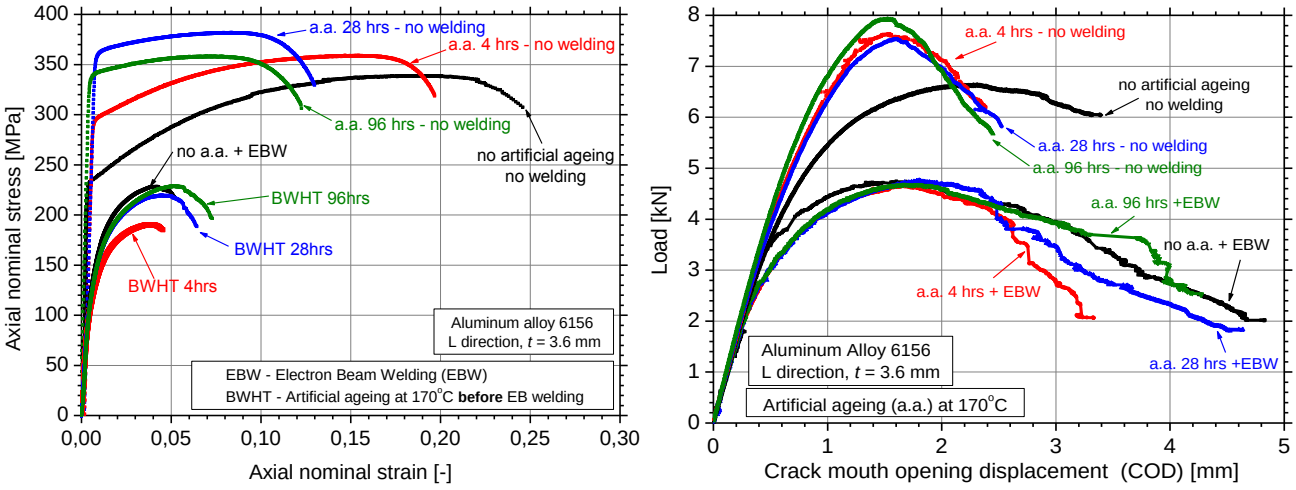

(a) (b)

Figure 1. Typical (a) tensile flow curves and (b) load-CMOD curves of artificially aged specimens before electron beam welding of aluminum alloy 6156 at 170 ^{o}C and comparison against non-welded specimens.

References

[1] P. Lequeu, P. Lassince and T. Warner (2007). Aluminum alloy development for the Airbus A380 Part 2, *Advanced Materials and Processes*, **165**, 41-44.

[2] L. Lin, Z. Zheng and J. Li (2012). Effect of aging treatment on the mechanical properties and corrosion behavior of 6156 aluminum alloy, *Rare Metal Materials and Engineering*, **41**, 1004-1009.

[3] K. Jin, Y. L. Deng, L. Zhou, L. Wan and X. M. Zhang (2011). Investigation on artificial aging and creep aging of 6156 Aluminum Alloy, *Journal of Aeronautical Materials*, **31**, 18-22.

[4] H. Zhang Z. Zheng, S. Zhong J. X. Luo and J. Zhong (2012). Effects of two-step aging treatment on microstructure and properties of 6156 aluminum alloy, *Chinese Journal of Nonferrous Metals*, **22**, 1025-1032.

[5] H. Zhang, Z. Zheng, Y. Lin, X. Luo and J. Zhong (2012). Effects of Ag addition on the microstructure and thermal stability of 6156 alloy, *Journal of Materials Science*, **47**, 4101-4109.

[6] G. Stefanou, E. Migklis, S. K. Kourkoulis and N. D. Alexopoulos (2014). Mechanical behaviour of aeronautical aluminum alloy 6156 for different artificial aging conditions, in *Proceedings of International Symposium on Aircraft Materials (ACMA 2014)*, Marrakech, Morocco, 23-26 April, 2014.

Polymers and Composites

MECHANICAL PROPERTIES OF UNIDIRECTIONAL NATURAL FIBER - POLYMER COMPOSITES

P. Georgiopoulos, A. Christopoulos and E. Kontou
National Technical University of Athens, School of Applied Mathematical and Physical Sciences, Department of Mechanics, Laboratory for Testing and Materials, 157 73 Athens, Greece

1. Introduction

Recently, there is a trend of employing natural fibers, derived from renewable resources, for the reinforcement of polymeric matrices. The produced composite materials are environementally friendly, and meet the rquirement for developing sustainable materials.

In the present work, natural fiber-polymeric composite materials have been prepared and their thermomechanical performance was experimentally studied, in terms of various experimental methods. The materials are unidirectional flax fiber composites, based on several types of biodegradable polymeric matrices. The so-called film-stacking method has been employed, to obtain unidirectional fiber composites, leading to a high improvement of the mechanical properties of the composites prepared. The mechanical enhancement is mainly dependent on the fiber-matrix adhesion, which leads to an efective stress transfer from the matrix to the fiber [1].

The addition of flax fibers with this method was proved to result to a significant toughening of the polymers under investigation. For a further improvement of the composites mechanical enhancement, three different surface treatments of flax fibers, namely silanization, plasticization and treatment with maleic anhydride, were employed [2]. The effect of the fibers treatment on the mechanical properties of the composites has been comparatively studied by various experimental techniques. Focusing on silane treatment, the amount of silane treatment was separately studied, by three-point-bending, creep and dynamic mechanical analysis tests.

2. Materials

Three different types of polymer biodegradable matrices, namely Poly-lactic Acid (PLA), a biodegradable polymer, under the commercial name Ecovio®, which consists of 45% of renewable resources and Bionolle® 1001, based on Poly-butylene succinate were employed. By applying the film stacking method, plates of unidirectional fiber polymer composites were prepared, at the same average weight fraction 22% and an average thickness of 1 mm.

3. Flax fiber processing

Three different methods improving the compatibility of flax fibers with the matrix were employed: silanization, plasticization and maleic anhydride treatment of the fibers. Regarding silanization, flax fibers were treated with amino-silane coupling agent, at different silane content values, in order to optimize the composite properties regarding this parameter.

4. Experiments

Tensile testing, dynamic mechanical analysis in a wide range of frequencies and temperatures and creep experiments in terms of flexural mode of deformation, as well as scanning electron microscopy (SEM) have been employed in the present work.

5. Results

The presence of unidirectional flax fibers result to a significant mechanical enhancement, while hereafter, depending on the surface modification type, Young's modulus (Fig.1), flexural modulus, as well as storage modulus were found to be further increased. Regarding Young's modulus, its values

varied between 8 GPa for ECflax and 25 GPa for ECflax/MA and PLAflax/MA, whereas the highest tensile strength was observed in the untreated flax fiber composites, followed by the Silane and TBC treated ones. A similar response was obtained by the flexural experiments. All flax fiber composites exhibit an improved resistance to creep, therefore they are promising for long-term load-bearing applications.

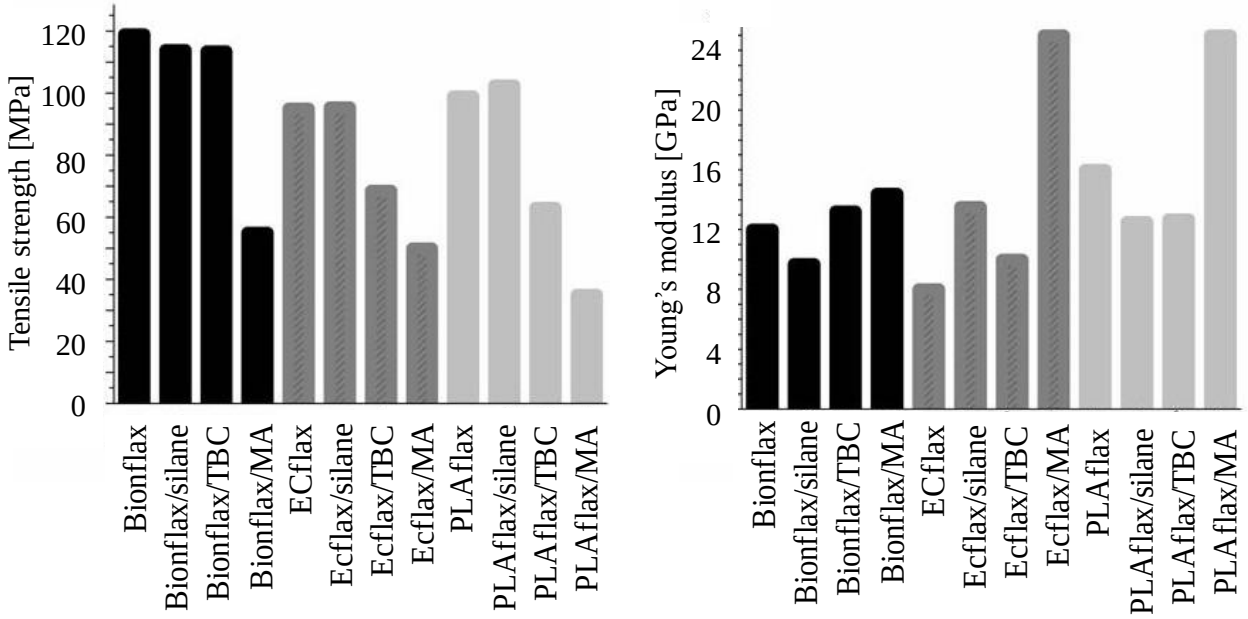

Figure 1. Tensile results of the composites with different fiber treatments.

Regarding silanization, it has been found that silane loading over a specific amount results to deterioration of the composite's properties, compared with lower levels of silane treatment (Fig.2). Both three-point-bending and creep results, confirm that optimum treatment is achieved by silane content between 1-2 % w/w (silane/fiber weight).

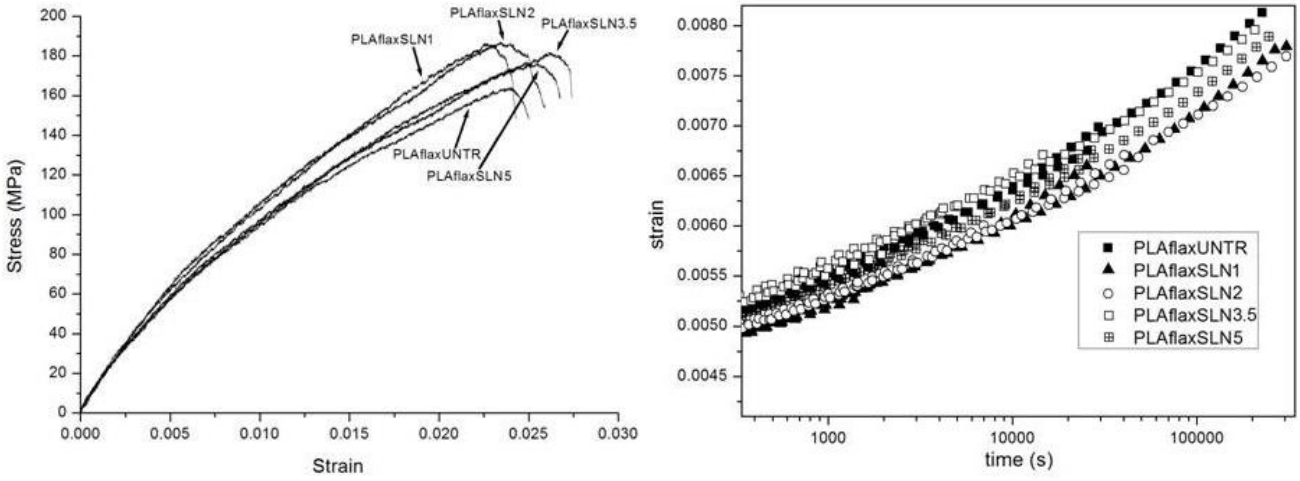

Figure 2. Three-point bending (left) and creep (right) results of silane treated composites with different silane content.

References

[1] P. Georgiopoulos, A. Christopoulos, S. Koutsoubis and E. Kontou (2016). The effect of surface treatment on the performance of flax/biodegradable composites, *Composites Part B,* **106,** 88-98.

[2] S. Alix, E. Philippe, A. Bessadok, L. Lebrun, C. Morvan and S. Marais (2009). Effect of chemical treatment on water sorption and mechanical properties of flax fibres, *Bioresour Technol*, **100(20)**, 4742-4749.

TENSILE PERFORMANCE OF GRAPHENE NANOPLATELETS/GLASS FABRIC/EPOXY NANOCOMPOSITE LAMINAE

G. V. Seretis, A. K. Polyzou, D. E. Manolakos and C. G. Provatidis
National Technical University of Athens,
School of Mechanical Engineering, 9 Heroon Polytechniou Str., 15780 Athens, Greece

1. General

In this paper, the tensile performance of hand lay-up produced graphene nanoplatelets (GNPs) reinforced E-glass fabric/epoxy nanocomposite laminae was investigated. The GNPs contents tested were ranging from 1% w.t. to 5% w.t., using an increasing step of 1%. Two different types of E-glass fabric, i.e. Twill 2×2 and Uni-Directional, were used to produce the tested nanocomposite laminae. The tensile response of the produced nanocomposites is being explained by an inter-yarn friction mechanism which takes place at the weaving nodes and it is controlled by the GNPs content in each specimens' series as well as by the settling of the GNPs onto the surface of the fiberglass fibrils.

Due to the "young" age of the specific nanoparticles, graphene nanoplatelets (GNPs) reinforced nanocomposites have been limited investigated as per the dispersion techniques and methods, which are still being developed, and their mechanical and physical properties. Tensile properties are of the most important mechanical properties for all composite/nanocomposite materials as well as for all engineering materials [1-3].

This study focuses on the effect of the GNPs content on the tensile performance of GNPs/glass fabric/epoxy nanocomposites. Five different GNPs contents were tested, i.e. 1%, 2%, 3%, 4% and 5% w.t., for two different specimens' series. For the specimens of the first series a Twill 2×2 E-glass fabric and for the specimens of the second series a Uni-Directional E-glass fabric was employed. The specimens were investigated using a scanning electron microscope as well as an atomic force microscope.

2. Materials and specimens

The medium viscosity epoxy system ES35A/B (ES35A monomer and ES35B hardener) was used as matrix material for the composite laminae investigated in the present study. Two E-glass fabric types were used for matrix reinforcement, a Twill 2×2 (T2×2) and a Uni-Directional (UD), the properties of which can be found in Table 1. Pre-dried graphene nanoplatelets (GNPs) of surface area (S.A.) 500 m^2/g were also used as additives, to produce a particulate nanocomposite matrix material.

Fabric type	**Twill 2x2**	**Uni-Directional**
Filaments/yarn	1141	3230
Average yarn linear density [dtex]	1.9	2.3
Density [g/m^2]	300	600
Thickness [mm]	0.2	0.25
Filaments diameter [μm]	12 μm	9 μm

Table 1. Properties of the fabric types used.

After the hand lay-up process used for nanocomposite laminae production, each specimen was left to cure in ambient conditions for one week, according to the guidelines of the manufacturer for the curing process. Five specimens of each GNPs content and of each fabric type were prepared and underwent tensile test.

3. Analysis

To evaluate the proper embodiment of the GNPs into both the epoxy matrix and the fibers, i.e., whether the GNPs were located between the fibrils, microstructural investigation of the produced nanocomposites was carried out using a scanning electron microscope (SEM) and an atomic force microscope (AFM).

A typical example of the observation of a GNP using the above equipment is given in Fig. 1. Graphene nanoplatelets (GNPs) reinforced glass fabric/epoxy nanocomposite laminae of different GNPs contents were produced using two different E-glass fabric types. The produced nanocomposite specimens were investigated as per their tensile performance and examined using a scanning electron microscope (SEM) and an atomic force microscope (AFM).

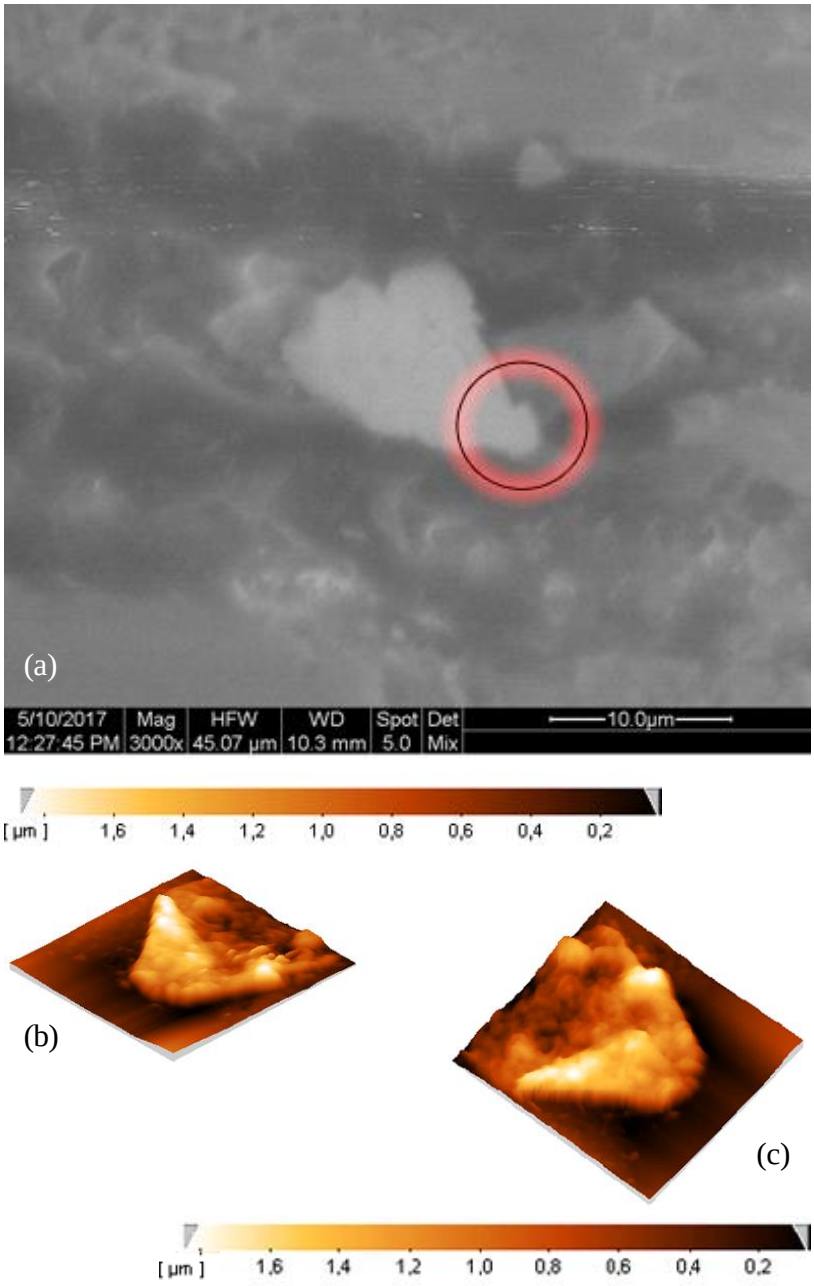

Figure 1. (a) SEM micrograph showing a GNP in the epoxy matrix and (b, c) AFM micrographs showing details of its boundary.

References

[1] G. V. Seretis, G. Kouzilos, D. E. Manolakos and C. G. Provatidis (2017). On the graphene nanoplatelets reinforcement of hand lay-up glass fabric/epoxy laminated composites, *Compos. Part B-Eng.*, **118**, 26-32.

[2] G. Gusel and H. Deveci (2017). Physico-mechanical, thermal, and coating properties of composite materials prepared with epoxy resin/steel slag, *Polymer. Compos.*, **38(9)**, 1974-1981.

[3] C. L. Wu, M. Q. Zhang, M. Z. Rong and K. Friedrich (2002). Tensile performance improvement of low nanoparticles filled-polypropylene composites, *Compos. Sci. Technol.*, **62**, 1327-1340.

A COMPARATIVE THERMOMECHANICAL STUDY OF FERRITE / POLYMER NANOCOMPOSITES

A. Sanida, S. G. Stavropoulos and G. C. Psarras
Smart Materials & Nanodielectrics Laboratory, Department of Materials Science, School of Natural Sciences, University of Patras, Patras 26504, Greece

1. Introduction

Organic-inorganic nanocomposites combine advantages of inorganic materials (mechanical strength, electrical and magnetic properties and thermal stability) and organic polymers (flexibility, dielectric, ductility and processibility), which are difficult to be obtained from a single component [1]. Furthermore, the magnetic properties of the nanocomposite can be simultaneously improved by using a suitable particulate material, such as ferrites [2].

Ferrites can be divided into three important classes based on their specific crystal structure, namely: (a) Soft ferrites with the garnet structure such as the microwave ferrites (e.g: YIG), (b) Soft ferrites with the cubic spinel structure such as $ZnFe_2O_4$, and Fe_3O_4 ferrites and (c) Hard ferrites with the magnetoplumbite (hexagonal) structure such as Ba and Sr hexaferrites. Due to their good magnetic and electrical properties, ferrites are used predominately in three areas of electronics: low level applications, power applications, and Electro-Magnetic Interference (EMI) suppression. The breadth of application of ferrites in electronic circuitry continues to grow. The wide range of possible geometries, the continuing improvements in material characteristics and their relative cost-effectiveness make ferrite components the choice for both conventional and innovative applications [3]. There is a growing demand for multifunctional composites to meet special requirements of electronic components [2]. A probable drawback of these devices could be not their electromagnetic behavior but their thermomechanical stability, which is the exact purpose of this study.

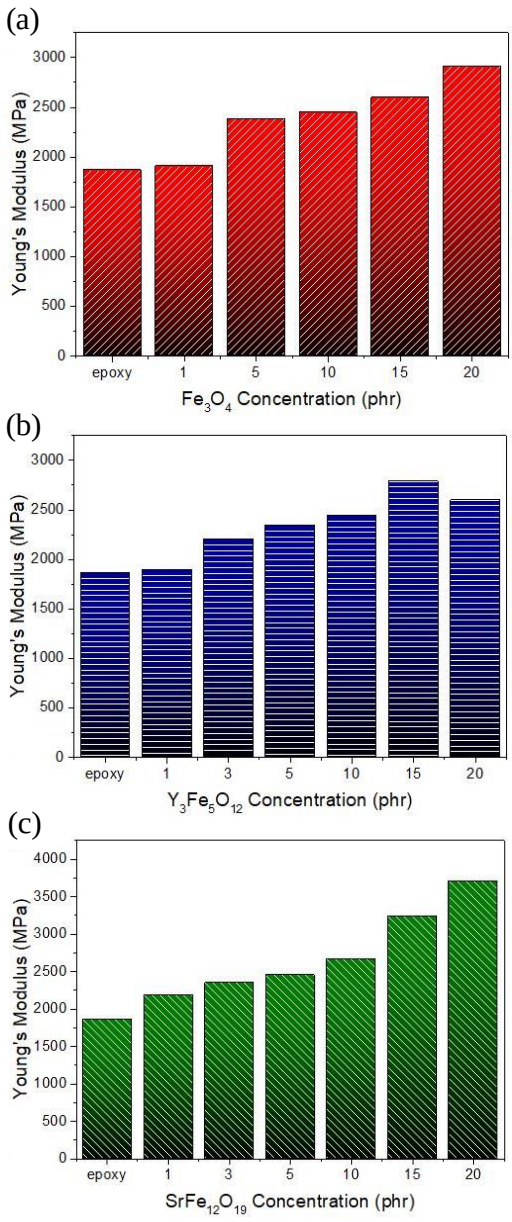

Figure 1. Young's modulus versus the concentration, for nanocomposites with: (a) Fe_3O_4, (b) $Y_3Fe_5O_{12}$ and (c) $SrFe_{12}O_{19}$ nanoparticles.

2. The experimental protocol

In the present study, series of nanocomposite systems consisting of an epoxy resin as matrix and five different magnetic iron oxides nanoparticles (YIG, $ZnFe_2O_4$, Fe_3O_4, $BaFe_{12}O_{19}$ and $SrFe_{12}O_{19}$) as reinforcing phase, have been prepared and studied, varying the filler content. Specimens' morphology was assessed via Scanning Electron Microscopy (SEM). The thermal properties were investigated by Thermogravimetric Analysis (TGA) and Differential Scanning Calorimetry (DSC) and the mechanical characterization was conducted via Dynamic Mechanical Analysis (DMA) and static tensile tests.

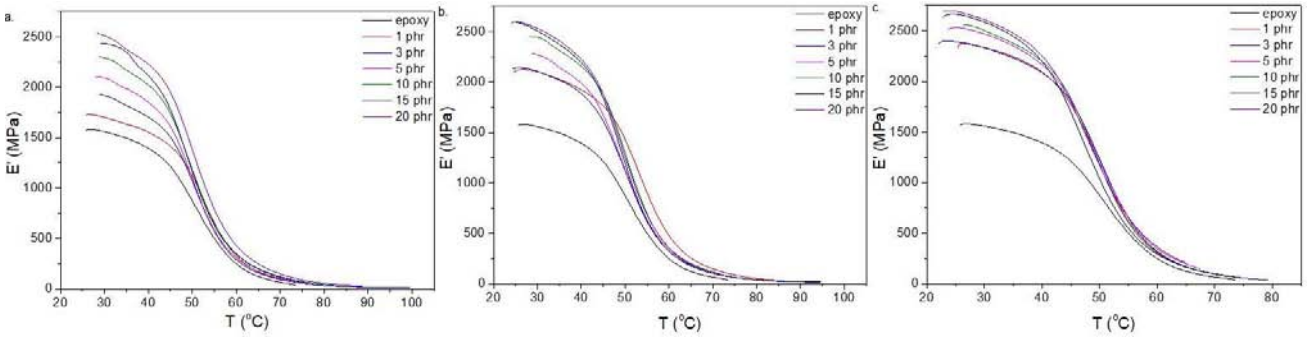

Figure 2. Storage modulus as a function of temperature, for the nanocomposites with: (a) Fe_3O_4, (b) $Y_3Fe_5O_{12}$ and (c) $SrFe_{12}O_{19}$ nanoparticles.

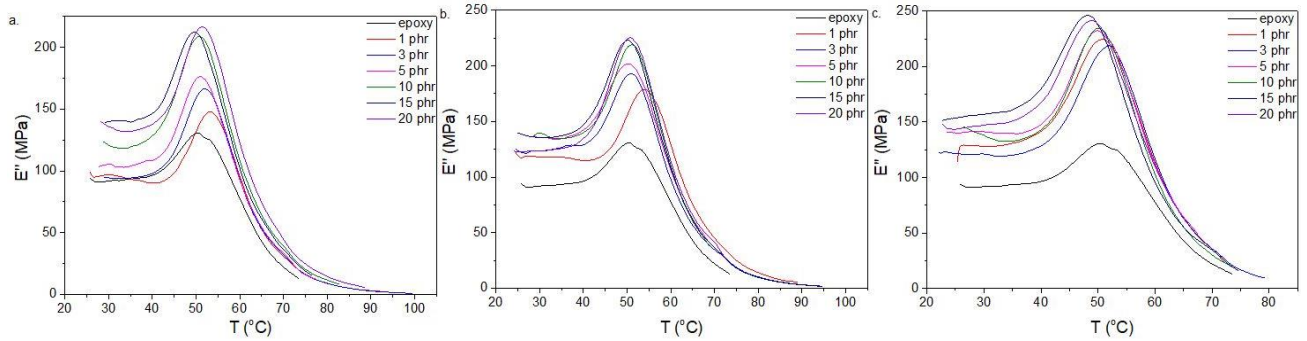

Figure 3. Loss modulus as a function of temperature, for the nanocomposites with: (a) Fe_3O_4, (b) $Y_3Fe_5O_{12}$ and (c) $SrFe_{12}O_{19}$ nanoparticles.

3. Results and conclusions

Experimental data revealed increasing values of Young's modulus and storage modulus with the addition of filler due to the enhancement in stiffness of the material, Figs.1 and 2. The achieved increase varies with filler type and optimum performance corresponds to different reinforcing material at low, moderate and high filler content.

Relaxation phenomena arising in polymer composites are related to the polymer matrix and the presence of filler. For all nanocomposites, a relaxation attributed to the glass to rubber transition of the polymer matrix was identified in the DMA (Fig.3) and DSC measurements. The characteristic temperature of this transition (T_g) can increase, decrease or remain constant depending on the matrix-inclusions interactions which can be attractive, repulsive or neutral respectively [4].

Acknowledgments

This research has been financed by the General Secretariat for Research and Technology (GSRT) and the Hellenic Foundation for Research and Innovation (HFRI).

References

[1] A. H. Elsayed et al. (2011). Synthesis and properties of polyaniline/ferrites nanocomposites, *Int. J. Electrochem. Sci.*, **6**, 206-221.

[2] L. A. Ramajo et al. (2009). Dielectric and magnetic response of Fe_3O_4/epoxy composites, *Compos. Part A Appl. Sci. Manuf.*, **40**, 388–393.

[3] V.- A. Scarlatache et al. (2012). Magnetic and dielectric losses of a nanocomposites polymer matrix reinforced with ferromagnetic powders, in *Procedings of 2012 Int. Conf. Expo. Electr. Power Eng., IEEE,* 125-128.

[4] A. Sanida, S. G. Stavropoulos, T. Speliotis and G. C. Psarras (2017). Development, characterization, energy storage and interface dielectric properties in $SrFe_{12}O_{19}$/epoxy nanocomposites, *Polymer*., **120**, 73-81.

AN EXPERIMENTAL EVALUATION OF MICRO-DAMAGE IN METAL MATRIX COMPOSITES BY MEANS OF A SEM - EPMA TECHNIQUE

V. N. Kytopoulos[1], A. Altzoumailis[2], J. Venetis[1] and E. Sideridis[1]
[1] Laboratory of Testing and Materials, Department of Mechanics
School of Applied Mathematical and Physical Sciences
National Technical University of Athens, Theocaris Building, 157 73, Zografou, Greece
[2] School of Chemical Engineering, Section of Chemical Sciences, NTUA, Greece
National Technical University of Athens, Theocaris Building, 157 73, Zografou, Greece

1. General

In this study an experimental technique is presented, permitting evaluation of mechanical damage in solid materials. The specific technique is based on the principle of Electron Probe Microanalysis (EPMA) by which certain analytical possibilities of the Scanning Electron Microscopy (SEM) are used [1-3]. In this sense, the main scope of the present study is to attempt application of this technique for the determination of micro-cracking damage in certain edge-cracked metal matrix composites (MMCs). Based on previous similar studies [4, 5] the present investigation has shown that by this technique the micro-cracking distribution ahead of an edge-crack under tensile loading conditions can be determined with relatively high reliability.

2. The experimental protocol

To demonstrate the above statement two types of MMCs were selected to be investigated, namely the BP8090 Al-Li and the BP2124 Al-Cu, reinforced with fine SiC particles. The mechanical properties and constants of both materials are described analytically in references [6, 7]. The specimens were shaped according to the dog-bone configuration and an edge crack was machined using a rotation cutting disc of thickness 300 μm. The specimens were subjected to quasi-static tensile loading (in-situ on the scanning electron microscope) up to a stress-level approaching the materials' ultimate stress. At the specific stress the loading process was terminated and the EPMA technique was applied. An adequate scanning range and duration of the electron beam ahead of the edge-crack-root was selected.

The basic physical principle of the EPMA technique can be shortly outlined as follows: Due to interactions of the electron beam with the material, certain characteristic X-rays are emitted from surface and subsurface layers of the scanned volume of the material. The collected X-rays are then measured and used as a local signal intensity, I, of the specimen (Fig.1).

Knowing that for the volumetric microcracking damage, D, it holds that $D \sim 1/\rho$ (where ρ is the density of the material), and, also, that $I \sim \rho$, it follows that $D \sim 1/I$. In other words, the experiment consists in obtaining a modulation of the X-ray signal intensity with local changes in the materials density. Consequently, by this simple relationship the local changes of microcracking damage can be properly evaluated and analyzed experimentally.

3. Discussion and conclusions

The experimental data gathered revealed that, within the experimental scatter range and under the same loading conditions, the MMC material with higher ductility of the matrix exhibits a higher damage degree compared to the MMC material with matrix of lower ductility. This behavior can be explained by the fact that larger differences between matrix ductility and SiC-inclusions may result to a corresponding larger misfit and disaccommodation degree between inclusion and matrix. This, in turn, leads to an associated intensive micro-cracking and debonding damage activity, which takes place within the interphase of the composites.

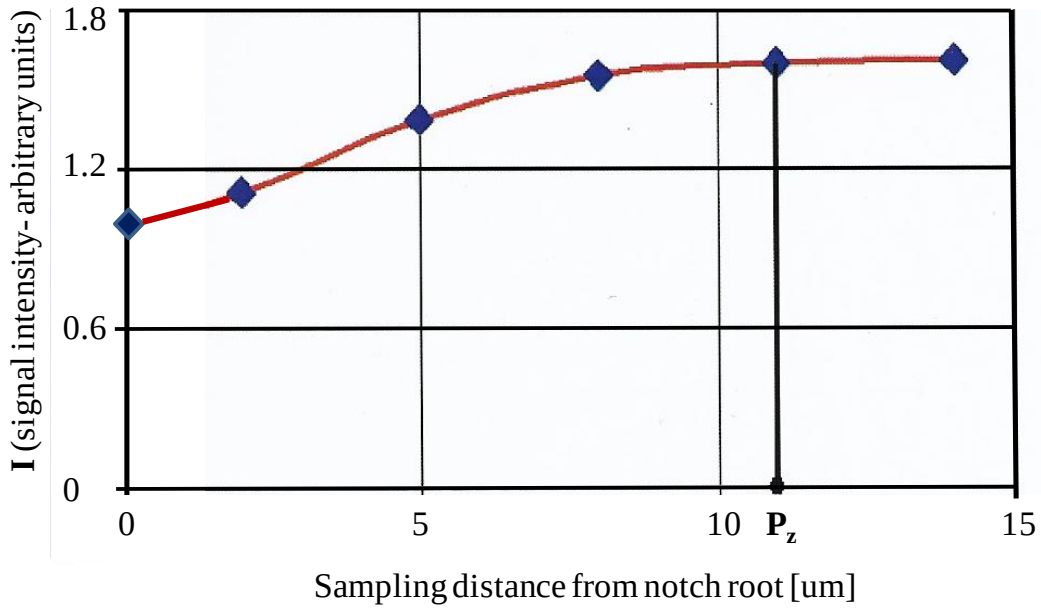

Figure 1. The intensity of the signal (expressed in arbitrary units) versus the sampling distance from the root of the notch.

Furthermore, it was also shown that, increasing deformation rate tends to increase the damage activity ahead of edge-crack, a fact that should be equivalent with a strain rate-induced embrittlement behavior of the material. This behavior seems to be more pronounced in the MMC-material with higher matrix ductility.

References

[1] J. Goldstein, D. E. Newbury, P. Echlin, D. C. Joy, A. D. Romig Jr., C. E. Lyman, C. Fiori and E. Lifshin (1992). *Scanning Electron Microscopy and X-Ray Microanalysis, A Text for Biologists, Material Scientists, and Geologists*, 2nd edition, Plenum Press, New York and London.

[2] L. Reimer (1998). *Scanning Electron Microscopy, Physics of Image Formation and Microanalysis*, 2nd edition, Springer-Verlag.

[3] P. E. J. Flewitt and R. K. Wild (1994). *Physical Methods for Materials Characterisation*, Institute of Physics Publishing, Bristol and Philadelphia.

[4] V. N. Kytopoulos, Ch. Riga and S. K. Kourkoulis (2007). Notch root opening displacement versus damage for particulate MMCs, in *Proceedings of the 13th International Conference on Experimental Mechanics (Alexandroupolis, Thrace, Greece, 1-6 July 2007): Experimental Analysis of Nano and Engineering Materials and Structures*, E. E. Gdoutos (ed.), Springer A. A., Dordrecht, The Netherlands, 133-134.

[5] G. Papadopoulos and V. N. Kytopoulos (2001). Micro-failure behaviour of Al_2O_3-Ceramics studied by X-ray EPMA, in *Proceedings of the 8th Annual International Conference on Composites Engineering (ICCE/8)*, D. Hui (ed.), Tenerife, Canary Islands, Spain, August 5-11, 2001, 715-716.

[6] S. Saragas, S. K. Kourkoulis and N. P. Andrianopoulos (1996). A comparative study of COD measurements for novel metal matrix composites and alloys. *Int. J. Fract.*, **79(2)**, 179-187.

[7] N. P. Andrianopoulos, S. K. Kourkoulis and S. Saragas (1997). COD measurements and optimum exploitation of metal matrix composites for aerospace applications, *Engng. Fract. Mech.*, **57(5)**, 565-576.

Metals

THE EFFECT OF ARTIFICIAL AGEING HEAT TREATMENT ON THE TENSILE PROPERTIES OF LASER BEAM-WELDED AA2198 JOINTS

D. Karanikolas[1], N. Kashaev[2], S. Riekehr[2], J. Enz[2] and N. D. Alexopoulos[1]
[1] University of the Aegean, Dept. of Financial Engineering and Management, 82132 Chios, Greece
[2] Helmholtz-Zentrum Geesthacht, Institute of Materials Research, Materials Mechanics, Max-Planck-Str. 1, D-21502 Geesthacht, Germany

1. Introduction

Structural airframes are primarily joined by riveted Al-alloy panels of skin/stringer configurations. During the last decades, the aerospace industries focus on reducing manufacturing and operational costs along with increasing damage tolerance of aircrafts. Hence, there is an increasing demand for new attractive ways to replace the conventional riveting techniques in airframes that is well-known that reduce fatigue properties and increase structural weight. Advanced welding technologies such as friction stir and laser beam welding are considered as candidate processes to replace riveting [1]. Welding processes along with the incorporation of third generation aluminium-lithium alloys, can lead to the reduction of the airplane's structural weight by 15% [1]. Their main advantages can be summarized to the low density, increased modulus of elasticity, good damage tolerance capabilities, and increased combination of strength and ductility properties. Their mechanical properties are quite often associated with the complex microstructure and precipitation system including the formation of several strengthening precipitates such as δ' (Al_3Li), T_1 (Al_2CuLi) and θ' (Al_2Cu) [2].

Difficulties on welding Al-Li alloys includes unstable key-hole as well as intermittent closure that may result in gas entrapment, macro-pores and hot cracking that leads to the necessity of optimizing the welding process parameters [3]. In the present work, the effect of artificial ageing heat treatment on the welding performance as well as on tensile mechanical behavior of laser beam welded aluminium alloy 2198 is investigated. In case of high cracking sensitivity of a certain Al-alloy due to its chemical composition, the exploitation of filler wire as well as the adjustment of the laser beam welding parameters were investigated. Two different filler wires were examined, namely AA 4047 (Al-Si wire) and AA2319 (Al-Cu wire) having 1.2 and 1.0 mm diameter, respectively [4].

2. Experimental procedure

In order to evaluate the weldability of materials, a number of factors that affects the characteristics of the weld were examined. In the present case, four factors typically dictate weldability: (1) mechanical property degradation, or loss of weld joint "efficiency", (2) susceptibility to cracking during fabrication, usually due to solidification or liquation cracking mechanisms, (3) porosity formation and (4) corrosion resistance. An IPG - YLS 10000 laser power of 10 kW was chosen for the welding with an initial beam diameter of 746 μm (in focus) and a KUKA industrial robot of 6 axis movement and a maximum welding speed of 10^4 mm/min. The main process parameters examined were the laser power, the velocity of the laser, the filler wire velocity and the filler wire feeder angle in order to obtain the optimum welding. Since all these factors are influenced by the microstructure, their discussion is prefaced by a section on microstructure evolution [5].The hardness tests were performed using a HMV-2000 Hardness Tester from Struers, according to ISO6507-1:2004 standard. Tensile specimens were machined from the welded sheets of 3.2 mm nominal thickness from the transverse (T) rolling direction, according to ASTM standards. Some specimens were post-weld heat treated (PWHT) and some were heat treated before the welding process (BWHT) at 170^{o}C and for different ageing times so as to simulate all possible ageing conditions, namely under-ageing (UA), peak-ageing (PA) and over-ageing (OA). Tensile tests were carried out using a servo-hydraulic Instron 100 kN testing machine. An extensometer was attached to the specimen surface at the gauge length. The ASTM E8 specification was adopted at a constant strain rate equal to 0.833 s^{-1}.

3. Results and discussion

The experimental results showed that using filler wire AA4047, more sound joints were produced with the absence of structural faults. This was not the case for filler wire AA2319, where hot cracking and porosity were observed. The angle of the filler wire feeder was found to play a significant role on the surface of the welded seam and the distribution of the filler material during welding. As expected, filler wire AA4047 is less sensitive to artificial ageing conditions (Fig.1) than AA2319 (Fig.2) due to low precipitation fraction that has a profound effect on the evaluated tensile properties.

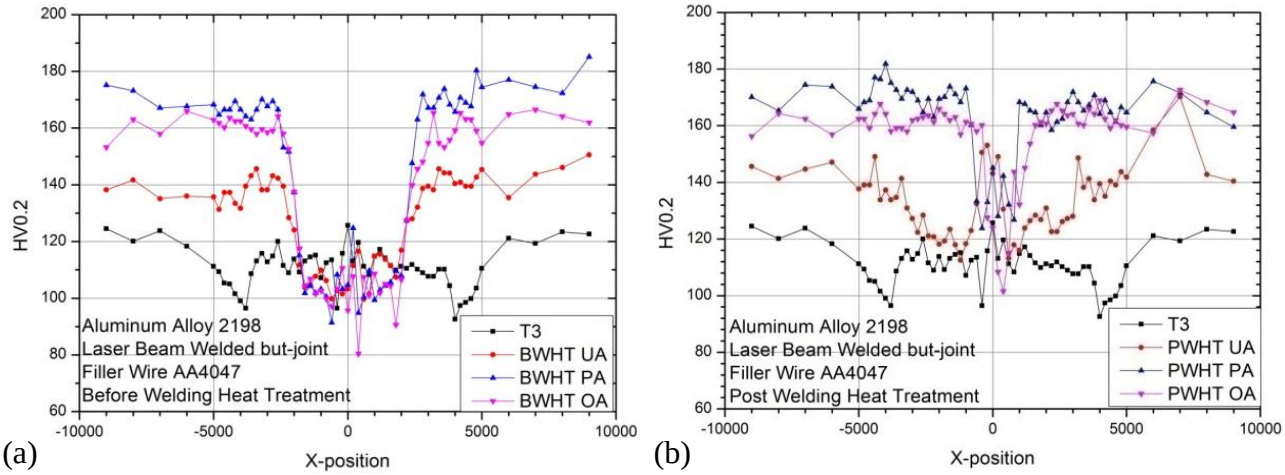

Figure 1. Microhardness variation in the weld region determined at the middle of the cross section of the LBW joint with AA4047 filler wire. (a) BWHT specimens, (b) PWHT specimens.

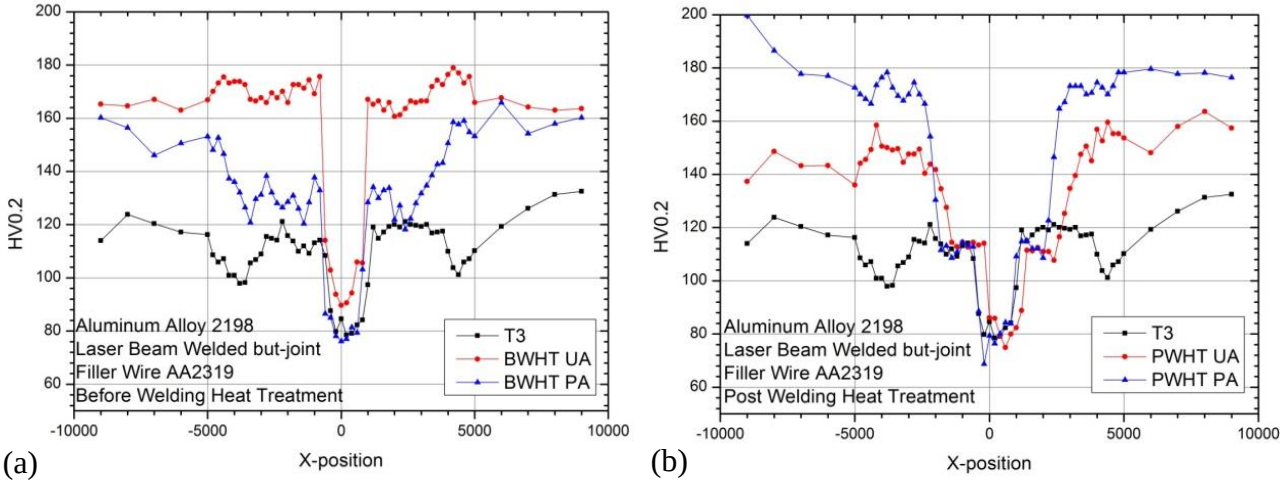

Figure 2. Microhardness variation in the weld region determined at the middle of the cross section of the LBW joint with AA2319 filler wire: (a) BWHT specimens, (b) PWHT specimens.

References

[1] N. D. Alexopoulos, E. Migklis, A. Stylianos and D. P. Myriounis (2013). Fatigue behavior of the aeronautical Al-Li (2198) aluminum alloy under constant amplitude loading, *Int. J. Fatigue*, **56**, 95-105.

[2] H. Li, Y. Tang, Z. Zeng, Z. Zheng and F. Zheng (2008). Effect of ageing time on strength and microstructures of an Al-Cu-Li-Zn-Mg-Mn-Zr alloy, *Mater. Sci. Eng. A*, **498**, 314-320.

[3] V. Alfieri, F. Caiazzo and V. Sergi (2015). Autogenous laser welding of AA 2024 aluminium alloy: Process issues and bead features, *Procedia CIRP*, **33**, 406-411.

[4] J. Enz, S. Riekehr, V. Ventzke, N. Huber and N. Kashaev (2016). Fibre laser welding of high-alloyed Al–Zn–Mg–Cu alloys, *J. Mater. Process. Technol.*, **237**, 155-162.

[5] A. Kostrivas and J. C. Lippold (1999). Weldability of Li-bearing aluminium alloys, *Int Mater Rev.* **44**, 217-237.

AN EXPERIMENTAL STUDY FOR THE CHARACTERIZATION OF ELASTIC-BRITTLE FRACTURE BEHAVIOR OF MATERIALS BY MEANS OF CONTINUOUS DAMAGE MECHANICS-AIDED APPROACHES

V. N. Kytopoulos, J. Venetis and E. Sideridis
Laboratory of Testing and Materials, Department of Mechanics
School of Applied Mathematical and Physical Sciences
National Technical University of Athens, Theocaris Building, 157 73, Zografou, Greece

1. Introduction

In this study an attempt is made to introduce some novel operational techniques for the characterization of materials fracture, assisted by certain approaches of continuum brittle damage mechanics. This was done by using some variant parameters of continuum damage mechanics [1-4], i.e.: Initial damage, D_0, Damage at failure, D_f, Structural instability number, ω_f^{-1}, Damage formation efficiency number, $II_{\theta f} / I_{\theta f}$, Damage energy intensity number, K, and Damage potential number, D_p. As such, the ultimate scope of the present study was to characterize in the last instance the influence of initial damage, D_0, on all the above mentioned parameters.

2. The experimental protocol

The tensile loading experiments were carried out by taking into consideration the basic assumptions of continuum damage mechanics, which allow analysis of brittle damage to be applied to elastic-brittle solids under low dynamic loading conditions. Under these circumstances, a polymer material, under the commercial name PMMA (Plexiglas), was selected, which has shown to fulfill, according to a satisfactory manner, most of the desired assumptions. Due to the complexity of the problem some convenient and simplifying approximations and assumptions were needed to be taken into considerations. These were based on the following formulas:

$$\frac{D_f^{1-k} - D_0^{1-k}}{1 - D_f} = \ln \frac{D_f}{D_0} \tag{1}$$

$$D_0 = A\left(1 - D_f^{\,B}\right) \tag{2}$$

$$D_f = e^{-(1-x)c} \tag{3}$$

where:

$$x = \sigma_{fd} / \sigma_{f0}$$

and σ_{fd} is the fracture stress of the initially-damaged material and σ_{f0} is the fracture stress of the damage-free (virgin) material.

Eq.(1) presents the given basic theoretical relationship between the initial damage D_0 and the fracture damage D_f of the material, whereas Eqs.(2) and (3) correspond to the proposed simplifying approaches. Knowing that $0.5 < D_f < 1$ and using Eq.(1) for some given values of fracture damage D_f, the corresponding theoretical values of the initial damage D_0 can be calculated. This was done for two fixed, most probable theoretical values of k=0 and k=0.5. Afterwards, by means of the theoretical values of the (D_0, D_f) set and using Eq.(2), the constants A and B can be determined. The desired best fit procedure provided the corresponding correlation coefficient equal to about 0.985, which may reflect the relative correctness of Eq.(2). By combination of Eqs.(2) and (3) one can obtain the following equation:

$$D_0 = A\left(1 - e^{-B(1-x)c}\right) \tag{4}$$

By putting the experimental values of the set (D_0,x) into Eq.(4) the new constants A,B,C may be calculated. Thereafter, in turn, by means of Eq.(3) the "true" fracture damage D_f may be evaluated. Bearing in mind the theoretical model [1], it follows that the calculation of all the above mentioned parameters were based on the true sets (D_0, D_f), obtained according to the above described manner. Two kinds of initial damage of the material were investigated and compared: Edge-crack formed damage and microhole formed damage.

3. Concluding remarks

Under the above-described circumstances the present study has shown that (see, also, Fig.1):

i. The damage at failure is more affected by the microhole initial damage than by edge-crack initial damage.
ii. The damage potential number changes with of higher rate for microhole initial damage than for edge-crack initial damage.

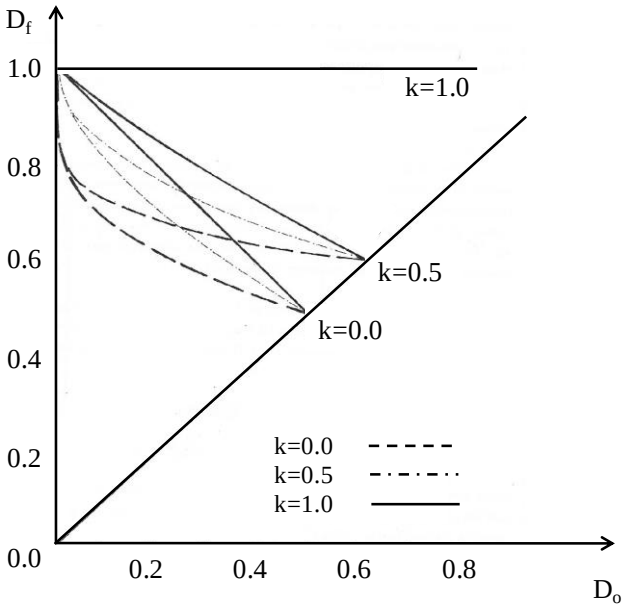

Figure 1. Damage at failure versus initial damage (theoretical simulations).

iii. Structural instability number increases rapidly towards the upper bound of the initial damage.
iv. Damage formation efficiency number shows a higher rate of change with microhole initial damage than with edge-crack initial damage.
v. In general, it can be stated that, all the above investigated damage parameters of microhole damaged material, showed a greater sensitivity in function of initial damage than those of edge-crack damaged material.

References

[1] J. Najar (1987). Continuous damage of brittle solids, in *Continuum Damage Mechanics, Theory and Applications*, D. Krajcinovij and J. Lemaitre (eds), Springer Verlag Wien-New York.
[2] L. M. Kachanov (1986). *Introduction to Continuum Damage Mechanics*, M. Nijhoff Publ., Dordrecht.
[3] G. P. Cherepanov (1974). *Mechanics of brittle fracture* (in Russian), Nauka Publ., Moscow.
[4] D. Krajcinovij and R. Ilankamban (1985). Mechanics of solids with defective microstructure, J. *Struct. Mech.*, **13**, 267-282.

$LaAlO_3$ AS OVERLAYER IN CONVENTIONAL THERMAL BARRIER COATINGS

I. Georgiopoulos[1], N. Vourdas[2], S. Mirza[3],
K. A. Papadopoulos[2], C. Andreouli[1] and V. N. Stathopoulos[2]

[1] MIRTEC S.A., Thiva Branch,
72nd km of Athens-Lamia National Road 34100, Chalkida, Greece
[2] Laboratory of Chemistry and Materials Technology, School of Technological Applications,
Technological Educational Institute of Sterea Ellada, Psachna campus, Evia, Greece
[3] ELEMENT S.A., Hitchin, UK

1. Introduction

Thermal Barrier Coatings (TBCs) are used to insulate and protect the metallic gas turbine engine components from the hot gas stream, against high temperature corrosion, and subsequent damage. Improvement in this field will facilitate higher combustion temperatures and thus improved engine efficiency, not only in power generation but, also, in aerospace and marine propulsion [1, 2].

In general, a typical TBC consists of two deposited layers, the bond coat (BC) and the top coat (TC).

Recently Lanthanum aluminates have been used in such systems, towards increasing the performance of TBCs. Even though $LaAlO_3$ is claimed as a potential YSZ replacement in various patents [3, 4], the focus is more for the substituted Lanthanum aluminates exhibiting the hexaaluminate structure [5, 6]. Even in hexaaluminates, as well as in Lanthanum zirconates [7, 8] etc, $LaAlO_3$ gradually evolves with thermal aging [6], due to the reaction of La with the Al from the evolved TGO.

More interestingly La oxide seems to stabilize the sintering and hence the creep resistance of Al oxide [9]. Its evaluation as a TC material has been reported recently [10-11]. In this work we present experimental results for the evaluation of $LaAlO_3$ (LA) as overlayer in conventional YSZ-based TBCs.

2. The experimental protocol

In Table 1 the multi-layered TBC systems developed are presented and compared. The substrate in all cases is Nimonic alloy, and the BC is NiCrAlY superalloy, deposited with Atmospheric Plasma Spraying (APS). The TC is YSZ in all cases deposited either by APS or Suspension Plasma Spraying (SPS).

The effect of the addition of a $LaAlO_3$ (LA) overlayer delivered by Solution Precursor Plasma Spraying (SPPS) is studied in this work. Fracture toughness, hardness, total duration (number of cycles) under thermal cycling at 1200 ^oC and thermal shock testing at 1200 ^oC, four-point bend test and the effect of annealing were studied and will be discussed in this work.

Substrate	**Bond Coat**	**Top Coat**	**Overlayer**
Nimonic	NiCrAlY(APS)	YSZ(APS)	-
Nimonic	NiCrAlY(APS)	YSZ(SPS)	-
Nimonic	NiCrAlY(APS)	YSZ(APS)	LA(SPPS)
Nimonic	NiCrAlY(APS)	YSZ(SPS)	LA(SPPS)

Table 1. Overview of the samples prepared and compared.

3. Conclusions

$LaAlO_3$ was used as overlayer in multi-layered TBC systems. The additional thermal sealing provided by $LaAlO_3$ along with its lower fracture toughness improved the TBC performance during thermal cycling. The effect of annealing on the mechanical properties is discussed.

References

[1] N. P. Padture, M. Gell and E. H. Jordan (2002). Thermal barrier coatings for gas-turbine engine applications, *Science*, **296**, 280-284.
[2] D. R. Clarke, M. Oechsner and N. P. Padture (2012). Thermal-barrier coatings for more efficient gas-turbine engines. *MRS Bulletin*, **37**, 891-898.
[3] M. Fu, R. Darolia, M. Gorman and B. A. Nagaraj (2011). Thermal barrier coating systems including a rare earth aluminate layer for improved resistance to CMAS infiltration and coated articles, *Patent US8062759B2* US Grant.
[4] R. Subramanian, S. M. Sabol, J. G. Goedjen, K. M. Sloan and S. J. Vance (2001). Thermal barrier coatings for turbine components, *World Patent WO 01/23642 A2*.
[5] R. Gadow and M. Lischka (2002). Lanthanum hexaaluminate - novel thermal barrier coatings for gas turbine applications - materials and process development, *Surface and Coatings Technology*, **151**, 392-399.
[6] X. Chen, Y. Zhao, W. Huang, H. Ma, B. Zou and Y. Wang (2011). Thermal aging behavior of plasma sprayed LaMgAl11O19 thermal barrier coating, *Journal of the European Ceramic Society*, **31**, 2285-2294.
[7] X. Q. Cao, R. Vassen, W. Jungen, S. Schwartz, F. Tietz and D. Stöver (2001). Thermal stability of lanthanum zirconate plasma-sprayed coating, *Journal of the American Ceramic Society*, **84**, 2086-2090.
[8] Y. Wang and P. Xiao (2014). The phase stability and toughening effect of 3Y-TZP dispersed in the lanthanum zirconate ceramics, *Materials Science and Engineering A*, **604**, 34-39.
[9] H. Schaper, E. B. M. Doesburg and L. L. Van Reijen (1983). The influence of lanthanum oxide on the thermal stability of gamma alumina catalyst supports, *Applied Catalysis*, **7**, 211-220.
[10] V. Stathopoulos, V. Sadykov, S. Pavlova, Y. Bespalko, Y. Fedorova et al. (2016). Design of functionally graded multilayer thermal barrier coatings for gas turbine application, *Surface and Coatings Technology*, **295**, 20-28.
[11] I. Georgiopoulos, E. Marathoniti, N. Vourdas, K. Andreouli and V. Stathopoulos (2014). Comparative study on liquid plasma sprayed lanthanum aluminate oxide coatings using different feedstock materials for potential TBC application, *25th Advanced Aerospace Materials and Processes (AeroMat) Conference and Exposition*, June 16-19, 2014, Florida, USA.

EXPERIMENTAL AND ANALYTICAL APPROACH OF FATIGUE BEHAVIOUR OF STEPPED CK45 SHAFT WITH ADJACENT KEY GROOVE

D. G. Ntritsos, A. D. Tsolakis and K. I. Giannakopoulos
School of Engineering, Department of Mechanical Engineering
Piraeus University of Applied Sciences,
Egaleo-Athens, Greece

1. Introduction

Stress concentration areas such as keyways and shaft steps are extensively used in mechanical engineering design. Areas like these are charecterized by a problem in accurately predicting part operating lifetime, frequently driving into premature fracture of parts causing unplanned machine stoppages. The impact of such areas in engineering design is assessed with the aid of the "k-factors" [1], however these corrective factors cover the effect of only a single notch on the whole structural element.

Given that, in mechanical engineering design, it is common for multiple stress concentration areas to coexist adjacently, one cannot use the factors found in ref.[1] to assess the effect. The effect of adjacent steps and grooves on a DIN CK 45 shaft has been investigated in ref.[2]. In the present paper the interaction of two distinct stress concentration areas, a standardized keyway one and a step one, on a DIN CK45 steel shaft specimen under rotating bending are studied experimentally. The experimental results are then compared against the respective concerning the fatigue life estimation obtained by a numerical model and the differences between them are discussed.

2. Experimental protocol and numerical analysis

The experiments were performed on a rotating bending fatigue testing apparatus under various loads. Two different sets of specimens were tested and the experimental data were recorded and analyzed. The specimens (Fig.1) were manufactured using conventional lathe and milling machinery. The same steel batch was used for all the specimens and after manufacturing they were stress relieved. In order to minimize surface roughness, after stress relieving, the specimens were polished. The tests were performed following the guidelines of ref.[3].

The mathematical model of the specimens was created with Inventor Autodesk solid modeler and simulated using finite element analysis Nastran solver for the estimation of the maximum stresses. Typical results of the numerical analysis are shown in Fig.2. The stress results from the FEM analysis were used to approach the fatigue behaviour of both single notched and double notched shaft by the Thum and Petersen method and the application of Smith Ck45 diagram.

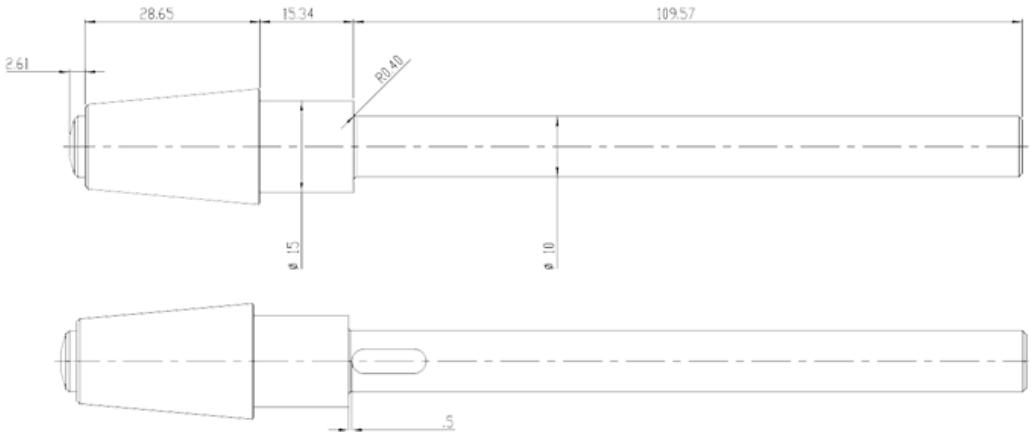

Figure 1. The geometry and the dimensions (in mm) of the specimens.

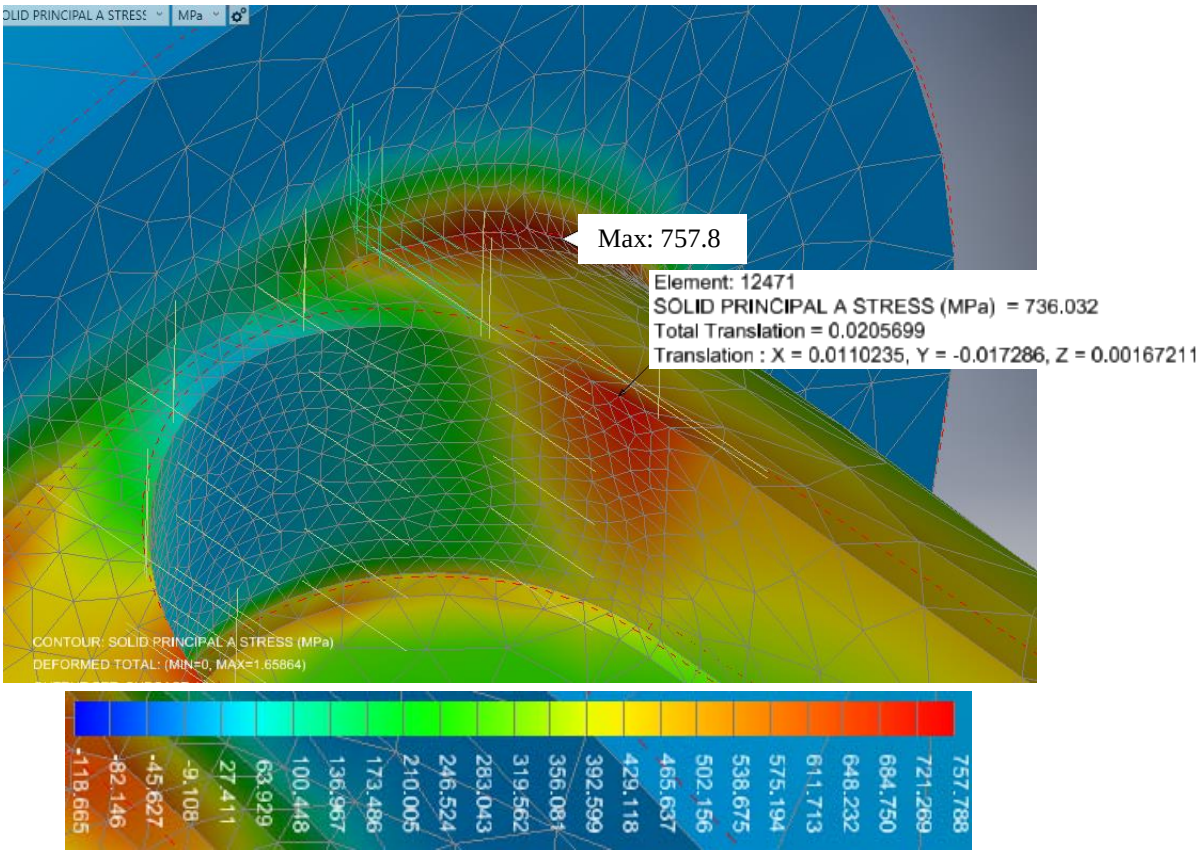

Figure 2. The first principal stress (in MPa) according to the numerical model.

3. Conclusions

It is conluded that the part with the single notch had better fatigue life than the one with the dual notches (Fig.3). It is also evident that when there are two adjacent notches the maximum stress imposed on the specimen is greater than that of the single notched one under the same conditions. In the future, the relative position of two notches under fatigue loading can be examined as one key factor into determining the level of effect of the second notch to the overall fatigue life of the specimen.

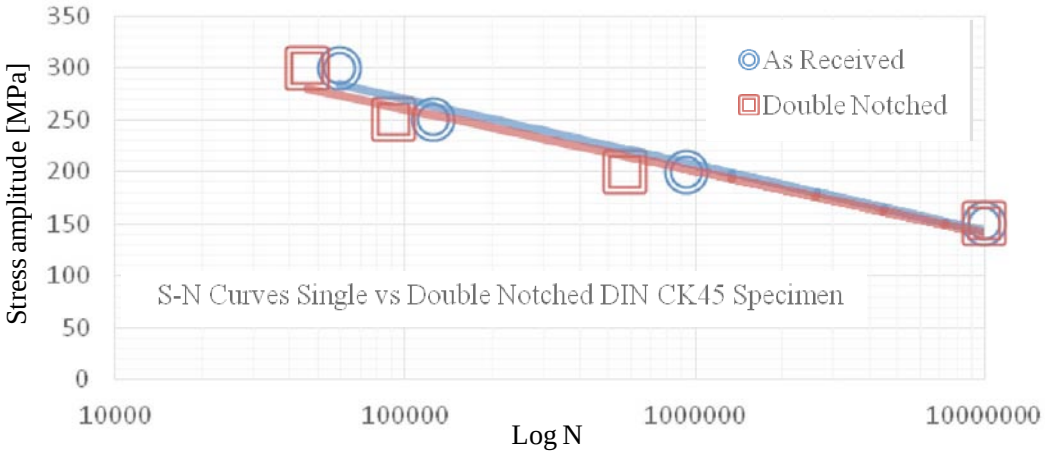

Figure 3. Fatigue behaviour of as received- versus double notched-specimens.

References

[1] R. E. Peterson (1953). *Stress Concentration Design Factors*, John Wiley & Sons, New York.
[2] A. R. Gowhari-Anaraki, S. J. Hardy and M. K. Pipelzadeh (2003). Experimental and analytical fatigue data for notched shafts in bending, *Jurnal Kejuruteraan*, **15**, 15-31.
[3] ISO 1143:2010, *Metallic materials - Rotating bar bending fatigue testing*.

EVALUATION OF ORGANIC COATINGS FOR CORROSION PROTECTION OF CONDENSING ECONOMIZERS

I. Iliopoulos[1], A. Karampekios[1], P. K. Pandis[1], N. Vourdas[1], H. Jouhara[2], S. Tassou[2] and V. N. Stathopoulos[1]

[1] Laboratory of Chemistry and Materials Technology, School of Technological Applications, Technological Educational Institute of Sterea Ellada, GR-34400, Psachna Campus, Evia, Greece

[2] Institute of Energy Futures, Centre for Sustainable Energy Use in Food Chains, Brunel University London, Uxbridge, Middlesex, United Kingdom, UK

1. Introduction

The European directive (Ecodesign) for Energy-related Products (ErP) oblige to a gradual upgrade of conventional boilers towards condensing economizers, condensing heat exchangers etc [1] with simultaneous exploitation of flue gases. The three main issues that need to be addresses, though, are the [2]: i) improvement of anticorrosion ability of the material either their replacement by high cost alternatives or by coatings' applications in order to easily remove condensates of flue gases [3] , ii) promotion of the dropwise condensation (DwC) over the filmwise condensation (FwC) on the heat exchange surface. DwC can deliver heat transfer coefficients (HTC) increased by a factor of 2 compared to FwC [4, 5] and iii) self-removal ability of the condensates from the heat exchange surface, which yield to increased HTC [6]. In this work we assess a series of commercially available coating solutions (epoxy, polyurethane (PU) and acrylic based) in meeting the above mentioned requirements.

2. Experimental

SS304 specimens were used as substrates and the materials used for the development of the organic coatings were commercial EPOXY, PU and ACRYLIC based paints purchased from STANCOLAC, CHROTEX and VIVECHROM respectively. The preparation of the SS304 surface involved polishing with a 800-grit silicon-carbide abrasive paper and the further degreasing with sonochemical treatment in ethanol and acetone. The application of the coatings was developed with the CRESCENDO MODEL 175 spraying gun. The spraying air pressure was kept at 2 bar and the distance of the nozzle and SS304 sample at 20 cm. For Epoxy and PU coatings epoxy primers were used (914 Epoxy and Novepox 915, respectively) in order to provide a suitable bond coat to the final coating. In acrylic coatings no primer was used. Corrosion rates were estimated on harsh environments (40% of H_2SO_4, HNO_3 and HCl solutions) at room temperature (not shown here) and at 60^{o}C. The OCP was followed using a 2-electrode setup in 3.5% NaCl solution using SCE as reference electrode. Water collection rates are measured with sample temperature range 5-10^{o}C with RH = 100% at 20 ^{o}C (not shown here).

3. Results

Epoxy primers (914 Epoxy and Novepox 915) provided a suitable bond coat to enhance the anticorrosive capabilities of EPOXY and PU topcoats. Based on Figs.1(a,b), polyurethane and epoxy coatings presented an enhanced corrosion resistance in comparison to acrylic coatings. The high resistance of PU coating is probably attributed to its chemical composition in comparison to EPOXY. OCP results (Fig.1c) confirmed the stability of the epoxy and PU coatings in 3.5% NaCl solution. Fig.2 depicts the results on the condensation phenomena at 100% RH at 20 ^{o}C. The preliminary condensation tests with water vapor at room temperature are presented in relation with time.

4. Conclusions

Among PU and Epoxy top coatings, PU provided the higher resistance in H_2SO_4 environments, while EPOXY in HCl. Acrylic coatings exhibited inferior resistance in comparison with the EPOXY and PU coatings in H_2SO_4. Estimation of condensation effects are still in progress.

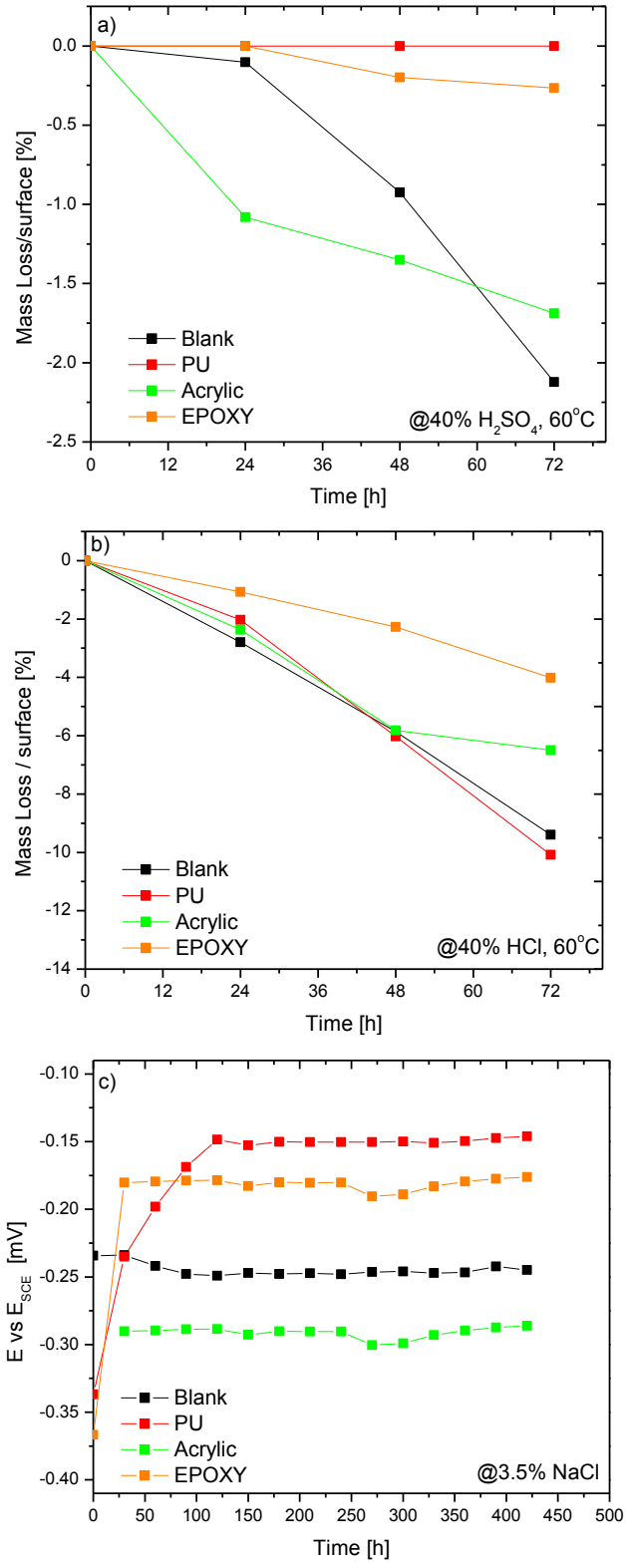

Figure 1. Corrosion rates at 60 °C with 40% a) H_2SO_4, b) HCl solutions and c) OCP results.

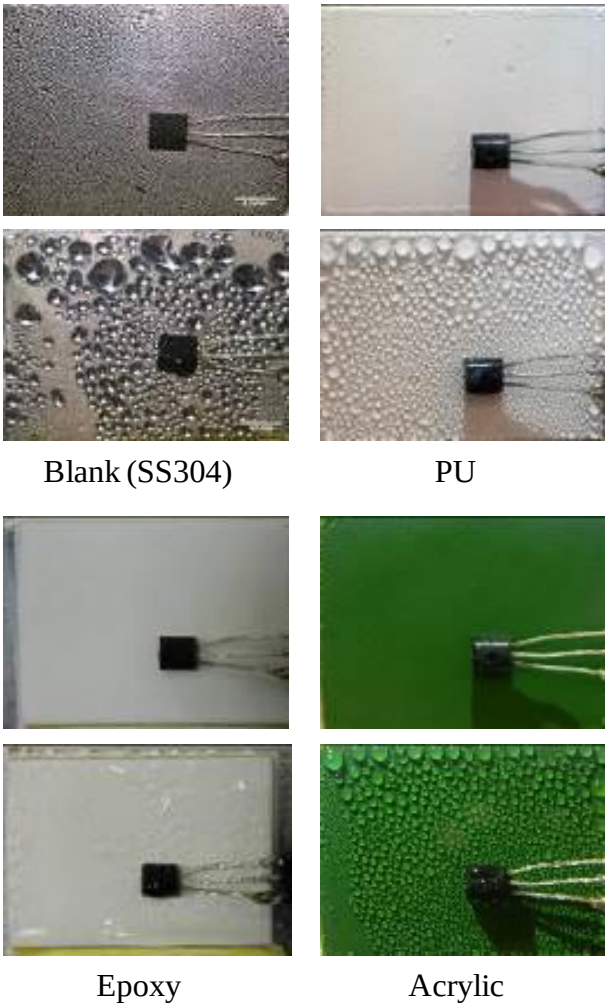

Figure 2. Condensation effects on blank and coated samples . The top photo of each pair presents the condensation state after 5 min whilst bottom one after 1 h.

References

[1] D. Attinger et al. (2014). Surface engineering for phase change heat transfer: A review, *MRS Energy & Sustainability*, **1**, E4.

[2] C. Dietz, K. Rykaczewski, A. G. Fedorov, Y. Joshi (2010). Visualization of droplet departure on a superhydrophobic surface and implications to heat transfer enhancement during dropwise condensation, *Appl. Phys.Lett.*, **97**, 033104.

[3] H. Chen, Y. Zhou et al. (2017). Heat exchange and water recovery experiments of flue gas with using nanoporous ceramic membranes, *Appl. Therm. Eng.*, **110**, 686-694.

[4] D. J. Preston et al. (2015). Scalable graphene coatings for enhanced condensation heat transfer, *Nano Lett.*, **15**, 2902-2909.

[5] N. Vourdas, G. Pashos, G. Kokkoris, A. G. Boudouvis and V. N. Stathopoulos (2016). Droplet mobility manipulation on porous media using backpressure, *Langmuir*, **32**, 5250-5258.

[6] A. Ghosh, S. Beaini, B. J. Zhang, R. Ganguly, C. M. Megaridis (2014). Enhancing dropwise condensation through bioinspired wettability patterning, *Langmuir*, **30**, 13103-13115.

Sensing Techniques 2

RELATION BETWEEN DAMAGE PROCESSES OF REINFORCED CONCRETE UNDER UNIAXIAL COMPRESSION AND ELECTRIC RESPONSE TO PULSED MECHANICAL IMPACT

M. Petrov, T.V. Fursa and D. D. Dann
National Research Tomsk Polytechnic University,
Tomsk, Russia

1. Introduction

Long-term use of concrete under static and dynamic mechanical stresses results in the appearance and development of cracks, which eventually may lead to unexpected structural failure. One of the methods for monitoring the damage processes of concrete is a method based on the phenomenon of mechanoelectric transformations [1, 2]. The underlying principle of the method is that the element tested is exposed to a weak elastic shock action that results in acoustic waves starting to propagate within the sample. The mechanical stresses caused by acoustic waves produce an alternating electric field as a consequence of the elastic wave deforming and displacing double electric layers located at the boundaries of the concrete components, and the polarization of piezoelectric quartz contained in the sand and gravel. The research conducted has revealed that piezoelectric inclusions play a decisive role in mechanoelectrical transduction in concrete [2]. The electric measuring receiver, placed next to the sample and within the range of this field, recorded the electric response parameters related to the characteristics of elastic waves and therefore reliably reflecting the processes of their interaction with internal structural heterogeneities and defects.

2. Materials and methods

Compressive tests of laboratory samples of concrete reinforced with steel and fiberglass rebar were carried out. The influence of reinforcement type, the structural characteristics of reinforced concrete and the concrete strength on the process of concrete samples destruction during compression tests was investigated. The compression load was applied using a press at a constant rate of 0.3 kN/s. Fig.1a shows a typical stress-strain curve for concrete sized 100 x 100 x 100 mm reinforced with steel rebar. The stress-strain curves for other types of sample size and reinforcement are similar. The strain-stress relationship for the reinforced concrete under constant loading rate is characterized by three distinct stages. The first nonlinear stage is associated with compaction of surface layer, the second one is the stage of quasi-elastic deformation and the third stage (that of the second nonlinear deformation) is associated with the process of crack formation and growth.

During quasi-static loading of samples under constant rate, at certain time-intervals, a weak elastic impact is imposed on the side surface of the sample and an electric response to this action is recorded. Measurement of electric response has been performed using the hardware and software system which allows to produce weak mechanical impact on concrete and record the electric response to this action. A differential capacitive electrical sensor, which can significantly improve the signal-to-noise ratio, has been used to record the electrical signal. The mode of differential electric sensor operation is described in detail in ref.[1].

During compression, stresses in various regions of the specimens may exceed the tensile strength and, therefore, at these regions the cracking process begins. In the ANSYS software package, the mechanical stress distribution within the volume of a reinforced concrete cube, subjected to uniaxial compression has been determined using the finite element method. Determination of the onset of crack formation process in reinforced concrete during uniaxial compression was performed by calculating the ultimate stresses at the concrete-reinforcement interface. Comparison of calculated and experimental data shows that they are in a good agreement.

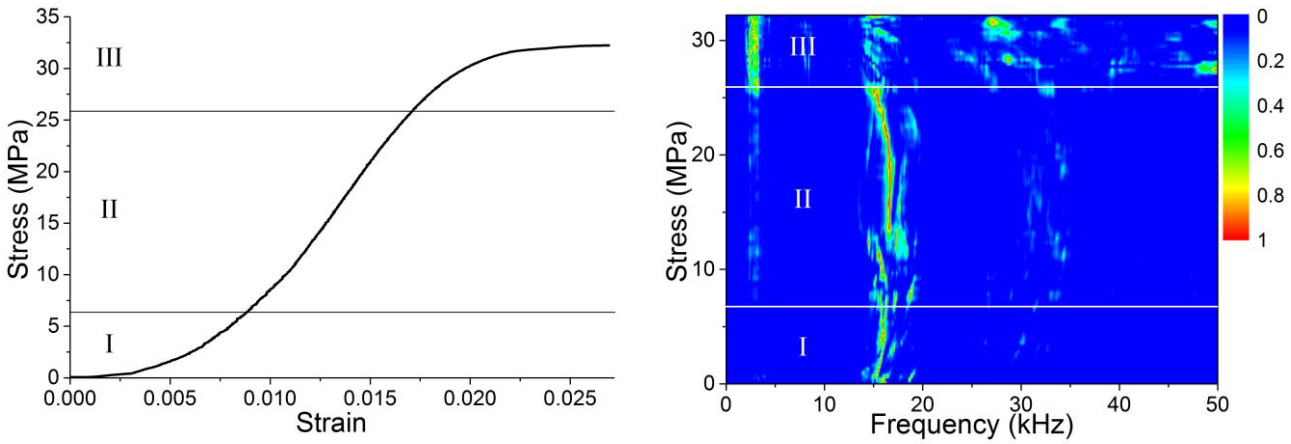

(a) (b)

Figure 1. (a) A typical stress-strain curve for concrete samples sized 100 x 100 x 100 mm, reinforced with steel rebar 10 mm in diameter;
(b) Change in the normalized spectrum of electric response as a function of the compressive stress registered from concrete reinforced with steel rebar.

3. Results and discussion

Instances of mechanical stress appearing in reinforced concrete under external load lead to the development of cracks in the radial zone around the reinforcement, at the boundary between the cement matrix and the coarse aggregate, and in the cement matrix itself. As the load increases, the size and quantity of the cracks increase also. The front of the acoustic wave created by mechanical impact crosses these areas and gets distorted. The distortions must be reflected in the spectral characteristics of the electric response, since the latter is interdependent of the elastic waves. Fig.1b shows a two-dimensional picture illustrating the nature of change in the electric response spectrum during the uniaxial compression of reinforced concrete. As it is shown in Fig.1b, maximum transformation of electric response spectrum occurs during the transition into destruction stage.

The investigation of a number of measured and calculated parameters of electric response was conducted and their relationship with damage processes in reinforced concrete under external compression load was established.

Acknowledgements

This work was performed under Russian science foundation (Project №16-19-10119).

References

[1] T. V. Fursa, D. D. Dann, M. V. Petrov and A. E. Lykov (2017). Evaluation of damage in concrete under uniaxial compression by measuring electric response to mechanical impact, *J. Nondestruct. Eval.*, **36**: **30**, DOI: 10.1007/s10921-017-0411-y.

[2] T. V. Fursa, D. D. Dann and M. V. Petrov (2017). Evaluation of freeze-thaw damage to reinforced concrete based on the parameters of electric response to mechanical impact, *Constr. Build. Mater.*, **155**, 451-462.

MONITORING SPATIOTEMPORAL DAMAGE EVOLUTION IN MARBLE USING ELECTRICAL CURRENT AND ACOUSTIC EMISSIONS

I. Stavrakas[1], S. K. Kourkoulis[2] and D. Triantis[1]
[1] Laboratory of Electronic Devices and Materials, Department of Electronics Engineering, Technological Educational Institute of Athens, 122 10, Greece
[2] Laboratory for Testing and Materials, School of Applied Mathematical and Physical Sciences, Department of Mechanics, National Technical University of Athens, 157 73, Athens, Greece

1. Introduction

Monitoring damage in the interior of mechanically loaded elements is, nowadays, implemented with the aid of various innovative experimental techniques like, for example, the Acoustic Emissions (AE) and the Pressure Stimulated Currents (PSC) [1] ones. In the present study, both the AE and PSC techniques are employed in a combined manner in order to monitor damage evolution within Dionysos marble specimens, subjected to uniaxial compression until fracture. The novelty of the study is that the PSC technique is applied for the first time by means of a grid of sensors rather than a single one or a pair of sensors. Interesting data are obtained enlightening the spatial and temporal distribution of micro-cracking processes, which precede the fatal catastrophic crack propagation.

2. The experimental protocol

The specimens of the protocol were made of Dionysos marble, the compressive strength of which is equal to about σ_f=63MPa. Their shape was prismatic of square cross section 40 x 40 mm^3 and height L=100 mm. The experimental set-up was described analytically in previous works [2, 3] and it is, thus, only shortly outlined here (Fig.1). Concerning the PSC technique, the measuring system consisted of a sensitive programmable electrometer (Keithley 6517A) and a 10-channel scanner card (Keithley 6521). The sensing system consisted of five pairs of electrodes, installed along the loading axis, enabling recording of electric emissions close to any potential source of PSC (Fig.1). The loading scheme consisted of a loading-unloading-reloading compression loop (see Figs.2a,d). Both the loding- and the reloading-branch of the loop attained levels resulting to axial stress closely approaching the material's compressive strength.

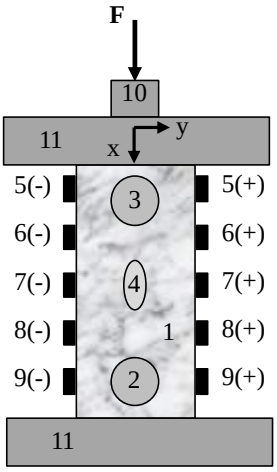

1: Specimen
2,3: Lower und upper Acoustic sensors
4: Strain gauge
5(+) to 9(+): Positive edge of five successive channels (chan0-chan4) of the electrometer
5(-) to 9(-): Negative edge of the as above channels
10: Load cell
11: Loading plate

Figure 1. Sketch of the specimens and the experimental set-up.

3. Results and discussion

The correlation between the data concerning the PSC-technique and the AE hits is here attempted in terms of the PSC energy and the corresponding temporal variation of the AE Improved b-value [4]. From Figs.2(b, e) it is obvious that during the loading branch and for stress values which do not exceed about 50% of the respective maximum value attained, PSCs of relatively low energy are recorded. Increasing further the stress level high energy PSC emissions are recorded approximately at the mid-height of the specimen spreading gradually towards the bases of the specimen. It is to be noticed here that during the reloading branch, well before macroscopic fracture is observed, the upper and lower bases of the specimen, start suddenly emitting PSC signals of high energy (Fig.2e). Concerning the amplitudes of the AE events they were processed in the direction of conducting improved b-value (Ib) analysis for both loading branches.

Concerning the first loading branch, the Ib value (after a slight increase) decreases upon increasing the axial stress. This decrease is terminated when the stress approaches its maximum level. During the second loading branch, Ib exhibits a more or less similar behavior. The most important observation during the second loading branch is that about 60s after the stress has reached its maximum value (and is kept constant at this level) the Ib-value starts decreasing implying that new AE events of higher amplitudes occur. Then a characteristic drop of the Ib-value at levels lower than Ib=1 is observed, slightly before the collapse of the specimen, in excellent accordance to the respective behavior of the PSC energy.

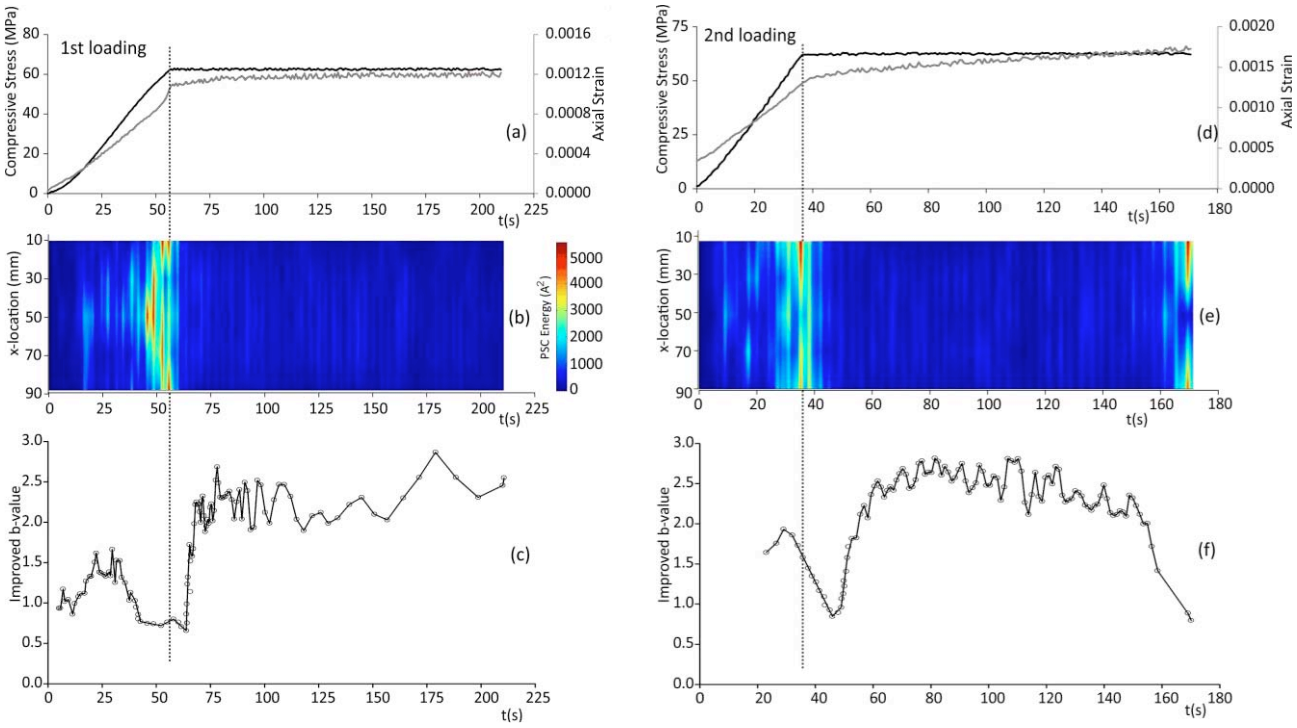

Figure 2. Time variation of the: Axial stress and axial strain (a, d), Spatial distribution of PSC (b, e) and, Ib-value (c, f). Plots and figures of the left column correspond to the 1st loading branch while those of the right column to the 2nd one.

4. Conclusions

The PSC and the AE sensing techniques were used to study the spatiotemporal evolution of internal damage in marble specimens subjected to compression, at stress levels approaching the respective fracture stress. Very satisfactory qualitative and quantitative agreement between the data provided by the two techniques was revealed in terms of the PSC energy and the Ib-value. Moreover, it was proven that both the quantities (PSC energy and Ib-value) provide useful indications of upcoming failure (pre-failure warning indicators) well in advance of the macroscopic fracture of the specimens.

References

[1] I. Stavrakas, D. Triantis, Z. Agioutantis, S. Maurigiannakis et al. (2004). Pressure stimulated currents in rocks and their correlation with mechanical properties, *Nat. Hazard Earth Sys.*, **4**, 563-567.

[2] D. Triantis, I. Stavrakas, C. Anastasiadis, A. Kyriazopoulos et al. (2006). An analysis of Pressure Stimulated Currents (PSC) in marble samples under mechanical stress, *Phys. Chem. Earth*, **31**, 234-239.

[3] C. Stergiopoulos, I. Stavrakas, G. Hloupis, D. Triantis et al. (2013). Electrical and acoustic emissions in cement mortar beams subjected to mechanical loading up to fracture, *Eng. Fail. Anal.*, **35**, 454-461.

[4] T. Shiotani, K. Fujii, T. Aoki and K. Amou (1994). Evaluation of progressive failure using AE sources and improved b-value on slope model tests, *Prog. Acoust. Emission*, **VII**, 529-534.

COMBINING ACOUSTIC EMISSIONS AND ELECTRICAL CONDUCTIVITY MEASUREMENTS TO MONITOR FRACTURE OF POROUS SANDSTONE SAMPLES DURING UNIAXIAL COMPRESSION

V. Saltas[1,2], T. Koumoudeli[1,2], M.-Z. Koutsoukou[2,3] and F. Vallianatos[1,2]
[1] *Laboratory of Geophysics and Seismology, Department of Environmental and Natural Resources Engineering, Technological Educational Institute of Crete, Greece*
[2] *UNESCO Chair, Solid Earth Physics and Geohazards Risk Reduction*
[3] *Department of Physics, University of Crete, Greece*

1. Introduction

Fracture-induced phenomena in rocks and brittle materials that are subjected to mechanical stress include the emission of transient weak electric currents and elastic waves known as Acoustic Emissions (AE). These fractoemission phenomena are of great importance in searching precursory signals in mechanical damage of materials and in earthquakes prediction [1, 2]. The underlying physical mechanisms of the pressure-induced charge transport may be investigated by means of Impedance Electrical Spectroscopy (IES) and the measured electrical and dielectric properties may be correlated with the damage evolution of the material during the applied mechanical stress [3].

In the present work, electrical ac-conductivity measurements were carried out simultaneously with AE monitoring in dry and water-saturated sandstone specimens subjected to different types of uniaxial compressive stress (linear, stepped-like, saw-tooth), up to ultimate failure. The high porosity of the specimens (~7%) allows the investigation of the influence of the water concentration to the changes of the electrical conductivity and to the AE activity during compression.

2. Experimental results

The experimental apparatus for the simultaneous recordings of the ac-conductivity and the AE activity is described in detail elsewhere [4]. Two different geometries (cylindrical and prismatic) of the sandstone specimens were used in order to measure the ac-conductivity in parallel and perpendicular direction to the applied uniaxial compressive stress, respectively (refer to Fig.1). The AE activity is recorded as time series of detected signals (hits) in each sensor, their amplitudes (measured in dB) and other AE features like signal energy and rise-time. The latter is an important AE parameter since it is related to the fracture process (tensile or shear).

The time evolution of the measured ac-conductivity and the corresponding AE activity (expressed in rise-time) during uniaxial loading of two representative specimens with different water

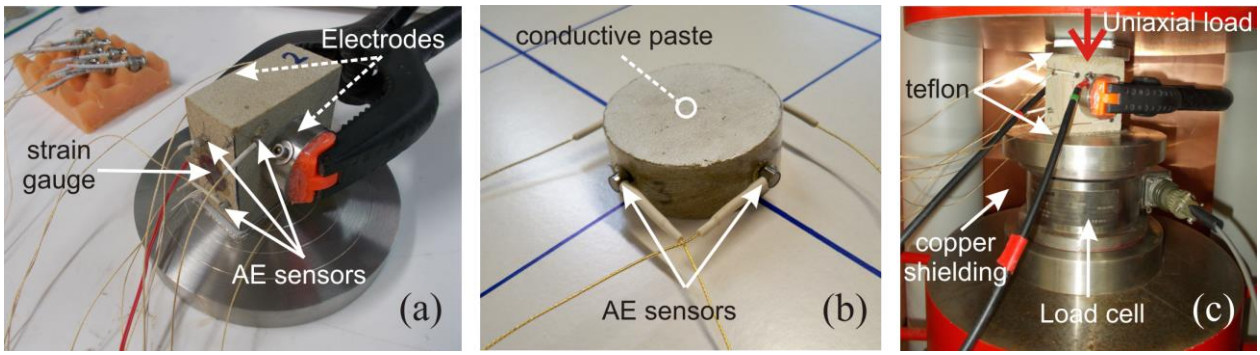

Figure 1. The experimental setup for the simultaneous measurements of ac-conductivity and AE activity in (a) prismatic and (b) cylindrical sandstone specimens. (c) A prismatic specimen inside the load machine before the test.

content, is shown in Figs.2(a,b). In both cases, ac-conductivity exhibits significant variation with pressure when considerable AE activity takes place, i.e, at high values of rise-time. This variation is either positive or negative, depending on the water content of the sandstone specimens and is attributed to the charge transfer caused by micro-cracks generation and propagation in the sandstone.

At low water contents, i.e., in specimens containing water from air humidity, ac-conductivity decreases with pressure, while in water-saturated sandstone specimens, ac-conductivity increases significantly. This observation suggests that a critical water content should exist which corresponds to the transition from positive to negative changes of ac-conductivity [3]. Notably, changes in ac-conductivity are greater in the parallel than in the vertical direction relative to the applied stress, suggesting the formation of specific shear planes inside the specimen prior to its failure. Similar results are also observed in stepped and saw-tooth type of uniaxial loading.

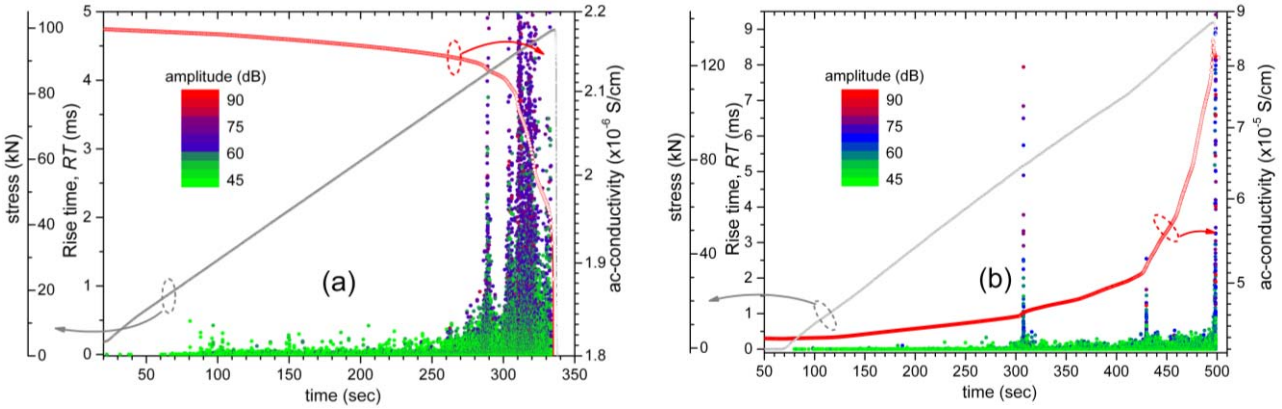

Figure 2. Time-series of ac-conductivity at 10 kHz in conjuction with the corresponding AE activity expressed in rise-time of recorded hits, during linear uniaxial loading of (a) dry and (b) partially water-saturated cylindrical sandstone specimens.

3. Conclusions

A strong correlation of ac-conductivity with the AE activity is observed during all types of uniaxial loading in the porous sandstone specimens. The concentration of the pore fluid (water) determines the sign and the value of the variation of the electrical ac-conductivity. Our observations are of great importance in investigating precursory phenomena in the meso- and macro-scale, such as the mechanical failure of materials and the occurrence of pre-seismic electric signals.

References

[1] A. Lavrov (2005). Fracture-induced physical phenomena and memory effects in rocks: A review, *Strain*, **41**, 135-149.

[2] I. Stavrakas, D. Triantis, Z. Agioutantis, S. Maurigiannakis, V. Saltas, F. Vallianatos and M. Clarke (2004). Pressure stimulated currents in rocks and their correlation with mechanical properties, *Nat. Hazards Earth Syst. Sci.*, **4**, 563-567.

[3] V. Saltas, I. Fitilis and F. Vallianatos (2014). A combined complex electrical impedance and acoustic emission study in limestone samples under uniaxial loading, *Tectonophysics*, **637**, 198-206.

[4] V. Saltas, I. Fitilis, J. P. Makris and F. Vallianatos (2015). Acoustic and electrical emissions from sandstone under uniaxial compression, in *Proceedings of the Conference Science in Technology (SCinTE 2015)*, 67-70, November 5-7, Athens, Greece.

PREDICTION OF RESIDUAL STRENGTH OF THICK MASONRIES UTILIZING ULTRASONICS

P. A. Kakavas-Papaniaros[1], D. K. Baros[1], N. A. Kalapodis[2] and N. K. Anifantis[3]
[1] Technological Educational Institute of Western Greece,
Department of Civil Engineering T.E., Patras, Greece,
[2] University of Patras, Department of Civil Engineering, Rio, Patras, Greece
[3] University of Patras, Department of Mechanical and Aeronautical Engineering, Rio, Patras, Greece

1. Description of the problem

The strength of thick walls constructed by various materials such as concrete, stone, brick etc. is difficult to be determined by classical ultrasonic methods due to cavities, cracks or other imperfections within the structure. In addition, in cases of historical buildings where the masonry is very thick (~1 m especially in the lower floors) the high attenuation of the transmitted pulse makes it practically impossible to detect the acoustic signal on the other side of thick masonry.

In such cases the piezoelectric transducers that generate the acoustic signal, which is transmitted through the masonry, may be placed in corners, so that the distance between them to be reduced. When the transducers are placed at the corners of a structure, then they do not lie on opposite directions and hence they do not transfer the maximum energy. This can strongly impact the results and reliability of the method. In order to optimize the sensitivity of the method, in the present work the use of properly placed triangular Plexiglas prisms is proposed. The transducers are placed on the proper side of the prism, thus changing their orientation and the direction of the emitted acoustic wave with respect to the wall surface (Fig.1). The signal emitted from the transmitter passes through the prism for a certain time, travels through the masonry, and next travels through the second prism before arriving to the receiver. In order to accurately calculate the strength of the masonry using this setup, the "travel times" for each segment must be calculated. Finally, wave scattering should be directly considered. Both of these issues are discussed in the present paper.

2. Experimental measurements for the ultrasound "travel-times"

For the experimental setup shown in Fig.1, the standard ultrasonic velocity equipment can be used to determine the time of travelling from the transmitter to the receiver. Since the Plexiglas is an isotropic material, sound is travelling with the same velocity in all directions. From the distance that the sound travels within the Plexiglas, which can be easily measured, and the value of speed of sound one can determine the travelling time in this material. Subtracting it from the total time, which is directly determined by the ultrasonic equipment, the time of traveling of the sound in the masonry can also be determined. From this value and the travelling distance of the wave within the masonry, the speed of sound in the wall can be calculated using well known equations [1].

3. Consideration of wave scattering using slowness curves

To determine the number and direction of possible scattered modes, one can match the magnitude of the tangential component of the scattered modes to the tangential components of the incident wave. Assume a longitudinal wave is incident on the surface of the Plexiglass/masonry interface. The length of the arrow represents k_{il} as given by the definition of the slowness curve. The incident angle is θ_{il} and is measured from the interface. For clarity one curve indicates the angle and the other indicates the spatial frequency [2].

In this study the slowness curves for the Plexiglass/masonry interface are examined. These curves can be computed using an appropriate program [3]. Indicative results for sandstone masonry units are presented in Fig.2.

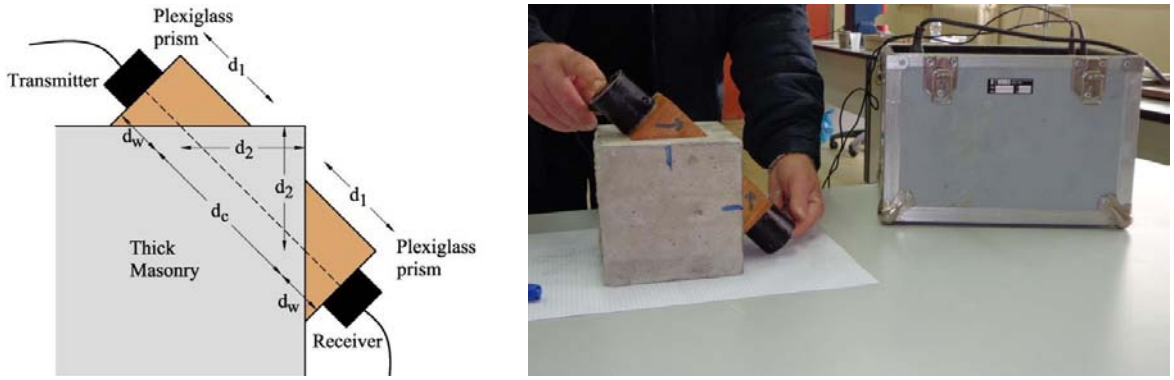

Figure 1. Proposed setup and initial laboratory measurements using wooden prisms.

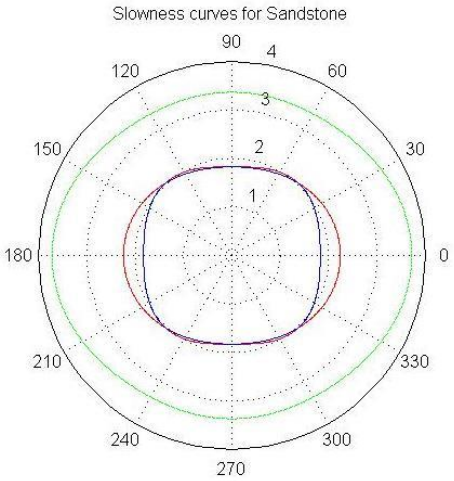

Figure 2. Indicative slowness curves for sandstone masonry units.

4. Results and discussion

Slowness curves are produced for an isotropic (Plexiglass) and an anisotropic solid (masonry). In anisotropic solids the wave velocity is not the same in all directions. The slowness curves trace the length (magnitude) of the spatial frequency vector *k* for all possible angles of incident or scattered waves. The phase of the wave travels in the direction of *k* with phase velocity v, but the energy (momentum transfer) of the wave propagates in the direction normal to the curve at group velocity. For isotropic materials, these directions coincide. This theoretical approach leads to a more detailed study for the propagation of the ultrasonic waves in the Plexiglass/masonry interface allowing a more accurate determination of the strength of large thickness masonry.

References

[1] P. A. Kakavas, D. Baros, G. Giannopoulos, N. Kalapodis and N. Anifantis (2016). Experimental and numerical investigation of an alternative setup for the determination of the compressive strength of concrete with the ultrasound method, in *Proceedings of the Panhellenic Conference on Concrete Structures*, November 10-12, Thessaloniki, Greece.

[2] A. H. Nayfeh (1995). *Wave propagation in layered anisotropic media with applications to composites*, **39**, Elsevier.

[3] M. Duarte, C. Piedrahita, T. Salinas, H. Altamar and K. Pachano (2004). Slowness surface calculation for different media using the symbolic mathematics language maple, *Earth Sci. Res. J.*, **8(1)**, 63-67.

INVESTIGATING ACOUSTIC EMISSIONS AND PRESSURE STIMULATED CURRENTS DETECTED DURING THE BENDING OF RESTORED MARBLE EPISTYLES WITHIN THE FRAME OF LOG-PERIODIC POWER-LAW MODELS

D. Mastrogiannis[1], S. I. Andreopoulos[2], S. M. Potirakis[2],
I. Stavrakas[2], D. Triantis[2] and S. K. Kourkoulis[3]
[1] Section of Solid State Physics, Department of Physics, University of Athens
[2] Department of Electrical and Electronics Engineering, School of Engineering, University of West Attica
[3] Department of Mechanics, School of Applied Mathematical and Physical Sciences, National Technical University of Athens

1. General

The deformation of solid materials is a procedure which is accompanied by numerous effects like the emission of acoustic and electromagnetic signals or the generation of Pressure Stimulated Currents (PSCs) [1-3]. In the present paper, attention is focused on the study of acoustic emissions and PSCs, detected during a recent bending experiment on an accurate copy of an authentic marble epistyle of the Parthenon Temple. The aim of the study is to investigate the emitted acoustic signals and PSCs within the frame of log-periodic power-law models. While acoustic and electromagnetic emissions detected during fracture experiments of well-defined and specially crafted specimens have already been successfully described by such models, it is interesting to investigate whether these models could also describe pressure stimulated currents as well as acoustic emission signals originating from complex structural set ups.

2. Theoretical background

Solid materials that are being deformed develop a complex network of damaged areas into their bulk volume, which eventually leads to the macroscopic rupture of the lattice. The whole process is accompanied by various phenomena like acoustic emissions [4] and PSCs [2, 3]. Processes like dislocation movement, formation of dislocation pile-ups and crack opening are associated with the generation of AE [5]. All these interactions, that take place in this network of faults and micro-cracks, exhibit a critical behavior with scale invariance characteristics [1, 5]. This leads to the assumption that phenomena which accompany the deformation of a solid material could possibly be described by relevant power laws. Bearing this in mind the cumulative energy released through the acoustic signals can be described by a general log periodic power law given as [5]:

$$E \sim \left(t_f - t\right)^m \left[1 + C\cos\left(2\pi \frac{\log\left(t_f - t\right)}{\log\lambda} + \Psi\right)\right] \quad (1)$$

3. The experimental protocol - Modeling the data by means of log-periodic power-law models

In the present work an effort is being made to apply the aforementioned log periodic power law model of Eq.(1) in a set up that simulates an authentic marble epistyle of the Parthenon Temple [3]. The epistyle is fragmented into two pieces and its integrity is restored by means of a number of threaded titanium bars placed in predrilled holes filled with a suitable cementitious material, according to the technique developed by the scientists of the Acropolis worksite [6]. After restoration the epistyle was subjected to multi-point bending [3]. During loading both the acoustic signals emitted and the PSCs produced were recorded as functions of time. These data are here analyzed, for the first time in juxtaposition, by means of log-periodic power-law models, in an attempt to enlighten critical aspects of the deformation procedure and possible correlations between acoustic emissions and PSCs. The application of the aforementioned log-periodic model is shown in Fig.1.

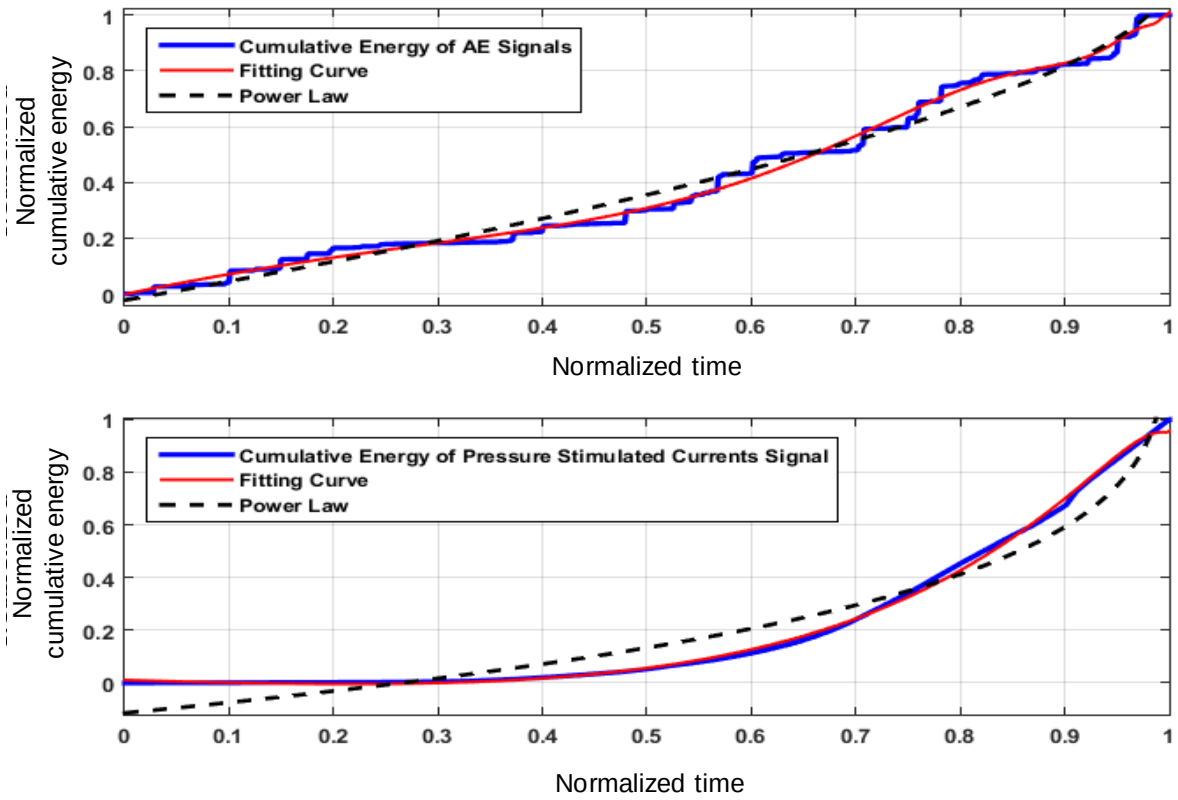

Figure 1. The cumulative energy released through acoustic emissions (upper) and the pressure stimulated currents (lower). Blue solid curves denote the experimental data, red solid curves are the corresponding log-periodic power law fittings in each case and the black dashed curves are the corresponding fitted power laws.

4. Discussion and conclusions

It seems that the log-periodic power law model can successfully be applied in the case of more complex structural set ups and it could probably be used as a tool of studying the behavior of such structures. An interesting point is that the PSCs provide data that can be, also, fitted by this mathematical model. The importance of using a log-periodic power law is apparent through the comparison with the corresponding power laws; log-periodic power law provides more accurate modeling. This opens up new possibilities of studying the deformation procedure of a material and extracting useful conclusions of the fracturing phenomena of a material.

References

[1] S. M. Potirakis and D. Mastrogiannis (2017). Critical features revealed in acoustic and electromagnetic emissions during fracture experiments on LiF, *Physica A*, **485**, 11-22.

[2] V. Hadjicontis, C. Mavromatou and D. Ninos (2004). Stress induced polarization currents and electromagnetic emission from rocks and ionic crystals, accompanying their deformation, *Natural Hazards and Earth System Science*, **4(5/6)**, 633-639.

[3] S. K. Kourkoulis et al. (2017). Acoustic emissions versus pressure stimulated currents during bending of restored marble epistyles: Preliminary results, *Fracture and Structural Integrity*, **11**, 536-551.

[4] D. Mastrogiannis and S. M. Potirakis (2017). Experimental study of the dynamic evolution of cumulative energy release during LiF fracture under uniaxial compression, *International Journal of Solids and Structures*, **132**, 59-65.

[5] M. Sahimi and S. Arbabi (1996). Scaling laws for fracture of heterogeneous materials and rock, *Physical Review Letters*, **77(17)**, 3689-3692.

[6] K. Zambas (1994). *Study for the Restoration of the Parthenon - Vol. 3b* (in Greek), Ministry of Culture, Committee for the Preservation of the Acropolis Monuments, Athens, Greece.

THE USE OF ACOUSTIC EMISSIONS TECHNIQUE IN THE MONITORING OF FRACTURING IN BRITTLE MATERIALS USING EXPANSIVE MORTAR

V. Saltas[1,2], D. Peraki[1,2] and F. Vallianatos[1,2]
[1] Laboratory of Geophysics and Seismology, Department of Environmental and Natural Resources Engineering, Technological Educational Institute of Crete, Greece
[2] UNESCO Chair, Solid Earth Physics and Geohazards Risk Reduction

1. Introduction

Expansive cracking agents have been used during the last two decades in the demolition of boulders and concrete structures as well as in open-surface and sub-surface rock excavation, as an alternative to the use of explosives posing safety risks. The effect of these non-explosive agents on fracturing of the surrounding media inside a borehole is based on the volume thermal expansion of the cracking agent, caused by its hydration reaction with water. Non-explosive expansion material has been used in laboratory experiments to evaluate its fracturing capacity of synthetic specimens, and its potential application for fracturing coal roofs in coal mines has been proposed [1]. Furthermore, soundless cracking agent has been used in laboratory scale to form a fracture network in shale specimens, in order to establish an evaluation method for the hydraulic fracturing in shale reservoirs [2]. In both previous cases, the acoustic emission (AE) technique was used for the dynamic monitoring and analysis of the fracture network formation. In the present study, the AE technique is used to monitor in real time the generation and propagation of cracks into various brittle materials by adding a commercially available expansion mortar to suitable holes of the specimens.

2. Experimental setup and results

Different brittle materials such as concrete and sedimentary rocks were cut in prismatic specimens and a hole, of 10 mm diameter and a depth of a few cm, was drilled, normally to one of their surfaces (Fig.1a). Seven AE pico-sensors were mounted with silicon glue on all the surfaces of each specimen (see Fig.1a) to monitor the AE activity under the effect of the expansive mortar and determine the three dimensional distribution of the induced cracks. The AE activity was recorded as time series of detected signals (hits) in each sensor, their amplitudes (measured in dB) and other AE features like signal energy and rise-time. The latter is an important AE parameter since it is related to the fracture process (tensile or shear).

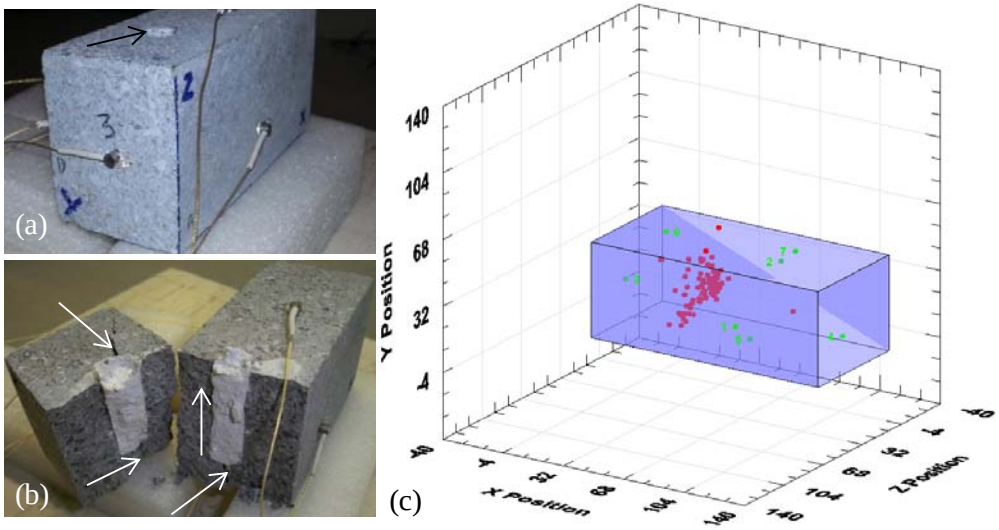

Figure 1. (a) The concrete specimen with the AE sensors mounted on it. The arrow indicates the hole filled with the expansive mortar. (b) The specimen was spllited into two main pieces. White arrows indicate the main visible macro-cracks. (c) 3D distribution of the cracks inside the concrete specimen, at the time 13:26:00 of the monitoring test. The events were filtered to include only hits with amplitudes > 52 dB.

The case of fracturing of a concrete specimen which was monitored for 24 h is illustrated in Figs.1(a,b). The corresponding time evolution of the amplitude distribution, the rise-time and the cumulative energy of the recorded hits in all channels are depicted in Figs. 2(a-c). Considerable AE activity was recorded after the time instant t=43438 s, due to the initiation of fracture of the specimen. The AE activity was continuous until the end of the recording, i.e., after 12 hours. High values of amplitude (>90 dB) are observed at the beginning of fracture and throughout the duration of monitoring, until the specimen is finally splitted into two fragments (Fig.1b).

The low AE activity, that is occasionally observed before the onset of fracture (refer to Fig.2) could be attributed to friction effects caused during the thermal expansion of the expansive mortar inside the hole. The three-dimensional determination of the cracks location at the early stages of fracture (see Fig.1c) is in good agreement with the position of the hole and the final picture of the specimen after its fracture.

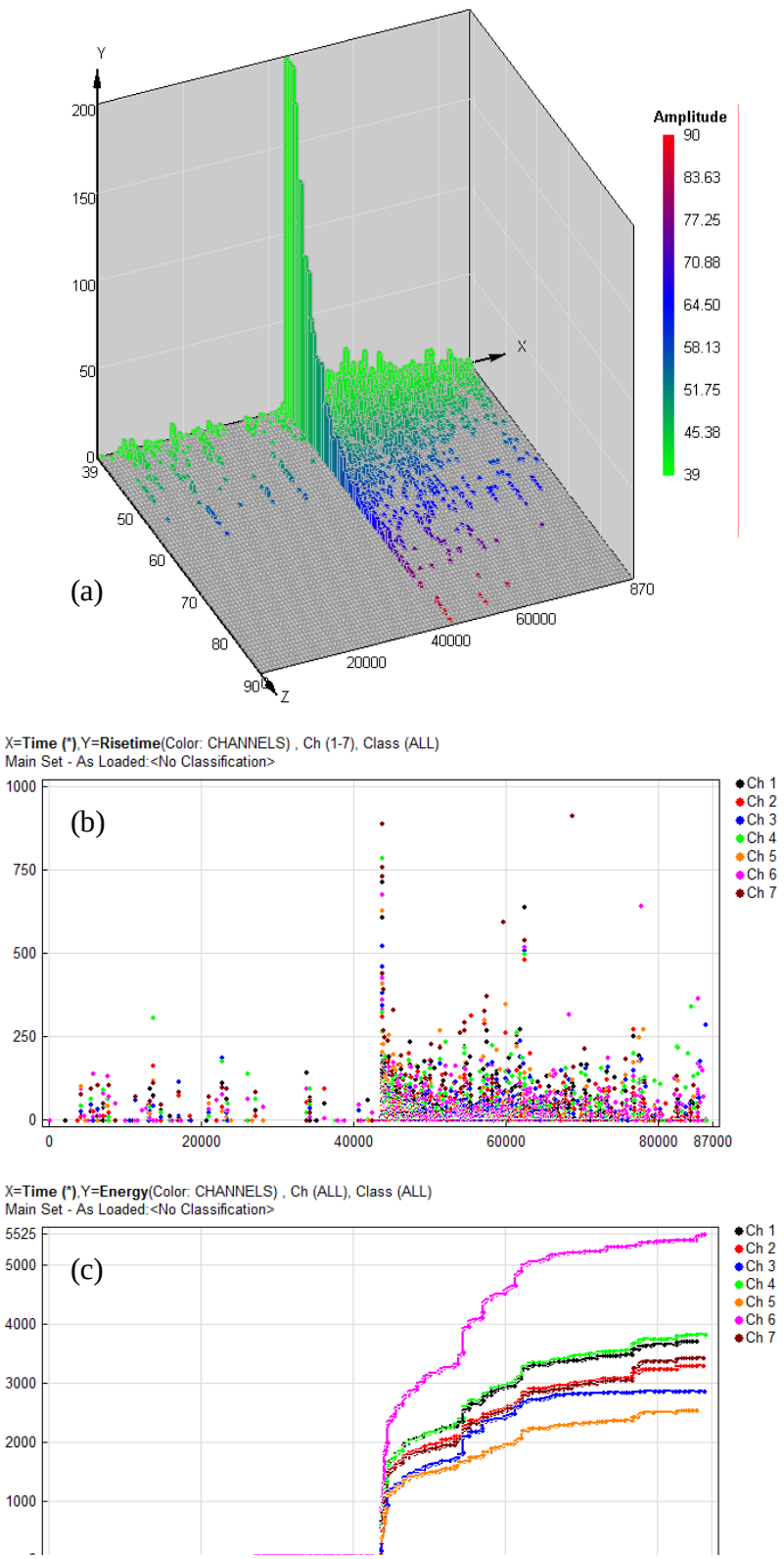

Figure 2. (a) Time evolution of the distribution of amplitudes of the recorded hits, during the 24-h monitoring of the concrete fracturing. (b), (c) the rise-time and the cumulative distribution of energy are shown, respectively.

References

[1] J. Xu, C. Zhai, L. Qin and G. Yu (2017). Evaluation research of the fracturing capacity of non-explosive expansion material applied to coal-seam roof rock, *Int. J. Rock Mech. Min. Sci.*, **94**, 103-111.

[2] T. Guo, S. Zhang, H. Ge, X. Wang, X. Lei and B. Xiao (2015). A new method for evaluation of fracture network formation capacity of rock, *Fuel*, **140**, 778-787.

Author's index

Author's index

Greek Society of Experimental Mechanics of Materials

The Greek Society of Experimental Mechanics of Materials (GSEMM), is a non-profit scientific body founded in November 2016, intending to contribute towards the production, promotion, pooling and dissemination of scientific knowledge, on issues related to the Experimental Mechanics of Materials. Since February 2017, GSEMM has been a member of the European Structural Integrity Society (ESIS).

Implementing one of the main aims of GSEMM, its Interim Board has undertaken the organization of the 1st International Conference of the Greek Society of Experimental Mechanics of Materials, an interdisciplinary Conference pursuing to cover a wide range of fields of Experimental Mechanics.

The prompt participation of a significant number of scientists and engineers from academia, research centers, research institutes and industry in this 1st International Conference, in order to present and discuss the latest scientific achievements in the field of Experimental Mechanics of Materials, sets the perspective for the successful continuation of this Conference.

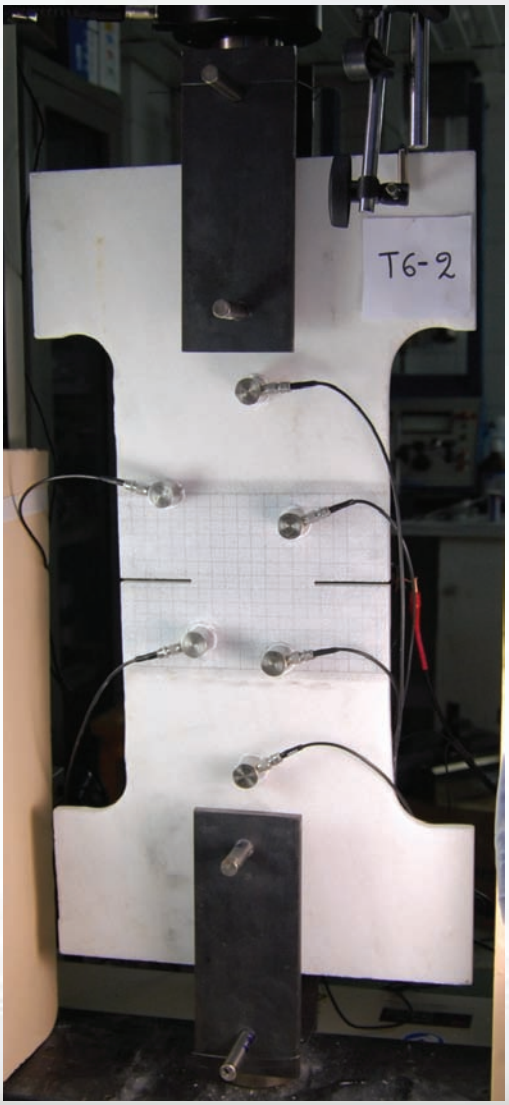

ISSN: 2623-3541